

NMR Imaging of Solids
with Multiple-Pulse Line Narrowing
and Radiofrequency Gradients

Thesis by
Margat Hoppe Werner

In Partial Fulfillment of the Requirements
for the Degree of
Doctor of Philosophy

California Institute of Technology
Pasadena, California

1993
(Submitted August 19, 1992)

*With what shall I come before the Lord
and bow down before the exalted God?
Shall I come before him with burnt offerings,
with calves a year old?
Will the Lord be pleased with thousands of rams,
with ten thousand rivers of oil?
Shall I offer my firstborn for my transgression,
the fruit of my body for the sin of my soul?
He has showed you, O man, what is good.
And what does the Lord require of you?
To act justly and to love mercy
and to walk humbly with your God.*

Micah 6:6–8

Dedicated to my family

Acknowledgments

I would like to thank my advisor Dan Weitekamp for making this all possible. I also owe many thanks to David Shykind, without whom the experiments described herein may never have happened, and to John Marohn for his participation in all aspects of this work. I wish him well as he continues this project. Thanks go to Tom Lenosky for his theoretical work, and to other members of the Weitekamp group who made my graduate school experience more pleasant than it otherwise could have been: K. D. Kurur, Steve Buratto, Dan Jones, Pedro Pizarro, Paul Carson, Len Mueller, Jack Hwang, and Herman Cho.

I thank Steve Sinton and Joe Iwamiya at Lockheed for their interest in this project, the samples they provided, and their help in implementing the imaging experiments on the MSL200.

I also want to thank the members of the Caltech Christian Fellowship for their love, prayers, and encouragement. Thanks for being my friends, guys! I especially thank Janice Peters and Keith Kuwata for long hours of proofreading and production assistance, and Laurine Tuleja for timely and much appreciated notes of encouragement.

Many, many thanks go to my husband Charlie for being the best of teammates: for providing much needed technical assistance, for being an endless (and entertaining) source of new ideas, for spurring me on when I was ready to give up, for being my best friend. I am deeply grateful to my family, Mom, Dad, and Bruce (and Angus too), for their love and support, letters and e-mail messages (keep 'em coming!); and to Charlie's family for

loving and encouraging me too.

Most of all, I thank God for teaching and sustaining me through these past six years: for providing family, friends, and coworkers to help me, for gently but firmly turning me around when I was headed down the wrong path, for being my source of hope and joy.

Abstract

The usual methods of magnetic resonance imaging fail in rigid solids due to the line-shape contributions of dipolar coupling, chemical shift dispersion and anisotropy, and bulk magnetic susceptibility. This dissertation presents a new method of solid-state imaging by nuclear magnetic resonance which averages away these contributions with multiple-pulse line-narrowing and encodes spatial information with pulsed radiofrequency field gradients. This method is closely related to simultaneously developed methods utilizing pulsed DC gradients, and offers similar improvements in sensitivity and resolution. The advantage of rf gradients is that they can be rapidly switched without inducing eddy currents in the probe or the magnet. In addition, the phases and amplitudes of the rf gradients can be switched by equipment which is already part of an NMR spectrometer capable of solid-state spectroscopy. The line-narrowing and gradient pulses originate in separate rf circuits tuned to the same frequency. Interactions between the circuits have been minimized by a method of active Q-switching which employs PIN diodes in the matching networks of these circuits.

Both one- and two-dimensional images are presented. The latter are obtained by a novel method in which the two dimensions of imaging transverse to the static magnetic field are encoded by two orthogonal components of a single rf gradient. A $\pi/2$ phase shift of the rf phase relative to that of the line-narrowing pulses selects one component or the other. This arrangement allows the solid-state analogs of versatile imaging sequences based on Fourier imaging and eliminates the need for sample rotation and back-projection

methods.

Coherent averaging theory is used to analyze this imaging technique and exact numerical simulations on several coupled spins are discussed. These lend insight to the residual linewidth and its dependence on pixel position as well as to the range of applicability of this technique.

Contents

Acknowledgments	iv
Abstract	v
1 Overview	1
2 Review of Solids Imaging	5
2.1 Introduction	5
2.2 Liquid-Like Techniques	9
2.3 Wide-Line Imaging Methods	10
2.4 Line-Narrowed Imaging	14
2.5 Other Nuclei	23
2.6 Spatially Selective Techniques	25
3 NMR Imaging of Solids with Multiple-Pulse Line Narrowing and RF Gradients	38
3.1 Introduction	38
3.2 RF Gradients	40
3.3 SWW-16	42
3.4 RF Coils	44
3.5 One-Dimensional Images	46
3.6 Conclusions	50

4	Theory and Simulations	55
4.1	Introduction	55
4.2	Average Hamiltonian Theory	55
4.3	Average Hamiltonian Treatment of Pulse Imperfections	56
4.4	Treatment of Gradient Pulses	64
4.5	Average Hamiltonian Including Finite Pulse Effects	65
4.6	Compensated Sets	70
4.7	Symmetric Placement of Gradient Pulses	72
4.8	Simulations	74
4.9	Conclusions	85
5	Two Dimensions of NMR Imaging from a Single Radiofrequency Gradient Coil	89
5.1	Introduction	89
5.2	The Quadrupole Coil	90
5.3	The Gradient Hamiltonian	94
5.4	Error Terms Introduced by the Gradient Pulses	100
5.5	Two-Dimensional Images	100
5.6	Resolution and S/N	122
5.7	Spatial Variation of the Phase of the Solenoid RF Field	127
5.8	Conclusions	133
5.9	Appendix: Calculating the Quadrupole Coil Gradient Term of the Average Hamiltonian	134
6	Experimental Apparatus	141
6.1	Introduction	141
6.2	Solids Imaging Probes	141

6.3	S/N Comparison of the Q-Switched Imaging Probe and a Standard Solids Probe	149
6.4	Gradient Strength of the Vertical Quadrupole Coil	150
6.5	Tuning the Spectrometer	156
6.6	Decoupling the Solenoid and Quadrupole Circuits	158
6.7	Previous Decoupling Schemes	160
6.8	Q-Switching	163
6.9	Conclusions	178
A	Modifications to the Homebuilt NMR Spectrometer	182
A.1	Second RF Channel	182
A.2	Improvements to the Receiver	183
B	Multiple-Pulse NMR Imaging of Solids with Radiofrequency Gradients on a Commercial Spectrometer	190
B.1	Imaging on the MSL200	190
B.2	External Logic Pulses	192
B.3	RF Amplifiers	193
C	Tuning and Matching Lumped Elements	195
C.1	Tuned Resonant Circuits	196
C.2	Tuned and Matched Resonant Circuits	200

List of Figures

3.1	SWW-16 for 1-D Imaging	43
3.2	RF Coils for 1-D Imaging	45
3.3	Schematic Imaging Probe Circuit	47
3.4	1-D Images of Two-Point Phantoms	49
4.1	Solid Echo Group	66
4.2	Solid Echo Timing	67
4.3	Solid Echo Groups of SWW-16	68
4.4	Solid Echo Groups of LW-24	72
4.5	A Model Five-Spin System	75
4.6	One-Pulse Simulation on the Model Five-Spin System	75
4.7	Comparison of DC and RF Gradients	78
4.8	Effect of Unwanted Gradient Terms	80
4.9	Effect of Unwanted Gradient Terms	81
4.10	Effect of Unwanted Gradient Terms	82
4.11	Comparison of SWW-16 and LW-24	84
5.1	The Ideal Quadrupole Coil	91
5.2	Four- and Eight-Wire Quadrupole Coils	92
5.3	SWW-16	94
5.4	RF Coils for 2-D Imaging	101

5.5	2D-FT Solid Imaging Sequence	103
5.6	Adamantane Spectra	104
5.7	Five Point Adamantane Phantom	106
5.8	1-D Projections of the Five-Point Adamantane Phantom	107
5.9	Two-Dimensional Image of the Five-Point Adamantane Phantom	108
5.10	Phase Cycling	109
5.11	Six Point Hexamethylbenzene Phantom	111
5.12	Hexamethylbenzene Spectra	112
5.13	Hexamethylbenzene Line-Narrowed Spectra	113
5.14	Two-Dimensional Image of HMB Phantom	114
5.15	One-Dimensional Projections of HMB Phantom	115
5.16	2D-FT Pulse Sequence for a Phaseable Image	118
5.17	Polyphenylene Sulfide Phantom	119
5.18	Polyphenylene Sulfide Spectra	120
5.19	Phased Image of Polyphenylene Sulfide	122
5.20	Magnitude Image of Polyphenylene Sulfide	123
5.21	Comparison of Phased and Magnitude Images	124
5.22	Two Water Phantoms	128
5.23	One-Dimensional Projections of a Single Capillary Tube of Water	129
5.24	Two-Dimensional Image of a Single Capillary Tube of Water	130
5.25	One-Dimensional Projections of Two Capillary Tubes of Water	131
5.26	Two-Dimensional Image of Two Capillary Tubes of Water	132
6.1	Probe for 2-D Imaging	143
6.2	Detail of the RF Coils	144
6.3	Detail of the Diodes	147

6.4	Low Power Tuning and Matching the Imaging Probe	148
6.5	A Signal-to-Noise Comparison: Two Signal Averages of a One-Pulse Experiment	151
6.6	A Signal-to-Noise Comparison: Sixteen Signal Averages of a One-pulse Experiment	152
6.7	A Signal-to-Noise Comparison: Two Signal Averages of SWW-16	153
6.8	A Signal-to-Noise Comparison: Sixteen Signal Averages of SWW-16	154
6.9	Four-Point Phantom for Measuring Gradient Strength	156
6.10	Four-Point Phantom Nutation Data	157
6.11	Demonstration of Coil Decoupling	175
6.12	Optoisolator Circuit for Bipolar PIN Diode Driver	176
6.13	Bipolar PIN Diode Driver	177
6.14	Low Power Diode Switching Time	178
A.1	New Transmit Control	184
A.2	New Receiver Front End	186
A.3	Audio Stage DC Voltage Reference	187
A.4	Audio Stage	188
B.1	MSL200 Configuration for Solids Imaging	191
C.1	Impedances of a Capacitor and an Inductor	196
C.2	Parallel Resonant Circuit	197
C.3	Parallel Resonant Circuit with Coil Resistance	197
C.4	Frequency Response of a Parallel Tuned Resonant Circuit	199
C.5	Series Resonant Circuit	199
C.6	Series Resonant Circuit with Small Resistance	200

C.7	Frequency Response of a Series Tuned Resonant Circuit	200
C.8	Series Tuned Parallel Matched Resonant Circuit	201
C.9	Parallel Tuned Series Matched Resonant Circuit	203

List of Tables

4.1	SWW-16 Toggling Frame Transformations.	63
4.2	Compensation of SWW-16 and LW-24 for Various Hamiltonian Terms. . .	73
5.1	RF Gradient Phase and Toggling Frame Values of I_x and I_y for SWW-16	98
5.2	Image Resolution	124
6.1	Comparison of Signal-to-Noise Ratios for a Standard Solids Probe and a Q-Switched Imaging Probe	150
6.2	Specifications for HP 5082-3203 PIN Diodes	168
6.3	Specifications for M/A-COM MA4P504 PIN Diodes	168

Chapter 1

Overview

This dissertation presents the design and realization of a new method of solid-state nuclear magnetic resonance imaging. The principle behind NMR imaging experiments is to encode spatial information as frequencies that can be measured by an NMR spectrometer. This is usually achieved through the Larmor frequency of the nuclei, which is directly proportional to the strength of the static magnetic field. Instead of performing an experiment in a highly homogeneous field, as is the case for high-resolution NMR spectroscopy, the field is made inhomogeneous through the application of linear field gradients. The spatial distribution of the spin density in the sample can then be recovered from the NMR spectrum.

Standard liquid-state imaging methods such as those used in medical applications generally fail to work for solid or solid-like samples where local variation in the internal fields present masks the effects of the applied gradients. The most promising solid-state imaging techniques utilize multiple-pulse line narrowing to remove the contribution of these internal fields from the solid lineshape, thereby increasing the signal-to-noise ratio and resolution obtainable.

A review of the work to date in solids imaging is presented in Chapter 2. Solid-state imaging, while introduced nearly two decades ago, is not as mature a technique as liquid-state imaging. Many groups have made contributions to this area of research, the vast majority of which have been studies of “liquid-like” solids or of liquids introduced

into solids. Imaging such samples is possible with standard, or only slightly modified, liquid-state techniques. While these studies have yielded useful information, the range of samples that can be imaged in this manner is limited. Techniques which are applicable to proton-rich rigid solids, of interest in materials research, fall under two general categories: those which accept the broad lines and those that actively narrow them by coherent manipulations in sample or spin orientation. To produce an image with acceptable resolution, techniques which provide no line narrowing require large gradient strengths and broad receiver bandwidths and therefore suffer from low signal-to-noise ratio. On the other hand, line-narrowing techniques allow much smaller gradient strengths to be used and, in some cases, smaller receiver bandwidths as well. Of all the line-narrowing techniques, multiple-pulse sequences provide the most complete line narrowing, provided that the sample is free of motions which occur with a correlation time similar to the multiple-pulse cycle time. While multiple-pulse sequences do require large receiver bandwidths to sample a few microseconds after an rf pulse, the noise bandwidth can be reduced to just several times the image spectral width, which is orders of magnitude smaller than in alternative methods. The resulting sensitivity gain allows a smaller pixel and thus a gain in resolution. Thus, multiple-pulse line narrowing is generally the technique of choice for imaging solid samples.

Chapter 3 presents the first one-dimensional images obtained by multiple-pulse line narrowing and pulsed radiofrequency (rf) gradients. The sequence used, SWW-16, reduces the linewidths of the solid samples by two orders of magnitude. These are also the first rf gradient images in which positive and negative spin nutation frequencies can be distinguished. This enables the rf gradient to pass from positive to negative field values within the sample and the full spectral width to be used in the image. The probe used in these experiments has two rf coils, one which delivers the homogeneous line-narrowing

pulses and one which delivers the gradient pulses. These coils are in close proximity and are tuned to the same resonance frequency, and so must be decoupled during the imaging experiment. A new means of actively decoupling rf coils was used. The images presented here also demonstrate the success of this new decoupling method.

Chapter 4 discusses SWW-16 in terms of average Hamiltonian theory, a time-dependent perturbation theory in which a propagator is expressed as a time-independent averaged Hamiltonian. Average Hamiltonian theory provides a convenient means to describe the net effect of multiple-pulse sequences on a spin system. This description includes analysis of residual interactions that interfere with the intended function of the pulse sequence. Here, average Hamiltonian theory is used to identify the cross terms that limit the line-narrowing capability of SWW-16. A new pulse sequence, LW-24, designed to eliminate the largest of these cross terms is also discussed. Included in this chapter are a series of exact numerical simulations which further characterize SWW-16 and LW-24. Simulations are presented which compare the theoretical performance of pulsed DC and rf gradients when used in SWW-16. Other simulations investigate the error terms introduced by the gradient coil arrangement used for 2-D imaging. Finally, the line-narrowing capabilities of SWW-16 and LW-24 are compared.

Chapter 5 presents the first two-dimensional images obtained using SWW-16. These are unique in that both dimensions are encoded with a single gradient coil, without recourse to sample rotation and back-projection. The quadrupole coil used in these imaging experiments is discussed as well as how the pulse sequence enables one gradient component at a time to affect the spins on average. The first multidimensional phased image of a rigid solid is also presented. The residual coupling between the coils is discussed, as well as the likelihood of a resolution-limiting problem with inhomogeneity in the phase of the solenoid rf field. Finally, there is a discussion of signal-to-noise and resolution

considerations.

Chapter 6 describes the novel experimental apparatus required for solids imaging by multiple-pulse line narrowing and pulsed rf gradients. Included are the probes for 1- and 2-D imaging. These were designed to be used in a wide-bore 4.7 T superconducting magnet. The procedure used to tune and match these probes is discussed, as well as an NMR nutation experiment used to measure the strength of the 2-D gradient coil. The signal-to-noise ratio available from the 2-D probe is compared with that available from a conventional probe for use in solid-state spectroscopy. Finally, the novel technique used to actively decouple the homogeneous and gradient rf coils is described. This is a form of active Q-switching requiring PIN diodes in the matching networks of the resonant circuits of both coils.

Some of the experiments discussed in this dissertation were performed on the home-built spectrometer located in the Weitekamp group laboratory. The modifications made to this spectrometer during the course of these experiments are presented in Appendix A. Other experiments were performed on a Bruker MSL200. The steps necessary to implement multiple-pulse rf gradient imaging on this spectrometer are described in Appendix B. Finally, a guide to tuning and matching NMR probes is presented in Appendix C.

Chapter 2

Review of Solids Imaging

2.1 Introduction

Nuclear magnetic resonance imaging has enjoyed tremendous progress in the two decades since it was first introduced by Lauterbur [1]. Applied to liquid systems, it has become a mature and sophisticated technique [2–4]. NMR imaging of solids was also first introduced nearly two decades ago [5]. Until recently, however, progress in solids imaging has been less dramatic. There has been increased interest in the field of solids imaging in the past few years as evidenced by several recent review articles [6–14].

In NMR, the resonance or Larmor frequency of the nuclei is directly proportional to the magnetic field strength they experience. In NMR imaging a magnetic field gradient applied in addition to the main homogeneous field B_0 causes a spread in the observed resonance frequencies. The spread in frequency of a given sample element is a function of the spatial position of that element along the gradient; therefore, the NMR “spectrum” in the presence of a field gradient is a one-dimensional projection of the spin density along the gradient. Multidimensional images can be obtained by rotating the sample with respect to the gradient (or vice versa) to obtain a series of spin-density projections. In this approach, the final image is reconstructed from the projections by means of a back-projection reconstruction algorithm [15]. Lauterbur’s original imaging experiment was performed in this manner, and many of the solids imaging techniques discussed below use back-projection reconstruction. Alternatively, a multidimensional NMR experiment

can be used to map the resonance frequencies of the spins subjected to two or more field gradients [16, 17]. This method, referred to as Fourier imaging because the image is reconstructed by means of a Fourier transform, is the one most frequently used in medical applications, all of which use liquid-state methods.

The basic difficulty with NMR imaging of solids is that the internal fields broaden the lines such that the effects of the applied gradients are masked. In solid materials, the molecular mobility is restricted and the dipolar spin interactions and chemical shift anisotropy are not averaged to zero by molecular motion. As a result, the linewidths can be as high as 50 to 100 kHz for protons in rigid polymers, compared to the 100 Hz, or smaller, linewidths of liquids in typical biomedical applications. In addition, any spatial variation of bulk magnetic susceptibility, as would be expected in heterogeneous samples, causes the magnetic field to be nonuniform throughout the sample. This effect also contributes to the linewidth of the sample.

The linewidth is an essential parameter which determines the spatial resolution. In order to resolve spins separated by a distance Δx along the direction of a gradient G_x , the gradient must induce a frequency spread greater than or equal to the linewidth $\Delta\nu$, that is, $\gamma G_x \Delta x / 2\pi \geq \Delta\nu$, where γ is the gyromagnetic ratio. Thus, in order to resolve broader lines, stronger gradients are required. For example, the maximum gradients currently used in NMR microscopy (50 G/cm) [10] yield a resolution of 5 μm for protons in water ($\Delta\nu = 100$ Hz) but would yield a resolution of only 1 mm for protons in a rigid organic polymer with a typical linewidth of 20 kHz. An even more serious problem is the need to sample the signal with very short dwell times, and hence very large acquisition bandwidths, in order to obtain a sufficient number of pixels in the image. The signal-to-noise (S/N) penalty inherent in such an approach is quite severe and hinders the possibility of imaging at high resolutions [4]. One solution to this problem is to record

images while manipulating the nuclear spin Hamiltonian such that the linewidth of the solid appears to be as narrow as that typically encountered in liquids.

The attainable resolution of NMR imaging is limited by physical factors including the linewidth and chemical shift of the NMR signal; diffusion processes and susceptibility gradients, both within the object and at its boundaries; and by technical factors such as magnetic field inhomogeneity or instability, non-linearity of the magnetic field gradients, and the achievable signal-to-noise ratio (S/N) [9]. For solids imaging, the limiting factor is the achievable (S/N), i.e., the number of nuclei producing the signal. NMR is an insensitive technique, with sensitivity rarely better than 2.5×10^{15} protons, which for typical polymers corresponds to a cube with edges of 30 to 40 μm [18]. Other limits to the resolution such as the gradient strength and the digital resolution are easily made finer than this. Because of the low sensitivity of NMR microscopy, it cannot presently achieve the resolution of optical microscopes (approx. 0.5 μm). A typical S/N -limited resolution for a solid-state image is 100 μm .

NMR imaging of solids is useful as a means of non-destructive evaluation (NDE). Non-invasiveness is a prerequisite for the investigation of properties dependent on sample shape or function. These include, for example, nonequilibrium distributions of heat or strain, transport phenomena, and the progress and extent of chemical reactions [6]. NMR imaging of solids is also a means of investigating the spatial variation of chemistry or physics in a sample which may be destroyed (for example, by slicing or by infiltration with liquid). Here NMR is useful because it offers forms of contrast (e.g., relaxation times T_1 , T_2 , and $T_{1\rho}$) that are unavailable from other imaging techniques. Suggested applications of NMR include the following [9]: imaging of spin density leading to quantitative concentration measurements; chemical shift selective imaging for determining spatial distribution of substances in a sample; investigation of dynamic processes via relaxation-time weighted

images; evaluation of dynamic properties by determining diffusion constants of differing chemical species; spectroscopy of defined partial volumes of the whole sample or multidimensional spectroscopic imaging. Some examples of applications to the field of materials research include pore-distribution in an unsintered ceramic measured by proton-density images of absorbed fluids; distribution of the low molecular weight polymers and waxes used as binding agents in unsintered ceramics; fluid (e.g., water or solvent) distribution and diffusion within polymers; inhomogeneous temperature distributions, e.g., in melts; cross-linking of polymers as a function of spatial and relaxation-time-dependent values; diffusion processes from fluids into solids and interfluid diffusion [9].

NMR imaging of solids provides a means to answer several important questions in materials research. For example, what is the relationship between structure and function? This is an important consideration for the composite materials used in aerospace applications. These composite materials are typically a polymer matrix filled with solid particles (e.g., aluminum). The solid particles are often introduced by mixing with a viscous polymer melt which is later cured to a solid matrix. The uniformity of the solids concentration throughout the cured composite is of great importance to its end use and mechanical properties. Ideally, this question can be answered by NMR where T_2 or proton density is used as a contrast agent to distinguish between polymer matrix and solid particles [8].

Other parameters important in determining the macroscopic properties of various heterogeneous materials include: the degree of crystallinity of semicrystalline polymers, the phase structure in polymer blends and copolymers, the pore size and binder distribution in green-state ceramics, and changes in chemical or physical composition, such as stress-induced crystallization in rubber-elastic materials [10]. Flow-induced molecular orientation and local changes of molecular mobility as a result of distributions in plasti-

cizer concentrations are important considerations in the fabrication of high-tech polymer products.

Solid-state NMR imaging can be applied for the nondestructive analysis of these and other heterogeneities. Structures above 10 μm can potentially be investigated using solid-state NMR imaging techniques. These can be designed to yield not only spatial information, but also information on molecular order, molecular mobility, and chemical structure [10].

2.2 Liquid-Like Techniques

Because of the large natural linewidths encountered in imaging of solids, most such work to date has involved imaging liquid already present in, or added to, the solid material. The structure of the solid material is then deduced from the image of the fluid-filled pores. In these instances, images can be obtained with methods similar to those of medical imaging. Such techniques have been used to investigate the packing and concentration distributions in liquid chromatography columns [21] and colloidal suspensions [22], the distribution of binder and the porosity of green-state ceramics [7,40–47], and the uptake of penetrant by solids [23–39]. NMR studies of solvent ingress in glassy polymers have focused on anomalous diffusion behavior [26, 27, 29, 31, 32, 35]. Liquid-state imaging techniques have also been used to image the natural water content in wood [74–78]. These images have been useful in studying the internal structural features of wood [75], clearly delineating the growth rings, knots, and heartwood [74]. There have been similar studies of fluids in porous rocks [57–64] as well as in other porous systems, including clays and cements [65–68]. Here imaging has been used to characterize the voids present, as well as to visualize filtration and flow through the porous media. Finally, liquid-state imaging studies of oil core samples have been used to determine several core properties includ-

ing porosity, bulk density, grain density, oil and water saturations, lithology, pore-size distribution, oil viscosity, wetting state, and diffusion coefficients [57, 59].

Some physically solid materials possess high molecular mobility and near liquid linewidths. For example, typical proton linewidths in rubbers include 600 Hz for *cis*-poly(isoprene) and 2 kHz for poly(isobutylene) [10]. This is still sharp enough that reasonable images can be obtained with conventional NMR imaging techniques. With a slightly modified gradient system, but otherwise standard liquid-state NMR apparatus and pulse sequences, it is possible to image solids with T_2 relaxation times as short as 0.5 ms [19]. Many elastomers can be investigated by conventional imaging techniques. To date, NMR imaging studies of elastomers have focused on detecting inhomogeneities [48–55], phase separation [56], and effects from stress-induced crystallization and aging [6, 56]. Similarly, waxes and adhesives have near-liquid linewidths. Waxes used as binders in ceramics have been imaged by conventional means [7, 42, 44, 46]. The removal of solvent during the cure of adhesives has also been monitored by liquid-state imaging [69–73].

For the imaging of polymers below the glass transition and solids with low molecular mobility, however, these liquid-state techniques fail. One solution to this problem is to elevate the temperature of the solid sample, thereby increasing molecular motions and T_2 , and then perform imaging with standard liquid-state techniques. Liquid-state imaging has been demonstrated on a heated sample of poly(vinyl acetate) [20]. Often, heating the sample is not an option, in which case a different imaging technique is required.

2.3 Wide-Line Imaging Methods

True solid-state imaging techniques can be divided into two broad categories: those which improve spatial resolution while accepting the low sensitivity associated with broad lines (i.e., wide-line methods) and those which improve both sensitivity and spatial res-

olution (i.e., line-narrowing methods).

In wide-line methods improved resolution is obtained by using larger gradients, by employing phase encoding during constant evolution times, or by increasing the effect of the gradient by using multiple-quantum coherence to phase encode spatial information. These techniques are discussed below.

2.3.1 STRAFI

Samoilenko and coworkers have used the very large gradient of the fringe (or stray) field of the main superconducting magnet in a brute force method of solids imaging named stray field imaging or STRAFI [79, 80, 81]. Every solenoid magnet has a region near the end of the magnet windings where there is a very large magnetic field gradient which can be used for imaging [79]. The region corresponding to the largest magnetic field gradient has a field strength of approximately 0.4 times the field strength of the homogeneous region of the magnetic field. The maximum gradient varies with the central field strength of the magnet, being about 40 T/m for a 4.7 T magnet. The gradient is homogeneous over a disk approximately 30 mm in diameter for a wide-bore magnet.

The basic idea of STRAFI is to apply an rf pulse train to the sample as it sits in the magnetic field gradient. Since the gradient is extremely large, the rf pulses selectively excite a plane transverse to the gradient. The selected plane has a thickness on the order of 100 μm . The sample is translated along the direction of the gradient, and additional slices are excited. Each slice is observed separately, eliminating the need for a relaxation delay and allowing successive slices to be scanned quite rapidly. The signal can also be measured as a series of echoes in a pulsed spin-locking train. This can be used both to enhance the sensitivity of the measurement and to introduce contrast. Each scan of the sample through the gradient yields a spin density projection directly without a Fourier transformation. For multidimensional imaging, additional projections are obtained by

rotating the sample with respect to the gradient. The final image is acquired by back-projection reconstruction.

Images of an IC socket with the metal leads still in place and of a plexiglass (polymethylmethacrylate) phantom have been obtained by this method. The image of the PMMA phantom shows 100 μm resolution.

One difficulty of STRAFI is that the probe, which must reproducibly reorient the sample about two orthogonal axes and translate it along a third, all the while in a strong magnetic field, is quite complex. Another point against STRAFI is that because a large static magnetic gradient is used, spectroscopic information is lost. Thus it is not possible with this technique, as it is with others, to combine imaging in one dimension with spectroscopy in another.

2.3.2 Constant Time

The second wide-line imaging technique is the constant time (or phase encoding) imaging scheme first demonstrated on solids by Emid and Creyghton [82]. Constant time imaging relies on the fact that when a spin system evolves under the influence of a series of commuting Hamiltonians, for example the secular components of the chemical shift, susceptibility, and dipolar coupling Hamiltonians, and the gradient Hamiltonian, the evolution is strictly the sum from each Hamiltonian. By manipulating the gradient strength, then, it is possible to separate the effect of the gradient Hamiltonian from that of the secular internal Hamiltonians. With this technique, images can be obtained with only modest field gradients.

Constant time techniques encode spatial information into one dimension of a two-dimensional data set. In this manner, improved spatial resolution is attained at the cost of increased imaging time. Spatial encoding occurs during the evolution time t_1 . The evolution time is kept constant and the gradient is changed incrementally in the series of

acquisitions that make up the two-dimensional data set. Since the t_1 dimension is time independent, the spin evolution due to chemical shifts, susceptibility shifts, and dipolar couplings is constant and unobserved. On the other hand, the gradient interaction is not constant, so the spin evolution due to the gradient is observed. Unfortunately, although the undesired interactions do not contribute to the observed linewidth, they do cause an attenuation of the signal intensity. Nothing has been done to lengthen the apparent T_2 of the sample, so only a very short t_1 window is available for a typical solid.

One advantage of constant time techniques is that the second dimension can be used to encode spectroscopic information. In addition, line-narrowing methods which retain linear terms in the spin Hamiltonian can be introduced during the t_1 to recover some of the S/N loss. Types of line-narrowing which have been incorporated into t_1 include solid echoes [83–86], Jeener-Broekaert echoes [86, 87], magic echoes [88–91], rotary echoes [91], magic angle spinning (MAS) [92], and multiple-pulse line narrowing [93]. It is not possible in true fixed-gradient experiments to remove linewidth due to chemical shift dispersion.

Although quite time consuming, the constant time technique is a robust one, being extremely insensitive to artifacts [13].

2.3.3 Multiple-Quantum Imaging

Multiple-quantum imaging overcomes limited gradient strengths by encoding the gradient evolution in a state of n -quantum coherence [94]. This has two advantages: first, an n -quantum coherence evolves n times more rapidly in a field gradient than the usual single-quantum coherence; and second, some multiple-quantum transitions have considerably narrower lines. Because multiple-quantum coherences cannot be observed directly, however, multiple-quantum imaging experiments are always two-dimensional or higher.

Multiple-quantum imaging has been used to image protons in adamantane [94]. A double-quantum version has been used to image deuterons in ring-deuterated poly(styrene)

and poly(carbonate) [96]. The double-quantum transition of $I = 1$ nuclei is insensitive to the strength of the quadrupole interaction, and so it is possible to obtain images with a resolution on the order of $100 \mu\text{m}$ (which is orders of magnitude better than that achievable by imaging with conventional ^2H wide-line spectra) [96]. In this experiment, spatial encoding occurs during t_1 in the presence of double-quantum coherence. The double-quantum coherence is then converted back to single-quantum coherence, and the full ^2H wide-line spectrum is acquired during t_2 . The final image, then, has spatial information along the ω_1 axis and spectroscopic information along the ω_2 axis. Since the deuteron wide-line spectral lineshapes are very sensitive to the degree of molecular order and to the different types and time-scales of molecular motion, this is an image of molecular mobility. The multiple quantum imaging technique is a good choice only in cases where the highest order coherence of a spin or small group of isolated spins can be created efficiently. Usually, as for deuterons, this requirement results in the need for chemical labeling of the material [10].

2.4 Line-Narrowed Imaging

In general it is desirable to have an imaging technique that improves the sensitivity as well as the resolution. This can be achieved by the various line-narrowing techniques discussed below. These make use of the fact that it is possible to manipulate Hamiltonians during an experiment so that, effectively, those of interest are kept and the remainder are discarded. The Hamiltonians describing the spin interactions that cause line broadening, in particular the dipolar interaction and the chemical shift, have factors which depend on the states of the spins and factors which depend on their spatial orientation in the magnetic field. Thus, either the states of the spins or their spatial orientations may be manipulated to effect line narrowing. Three types of line-narrowing have been used in

solids imaging: magic angle spinning (MAS), magic-angle rotating frame (MARF), and multiple-pulse sequences.

2.4.1 MAS Imaging

In magic angle spinning, the sample is rotated rapidly about an axis inclined at an angle of 54.7° to the magnetic field. The motion of the sample averages spatially inhomogeneous spin interactions, such as the chemical shift, to their isotropic values. Dipolar interactions are averaged to zero if the spinning rate greatly exceeds the dipolar linewidth. Magic angle spinning is a simple method for averaging homonuclear and heteronuclear dipolar couplings for those materials with dipolar linewidths less than approximately 10 kHz.

The idea for MAS imaging was patented by Wind and Yannoni [97], although they did not attempt the experiment. All implementations of MAS imaging to date have made use of synchronously rotating gradients [92,98–104], i.e., field gradients rotating at the same frequency as the spinner so that each point in the sample experiences a time-independent magnetic field. When this is the case, any technique for imaging in a static gradient may be applied, but now the implementation is in the frame rotating with the spinning sample. MAS imaging has been combined with back-projection reconstruction [100] as well as 2-D Fourier transform (2D-FT) techniques [98].

With MAS imaging, spatial resolution better than $50 \mu\text{m}$ has been obtained for proton images of polymers [92]. ^1H images of a poly(isoprene) phantom have been obtained, which showed sample deformation due to centrifugal forces [92]. Images of polybutadiene/polystyrene blends have also been reported [92]. Here the MAS successfully line-narrows the polybutadiene fraction of the sample, but the large homonuclear couplings of the rigid polystyrene fraction are not eliminated by the 5 kHz of MAS; thus, the polystyrene fraction is not observed. MAS can also be combined with multiple-pulse line

narrowing (CRAMPS) for cases in which the linewidths are too broad to be averaged by MAS alone. CRAMPS imaging has been achieved in a limited number of experiments [103]. CRAMPS imaging is similar to multiple-pulse line narrowing with a static magnetic field gradient, discussed below, in that it leads to a spatially varying image resolution. As is the case with multiple-pulse line narrowing, pulsed gradients would solve this problem, but these have not yet been implemented in combination with CRAMPS [13]. MAS imaging with non-synchronously rotating gradients has also been proposed but not implemented [105, 106].

While MAS imaging does not have the low receiver duty cycle problem discussed below for multiple-pulse line-narrowing imaging techniques, it has several limitations. First, the size of the sample is restricted to the size of the spinner, which is typically a cylinder 5 mm wide and 12 mm high. Also, this technique is best suited for samples that do not deform under the several kilohertz of MAS. Finally, in order to produce magnetic field gradients which rotate with the sample, considerable modifications to standard imaging equipment are required.

2.4.2 Rotating-Frame Imaging

Similar in spirit to MAS imaging is magic-angle rotating-frame (MARF) imaging, a technique in which the sample remains stationary while the effective field is rotated at the magic angle [107, 108, 109]. In MARF imaging, the rotating effective field is the vector sum of an rf field and a resonance offset. The effective resonance frequency in the magic-angle rotating frame is much lower than the Zeeman frequency in the static field. By superimposing a magnetic field gradient and a radiofrequency magnetic field gradient, the MARF condition can be fulfilled simultaneously throughout the sample. MARF results in line-narrowing (dipolar broadenings vanish and linear spin interactions are scaled by $1/\sqrt{3}$) provided the spin evolution is followed in the magic-angle rotating

frame.

In one version of MARF imaging, a short rf pulse tips the spins to the magic angle and the spins are locked at this orientation by means of simultaneous B_1 and B_0 gradients [109]. Audiofrequency pulses are applied to tip the spins into a plane perpendicular to the spin-locking axis so that an image may be detected. Note that audiofrequency pulses in the MARF act like rf pulses in the rotating frame. Any audiofrequency pulse sequence can be applied, for example spin-echo or solid-echo [109].

The hardware required for MARF imaging is rather demanding. For simplicity, thus far the audiofrequency pulses have been applied along z . The effective audio field strength is then scaled accordingly. Also for simplicity, a single coil has served the double purpose of creating both the rf and dc gradients. Two-dimensional images have been generated by back-projection reconstruction with sample rotation. The degree of line-narrowing possible with MARF is at least an order of magnitude less than with the multiple-pulse techniques reviewed in the following section.

2.4.3 Multiple-Pulse Line Narrowing

For rigid samples, multiple-pulse sequences provide improved line narrowing compared with MAS and MARF. Multiple-pulse sequences can be designed to eliminate chemical shift and bulk magnetic susceptibility contributions to the solid linewidth, in addition to the dipolar contributions. A simple form of multiple-pulse line narrowing with imaging was first demonstrated in a one-dimensional experiment, the original solids imaging experiment, by Mansfield and Grannell [5] and improved pulse sequences were suggested. Multiple-pulse line-narrowing approaches to solids imaging can be grouped into three categories according to the type of gradient modulation used: static gradients, oscillating gradients, and pulsed gradients.

Static Gradients

Because of their simplicity, static gradients are widely used in multiple-pulse imaging. The first one- [5] and two-dimensional [93] images of solids were obtained by this approach. The multiple-pulse sequence most frequently used in imaging experiments with static gradients is MREV-8, which is a robust pulse sequence that is compensated for many sources of experimental imperfections [113, 114, 115]. In this technique, the image is generally acquired after the gradient has been turned on and allowed to stabilize [5, 116, 117]. If no gradient switching is used, multidimensional images must be generated by back-projection reconstruction techniques. For example, by this method Botto and coworkers have obtained 2-D ^1H images of coal [116], and 3-D ^1H images of the rigid polymer polycarbonate [117]. In the latter experiment, the resolution was $150\ \mu\text{m}$ in all three dimensions. Sinton *et al.* have also used MREV-8 in the presence of a constant gradient to image ^{27}Al in the solid powder of solid rocket fuel [54].

MREV-8 line-narrowing has also been used during the evolution and detection periods of a two-dimensional imaging sequence [93]. Using static gradients in a 2D-FT multiple-pulse imaging experiment requires that the gradient direction be switched between the evolution and detection periods. In order to switch the direction of the gradient in the middle of the experiment, and avoid the difficulty of gradient settling time, the magnetization can be stored [136] along the Zeeman field or along a spin-locking field while the gradients are switched. The relaxation which occurs during this storage period (T_1 if the magnetization is stored along the Zeeman field and $T_{1\rho}$ if it is stored along a spin-locking field) can also be used as a source of contrast. For example, Chingas *et al.* recorded separate images of the neoprene rubber and adamantane components of a single phantom [93].

The spin evolution in the presence of MREV-8 in combination with line-narrowing

is a combination of chemical shift, bulk magnetic susceptibility, and gradient spin evolution. Ideally, the gradient is made sufficiently large that the other contributions can be ignored. It would be desirable, instead, to use a multiple-pulse sequence which eliminates chemical shift and susceptibility contributions (collectively referred to as linear inhomogeneous contributions) to the linewidth. However, since the Hamiltonian describing a static gradient has the same form as the secular chemical shift Hamiltonian, a multiple-pulse sequence that eliminates inhomogeneous contributions to the linewidth also eliminates the effects of static gradients. Thus, the first main problem with static magnetic field gradients is that the line-narrowing is not as efficient as it could be. The second main problem is that the line-narrowing efficiency of the multiple-pulse cycles varies with resonance offset. Since a static magnetic gradient behaves as a resonance offset, line-narrowing is not as efficient at the edges of the image. Using oscillating gradients in combination with multiple-pulse sequences solves this first problem, while using pulsed gradients solves both the first and second problems.

Oscillating Gradients

Multiple-pulse sequences have also been combined with audiofrequency gradients in a technique referred to as “refocused gradient imaging” [119, 120]. During the course of the pulse cycle, the effective field describing the average Hamiltonian is periodically reversed. By modulating the gradient strength synchronously with this, the spin evolution due to the gradient can be made to “refocus” and so accumulate over the cycle. The time-dependence of oscillating gradients means that pulse sequences can be designed to average the chemical shift and susceptibility shift while preserving the gradient spin evolution. Also, since the gradient is periodically zero, the zero point can be made to coincide with the rf pulses to avoid off-resonance effects during the rf pulses. It has been shown, however, that the gradient spin evolution between rf pulses has a greater influence on the

cycles' line-narrowing efficiency than the off-resonance effects during the rf pulses [118].

Synchronously oscillating gradients were first used with the Carr-Purcell sequence [119, 120, 121] to preserve gradient-induced evolution while eliminating chemical shift evolution. The Carr-Purcell sequence does not average homonuclear dipolar interactions, however, so is not useful for ^1H imaging in rigid solids. Oscillating gradients have been used with solid-echo pulse sequences to image ^{19}F and ^1H in solids [122–125]. Oscillating gradients have been combined with the Carr-Purcell sequence for ^{13}C solids imaging, and also with MREV-8 for ^1H solids imaging by Miller *et al.* [126–129].

Pulsed Gradients

In order for the gradient to produce the maximum spin evolution per multiple-pulse cycle, and also the minimum interference with the line-narrowing process, it must be pulsed. Pulsed gradients avoid the spatial dependence on resolution that is seen with multiple-pulse methods employing static or oscillating gradients. That pulsed gradients yield superior resolution compared to static gradients was shown by Miller *et al.* [118]

The first pulsed gradient imaging experiments used the pulse sequence MREV-8 and so did not, in fact, remove chemical shift effects [118, 112]. By this method, one-dimensional images of ^1H in Mylar film were obtained with a resolution of about $100\ \mu\text{m}$ [118]. One-dimensional images of ferrocene were also obtained to demonstrate the improvement in resolution available by sampling the magnetization more than once per cycle [112]. It was recognized, however, that in addition to encoding spatial information, the pulsed gradients were providing a means of “second averaging” the chemical shift. Briefly, the gradient evolution occurs about an axis which is not parallel with the MREV-8 effective field (the apparent axis about which chemical-shift induced evolution occurs). Provided that the gradient evolution is large with respect to the chemical shift terms, the chemical shift terms can be viewed as rotating about the gradient axis and

thus may be diminished in the zeroth- or higher-order Hamiltonian. In the original experiments [118, 112], however, the gradient and chemical shift axes were not orthogonal, so the chemical shift contributions were reduced but not eliminated.

By correctly choosing the amplitude of the gradient pulses and their placement in the MREV-8 sequence, the effective gradient Hamiltonian can be chosen to be orthogonal to the chemical shift effective Hamiltonian [131]. In this case, the second averaging observed is more complete [131, 130, 150]. One catch to using the gradient as a means of second averaging, though, is that if the gradient passes from negative to positive field values within the sample, there is a sample region which effectively experiences zero amplitude gradient pulses. Second averaging fails in this region. To correct for this, Garraway and coworkers introduced a phase shift to four of the pulses of each MREV-8 cycle. This phase shift behaves as a time-dependent resonance offset and so adds a constant term to the gradient Hamiltonian, thus effectively removing (or at least shifting) the region of zero gradient amplitude [131, 130, 150]. Using this technique, images of a polymethylmethacrylate phantom have been obtained with a resolution of approximately $100\ \mu\text{m}$ [131].

Removing chemical shift effects by second averaging works for ^1H because the range of chemical shifts is fairly small. A more robust method of suppressing chemical shifts is to eliminate them in a “first averaging” rather than in a “second averaging” sense. This can be done by means of multiple-pulse sequences specifically designed to eliminate *all* static contributions to the linewidth, not just the dipolar contributions. The sequence originally proposed, but not implemented, for imaging with pulsed gradients was such a sequence [5]. These sequences have since been named “time-suspension” sequences [132]. The difficulties associated with pulsing large DC gradients in the few microseconds of a typical multiple-pulse window, however, were unsurmounted until only very recently [134].

The first solids images produced using a time-suspension sequence and pulsed DC gradients were 1-D images of ferrocene and pressure-crystallized polyethylene [132]. The resolution obtained was $30\ \mu\text{m}$ for the ferrocene image and $300\ \mu\text{m}$ for the polyethylene image. This technique has also been used to study the solid state reaction of ammonia gas with substituted benzoic acid crystals [133]. The 1- and 2-D images obtained revealed an unexpected reaction anisotropy, probably due to crystal imperfections. The technology for creating short DC gradient pulses is still evolving. At this point, gradient coils of low inductance are still required [134, 13].

As suggested by Weitekamp and coworkers, another option is to use pulsed radiofrequency (rf) gradients (gradients in the transverse B_1 field), rather than pulsed DC gradients (gradients in the main B_0 field) [111]. It is technically easier to switch rf gradients in the microseconds necessary for their combination with multiple-pulse sequences. The rf amplifiers and phase-shifting networks necessary to generate rf gradient pulses necessary are identical to those already used in solid-state NMR spectroscopy. The novel experimental apparatus required is just a probe capable of delivering rf line-narrowing pulses and rf gradient pulses to the sample. The rf coils required for this must be tuned to the same frequency, so it is also necessary to actively decouple them. The remaining chapters of this dissertation describe the first experimental implementation of solid-state imaging with multiple-pulse line-narrowing and radiofrequency gradients, including a new method for the active decoupling of rf coils, and theoretical and numerical studies of this technique.

2.5 Other Nuclei

2.5.1 Spin = 1/2

All the imaging experiments described in this dissertation, as well as most solid-state imaging experiments to date, have ^1H as the observed nucleus. Several nuclei other than ^1H have been used in solid-state imaging, however. While the lower gyromagnetic ratio and natural abundance of ^{13}C make it much less sensitive than ^1H , it has the potential of offering more chemical information, as well as different modes of contrast, than ^1H and is often the nucleus of choice for solid-state NMR studies of polymers [13].

At natural abundance in organic materials and polymers, ^{13}C has a small probability of having another ^{13}C spin close enough to produce a significant homonuclear dipolar interaction. ^{13}C does experience heteronuclear dipolar coupling with attached protons, but because of the reduced ^{13}C gyromagnetic ratio, this is usually an order of magnitude less than the 20 kHz dipolar linewidths commonly experienced for protons in rigid polymers. In addition, the ^1H - ^{13}C dipolar broadening can be reduced substantially by continuous irradiation of the proton resonances during detection of the ^{13}C FID [137], provided the nutation frequency (i.e., $\gamma_H B_1$) exceeds the dipolar interaction strength. The chemical shift and magnetic susceptibility broadening must still be removed. The anisotropic shift can be removed by employing magic angle spinning methods [102]. Alternatively, all chemical shift effects, as well as the heteronuclear dipolar coupling, can be removed by employing a Carr-Purcell pulse train. This has been demonstrated in 1-D ^{13}C images by Maciel and coworkers [136, 138]. In these experiments the gradient was applied during the evolution period t_1 and the Carr-Purcell pulse train during detection t_2 . Miller and Garrowsay have demonstrated 2-D ^{13}C refocused gradient images in which oscillating gradients were combined with the Carr-Purcell pulse train during t_2 [128].

The low sensitivity of ^{13}C associated with its small gyromagnetic ratio can be partially

compensated by the use of Hartmann-Hahn cross-polarization to transfer spin polarization from the ^1H nuclei to the ^{13}C nuclei [136, 138, 128]. In instances where paramagnetic centers are present, enhancement is also possible by Dynamic Nuclear Polarization (DNP) in which the paramagnetic electron spin resonance is pre-irradiated and polarization is transferred from the much larger electron spin moments. DNP can be combined with imaging to obtain spatial images of paramagnetic centers responsible for the DNP phenomenon and has been used in ^{13}C images of pitch yielding transverse resolution below 1 mm [137].

Like ^{13}C , ^{19}F is also an appealing nucleus for polymer imaging applications. Several groups have obtained ^{19}F images using techniques nearly identical to those used in ^1H solid-state imaging [80, 123, 142, 140]. For biological studies, particularly those of bone, there is interest in ^{31}P imaging [84, 85, 141]. Ackerman *et al.* have used a slightly modified version of the gradient-echo liquid-state imaging technique to image synthetic calcium hydroxyapatite, which is roughly representative of the inorganic phase of vertebrate mineralized tissue [141]. Li has used solid echoes and refocused gradients in a phase-encoding technique to image sections of bone cleaned of their organic matter [84, 85]. Finally, ^{11}B [144, 143], as well as the quadrupolar ^{27}Al , has shown promise for studies of ceramics [143, 139].

2.5.2 Quadrupolar Nuclei

There have also been a few studies of solid-state imaging using various quadrupolar nuclei. Quadrupolar nuclei are significant because they are ubiquitous in inorganic materials and provide a sensitive probe of the local environment.

The studies of Suits and coworkers have focused on systems which have naturally narrow resonances. In one case they used a standard back-projection reconstruction technique to image ^{23}Na distribution in a β -alumina crystal [135]. Because of the high

mobility of the sodium ions in the superionic crystal, the ^{23}Na spectral width was only 1.1 kHz. In another study, the sensitivity of the ^{81}Br quadrupole resonance frequency to temperature variations was used to image an inhomogeneous temperature distribution in KBr [161]. A third study examined the spatial variation of ^{23}Na signal intensity in NaCl resulting from an impact-induced inhomogeneous defect distribution [160]. The quadrupolar ^{23}Na nuclei is a sensitive probe of defect densities in solids; it was estimated that defect densities as low as 10^6 or 10^7 cm^{-2} could be detected for measurements with a good signal-to-noise ratio [160].

Spiess and coworkers have obtained spectroscopic images of deuterated solids using ^2H [96, 104]. In one case, the gradient spin evolution was encoded in a state of double-quantum coherence. This has the advantage that the effective gradient strength is doubled and that the double-quantum transition of ^2H is not broadened by the quadrupole coupling to first order. The experiments were performed such that spatial information was encoded during t_1 and the full wide-line spectrum encoded during t_2 . In this manner the orientation of the polymer studied with respect to the static magnetic field could be determined [96]. The second study used ^2H MAS with synchronous gradients to obtain spectroscopic images which could clearly distinguish between deuterated samples of polystyrene and polycarbonate [104].

2.6 Spatially Selective Techniques

Spatially selective excitation techniques applicable to solids imaging are in a state of infancy. The vast majority of slice selection to date has been by sample cutting. Slice selective rf excitation techniques will be important in NDE applications of solid-state imaging in which the sample has no known symmetry. Due to the broad linewidths of solid samples, the shaped rf pulses used for slice selection in liquid-state imaging are not

useful in solid-state imaging. In general, however, it should be possible to create analogs of liquid-state slice selection techniques since line narrowing sequences reduce the effective Hamiltonian to that of a two-level system.

Wind and Yannoni proposed spin-locking as a wide-line approach to slice selection in solids imaging [145]. In this experiment, a weak rf spin-locking field selectively preserves those spins whose resonance offsets are close to the spin-locking frequency. For this to be effective, however, the spin-locking field must be stronger than the dipolar linewidth. One modification to spin-locking slice selection is to incorporate magnetization storage during the gradient switching, thereby reducing the S/N loss incurred [158, 147].

Another wide-line sensitive-slice method was devised by Rigamonti and coworkers [152]. A series of FID's are coadded after applying a nominal $\pi/2$ pulse in the presence of a linear gradient which is stepped in equal increments. The signal arising from the sensitive slice at the zero crossing point of the gradient increases while other signal averages to zero over a sufficient number of acquisitions. A few other slice-selection techniques have been presented [154, 155, 156].

One line-narrowed approach to slice-selection has been demonstrated by Garroway and coworkers [153]. This uses a homonuclear dipolar-decoupled DANTE sequence, which is a composite of the second-averaged MREV-8 sequence discussed above and the DANTE sequence used for selective excitation in liquid-state NMR.

In addition to slice selection, there is interest in obtaining images from a selected volume of a large sample, for example a sample too large even to fit inside a conventional superconducting magnet [13]. The use of a surface coil to obtain images from a selected volume of a large solid sample has been investigated by Garroway and coworkers [146, 151, 150].

References

- [1] P. C. Lauterbur, *Nature* **242**, 190 (1973).
- [2] P. Mansfield and P. G. Morris, "Advances in Magnetic Resonance," Supplement 2, (J. S. Waugh, Ed.), Academic Press, New York, 1982.
- [3] P. G. Morris, "Nuclear Magnetic Resonance Imaging in Medicine and Biology," Clarendon Press, Oxford, 1986.
- [4] P. T. Callaghan, "Principles of Nuclear Magnetic Resonance Microscopy," Clarendon Press, Oxford, 1991.
- [5] (a) P. Mansfield and P. K. Grannell, *J. Phys. C: Solid State Phys.* **6**, L422 (1973); (b) P. Mansfield, P. K. Grannell, A. N. Garroway, and D. C. Stalker, *Proc. 1st Spec. Colloque Ampere*, J. W. Hennel, Ed. p. 16, Krakow, 1973; (c) P. Mansfield and P. K. Grannell, *Phys. Rev. B* **12**, 3618 (1975).
- [6] B. Blümich, *Angew. Chem. Int. Ed. Engl.* **27**, 1406 (1988).
- [7] W. A. Ellingson, P. S. Wong, S. L. Dieckman, J. L. Ackerman, and L. Garrido, *Am. Ceram. Soc. Bull.* **68**, 1180 (1989).
- [8] J. M. Listerud, S. W. Sinton, and G. P. Drobny, *Analyt. Chem.* **61**, 23A (1989).
- [9] W. Kuhn, *Angew. Chem. Int. Ed. Engl.* **29**, 1 (1990).
- [10] B. Blümich, *Adv. Mater.* **3**, 237 (1991).

- [11] P. Jezzard, J. J. Attard, T. A. Carpenter, and L. D. Hall, *Prog. NMR Spectrosc.* **23**, 1 (1991).
- [12] J. B. Miller, *Trends Analytical Chem.* **10**, 59 (1991).
- [13] D. G. Cory, *Ann. Rep. NMR Spectr.* **24**, 87 (1992).
- [14] P. Jezzard, C. J. Wiggins, T. A. Carpenter, L. D. Hall, P. Jackson, N. J. Clayden, and N. J. Walton, *Adv. Mater.* **4**, 82 (1992).
- [15] R. A. Brooks and G. Di Chiro, *Radiology* **117**, 561 (1975).
- [16] A. Kumar, D. Welti, and R. Ernst, *J. Magn. Reson.* **18**, 69 (1975).
- [17] W. A. Edelstein, J. M. S. Hutchison, G. Johnson, and T. Redpath, *Phys. Med. Biol.* **25**, 751 (1980).
- [18] D. G. Cory, A. M. Reichwein, J. W. M. van Os, and W. S. Veeman, *Polym. Prepr.* **29(1)**, 92 (1988).
- [19] T. A. Carpenter, L. D. Hall, and P. Jezzard, *J. Magn. Reson.* **84**, 383 (1989).
- [20] P. Jezzard, T. A. Carpenter, L. D. Hall, P. Jackson, and N. J. Clayden, *Polym. Commun.* **32**, 74 (1991).
- [21] E. Bayer, W. Müller, M. Ilg, and K. Albert, *Angew. Chem. Int. Ed. Engl.* **28**, 1029 (1989).
- [22] M. A. Horsfield, E. J. Fordham, C. Hall, and L. D. Hall, *J. Magn. Reson.* **81**, 593 (1989).
- [23] W. P. Rothwell, D. R. Holecek, and J. A. Kershaw, *J. Polym. Sci. C: Polym. Lett.* **22**, 241 (1984).

- [24] S. Blackband and P. Mansfield, *J. Phys. C: Solid State Phys.* **19**, L49 (1986).
- [25] T. H. Mareci, S. Dønstrup, and A. Rigamonti, *J. Mol. Liq.* **38**, 185 (1988).
- [26] L. A. Weisenberger and J. L. Koenig, *Polym. Prepr.* **29(1)**, 98 (1988).
- [27] L. A. Weisenberger and J. L. Koenig, *Appl. Spectr.* **43**, 1117 (1989).
- [28] L. A. Weisenberger and J. L. Koenig, *J. Polym. Sci. C: Polym. Lett.* **27**, 55 (1989).
- [29] L. A. Weisenberger, and J. L. Koenig, *Macromolecules* **23**, 2445 (1990).
- [30] L. A. Weisenberger and J. L. Koenig, *Macromolecules* **23**, 2454 (1990).
- [31] A. G. Webb and L. D. Hall, *Polym. Commun.* **31**, 422 (1990).
- [32] A. G. Webb and L. D. Hall, *Polym. Commun.* **31**, 425 (1990).
- [33] A. J. de Crespigny, T. A. Carpenter, L. D. Hall, and A. G. Webb, *Polym. Commun.* **32**, 36 (1991).
- [34] C. A. Fyfe, L. H. Randall, and N. E. Burlinson, *Chem. Mater.* **4**, 267 (1992).
- [35] J. L. Koenig and R. Grinsted, *Polym. Prepr.* **33(1)**, 763 (1992).
- [36] S. R. Smith and J. L. Koenig, *Macromolecules* **24**, 3496 (1991).
- [37] A. G. Webb and L. D. Hall, *Polymer* **32**, 2926 (1991).
- [38] R. A. Grinsted and J. L. Koenig, *Macromolecules* **25**, 1229 (1992).
- [39] R. A. Grinsted, L. Clark, and J. L. Koenig, *Macromolecules* **25**, 1235 (1992).
- [40] W. A. Ellingson, J. L. Ackerman, L. Garrido, J. D. Weyand, and R. A. DiMilia, *Ceram. Eng. Sci. Proc.* **8**, 503 (1987).

- [41] L. Garrido, J. L. Ackerman, W. A. Ellingson, and J. D. Weyand, *Polym. Prepr.* **29(1)**, 97 (1988).
- [42] L. Garrido, J. L. Ackerman, W. A. Ellingson, and J. D. Weyand, *Ceram. Eng. Sci. Proc.* **9**, 1465 (1988).
- [43] K. Hayashi, K. Kawashima, K. Kose, and T. Inouye, *J. Phys. D: Appl. Phys.* **21**, 1037 (1988).
- [44] W. A. Ellingson, P. S. Wong, S. L. Dieckman, J. P. Pollinger, H. Yeh, and M. W. Vannier, *Ceram. Eng. Sci. Proc.* **10**, 1022 (1989).
- [45] J. L. Ackerman, L. Garrido, J. E. Moore, and W. A. Ellingson, *Polym. Prepr.* **31(1)**, 145 (1990).
- [46] L. Garrido, J. Ackerman, and W. A. Ellingson, *J. Magn. Reson.* **88**, 340 (1990).
- [47] S. L. Dieckman, P. Rizo, N. Gopalsami, and R. E. Botto, *Mat. Res. Soc. Symp. Proc.* **217**, 169 (1991).
- [48] C. Chang and R. A. Komoroski, *Polym. Prepr.* **29(1)**, 94 (1988).
- [49] C. Chang and R. A. Komoroski, *Macromolecules* **22**, 600 (1989).
- [50] R. S. Clough and J. L. Koenig, *J. Polym. Sci. C: Polym. Lett.* **27**, 451 (1989).
- [51] A. G. Webb, P. Jezard, L. D. Hall, and S. Ng, *Polym. Commun.* **30**, 363 (1989).
- [52] L. Garrido, J. L. Ackerman, C. Chang, and J. E. Mark, *Polym. Prepr.* **31(1)**, 147 (1990).
- [53] L. Garrido, J. E. Mark, C. C. Sun, J. L. Ackerman, and C. Chang, *Macromolecules* **24**, 4067 (1991).

- [54] S. W. Sinton, J. H. Iwamiya, B. Ewing, and G. P. Drobny, *Spectroscopy* **6**, 42 (1991).
- [55] L. Garrido, J. L. Ackerman, J. M. Vevea, J. E. Mark, and S. Wang, *Polymer* **33**, 1826 (1992).
- [56] P. Blümler and B. Blümich, *Macromolecules* **24**, 2183 (1991).
- [57] W. P. Rothwell and H. J. Vinegar, *Appl. Opt.* **24**, 3969 (1985).
- [58] L. D. Hall, V. Rajanayagam, and C. Hall, *J. Magn. Reson.* **68**, 185 (1986).
- [59] H. J. Vinegar, *J. Petrol. Technol.* **38**, 257 (1986).
- [60] L. D. Hall and V. Rajanayagam, *J. Magn. Reson.* **74**, 139 (1987).
- [61] A. Briguet, *Mol. Cryst. Liq. Cryst.* **161**, 413 (1988).
- [62] G. Guillot, A. Trokiner, L. Darrasse, and H. Saint-James, *J. Phys. D: Appl. Phys.* **22**, 1646 (1989).
- [63] P. A. Osment, K. J. Packer, M. J. Taylor, J. J. Attard, T. A. Carpenter, L. D. Hall, N. J. Herrod, and S. J. Doran, *Phil. Trans. R. Soc. Lond. A* **333**, 441 (1990).
- [64] J. J. Attard, S. J. Doran, N. J. Herrod, T. A. Carpenter, and L. D. Hall, *J. Magn. Reson.* **96**, 514 (1992).
- [65] A. K. Gaigalas, A. C. Van Orden, T. H. Mareci, and L. A. Lewis, *Nucl. Technol.* **84**, 113 (1989).
- [66] M. J. Lizak, M. S. Conradi, and C. G. Fry, *J. Magn. Reson.* **95**, 548 (1991).
- [67] E. J. Fordham, T. P. L. Roberts, T. A. Carpenter, L. D. Hall, G. C. Maitland, and C. Hall, *AIChE J.* **37**, 1895 (1991).

- [68] E. J. Fordham, T. P. L. Roberts, T. A. Carpenter, L. D. Hall, and C. Hall, *AIChE J.* **37**, 1900 (1991).
- [69] A. O. K. Nieminen and J. L. Koenig, *J. Adhes. Sci. Technol.* **2**, 407 (1988).
- [70] A. O. K. Nieminen and J. L. Koenig, *Appl. Spectr.* **43**, 1358 (1989).
- [71] A. O. K. Nieminen, J. Liu, and J. L. Koenig, *J. Adhes. Sci. Technol.* **3**, 455 (1989).
- [72] K.-P. Hoh, B. Perry, G. Rotter, H. Ishida, and J. L. Koenig, *J. Adhesion* **27**, 245 (1989).
- [73] B. C. Perry and J. L. Koenig, *J. Polym. Sci. A: Polym. Chem.* **27**, 3429 (1989).
- [74] L. D. Hall, V. Rajanayagam, W. A. Stewart, and P. R. Steiner, *Can. J. For. Res.* **16**, 423 (1986).
- [75] L. D. Hall, V. Rajanayagam, W. A. Stewart, P. R. Steiner, and S. Chow, *Can. J. For. Res.* **16**, 684 (1986).
- [76] L. D. Hall and V. Rajanayagam, *Wood Sci. Technol.* **20**, 329 (1986).
- [77] P. C. Wang and S. J. Chang, *Wood and Fiber Sci.* **18**, 308 (1986).
- [78] S. J. Chang, J. R. Olson, and P. C. Wang, *Forest Prod. J.* **39**, 43 (1989).
- [79] A. A. Samoilenko, D. Yu. Artemov, and L. A. Sibel'dina, *Russ. J. Phys. Chem.* **61**, 1623 (1987).
- [80] A. A. Samoilenko, D. Yu. Artemov, and L. A. Sibel'dina, *JETP Lett.* **47**, 417 (1988).
- [81] A. A. Samoilenko and K. Zick, *Bruker Rep.* **1**, 40 (1990).
- [82] S. Emid and J. H. N. Creyghton, *Physica (Amsterdam)* **128B**, 81 (1985).

- [83] P. J. McDonald, J. J. Attard, and D. G. Taylor, *J. Magn. Reson.* **72**, 224 (1987).
- [84] L. Li and R. A. Kruger, *Phys. Med. Biol.* **8**, 1153 (1990).
- [85] L. Li, *Phys. Med. Biol.* **36**, 199 (1991).
- [86] D. E. Demco, S. Hafner, and R. Kimmich, *J. Magn. Reson.* **94**, 333 (1991).
- [87] E. Rommel, S. Hafner, and R. Kimmich, *J. Magn. Reson.* **86**, 264 (1990).
- [88] S. Matsui, *Chem. Phys. Lett.* **179**, 187 (1991).
- [89] S. Matsui, *J. Magn. Reson.* **95**, 149 (1991).
- [90] S. Hafner, D. E. Demco, and R. Kimmich, *Meas. Sci. Technol.* **2**, 882 (1991).
- [91] D. E. Demco, S. Hafner, and R. Kimmich, *J. Magn. Reson.* **96**, 307 (1992).
- [92] D. G. Cory, J. C. De Boer, and W. S. Veeman, *Macromolecules* **22**, 1618 (1989).
- [93] G. C. Chingas, J. B. Miller, and A. N. Garroway, *J. Magn. Reson.* **66**, 530 (1986).
- [94] A. N. Garroway, J. Baum, M. G. Munowitz, and A. Pines, *J. Magn. Reson.* **60**, 337 (1984).
- [95] L. D. Hall and T. J. Norwood, *J. Magn. Reson.* **67**, 382 (1986).
- [96] E. Günther, B. Blümich, and H. W. Speiss, *Mol. Phys.* **71**, 477 (1990).
- [97] R. A. Wind and C. S. Yannoni, *U.S. patent 4 301 410*, 17 November 1981.
- [98] D. G. Cory, A. M. Reichwein, J. W. M. van Os, and W. S. Veeman, *Chem. Phys. Lett.* **143**, 467 (1988).
- [99] D. G. Cory, A. M. Reichwein, and W. S. Veeman, *J. Magn. Reson.* **80**, 259 (1988).
- [100] D. G. Cory, J. W. M. van Os, and W. S. Veeman, *J. Magn. Reson.* **76**, 543 (1988).

- [101] D. G. Cory and W. S. Veeman, *J. Magn. Reson.* **82**, 374 (1989).
- [102] D. G. Cory and W. S. Veeman, *J. Phys. E: Sci. Instrum.* **22**, 180 (1989).
- [103] W. S. Veeman and D. G. Cory, in "Advances in Magnetic Resonance" (W. S. Warren, Ed.), Vol. 13, pp. 43–56, Academic Press, San Diego, 1989.
- [104] E. Günther, B. Blümich, and H. W. Spiess, *Chem. Phys. Lett.* **184**, 251 (1991).
- [105] S. Matsui and H. Kohno, *J. Magn. Reson.* **70**, 157 (1986).
- [106] D. G. Cory, *J. Magn. Reson.* **82**, 337 (1989).
- [107] F. De Luca and B. Maraviglia, *J. Magn. Reson.* **67**, 169 (1986).
- [108] F. De Luca, C. Nuccetelli, B. C. De Simone, and B. Maraviglia, *J. Magn. Reson.* **69**, 496 (1986).
- [109] F. De Luca, B. C. De Simone, N. Luger, B. Maraviglia, and C. Nuccetelli, *J. Magn. Reson.* **90**, 124 (1990).
- [110] D. G. Cory and W. S. Veeman, *J. Magn. Reson.* **84**, 392 (1989).
- [111] H. M. Cho, C. J. Lee, D. N. Shykind, and D. P. Weitekamp, *Phys. Rev. Lett.* **55**, 1923 (1985).
- [112] D. G. Cory, A. N. Garroway, and J. B. Miller, *J. Magn. Reson.* **87**, 202 (1990).
- [113] P. Mansfield, *J. Phys. C: Solid St. Phys.* **4**, 1444 (1971).
- [114] W.-K. Rhim, D. D. Elleman, and R. W. Vaughan, *J. Chem. Phys.* **58**, 1772 (1973).
- [115] D. P. Burum and W.-K. Rhim, *J. Chem. Phys.* **71**, 944 (1979).
- [116] S. L. Dieckman, N. Gopalsami, and R. E. Botto, *Energy and Fuels* **4**, 417 (1990).

- [117] S. L. Dieckman, P. Rizo, N. Gopalsami, J. P. Heeschen, and R. E. Botto, *J. Am. Chem. Soc.* **114**, 2717 (1992).
- [118] J. B. Miller, D. G. Cory, and A. N. Garroway, *Chem. Phys. Lett.* **164**, 1 (1989).
- [119] P. Bendel, *IEEE Trans. Med. Imag.* **MI-4**, 114 (1985).
- [120] J. B. Miller and A. N. Garroway, *J. Magn. Reson.* **67**, 575 (1986).
- [121] R. F. Karlicek, Jr. and I. J. Lowe, *J. Magn. Reson.* **37**, 75 (1980).
- [122] S. P. Cottrell, M. R. Halse, P. J. McDonald, J. H. Strange, and P. F. Tokarczuk, *Bull. Magn. Reson.* **11**, 310 (1989).
- [123] P. J. McDonald and P. F. Tokarczuk, *J. Phys. E: Sci. Instrum.* **22**, 948 (1989).
- [124] S. P. Cottrell, M. R. Halse, and J. H. Strange, *Meas. Sci. Technol.* **1**, 624 (1990).
- [125] J. H. Strange, *Phil. Trans. R. Soc. Lond. A* **333**, 427 (1990).
- [126] J. B. Miller and A. N. Garroway, *Polym. Prep.* **29(1)**, 90 (1988).
- [127] J. B. Miller, D. G. Cory, and A. N. Garroway, *Bull. Magn. Reson.* **11**, 197.
- [128] J. B. Miller and A. N. Garroway, *J. Magn. Reson.* **85**, 255 (1989).
- [129] J. B. Miller and A. N. Garroway, *J. Magn. Reson.* **82**, 529 (1989).
- [130] J. B. Miller, D. G. Cory, and A. N. Garroway, *Phil. Trans. R. Soc. Lond. A* **333**, 413 (1990).
- [131] D. G. Cory, J. B. Miller, R. Turner, and A. N. Garroway, *Mol. Phys.* **70**, 331 (1990).
- [132] D. G. Cory, J. B. Miller, and A. N. Garroway, *J. Magn. Reson.* **90**, 205 (1990).

- [133] L. G. Butler, D. G. Cory, K. M. Dooley, J. B. Miller, and A. N. Garroway, *J. Am. Chem. Soc.* **114**, 125 (1992).
- [134] M. S. Conradi, A. N. Garroway, D. G. Cory, and J. B. Miller, *J. Magn. Reson.* **94**, 370 (1991).
- [135] B. H. Suits and D. White, *Solid State Commun.* **50**, 291 (1984).
- [136] N. M. Szeverenyi and G. E. Maciel, *J. Magn. Reson.* **60**, 460 (1984).
- [137] G. E. Maciel and M. F. Davis, *J. Magn. Reson.* **64**, 356 (1985).
- [138] C. G. Fry, A. C. Lind, M. F. Davis, D. W. Duff, and G. E. Maciel, *J. Magn. Reson.* **83**, 656 (1989).
- [139] M. S. Conradi, *J. Magn. Reson.* **93**, 419 (1991).
- [140] M. Ilg, K. Albert, W. Rapp, and E. Bayer, *J. Magn. Reson.* **90**, 370 (1990).
- [141] J. L. Ackerman, D. P. Raleigh, and M. J. Glimcher, *Magn. Reson. Med.* **25**, 1 (1992).
- [142] J. J. Attard and P. J. McDonald, *Int. J. Imaging Sys. Tech.* **2**, 47 (1990).
- [143] J. R. Moore, L. Garrido, and J. L. Ackerman, *Ceram. Eng. Sci. Proc.* **11**, 1302 (1990).
- [144] P. Bendel, M. Davis, E. Berman, and G. W. Kabalka, *J. Magn. Reson.* **88**, 369 (1990).
- [145] R. A. Wind and C. S. Yannoni, *J. Magn. Reson.* **36**, 269 (1979).
- [146] J. B. Miller and A. N. Garroway, *J. Magn. Reson.* **77**, 187 (1988).
- [147] S. Hafner, E. Rommel, and R. Kimmich, *J. Magn. Reson.* **88**, 449 (1990).

- [148] D. G. Cory, J. B. Miller, and A. N. Garroway, *Meas. Sci. Technol.* **1**, 1338 (1990).
- [149] S. Matsui, *J. Magn. Reson.* **97**, 335 (1992).
- [150] J. B. Miller, D. G. Cory, and A. N. Garroway, *Polym. Prepr.* **31(1)**, 143 (1990).
- [151] J. B. Miller and A. N. Garroway, *J. Magn. Reson.* **85**, 432 (1989).
- [152] M. Corti, F. Borsa, and A. Rigamonti, *J. Magn. Reson.* **79**, 21 (1988).
- [153] D. G. Cory, J. B. Miller, and A. N. Garroway, *J. Magn. Reson.* **90**, 544 (1990).
- [154] S. P. Cottrell, M. R. Halse, D. A. Ibbett, B. L. Boda-Novy, and J. H. Strange, *Meas. Sci. Technol.* **2**, 860 (1991).
- [155] D. E. Demco, R. Kimmich, S. Hafner, and H. -W. Weber, *J. Magn. Reson.* **94**, 317 (1991).
- [156] S. Hafner, D. E. Demco, and R. Kimmich, *Chem. Phys. Lett.* **187**, 53 (1991).
- [157] R. A. Wind, J. H. N. Creighton, D. J. Ligthelm, and J. Smidt, *J. Phys. C: Solid State Phys.* **11**, L223 (1978).
- [158] E. Rommel and R. Kimmich, *J. Magn. Reson.* **83**, 299 (1989).
- [159] A. J. Johnson, M. Garwood, and K. Uğurbil, *J. Magn. Reson.* **81**, 653 (1989).
- [160] B. H. Suits and J. L. Lutz, *J. Appl. Phys.* **65**, 3728 (1989).
- [161] B. H. Suits and D. White, *J. Appl. Phys.* **60**, 3772 (1986).

Chapter 3

NMR Imaging of Solids with Multiple-Pulse Line Narrowing and RF Gradients

3.1 Introduction

Magnetic resonance imaging of solids is hampered by linewidth contributions, predominantly direct dipolar coupling and chemical shift anisotropy. Nevertheless, because of the noninvasive nature of solid-state NMR, as well as its excellent chemical, orientational, and motional specificity, there is much interest in NMR imaging of solids [1]. Nearly two decades ago, Mansfield and Grannell proposed imaging solids by combining a multiple-pulse line-narrowing sequence with pulsed DC field gradients in such a way as to eliminate all static spin interactions while retaining the spin evolution under the gradient field [2]. At that time, however, the electronics necessary to switch the amplitude and direction of large field gradients in the few microseconds of a typical multiple-pulse sequence window were either unavailable or prohibitively expensive for the application. The technology for generating short, intense DC field gradient pulses is now available, although it is still developing [3], and imaging sequences akin to those of Mansfield and Grannell have recently been implemented [4, 5].

Most familiar multiple-pulse sequences (for example, WHH-4 [6], MREV-8 [7, 8], and BR-24 [9]) average to zero dipolar interactions, which are described by Hamiltonians bilinear in the spin operator I_z . They do not, however, entirely eliminate chemical shift (or

resonance-offset, or bulk magnetic susceptibility) effects, which are described by Hamiltonians linear in I_z . These effects then contribute to the linewidth. For imaging it is advantageous to average to zero the linear as well as the bilinear interactions, since this eliminates the problem of having to deconvolve chemical shift and spatial information in the final image. The line-narrowing sequence suggested by Mansfield and Grannell does average both types of interactions [2] and, as such, falls into the class of pulse sequences since named “time-suspension” sequences [4]. The line-narrowing pulse sequence used in the imaging experiments discussed below is also a time-suspension sequence. In order to encode spatial information, such line-narrowing sequences must be combined with time-dependent gradients so that the gradient-induced evolution accumulates over the pulse cycle and so that the gradient does not interfere with the line-narrowing capability of the cycle.

An appealing alternative to switched DC gradients is switched radiofrequency (rf) gradients. These are straightforward to incorporate in a multiple-pulse sequence. As previously demonstrated by Weitekamp and coworkers [10], rf pulse sequences can be designed which suppress dipolar (homonuclear and heteronuclear) and chemical-shift contributions to the linewidth, and also result in the frequency shift of the narrowed line position proportional to the rf field strength of certain of the pulses. These sequences can be classified as nutation sequences since, in addition to line narrowing, they provide a linear dependence of line position on rf field strength. It was proposed that a coil capable of producing a switched rf field gradient could be used to deliver certain of the pulses of such a nutation sequence and thus spatial discrimination of nuclear spins could be achieved. In this chapter the first experimental images obtained by this method are presented.

3.2 RF Gradients

The first advantage of using rf gradients rather than (nominally) DC gradients in NMR imaging is that the problem of eddy currents is eliminated. Radiofrequency magnetic fields behave differently than do low-frequency switched or square-wave modulated DC currents in the presence of conducting materials. This difference is expressed by the differences in skin depth. For example, the skin depth for copper at 20 kHz is about 0.05 cm but at 200 MHz it decreases to about 5×10^{-4} cm [11]. Since rf magnetic fields do not penetrate into the metal walls surrounding the imaging probe, rapidly switching an rf field does not produce long-lived eddy currents, which can have a detrimental effect on the imaging experiment or, in an extreme case, even damage the superconducting field coils of the NMR spectrometer [12].

Active shielding [13] can alleviate the problem of eddy currents with switched DC gradients. More commonly for solids imaging, though, the remedy is to keep the gradient coils well removed from any metal in the probe or magnet [14, 15]. Either approach compromises the usable volume of the magnet. The low audiofrequency gradients used by Garroway and coworkers in their refocused gradient imaging experiments also avoid the difficulty of eddy currents because the gradients do not need to be switched or modulated during the course of the experiment [16]. For compatibility with the best known line-narrowing sequences, however, it is necessary to switch the gradients.

Another advantage of rf gradients is that they are technically easier than DC gradients to incorporate into a multiple pulse train so that the evolution due to the gradient accumulates over the pulse cycle. RF gradients can be switched in the windows of a multiple-pulse sequence, and thus made to toggle along with the spins, by a simple phase-shifting network (see, for example, reference [17]) which is already present as part of the necessary spectrometer electronics. Similarly, it is possible to obtain an acceptable

gradient strength of 2 G/cm by using an rf amplifier capable of delivering 300 W pulses, which is true of most rf amplifiers used in solid-state NMR spectroscopy.

A possible advantage for living systems is that rf power is less likely than audiofrequency magnetic fields to have biological effects.

Radiofrequency gradients have been used previously in liquid-state experiments. The solids imaging technique described here is analogous to rotating-frame zeugmatography (RFZ), a liquid-state technique developed by Hoult [18]. In its simplest form, RFZ consists of a series of incremented pulse widths applied by an rf gradient coil. The nutation frequency induced by the rf gradient pulses varies across the sample, and so can be used to provide spatial information. The data collected are processed by a two-dimensional Fourier transformation to yield a plot of signal intensity versus chemical shift in one dimension and versus nutation frequency ν_1 in the other. In this and other liquid-state rf gradient techniques, nutation occurs about an axis in the transverse plane, so positive and negative frequencies cannot be distinguished.

Since Hoult's original experiment, there have been several rotating-frame imaging studies (for example, see references [19–27]). RFZ has also been developed as a method of localization spectroscopy, used primarily in *in vivo* applications (for example, see references [28–36]). In these experiments, the rf gradient coil is most commonly a surface coil. In some studies, a surface transmit coil was combined with a Helmholtz receive coil [20, 25, 26, 27, 34]. Other rf gradient coils used include an asymmetric saddle coil [19] and a straddle coil [32]. In cases where separate transmit and receive coils have been used, the coils were decoupled primarily by passive means. There have been a few previous examples of active decoupling. These are discussed in Chapter 6.

An NQR imaging procedure analogous to NMR rotating frame zeugmatography has been demonstrated on solids [37]. In these studies, the rf gradient coil was either a surface

coil or an anti-Helmholtz coil. In the latter case, the gradient transmit coil was coaxial with a solenoid receive coil and the two were decoupled by passive means.

3.3 SWW-16

The multiple-pulse rf gradient imaging sequence used for the experiments in this chapter, and in Chapter 5, is referred to as SWW-16. Each SWW-16 cycle is composed of 16 line-narrowing pulses and 12 gradient pulses, as shown in Figure 3.1. The cycle of 16 $\pi/2$ pulses which achieves the line-narrowing was originally proposed by Weitekamp, Garbow, and Pines for use in multiple-pulse double-resonance experiments [38]. This pulse sequence (SHRIMP) is a symmetrization of the 8-pulse sequence suggested by Mansfield and Grannell [2], and was used in the original proposal for nutation imaging in solids [10]. In SWW-16, however, the synchronous rf gradient pulses occur during selected windows of the line-narrowing sequence, as opposed to being concurrent with the $\pi/2$ pulses as in the earlier proposal [10]. This is critical to the practicality of the implementation described here.

The line-narrowing portion of SWW-16 is delivered by an rf coil producing a homogeneous B_1 field, while the gradient portion is delivered by a coil producing a B_1 field with a linear field gradient. Here a solenoid coil has been chosen as the homogeneous coil and, for one-dimensional imaging, a quadrupole coil as the gradient coil. For higher-dimensional imaging additional gradient coils may be added or back-projection reconstruction may be used. The rf coils are actively decoupled in such a way that the circuit that is not operating is held non-resonant or “Q-spoiled.” In this way, only one coil produces an rf field which influences the spins.

The pulses in Figure 3.1(a) are the line-narrowing pulses delivered by the solenoid coil. Each of these is a $\pi/2$ pulse with rotating-frame phase as indicated in the figure.

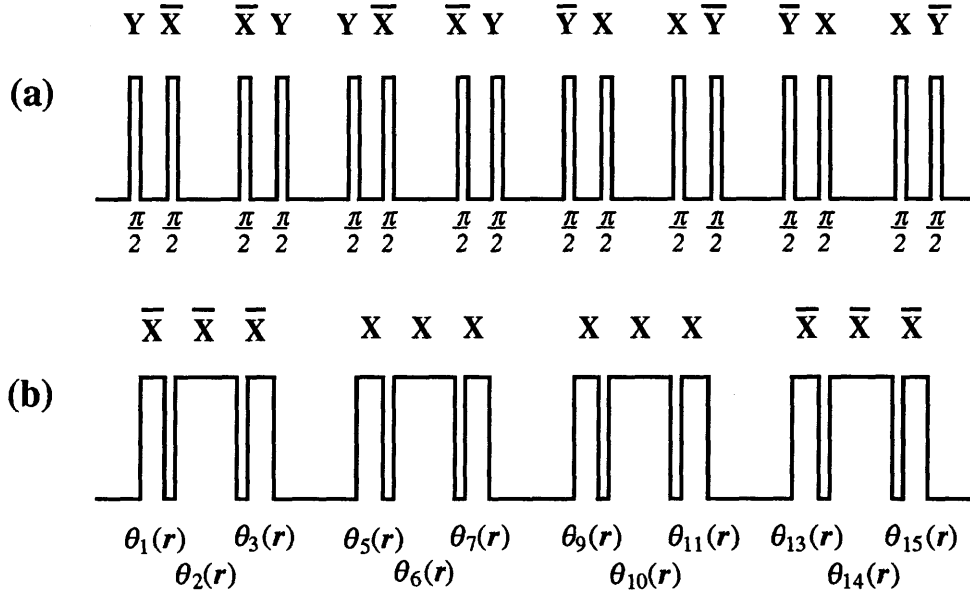


Figure 3.1: SWW-16 for 1-D imaging. This is equivalent to SWW-16- G_X discussed in Chapter 5. The pulses in (a) are the $\pi/2$ line-narrowing pulses delivered by a coil of homogeneous rf field. The rotating-frame phases are indicated. The pulses in (b) are the rf gradient pulses delivered by the gradient coil. These pulses have angles $\theta_n(\mathbf{r}) = \gamma \mathbf{G} \cdot \mathbf{r} t_n$, where $\theta_n(\mathbf{r})$ is the spatially varying angle of the n^{th} pulse and t_n the length of the n^{th} pulse.

The average Hamiltonian of the cycle in Figure 3.1(a) vanishes. That is, the net effect of these line-narrowing pulses is to eliminate any evolution of the transverse magnetization due to the rotating-frame spin Hamiltonian. The largest remaining terms are residual interactions between spins that scale as $D_{ij}^3 t_c^2$, where D_{ij} is the homonuclear dipolar coupling and t_c the cycle time.

The pulses in Figure 3.1(b) are the rf gradient pulses delivered by the quadrupole coil. At the level of the average Hamiltonian their effect is the same as if they were coincident with the neighboring $\pi/2$ pulses [10]. The rotating-frame phases of the gradient pulses, indicated in the figure, are selected such that, over a cycle, evolution due to them accumulates. The pulses have angles $\theta_n(\mathbf{r}) = \gamma \mathbf{G} \cdot \mathbf{r} t_n$ which vary linearly across the

sample. Here n designates the n^{th} pulse and t_n represents the length of the n^{th} pulse.

The combined effect of the gradient and the line-narrowing pulses can be described with a coherent averaging theory by treating the gradient pulses as a perturbation on the line-narrowing sequence, in analogy to the standard treatment of uncontrolled pulse-angle errors [10, 39]. Using this treatment, described in Chapter 4, the average Hamiltonian of SWW-16 can be shown to be

$$\overline{\mathcal{H}}^{(0)} = \frac{1}{t_c} \sum_n \theta_n(\mathbf{r}) I_z, \quad (3.1)$$

where $\theta_n(\mathbf{r})$ is defined as above and t_c is the sequence cycle time. Thus, what is observed is an apparent precession around the static field direction at a frequency proportional to $\theta_n(\mathbf{r})$, even though the immediate effect of each gradient pulse is to nutate the spins around the x -axis of the rotating frame. This is an important distinction between this sequence and those used in RFZ, mentioned above. That the average Hamiltonian scales as I_z is significant since this allows positive and negative frequencies to be distinguished by standard quadrature detection, and so the imaging gradient may pass from negative to positive field values within the sample without introducing any sign ambiguity.

3.4 RF Coils

The coils used to deliver the imaging pulse sequence are shown schematically in Figure 3.2. The sample is contained in the inner solenoid coil of diameter 8 mm and length 25 mm. The outer quadrupole coil of diameter 28 mm and length 45 mm creates a second field at the same frequency, which varies linearly in amplitude across the sample. Quadrupole coils are discussed more fully in Chapter 5. With the arrangement shown in the figure, there are two orthogonal components to the gradient: $G_{zz} = \partial B_{1z}/\partial z$ and $G_{xx} = \partial B_{1x}/\partial x$. However, G_{zz} is not time-independent in the rotating frame and so has no significant effect on the spins. Thus the only effective gradient produced by the

quadrupole coil is G_{xx} , a gradient in the transverse rf field which is perpendicular to the axis of the solenoid coil and to the main static magnetic field.

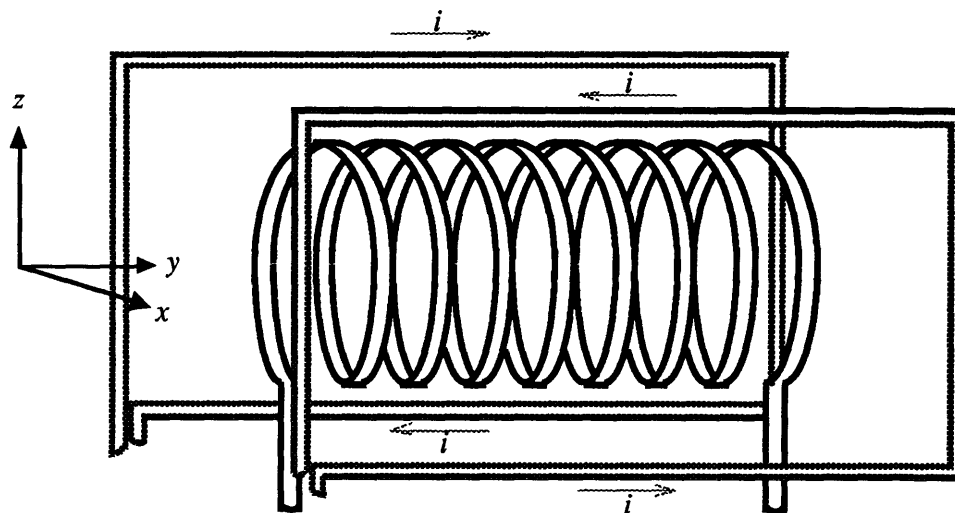


Figure 3.2: RF coils for 1-D imaging. The inner solenoid coil has a diameter of 8 mm and a length of 25 mm. The outer quadrupole coil has a diameter of 28 mm and a length of 45 mm. In the orientation shown, the quadrupole coil produces a gradient $G_{xx} = \partial B_{1x} / \partial x$, that is, a gradient in the transverse magnetic field B_1 oriented normal to the plane defined by the coil axis and the main static magnetic field B_0 .

Radiofrequency-gradient imaging of solid materials requires enclosing at least two resonant circuits tuned to the same frequency within the volume of the NMR probe. Despite the nominal orthogonality of the desired field patterns, parasitic inductance and capacitance couple the circuits, resulting in a network with multiple resonant frequencies displaced from the desired single frequency. Decoupling of the circuits is necessary for this reason, and also to prevent the interaction of the quadrupole rf field from disturbing the homogeneity of the solenoid rf field and so hindering the line-narrowing process. In the imaging experiments described here, decoupling is achieved, first, by operating the solenoid and quadrupole circuits during distinct time intervals (hence, the gradient pulses are delivered only during windows of the line-narrowing sequence), and second, by holding

non-resonant that circuit which is in the “off” state during a given interval. Thus, no more than one circuit is resonant and driven at a given moment. A circuit in the non-resonant “off” state is said to be Q-spoiled, and is an example of an extremely overcoupled resonator [40]. Switching between the resonant and Q-spoiled states is referred to as Q-switching. Q-switching is achieved by means of PIN diodes added in the matching networks of the series-tuned resonant LC circuits of both coils, as shown in Figure 3.3. When the PIN diodes of a given circuit are forward biased, that circuit is resonant, and, in this case, has a Q of 100. In the absence of forward biasing, or when under reverse bias as used in the 2-D probe, they behave as a very small capacitance in series with the matching capacitor, C_M . This effectively lowers C_M to the point that the circuit Q is reduced to 0.25. This low Q prevents the buildup of large circulating currents in the coil, and so this coil does not produce a magnetic field that affects the spins. The PIN diodes used in this 1-D imaging probe are HP5082-3202 and enable Q-switching to be achieved in approximately 200 ns. Q-switching is discussed further in Chapter 6.

3.5 One-Dimensional Images

One-dimensional images of two solid phantoms are shown in Figure 3.4. These were obtained on a homebuilt spectrometer operating at 200 MHz. The first phantom consists of two cylindrical samples of the hydrocarbon adamantane extending 1.5 mm along the gradient direction and separated by 1.5 mm. The second phantom consists of two samples of the polymer Delrin (polyoxymethylene) each extending 0.8 mm along the gradient direction and separated by 2.0 mm. Adamantane exhibits low chemical shift-anisotropy and chemical-shift dispersion, and is a common “benchmark” for solid-state imaging techniques. Delrin is a rigid polymer, free of molecular motions of a period similar to the cycle time, and so it also line-narrows well under multiple-pulse sequences [1]. For

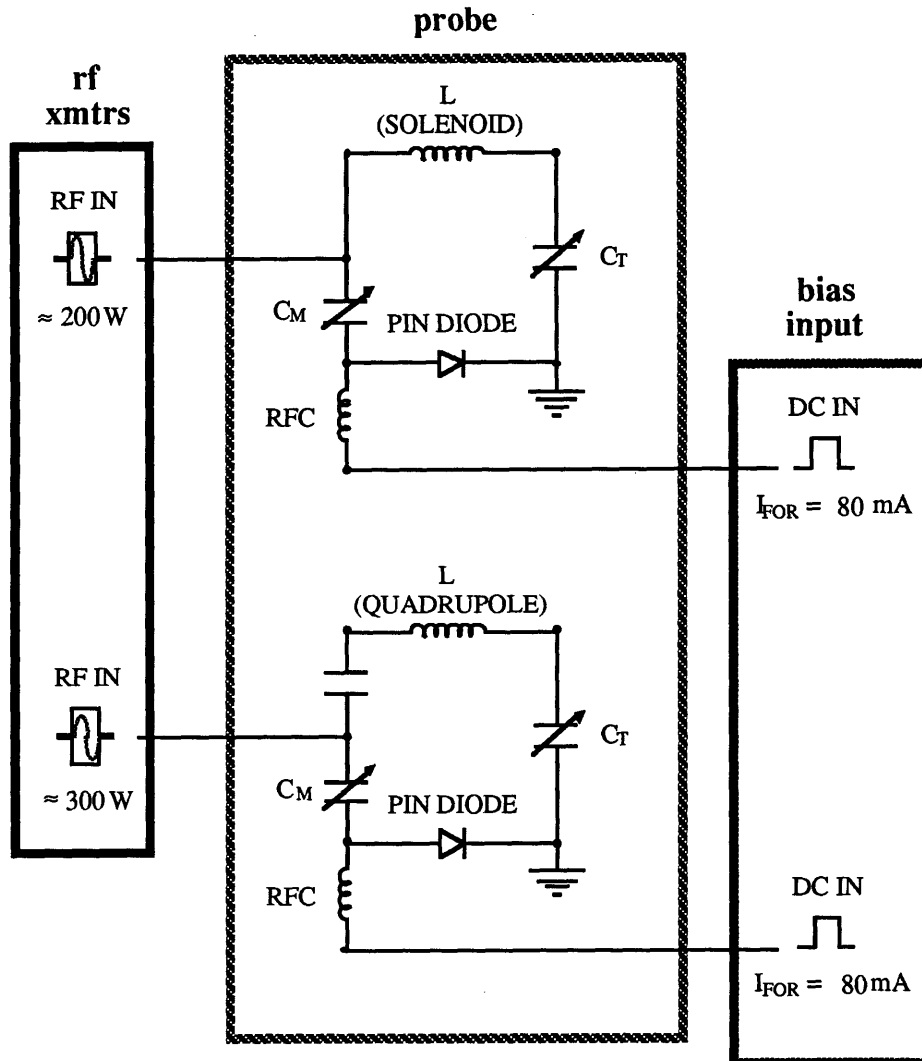


Figure 3.3: Schematic imaging probe circuit. To enable Q-switching, PIN diodes have been added in the matching network of the series tuned resonant LC circuit of both the solenoid and quadrupole coils. For the 1-D imaging probe discussed in this chapter, the diodes used were HP 5082-3202 PIN diodes. These were forward biased with $I_{\text{FOR}} = 80 \text{ mA}$. No reverse biasing was used. For the 2-D imaging probe discussed in Chapter 5, the diodes used were M/A-COM MA4P504 PIN diodes. These were forward biased with $I_{\text{FOR}} = 125 \text{ mA}$ and reverse biased with $-V_{\text{REV}} = -25 \text{ V}$.

both images the $\pi/2$ time used was $3.1 \mu\text{s}$ and the cycle time used was $307.2 \mu\text{s}$. For the adamantane image the gradient pulses were $3.4 \mu\text{s}$ for a total gradient time of $40.8 \mu\text{s}$, while for the Delrin image the gradient pulses were $3.7 \mu\text{s}$ for a total gradient time of $44.4 \mu\text{s}$. The rf power delivered to the solenoid coil was 200 W, and that delivered to the quadrupole coil was 300 W. Each coil was switched to its resonant state $1 \mu\text{s}$ before the application an rf pulse to that coil, and was held resonant for the duration of the pulse.

In both images, SWW-16 has successfully narrowed the linewidth from 12–13 kHz to 150 Hz and resolved the signal from the two objects. The effective rf gradient strength observed is 0.3 G/cm, which when corrected for the gradient duty cycle, corresponds to an unscaled gradient strength of 2 G/cm. Not all of the available gradient time was used. Given the window times used here, and the requirement for $1 \mu\text{s}$ bias pulses before each rf pulse, the maximum total gradient time available is $147.2 \mu\text{s}$. This would yield a gradient duty cycle of 0.48 and, given a gradient strength of 2 G/cm, an effective gradient strength of 0.96 G/cm. For the adamantane phantom this would separate the two peaks in the image by 1200 Hz, which is less than half the spectral width. For obtaining the highest resolution images of a given sample, the optimal gradient is the largest one possible that avoids aliasing [15]. There are three ways to increase the effective gradient strength: by increasing the gradient duty factor, increasing the gradient pulse strength, and by decreasing the size of the gradient coil. Any one of these may be used to obtain images of higher resolution. In our case, the power handling capability of the PIN diodes used in the 1-D imaging probe prevented us from using higher gradient pulse strengths and duty cycles. This problem was later solved in the 2-D imaging probe by using M/A-COM MA4P504 PIN diodes. Additional improvements to the image resolution may be obtained if the residual linewidth is minimized. This may be achieved through sequences designed to eliminate higher order correction terms to the effective Hamiltonian [4, 42]. Improved

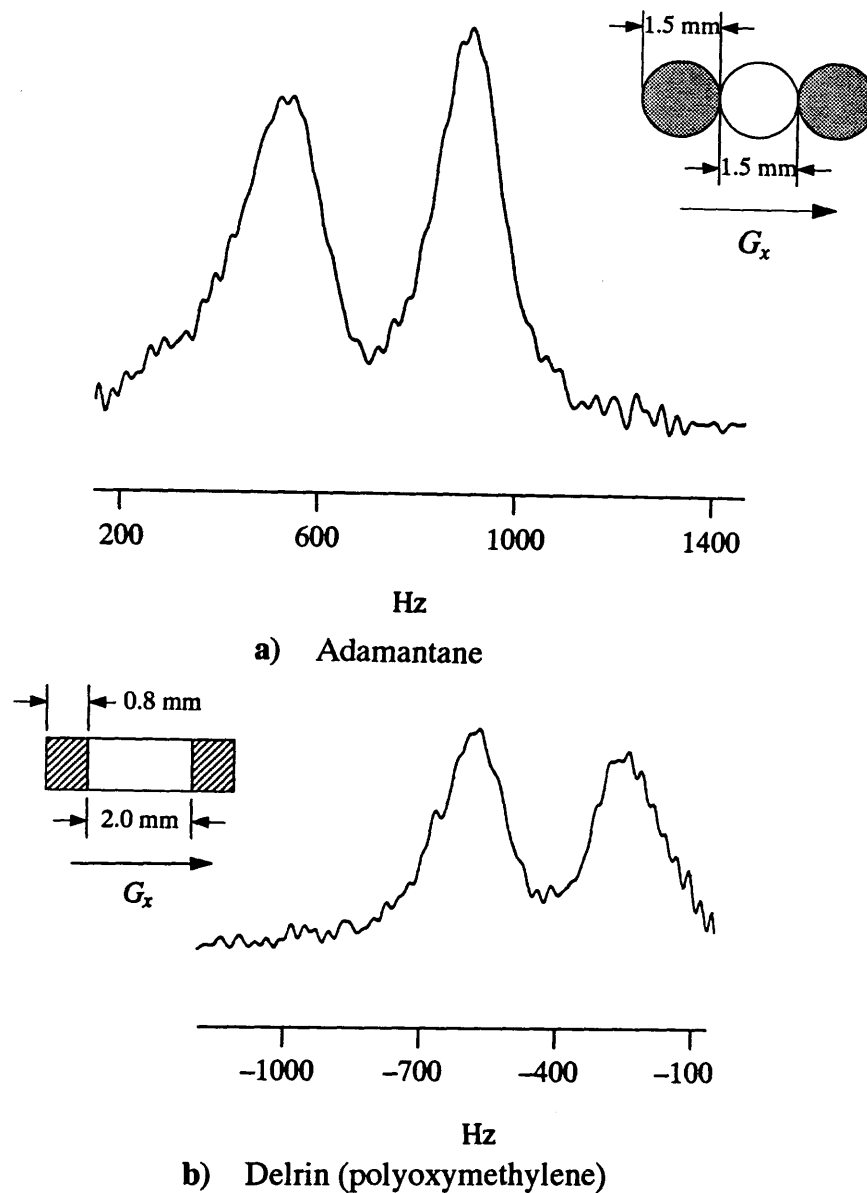


Figure 3.4: 1-D images of two-point phantoms. (a) The adamantane phantom consists of two cylindrical samples each extending 1.5 mm along the gradient direction and separated by a 1.5 mm diameter glass capillary tube. (b) The Delrin phantom consists of two pieces each extending 0.8 mm along the gradient direction and separated by a 2.0 mm glass spacer. In both images SWW-16 has successfully narrowed the linewidth from 12–13 kHz to 150 Hz and resolved the signal from the two objects.

resolution may also be obtained by oversampling (i.e., sampling more than once per pulse cycle) to increase the spectral width of the image [41].

3.6 Conclusions

The feasibility of combining multiple-pulse line narrowing with pulsed rf gradients has been demonstrated by 1-D images of adamantane and Delrin. With the probe and experimental parameters used here, 300 W rf pulses to the quadrupole coil produce an effective gradient strength of 0.3 G/cm. The effective gradient strength is related to the actual or unscaled gradient strength by the gradient duty factor.

The quadrupole coil used here has two orthogonal gradient components, only one of which is time-independent in the rotating frame. Using this gradient coil in combination with sample rotation, two- or three-dimensional imaging can be achieved by back-projection reconstruction. Alternatively, orthogonal gradients may be added to allow imaging stationary samples. A G_{yy} gradient could come from a quadrupole coil rotated 90° about z from that of Figure 3.2. A quadrupole coil coaxial with that of Figure 3.2 but rotated by 45° about the y -axis produces gradient components $G_{zx} = \partial B_{1x}/\partial z$ and $G_{xz} = \partial B_{1z}/\partial x$. In this case G_{zx} has no effect on the spins and G_{xz} provides the third orthogonal gradient, one parallel to the main static magnetic field.

References

- [1] D. G. Cory, *Ann. Rep. NMR Spectr.* **24**, 87 (1992).
- [2] (a) P. Mansfield and P. K. Grannell, *J. Phys. C: Solid State Phys.* **6**, L422 (1973);
(b) P. Mansfield, P. K. Grannell, A. N. Garroway, and D. C. Stalker, *Proc. 1st Spec. Colloque Ampere*, J. W. Hennel, Ed. p. 16, Krakow, 1973; (c) P. Mansfield and P. K. Grannell, *Phys. Rev. B* **12**, 3618 (1975).
- [3] M. S. Conradi, A. N. Garroway, D. G. Cory, and J. B. Miller, *J. Magn. Reson.* **94**, 370 (1991).
- [4] D. G. Cory, J. B. Miller, and A. N. Garroway, *J. Magn. Reson.* **90**, 205 (1990).
- [5] L. G. Butler, D. G. Cory, K. M. Dooley, J. B. Miller, and A. N. Garroway, *J. Am. Chem. Soc.* **114**, 125 (1992).
- [6] J. S. Waugh, L. Huber, and U. Haeberlen, *Phys. Rev. Lett.* **20**, 180 (1968).
- [7] P. Mansfield, *J. Phys. C: Solid St. Phys.* **4**, 1444 (1971).
- [8] W.-K. Rhim, D. D. Elleman, and R. W. Vaughan, *J. Chem. Phys.* **58**, 1772 (1973).
- [9] D. P. Burum and W.-K. Rhim, *J. Chem. Phys.* **71**, 944 (1979).
- [10] H. M. Cho, C. J. Lee, D. N. Shykind, and D. P. Weitekamp, *Phys. Rev. Lett.* **55**, 1923 (1985).
- [11] F. E. Terman, "The Radio Engineer's Handbook," McGraw-Hill, New York, 1943.

- [12] D. N. Shykind, Ph.D. Thesis, University of California, Berkeley, (1989).
- [13] P. Mansfield and B. Chapman, *J. Magn. Reson.* **72**, 211 (1987).
- [14] J. B. Miller, D. G. Cory, and A. N. Garroway, *Chem. Phys. Lett.* **164**, 1 (1989).
- [15] D. G. Cory, J. B. Miller, R. Turner, and A. N. Garroway, *Mol. Phys.* **70**, 331 (1990).
- [16] J. B. Miller and A. N. Garroway, *J. Magn. Reson.* **82**, 529 (1989).
- [17] D. N. Shykind, G. C. Chingas, A. Pines and A. J. Shaka, *Rev. Sci. Instrum.* **61**, 1474 (1990).
- [18] D. I. Hoult, *J. Magn. Reson.* **33**, 183 (1979).
- [19] S. J. Cox and P. Styles, *J. Magn. Reson.* **40**, 209 (1980).
- [20] M. J. Blackledge, D. J. Hayes, R. A. J. Challiss, and G. K. Radda, *J. Magn. Reson.* **69**, 331 (1986).
- [21] C. T. W. Moonen, S. E. Anderson, and S. Unger, *Magn. Reson. Med.* **5**, 296 (1987).
- [22] D. I. Hoult, C.-N. Chen, and L. K. Hedges, *Ann. NY Acad. Sci.* **508**, 366 (1987).
- [23] M. J. Blackledge, P. Styles, and G. K. Radda, *J. Magn. Reson.* **79**, 176 (1988).
- [24] M. J. Blackledge and P. Styles, *J. Magn. Reson.* **77**, 203 (1988).
- [25] J. P. Boehmer, K. R. Metz, J. Mao, and R. W. Briggs, *Magn. Reson. Med.* **16**, 335 (1990).
- [26] D. Boudot, D. Canet, and J. Brondeau, *J. Magn. Reson.* **87**, 385 (1990).
- [27] D. Boudot, F. Montigny, K. Elbayed, P. Mutzenhardt, B. Diter, J. Brondeau, and D. Canet, *J. Magn. Reson.* **92**, 605 (1991).

- [28] A. Haase, C. Malloy, and G. K. Radda, *J. Magn. Reson.* **55**,164 (1983).
- [29] J. P. Boehmer, K. R. Metz, and R. W. Briggs, *J. Magn. Reson.* **62**, 322 (1985).
- [30] K. R. Metz and R. W. Briggs, *J. Magn. Reson.* **64**, 172 (1985).
- [31] M. J. Blackledge, B. Rajagopalan, R. D. Oberhaensli, N. M. Bolas, P. Styles, and G. K. Radda, *Proc. Natl. Acad. Sci. USA* **84**, 4283 (1987).
- [32] J. Friedrich and R. Freeman, *J. Magn. Reson.* **77**, 101 (1988).
- [33] L. K. Hedges and D. I. Hoult, *J. Magn. Reson.* **79**, 391 (1988).
- [34] D. Canet, D. Boudot, A. Belmajdoub, A. Retournard, and J. Brondeau, *J. Magn. Reson.* **79**, 168 (1988).
- [35] F. Mitsumori and N. M. Bolas, *J. Magn. REson.* **97**, 282 (1992).
- [36] K. Hendrich, H. Liu, H. Merkle, J. Zhang, and K. Ugurbil, *J. Magn. Reson.* **97**, 486 (1992).
- [37] (a) E. Rommel, P. Nickel, R. Kimmich, and D. Pusiol, *J. Magn. Reson.* **91**, 630 (1991); (b) E. Rommel, D. Pusiol, P. Nickel, and R. Kimmich, *Meas. Sci. Technol.* **2**, 866 (1991); (c) P. Nickel, E. Rommel, R. Kimmich, and D. Pusiol, *Chem. Phys. Lett.* **183**, 183 (1991); (d) R. Kimmich, E. Rommel, P. Nickel, and D. Pusiol, *Z. Naturforsch.* **47a**, 361 (1992); (e) E. Rommel, R. Kimmich, H. Robert, and D. Pusiol, *Meas. Sci. Technol.* **3**, 446 (1992).
- [38] (a) D. P. Weitekamp, J. R. Garbow, and A. Pines, *J. Chem. Phys.* **77**, 2870 (1982); (b) D. P. Weitekamp, J. R. Garbow, and A. Pines, *J. Chem. Phys.* **80**, 1372 (1984); (c) J. R. Garbow, Ph.D. Thesis, University of California, Berkeley, (1983), published as Lawrence Berkeley Laboratory Report No. 16119.

- [39] W.-K. Rhim, D. D. Elleman, L. B. Schreiber, and R. W. Vaughan, *J. Chem. Phys.* **60**, 4595 (1974).
- [40] G. C. Chingas, *J. Magn. Reson.* **54**, 153 (1983).
- [41] D. G. Cory, A. N. Garroway, and J. B. Miller, *J. Magn. Reson.* **87**, 202 (1990).
- [42] T. J. Lenosky and D. P. Weitekamp, in preparation (1992).

Chapter 4

Theory and Simulations

4.1 Introduction

In this chapter SWW-16 is investigated using average Hamiltonian theory, which provides a means to describe the effect of the combination of line-narrowing and rf gradient pulses on the spin system. Average Hamiltonian theory also reveals what interactions contribute to the residual linewidth. By identifying these interactions and taking steps to eliminate them, one may hope to obtain images of higher resolution. Some of these interactions are difficult to characterize analytically, in which case exact numerical simulations provide additional helpful information. Simulations are presented here which compare pulsed rf versus DC gradients in combination with SWW-16, investigate the error terms introduced by the 2-D imaging coil arrangement (discussed further in Chapter 5), and compare SWW-16 with LW-24, a newly developed and more highly compensated pulse sequence.

4.2 Average Hamiltonian Theory

Multiple-pulse sequences are applied to the nuclear spins to produce coherent evolution of the spin states such that undesired interactions are averaged to zero over the course of a pulse cycle. Average Hamiltonian theory is a convenient means of describing the coherent evolution of nuclear spin states which takes into account higher order terms, i.e., interference terms of non-commuting operators in the cycle [1]. The “average Hamil-

tonian” provides a first order description of the evolution, such as whether the dipolar couplings and/or the chemical shifts are effectively removed by the pulse sequence. For imaging of solids by multiple-pulse line narrowing and radiofrequency gradients, the desired effect of the pulse sequence is to remove dipolar, chemical shift, and bulk magnetic susceptibility contributions to the linewidth while retaining spin-evolution due to the gradient. It is also desirable that the gradient-induced nutation be about the z axis since then the sign of the nutation can be discerned and spins placed symmetrically about the zero-crossing of a linear gradient can be distinguished. Thus, the desired average Hamiltonian is one which is proportional to the spin operator I_z and to the gradient strength.

The correction terms to the average Hamiltonian describe residual interactions which interfere with line-narrowing. For optimal image resolution it is desirable to minimize all correction terms. These include interactions among the dipolar, chemical shift, and gradient Hamiltonians, and also between these Hamiltonians and those of any experimental imperfections.

Pulse imperfections have been included in a discussion of average Hamiltonian theory by Rhim and coworkers [2, 3, 4]. This provides a convenient model for dealing with the effects of rf gradients [5], and is reviewed below.

4.3 Average Hamiltonian Treatment of Pulse Imperfections

Average Hamiltonian theory provides a theoretical framework which is well adapted for discussing multiple-pulse techniques and accounts for much of what is experimentally observed [2, 3, 6, 7, 8, 9]. In a multiple-pulse experiment several thousand rf pulses are applied in a time span of milliseconds to obtain a single spectrum. The cumulative effect of even small pulse errors can hinder the performance of such sequences. Rhim *et al.* have

demonstrated that a number of pulse imperfections, such as phase errors, length errors, rf inhomogeneity, and phase transient effects, can be quite generally incorporated into the average Hamiltonian formulation [3, 4]. It is possible to calculate an average Hamiltonian to describe the effects of these pulse imperfections, and to calculate the terms coupling pulse imperfections with other components of the Hamiltonian, such as the dipolar and off-resonance terms. This treatment successfully explains many of the features of spectra obtained with an improperly tuned spectrometer. Identifying the coupling terms between pulse errors and other components of the Hamiltonian can help to explain how specific pulse errors affect the experimental resolution [3].

The rotating frame Hamiltonian of a driven spin system in a solid state NMR experiment can be divided into terms describing the rf irradiation \mathcal{H}'_{rf} and the contributions from internal interactions as follows:

$$\mathcal{H}(t) = \mathcal{H}'_{\text{rf}}(t) + \mathcal{H}_{\text{int}} , \quad (4.1)$$

where the time-independent internal interactions are given by

$$\mathcal{H}_{\text{int}} = \mathcal{H}_O + \mathcal{H}_D , \quad (4.2)$$

and the time-dependent rf irradiation term may be written

$$\mathcal{H}'_{\text{rf}}(t) = -\gamma B_1(t) (I_x \cos \phi(t) + I_y \sin \phi(t)) , \quad (4.3)$$

where $B_1(t)$ is the amplitude of the applied field and $\phi(t)$ is the phase relative to the rf carrier.

In Equation 4.2 \mathcal{H}_O represents resonance offset and chemical shift terms which are linear in the spin operator I_z , and \mathcal{H}_D represents dipolar coupling which is bilinear in I_z . $\mathcal{H}(t)$ is already in an interaction representation, the rotating frame defined by the rf carrier frequency ω near the Larmor frequency ω_0 . In this frame \mathcal{H}_O and \mathcal{H}_D are “truncated”

to include only spin interactions that produce local fields parallel to the static magnetic field [10]. In truncating \mathcal{H}_O and \mathcal{H}_D it is assumed that the static magnetic field B_0 is very large compared to the local magnetic fields described by \mathcal{H}_{int} . These truncated Hamiltonians can be written

$$\begin{aligned}\mathcal{H}_O &= (\omega - \omega_0)I_z + \omega_0 \sum_i \sigma_{zzi} I_{zi} \\ &= \sum_i (\Delta\omega + \omega_0 \sigma_{zzi}) I_{zi},\end{aligned}\quad (4.4)$$

and

$$\mathcal{H}_D^z = \sum_{i<j} D_{ij} (I_i \cdot I_j - 3I_{zi} I_{zj}). \quad (4.5)$$

In Equation 4.4 $\Delta\omega$ is the resonant offset and σ_{zzi} the secular part of the chemical shift tensor. In Equation 4.5 the dipolar coupling constant D_{ij} may be written

$$D_{ij} = -\gamma^2 (1 - 3 \cos^2 \theta_{ij}) / 2r_{ij}^3, \quad (4.6)$$

where γ is the nuclear gyromagnetic ratio, and θ_{ij} is the angle between the internuclear vector r_{ij} and B_0 . Thus the internal Hamiltonians \mathcal{H}_O and \mathcal{H}_D^z depend on the structure of the solid and its orientation with respect to the static magnetic field [10].

$\mathcal{H}'_{\text{rf}}(t)$, the Hamiltonian describing the interaction of the spins with the applied rf pulses, can be divided into two parts as follows:

$$\mathcal{H}'_{\text{rf}}(t) = \mathcal{H}_{\text{rf}}(t) + \sum_k \mathcal{H}_k(t), \quad (4.7)$$

where $\mathcal{H}_{\text{rf}}(t)$ describes the effect of ideal rf pulses of piecewise constant phase and power and exactly the desired length, while the sum over k includes all the error terms which complete the description of the true experimental situation. These error terms include $k = P$ for phase misadjustments, T for phase transients, δ for pulse length misadjustments, and ϵ for rf inhomogeneity. For an x pulse, these can be written as follows: [4]

$$\mathcal{H}_P = -\omega_1 \sin \phi_x I_y, \quad (4.8)$$

$$\mathcal{H}_T = \omega_T(t)I_y, \quad (4.9)$$

$$\mathcal{H}_\delta = -\frac{\delta_x}{t_w}I_x, \quad (4.10)$$

$$\mathcal{H}_\epsilon = -\sum_i \frac{\epsilon_i}{t_w}I_{xi}. \quad (4.11)$$

Here, t_w is the pulse width so that $\omega_1 t_w = \pi/2$, ϕ_x and δ_x are the phase angle and pulse size misadjustments of the x pulse, ϵ_i is the error in rotation angle at the i^{th} nucleus caused by rf inhomogeneity, and $\omega_T(t)$ is the rf amplitude orthogonal to the x direction. Without loss of generality a coordinate system can be chosen such that

$$\sum_i \epsilon_i = 0 \quad (4.12)$$

and

$$\int_0^{t_w} \omega_T(t)dt = 0. \quad (4.13)$$

Similar definitions hold for pulses of different rf phases.

In order for the multiple-pulse sequence to produce sufficient line narrowing, the dominant term in the rotating frame spin Hamiltonian must be $\mathcal{H}_{\text{rf}}(t)$. In practice, the rotating frame magnetic field produced by the coil which delivers the line-narrowing pulses must usually be somewhat larger than the local fields due to the internuclear couplings and chemical shifts. Therefore, it is convenient to move from the rotating frame into another interaction representation, the toggling frame. The toggling frame is defined by $\mathcal{H}_{\text{rf}}(t)$, with other interactions treated as perturbations. The time development operator used to transform the rotating frame Hamiltonians to their toggling frame counterparts can be written [7]

$$U(t) = U_{\text{rf}}(t)U_{\text{int}}(t), \quad (4.14)$$

where

$$U_{\text{rf}}(t) = T \exp \left(-i \int_0^t \mathcal{H}_{\text{rf}}(t')dt' \right), \quad (4.15)$$

$$U_{\text{int}}(t) = T \exp \left(-i \int_0^t \tilde{\mathcal{H}}_{\text{int}}(t') dt' \right), \quad (4.16)$$

and T is the Dyson time ordering operator which orders later times on the left and earlier times on the right. In the toggling frame the terms of the internal Hamiltonian acquire a time dependence from \mathcal{H}_{rf} :

$$\tilde{\mathcal{H}}_{\text{int}}(t) = U_{\text{rf}}^{-1}(t) \mathcal{H}_{\text{int}}(t) U_{\text{rf}}(t), \quad (4.17)$$

where $\tilde{\mathcal{H}}_{\text{int}}(t)$ is the toggling frame Hamiltonian.

In the case where $\mathcal{H}_{\text{rf}}(t)$ is cyclic with cycle time t_c , the condition

$$U_{\text{rf}}(Nt_c) = \pm 1 \quad (4.18)$$

holds and the rotating frame and the toggling frame coincide at times Nt_c , for integers N . The spin evolution can be sampled in these windows and a spectrum produced through a Fourier transform. Furthermore, if \mathcal{H}_{rf} is periodic, i.e.,

$$\mathcal{H}_{\text{rf}}(t + Nt_c) = \mathcal{H}_{\text{rf}}(t), \quad (4.19)$$

then the time development operator in the toggling frame, U_{int} , has the following property:

$$U_{\text{int}}(Nt_c) = [U_{\text{int}}(t_c)]^N. \quad (4.20)$$

This means that the behavior of the system for an arbitrary number of pulse cycles can be deduced from the time development operator for a single cycle.

The division of \mathcal{H}'_{rf} into ideal and non-ideal terms is especially useful when \mathcal{H}'_{rf} satisfies the periodic condition, but because of $\sum_k \mathcal{H}_k(t)$ it fails to satisfy the cyclic condition. Here \mathcal{H}_{rf} continues to satisfy both the periodic and cyclic conditions, and assuming that

$$\|\mathcal{H}_{\text{rf}}\| \gg \left\| \sum_k \mathcal{H}_k(t) \right\|, \quad (4.21)$$

(where $\|\mathcal{H}_{\text{rf}}\|$ indicates the magnitude of \mathcal{H}_{rf}) the pulse non-idealities can be grouped together with $\mathcal{H}_{\text{int}}(t)$ to give

$$\mathcal{H}_{\text{int}} = \mathcal{H}_O + \mathcal{H}_D^z + \sum_k \mathcal{H}_k(t). \quad (4.22)$$

An effective Hamiltonian $\overline{\mathcal{H}}$ can be defined as follows:

$$U_{\text{int}}(t_c) = \exp(-i\overline{\mathcal{H}}t_c). \quad (4.23)$$

This expression has no time ordering and the effective Hamiltonian has no time dependence. Physically, this means that the spin evolution sampled at integral numbers of cycle times can be described solely by assuming the action of a time independent effective Hamiltonian, assuming such a Hamiltonian could be calculated.

The Magnus expansion [6, 11] can then be used to expand $U_{\text{int}}(t_c)$ so that it remains unitary no matter where the expansion is truncated:

$$U_{\text{int}}(t_c) = \exp \left[-it_c \left(\overline{\mathcal{H}}_{\text{int}}^{(0)} + \overline{\mathcal{H}}_{\text{int}}^{(1)} + \overline{\mathcal{H}}_{\text{int}}^{(2)} + \dots \right) \right]. \quad (4.24)$$

The Magnus expansion is useful only when the evolution due to $\tilde{\mathcal{H}}_{\text{int}}(t)$ is weak enough that the expansion is nearly convergent after a few terms. The convergence condition for the Magnus expansion is roughly

$$t_c \|\tilde{\mathcal{H}}_{\text{int}}\| \ll 1. \quad (4.25)$$

The first three terms of the Magnus expansion are

$$\overline{\mathcal{H}}_{\text{int}}^{(0)} = t_c^{-1} \int_0^{t_c} \tilde{\mathcal{H}}_{\text{int}}(t_1) dt_1 \quad (4.26)$$

$$\overline{\mathcal{H}}_{\text{int}}^{(1)} = (2it_c)^{-1} \int_0^{t_c} dt_2 \int_0^{t_2} dt_1 [\tilde{\mathcal{H}}_{\text{int}}(t_2), \tilde{\mathcal{H}}_{\text{int}}(t_1)] \quad (4.27)$$

$$\begin{aligned} \overline{\mathcal{H}}_{\text{int}}^{(2)} = & -(6t_c)^{-1} \int_0^{t_c} dt_3 \int_0^{t_3} dt_2 \int_0^{t_2} dt_1 \left\{ [\tilde{\mathcal{H}}_{\text{int}}(t_3), [\tilde{\mathcal{H}}_{\text{int}}(t_2), \tilde{\mathcal{H}}_{\text{int}}(t_1)]] + \right. \\ & \left. [\tilde{\mathcal{H}}_{\text{int}}(t_1), [\tilde{\mathcal{H}}_{\text{int}}(t_2), \tilde{\mathcal{H}}_{\text{int}}(t_3)]] \right\}. \end{aligned} \quad (4.28)$$

Notice that the $\overline{\mathcal{H}}^{(n)}$ contain terms of order $n + 1$ in $\tilde{\mathcal{H}}_{\text{int}}(t)$. In general, $\overline{\mathcal{H}}^{(0)}$ is referred to as the average Hamiltonian and $\overline{\mathcal{H}}^{(n)}$ ($n \neq 1$) as the n^{th} -order correction term to the average Hamiltonian.

By expressing \mathcal{H}_{int} according to Equation 4.22, the various terms in the Magnus expansion can be divided into contributions from each of the Hamiltonian terms in a straightforward way

$$\overline{\mathcal{H}}_{\text{int}}^{(0)} = \overline{\mathcal{H}}_O^{(0)} + \overline{\mathcal{H}}_D^{(0)} + \sum_k \overline{\mathcal{H}}_k^{(0)} \quad (4.29)$$

$$\overline{\mathcal{H}}_{\text{int}}^{(1)} = \overline{\mathcal{H}}_O^{(1)} + \overline{\mathcal{H}}_D^{(1)} + \overline{\mathcal{H}}_{DO}^{(1)} + \sum_k (\overline{\mathcal{H}}_{O,k}^{(1)} + \overline{\mathcal{H}}_{D,k}^{(1)}) \quad (4.30)$$

$$\overline{\mathcal{H}}_{\text{int}}^{(2)} = \overline{\mathcal{H}}_O^{(2)} + \overline{\mathcal{H}}_D^{(2)} + \overline{\mathcal{H}}_{DO}^{(2)} + \sum_k (\overline{\mathcal{H}}_{O,k}^{(2)} + \overline{\mathcal{H}}_{D,k}^{(2)}) , \quad (4.31)$$

and so forth. Here $\overline{\mathcal{H}}_{O,k}^{(n)}$ and $\overline{\mathcal{H}}_{D,k}^{(n)}$ represent the n^{th} -order cross terms between the type k pulse imperfection Hamiltonian and the offset and dipolar Hamiltonians, respectively. It can often be assumed that cross terms generated by the interaction of two imperfection terms, i.e., $\sum_k \overline{\mathcal{H}}_k^{(1)}$ and $\sum_k \overline{\mathcal{H}}_k^{(1)}$, are small and can be neglected.

As mentioned above, it is desirable to eliminate all correction terms possible. One convenient way of eliminating the largest correction terms, the $\overline{\mathcal{H}}^{(1)}$ terms, is to use a symmetric pulse sequence. If a Hamiltonian in the toggling frame $\tilde{\mathcal{H}}_A$ has reflection symmetry, that is, if

$$\tilde{\mathcal{H}}_A(t) = \tilde{\mathcal{H}}_A(t_c - t), \quad \text{for } 0 < t < t_c \quad (4.32)$$

then $\overline{\mathcal{H}}_A^{(n)} = 0$ for all odd n [12]. In addition, if $\tilde{\mathcal{H}}_B$ also has reflection symmetry, then $\overline{\mathcal{H}}_B^{(n)}$ and $\overline{\mathcal{H}}_{AB}^{(n)}$ vanish for all odd n . This means that for symmetric cycles, if the Magnus expansion is rapidly convergent, the only important correction terms that need to be considered are terms in $\overline{\mathcal{H}}^{(2)}$. As can be seen from the toggling frame transformations listed in Table 4.1, SWW-16 is symmetric, so $\overline{\mathcal{H}}_{\text{int}}^{(1)} = 0$.

window	U_{rf}^{-1}	\tilde{I}_x	\tilde{I}_y	\tilde{I}_z
0	1	+X	+Y	+Z
1	$\exp(i\frac{\pi}{2}I_y)$	-Z	+Y	+X
2	$\exp(i\frac{\pi}{2}I_y) \exp(-i\frac{\pi}{2}I_x)$	-Z	-X	+Y
3	$\exp(i\frac{\pi}{2}I_y) \exp(-i\pi I_x)$	-Z	-Y	-X
4	$\exp(i\frac{\pi}{2}I_y) \exp(-i\pi I_x) \exp(i\frac{\pi}{2}I_y)$	+X	-Y	-Z
5	$\exp(i\frac{\pi}{2}I_y) \exp(-i\pi I_x) \exp(i\pi I_y)$	+Z	-Y	+X
6	$\exp(i\frac{\pi}{2}I_y) \exp(-i\pi I_x) \exp(i\pi I_y) \exp(-i\frac{\pi}{2}I_x)$	+Z	-X	-Y
7	$\exp(i\frac{\pi}{2}I_y) \exp(-i\pi I_x) \exp(i\pi I_y) \exp(-i\pi I_x)$	+Z	+Y	-X
8	$\exp(i\frac{\pi}{2}I_y) \exp(-i\pi I_x) \exp(i\pi I_y) \exp(-i\pi I_x) \exp(i\frac{\pi}{2}I_y)$	+X	+Y	+Z
9	$\exp(i\frac{\pi}{2}I_y) \exp(-i\pi I_x) \exp(i\pi I_y) \exp(-i\pi I_x)$	+Z	+Y	-X
10	$\exp(i\frac{\pi}{2}I_y) \exp(-i\pi I_x) \exp(i\pi I_y) \exp(-i\frac{\pi}{2}I_x)$	+Z	-X	-Y
11	$\exp(i\frac{\pi}{2}I_y) \exp(-i\pi I_x) \exp(i\pi I_y)$	+Z	-Y	+X
12	$\exp(i\frac{\pi}{2}I_y) \exp(-i\pi I_x) \exp(i\frac{\pi}{2}I_y)$	+X	-Y	-Z
13	$\exp(i\frac{\pi}{2}I_y) \exp(-i\pi I_x)$	-Z	-Y	-X
14	$\exp(i\frac{\pi}{2}I_y) \exp(-i\frac{\pi}{2}I_x)$	-Z	-X	+Y
15	$\exp(i\frac{\pi}{2}I_y)$	-Z	+Y	+X
16	1	+X	+Y	+Z

Table 4.1: SWW-16 toggling frame transformations. Here $\tilde{I}_x = U_{rf}^{-1} I_x U_{rf}$ and the abbreviations $X = I_x$, etc., are used. RF gradient pulses are applied in windows 1-3, 5-7, 9-11, and 13-15.

4.4 Treatment of Gradient Pulses

A completely analogous approach may be used for describing the effect of the rf gradient pulses on the multiple pulse line-narrowing sequence. In this case the Hamiltonian describing the rf irradiation can be considered to be made up of the following parts:

$$\mathcal{H}'_{\text{rf}}(t) = \mathcal{H}_{\text{rf}}(t) + \mathcal{H}_G(t) + \sum_k \mathcal{H}_k(t), \quad (4.33)$$

where $\mathcal{H}_{\text{rf}}(t)$ represents spin interactions with the line-narrowing rf pulses delivered by a coil producing a homogeneous field over the sample region, $\mathcal{H}_G(t)$ represents spin interactions with the gradient rf pulses delivered by a coil producing a linear field gradient over the sample region, and $\sum_k \mathcal{H}_k(t)$ represents the pulse non-idealities mentioned above. In this case, the gradient Hamiltonian as well as the error term Hamiltonians are included with $\mathcal{H}_{\text{int}}(t)$ and only the homogeneous rf pulses are used to determine the toggling frame time development operator, i.e.,

$$U(t) = U_{\text{rf}}(t)U_{\text{int}}(t), \quad (4.34)$$

where $U_{\text{rf}}(t)$ and $U_{\text{int}}(t)$ are defined as in Equations 4.15 and 4.16, but now

$$\mathcal{H}_{\text{int}}(t) = \mathcal{H}_O + \mathcal{H}_D + \mathcal{H}_G(t) + \sum_k \mathcal{H}_k(t). \quad (4.35)$$

Using this formulation makes the gradient term of the average Hamiltonian of SWW-16 trivial to calculate. The Hamiltonian of each gradient pulse acts only during the window in which that pulse is applied. For the 1-D experiments discussed in Chapter 3, the rotating frame phases of the gradient pulses are $\pm X$, so these are described by Hamiltonians $\mathcal{H}_G = \pm\theta(\mathbf{r})I_x$, respectively. As seen in Table 4.1, when transformed into the toggling frame, these become $\mathcal{H}_G = \theta(\mathbf{r})I_z$ and the average Hamiltonian is the weighted sum:

$$\overline{\mathcal{H}}_G^{(0)} = \frac{1}{t_c} \sum_n \theta_n(\mathbf{r})I_z. \quad (4.36)$$

The chemical shift and dipolar contributions to the average Hamiltonian are calculated in the usual manner. For SWW-16 these contributions vanish and so $\overline{\mathcal{H}}^{(0)} = \overline{\mathcal{H}}_C^{(0)}$.

4.5 Average Hamiltonian Including Finite Pulse Effects

The δ -pulse approximation is often used in average Hamiltonian calculations. This approximation assumes that, in the rotating frame, the rf fields are much larger than the internal fields, so the latter may be neglected during the rf pulses [1]. It has been shown that if the correct timing and pulse angles are used, the average dipolar Hamiltonian $\overline{\mathcal{H}}_D^{(0)}$ of the multiple pulse sequence WHH-4 [13] can be made to vanish including finite pulse effects [10, 1]. In the case of WHH-4 it turns out that the optimum pulse angle depends on the duty factor (the fraction of the cycle time in which the pulses are on) and is not necessarily 90° .

Similarly, the average Hamiltonian including finite pulse effects can be calculated for SWW-16 to indicate the most favorable pulse sequence timing and pulse angle. Since SWW-16 is made up of solid echo groups, as is WHH-4, it is not surprising that the “ideal” timing of SWW-16 is the same as that for WHH-4. However, for SWW-16 there is a choice of two pulse angles which cause $\overline{\mathcal{H}}_D^{(0)}$ to vanish including finite pulse effects. The first is 90° , independent of pulse sequence duty factor, and the second is (like that for WHH-4) the solution to

$$\delta(1 - \tan \beta / \beta) = \frac{4}{3}, \quad (4.37)$$

where β is the pulse angle (and $\beta \geq 90^\circ$) and δ is the duty factor. These calculations are shown below.

First, it is helpful to use the notation similar to that of Mansfield and used for pulse sequences made up of solid echo groups [8]. This notation focuses attention on the state of the Hamiltonian in the toggling frame; specifically, a pulse cycle is expressed according

to the state of $\tilde{I}_z = U_{\text{rf}}^{-1} I_z U_{\text{rf}}$. In this notation a solid echo group is written (ABC) , where $A, \bar{A}, B, \bar{B}, C,$ and \bar{C} are six possible states of \tilde{I}_z , $A = -\bar{A}$, etc. and $A, B,$ and C are mutually orthogonal. An example is shown in Figure 4.1. For any given multiple pulse sequence there are generally several choices of pulse phases. However, each version of the pulse sequence can be expressed by the same toggling frame states written in ABC notation. This allows the study of the characteristics of a pulse cycle which do not depend on which specific version of the cycle is used.

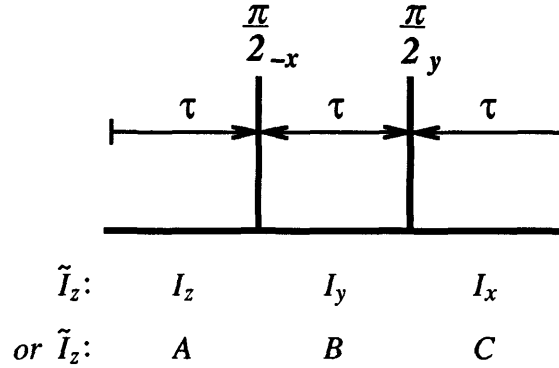


Figure 4.1: A solid echo group. The toggling frame values of I_z indicated assume $\pi/2$ pulses. This solid echo group may be written equivalently (ABC) .

Figure 4.2 shows the timing of the same solid echo group, but now with pulses of finite width. $\overline{\mathcal{H}}_D^{(0)}$ for SWW-16 can be calculated by first determining $\overline{\mathcal{H}}_D^{(0)}$ for the solid echo group, rewriting this in terms of (ABC) , using this answer to write down the individual terms for each solid echo group of the sequence, and then summing these terms.

To calculate $\overline{\mathcal{H}}_D^{(0)}$, the solid echo is divided into five time periods, p , corresponding to the three delays and two pulses, as shown in Figure 4.2. In these calculations, the pulse angle is kept general, i.e., $\beta = \omega_1 t_w$, where $\omega_1 = \gamma B_1$ and t_w is the pulse width. The result is

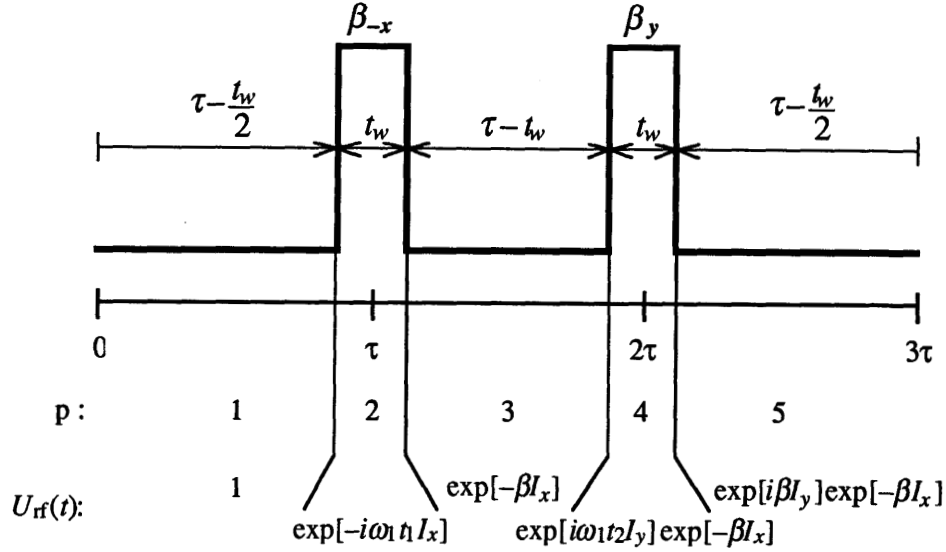


Figure 4.2: Solid echo timing including finite pulse widths.

$$\bar{\mathcal{H}}_D^{(0)} = \frac{1}{t_c} \int_0^{t_c} \tilde{\mathcal{H}}_D(t_1) dt_1 \quad (4.38)$$

$$= \frac{1}{3\tau} \sum_{p=1}^5 \tilde{\mathcal{H}}_D(p) t_p \quad (4.39)$$

$$= \frac{1}{3\tau} \sum_{p=1}^5 \sum_{i<j} D_{ij} (I_i \cdot I_j - 3\tilde{I}_{zi} \tilde{I}_{zj}) t_p \quad (4.40)$$

$$= \frac{1}{3\tau} \left\{ \sum_{i<j} D_{ij} I_i \cdot I_j (3\tau) - 3 \sum_{p=1}^5 \sum_{i<j} D_{ij} \tilde{I}_{zi} \tilde{I}_{zj} t_p \right\} \quad (4.41)$$

$$= \sum_{i<j} D_{ij} \left\{ \left[\left(1 - \frac{t_w}{2\tau} \right) \cos \beta + \frac{t_w}{2\tau} \frac{\sin \beta}{\beta} \right] \times \right. \\ \left[\cos \beta I_{xi} I_{xj} + \cos^3 \beta I_{yi} I_{yj} - (1 + \cos^2 \beta) \cos \beta I_{zi} I_{zj} - \right. \\ \left. \sin^2 \beta (I_{xi} I_{yj} + I_{yi} I_{xj}) - \sin 2\beta (I_{xi} I_{zj} + I_{zi} I_{xj}) - \right. \\ \left. \left. (1 + \cos^2 \beta) \sin \beta (I_{yi} I_{zj} + I_{zi} I_{yj}) \right] \right\}. \quad (4.42)$$

Equation 4.42 can be rewritten in the more general notation (where, in this particular

instance, $A = I_z$, $B = I_y$, and $C = I_x$) as follows:

$$\begin{aligned} \overline{\mathcal{H}}_D^{(0)} = \sum_{i < j} D_{ij} \left\{ \left[\left(1 - \frac{t_w}{2\tau} \right) \cos \beta + \frac{t_w \sin \beta}{2\tau \beta} \right] \times \right. \\ \left[\cos \beta C_i C_j + \cos^3 \beta B_i B_j - (1 + \cos^2 \beta) \cos \beta A_i A_j - \right. \\ \left. \sin^2 \beta (C_i B_j + B_i C_j) - \sin 2\beta (C_i A_j + A_i C_j) - \right. \\ \left. \left. (1 + \cos^2 \beta) \sin \beta (B_i A_j + A_i B_j) \right] \right\}. \end{aligned} \quad (4.43)$$

The eight solid echo groups of SWW-16 are shown in Figure 4.3. $\overline{\mathcal{H}}_D^{(0)}$ can be calculated by merely writing down $\overline{\mathcal{H}}_{D_n}^{(0)}$ for each solid echo group and then summing these terms. For simplicity, the following definition is made:

$$\mathcal{K} = \sum_{i < j} D_{ij} \left[\left(1 - \frac{t_w}{2\tau} \right) \cos \beta + \frac{t_w \sin \beta}{2\tau \beta} \right]. \quad (4.44)$$

	(ABC)	(C$\overline{B}\overline{A}$)	($\overline{A}\overline{B}\overline{C}$)	($\overline{C}\overline{B}\overline{A}$)	($\overline{A}\overline{B}\overline{C}$)	($\overline{C}\overline{B}\overline{A}$)	($\overline{A}\overline{B}\overline{C}$)	(CBA)
solid echo # :	1	2	3	4	5	6	7	8

Figure 4.3: Solid echo groups of SWW-16.

The average Hamiltonian terms $\overline{\mathcal{H}}_{D_n}^{(0)}$ for the n solid echo groups are then:

$$\begin{aligned} \overline{\mathcal{H}}_{D_1}^{(0)} = \mathcal{K} [\cos \beta (C_i C_j) + \cos^3 \beta (B_i B_j) - (1 + \cos^2 \beta) \cos \beta (A_i A_j) - \\ \sin^2 \beta (C_i B_j + B_i C_j) - \sin 2\beta (C_i A_j + A_i C_j) - \\ (1 + \cos^2 \beta) \sin \beta (B_i A_j + A_i B_j)] \end{aligned} \quad (4.45)$$

$$\begin{aligned} \overline{\mathcal{H}}_{D_2}^{(0)} = \mathcal{K} [\cos \beta (A_i A_j) + \cos^3 \beta (B_i B_j) - (1 + \cos^2 \beta) \cos \beta (C_i C_j) - \\ \sin^2 \beta (A_i B_j + B_i A_j) - \sin 2\beta (-A_i C_j - C_i A_j) - \\ (1 + \cos^2 \beta) \sin \beta (-B_i C_j - C_i B_j)] \end{aligned} \quad (4.46)$$

$$\begin{aligned}
\overline{\mathcal{H}}_{D_3}^{(0)} &= \mathcal{K} [\cos \beta (C_i C_j) + \cos^3 \beta (B_i B_j) - (1 + \cos^2 \beta) \cos \beta (A_i A_j) - \\
&\quad \sin^2 \beta (-C_i B_j - B_i C_j) - \sin 2\beta (C_i A_j + A_i C_j) - \\
&\quad (1 + \cos^2 \beta) \sin \beta (-B_i A_j - A_i B_j)] \tag{4.47}
\end{aligned}$$

$$\begin{aligned}
\overline{\mathcal{H}}_{D_4}^{(0)} &= \mathcal{K} [\cos \beta (A_i A_j) + \cos^3 \beta (B_i B_j) - (1 + \cos^2 \beta) \cos \beta (C_i C_j) - \\
&\quad \sin^2 \beta (-A_i B_j - B_i A_j) - \sin 2\beta (-A_i C_j - C_i A_j) - \\
&\quad (1 + \cos^2 \beta) \sin \beta (B_i C_j + C_i B_j)] \tag{4.48}
\end{aligned}$$

$$\begin{aligned}
\overline{\mathcal{H}}_{D_5}^{(0)} &= \mathcal{K} [\cos \beta (C_i C_j) + \cos^3 \beta (B_i B_j) - (1 + \cos^2 \beta) \cos \beta (A_i A_j) - \\
&\quad \sin^2 \beta (C_i B_j + B_i C_j) - \sin 2\beta (-C_i A_j - A_i C_j) - \\
&\quad (1 + \cos^2 \beta) \sin \beta (-B_i A_j - A_i B_j)] \tag{4.49}
\end{aligned}$$

$$\begin{aligned}
\overline{\mathcal{H}}_{D_6}^{(0)} &= \mathcal{K} [\cos \beta (A_i A_j) + \cos^3 \beta (B_i B_j) - (1 + \cos^2 \beta) \cos \beta (C_i C_j) - \\
&\quad \sin^2 \beta (-A_i B_j - B_i A_j) - \sin 2\beta (A_i C_j + C_i A_j) - \\
&\quad (1 + \cos^2 \beta) \sin \beta (-B_i C_j - C_i B_j)] \tag{4.50}
\end{aligned}$$

$$\begin{aligned}
\overline{\mathcal{H}}_{D_7}^{(0)} &= \mathcal{K} [\cos \beta (C_i C_j) + \cos^3 \beta (B_i B_j) - (1 + \cos^2 \beta) \cos \beta (A_i A_j) - \\
&\quad \sin^2 \beta (-C_i B_j - B_i C_j) - \sin 2\beta (-C_i A_j - A_i C_j) - \\
&\quad (1 + \cos^2 \beta) \sin \beta (B_i A_j + A_i B_j)] \tag{4.51}
\end{aligned}$$

$$\begin{aligned}
\overline{\mathcal{H}}_{D_8}^{(0)} &= \mathcal{K} [\cos \beta (A_i A_j) + \cos^3 \beta (B_i B_j) - (1 + \cos^2 \beta) \cos \beta (C_i C_j) - \\
&\quad \sin^2 \beta (A_i B_j + B_i A_j) - \sin 2\beta (A_i C_j + C_i A_j) - \\
&\quad (1 + \cos^2 \beta) \sin \beta (B_i C_j + C_i B_j)] . \tag{4.52}
\end{aligned}$$

Summing these yields

$$\begin{aligned}
\overline{\mathcal{H}}_D^{(0)} &= \sum_{n=1}^8 \overline{\mathcal{H}}_{D_n}^{(0)} = \mathcal{K} [\cos \beta 4(A_i A_j + C_i C_j) + \cos^3 \beta 8(B_i B_j) - \\
&\quad (1 + \cos^2 \beta) \cos \beta 4(A_i A_j + C_i C_j) - \sin^2 \beta \cdot 0 - \\
&\quad \sin 2\beta \cdot 0 - (1 + \cos^2 \beta) \sin \beta \cdot 0] , \tag{4.53}
\end{aligned}$$

which can be simplified to

$$\begin{aligned} \overline{\mathcal{H}}_D^{(0)} = \sum_{i < j} D_{ij} \left[\left(1 - \frac{t_w}{2\tau} \right) \cos \beta + \frac{t_w}{2\tau} \frac{\sin \beta}{\beta} \right] [4 \cos^3 \beta] \times \\ (-A_i A_j + 2B_i B_j - C_i C_j). \end{aligned} \quad (4.54)$$

Thus, there are two values of β for which $\overline{\mathcal{H}}_D^{(0)}$ vanishes, $\beta = \pi/2$ and β such that Equation 4.37 is satisfied. In practice, it is much easier to adjust the pulse amplitudes such that $\beta = \pi/2$, so this was the value used experimentally.

4.6 Compensated Sets

Whenever a given Hamiltonian term in the Magnus expansion for a compound cycle is the algebraic sum of the separate contributions from each of the pulse groups which make the entire compound cycle, the cycle decouples with respect to that Hamiltonian term; in other words, there are no cross terms between the pulse groups [4]. A simple example of this is the average Hamiltonian. $\overline{\mathcal{H}}^{(0)}$ decouples for all pulse cycles, since

$$\overline{\mathcal{H}}^{(0)} = \frac{1}{t_c} \int_0^{t_c} \tilde{\mathcal{H}}(t_1) dt_1. \quad (4.55)$$

Compensated sets are useful in the design of compound pulse sequences. If it is known when a compound cycle will decouple for higher order average Hamiltonian terms, then it is possible to combine the component pulse groups so that additional unwanted Hamiltonian terms are eliminated without reintroducing any of the undesired terms which vanish for each of the pulse groups considered separately. Considering the first order correction term, Burum and Rhim [4] have shown that if the average Hamiltonian of interaction A in the j^{th} subinterval of a pulse sequence ($\overline{\mathcal{H}}_{A_j}^{(0)}$) vanishes for each of the m subintervals of the sequence, then the cycle decouples for the first order correction term $\overline{\mathcal{H}}_A^{(1)}$. That is,

$$\overline{\mathcal{H}}_A^{(1)} = \frac{1}{t_c} \sum_{j=1}^m t_{c_j} \overline{\mathcal{H}}_{A_j}^{(1)}, \quad (4.56)$$

where $\overline{\mathcal{H}}_{A_j}^{(1)}$ is $\overline{\mathcal{H}}_A^{(1)}$ calculated for the j^{th} subinterval of length t_{c_j} . Furthermore, if $\overline{\mathcal{H}}_{A_j}^{(0)} = 0$ only assuming δ -pulses, $\overline{\mathcal{H}}_A^{(1)}$ still decouples to first order in t_w .

Similarly, if $\overline{\mathcal{H}}_{A_j}^{(0)}$ vanishes for each subinterval of a compound cycle, the cycle also decouples for $\overline{\mathcal{H}}_{A_j}^{(2)}$ [4], that is,

$$\overline{\mathcal{H}}_A^{(2)} = \frac{1}{t_c} \sum_{j=1}^m t_{c_j} \overline{\mathcal{H}}_{A_j}^{(2)}, \quad (4.57)$$

where $\overline{\mathcal{H}}_{A_j}^{(2)}$ is $\overline{\mathcal{H}}_A^{(2)}$ calculated for the j^{th} subinterval. In this case, finite pulse width effects have been neglected. Finally, if $\overline{\mathcal{H}}_{A_j}^{(0)}$ vanishes for each subinterval, for any other Hamiltonian $\tilde{\mathcal{H}}_B$, the cycle also decouples with respect to the cross-term $\overline{\mathcal{H}}_{AB}^{(1)}$, regardless of the behavior of $\tilde{\mathcal{H}}_B$. However, if $\overline{\mathcal{H}}_{A_j}^{(0)}$ vanishes over each subinterval only for δ -function pulses, the cycle may not decouple to first order in t_w with respect to $\overline{\mathcal{H}}_{AB}^{(1)}$, depending on the behavior of $\tilde{\mathcal{H}}_B$.

From these considerations Burum and Rhim drew up a list of compensated sets from which it is possible to build up a compound cycle that decouples with regard to some Hamiltonian term $\overline{\mathcal{H}}_A^{(n)}$ [4]. A compensated set is defined as a set of solid echo pulse groups that makes no net contribution to $\overline{\mathcal{H}}_A^{(n)}$ as long as each member of the set is included somewhere in the compound cycle. The list of compensated sets has been extended by Lenosky and Weitekamp [14] and used in the design of a new pulse sequence, LW-24, for multiple-pulse rf gradient imaging. The twelve solid echo groups of LW-24, written in *ABC* notation, are shown in Figure 4.4. The compensation of the line narrowing pulses of SWW-16 and LW-24 for various Hamiltonian terms is shown in Table 4.2.

Notice that SWW-16 is not compensated for $\overline{\mathcal{H}}_D^{(2)}$. It is decoupled for $\overline{\mathcal{H}}_D^{(2)}$, however, and so it is easy to show that

$$\overline{\mathcal{H}}_D^{(2)} = -\frac{\tau^2}{18} \left\{ \left[\mathcal{H}_D^A - \mathcal{H}_D^C, \left[\mathcal{H}_D^A, \mathcal{H}_D^B \right] \right] + \left[\mathcal{H}_D^C - \mathcal{H}_D^A, \left[\mathcal{H}_D^C, \mathcal{H}_D^B \right] \right] \right\}, \quad (4.58)$$

where, for example, \mathcal{H}_D^A is the dipolar Hamiltonian of the *A* state of \tilde{I}_z . Since SWW-16

$$\begin{array}{c}
(ABC)(CAB)(BCA)(ACB)(BAC)(CBA) \times \\
\text{solid echo \# : } 1 \quad 2 \quad 3 \quad 4 \quad 5 \quad 6 \\
(A\bar{C}B)(B\bar{A}\bar{C})(\bar{C}\bar{B}\bar{A})(\bar{A}\bar{C}\bar{B})(\bar{B}\bar{A}\bar{C})(\bar{C}\bar{B}\bar{A}) \\
\text{solid echo \# : } 7 \quad 8 \quad 9 \quad 10 \quad 11 \quad 12
\end{array}$$

Figure 4.4: Solid echo groups of LW-24.

is symmetric, $\overline{\mathcal{H}}_D^{(2)}$ is the largest correction term and a major source of the residual line-broadening. LW-24, which is also symmetric, was designed specifically to be compensated for $\overline{\mathcal{H}}_D^{(2)}$.

Since $\overline{\mathcal{H}}_O^{(0)} \neq 0$ for a solid echo group, assuming δ -function pulses, SWW-16 and LW-24 do not decouple with respect to $\overline{\mathcal{H}}_O^{(2)}$. For both SWW-16 and LW-24, the smallest group over which $\overline{\mathcal{H}}_O^{(0)}$ vanishes is one half of the cycle. Thus, calculating $\overline{\mathcal{H}}_O^{(2)}$ for these sequences is rather long and tedious. SWW-16 and LW-24 are not compensated for $\overline{\mathcal{H}}_O^{(2)}$, $\overline{\mathcal{H}}_{DO}^{(2)}$, $\overline{\mathcal{H}}_{OG}^{(2)}$, and $\overline{\mathcal{H}}_{DG}^{(2)}$. For LW-24 this latter term is the largest source of residual coupling and leads to a gradient-dependent increase in linewidth.

It has been shown that SWW-16 is compensated for symmetric phase transients and rf inhomogeneity to the level of the average Hamiltonian [15]. This is because the line-narrowing portion of SWW-16 is made up of four consecutive $X\Phi\Phi X$ or $\Phi X X \Phi$ pulse groups with either a 0° or a 180° overall phase shift between successive groups.

4.7 Symmetric Placement of Gradient Pulses

In SWW-16 there are twelve windows in which rf gradient pulses can occur leading to nutation about z . In general, using all twelve windows is desirable because it maximizes the gradient-induced spin nutation per cycle available from a gradient of a given strength.

Hamiltonian term	pulse width	SWW-16	LW-24
$\overline{\mathcal{H}}_D^{(1)}$	to first order in t_w	compensated over every 1/4 cycle	compensated over entire cycle
$\overline{\mathcal{H}}_{DO}^{(1)}$	δ -function pulses only	compensated over entire cycle	compensated over each 1/2 cycle
$\overline{\mathcal{H}}_D^{(0)}$	finite pulse width	compensated over entire cycle	compensated over every 1/4 cycle
$\overline{\mathcal{H}}_D^{(2)}$	δ -function pulses only	not compensated	compensated over every 1/4 cycle

Table 4.2: Compensation of SWW-16 line-narrowing pulses and LW-24 for various Hamiltonian terms.

One can envision instances in which it is desirable not to use all twelve windows, for example, if sampling occurs more than once per cycle. In these cases, care needs to be taken in selecting windows. First, the windows should be chosen so that the toggling frame gradient Hamiltonian remains symmetric. This ensures that $\overline{\mathcal{H}}^{(1)}$ still vanishes. In addition, for 2-D gradient experiments like those described in Chapter 5, only certain combinations of windows cause the unwanted gradient component to vanish at the level of the average Hamiltonian. This can be seen with the help of Table 4.1. The unwanted gradient component, as explained further in Chapter 5, scales as I_y , so when observed in the toggling frame it behaves as \tilde{I}_y in the Table. If gradient pulses occur in all twelve windows, the sum of the corresponding \tilde{I}_y values vanishes, thus the unwanted gradient component is averaged to zero. It is also averaged to zero if certain combinations of four or eight gradient windows are used. There are three combinations of four gradient windows for which $\tilde{\mathcal{H}}_G$ is symmetric and the unwanted component vanishes: 2, 6, 10,

and 14; 1, 7, 9, and 15; and 3, 5, 11, and 13. There are also three combinations of eight gradient windows for which this is the case: 1, 3, 5, 7, 9, 11, 13, and 15; 1, 2, 6, 7, 9, 10, 14, and 15; and 2, 3, 5, 6, 10, 11, 13, and 14. For all of the experiments described in this dissertation, all twelve gradient windows were used.

4.8 Simulations

Exact numerical simulations on a model five-spin system were run to further investigate SWW-16. The simulation program used is described in a thesis by N. D. Kurur [16]. The range of chemical shifts and dipolar couplings, shown in Figure 4.5, was chosen to represent the values found in many solids. The values were not chosen with respect to any given geometry or molecular arrangement, that is, they represent neither an arrangement with any special symmetry nor a target molecule. Previous simulation work had been done with the model three-spin system described by Weitekamp and coworkers [5]. This system was found not to provide a rigorous enough test of the pulse sequences simulated. In particular, the terms of the Magnus expansion that have an important effect on the resulting linewidth act on three or more spins. A particular three-spin system may lead to accidental cancellation of individual terms. A five-spin system reduces the chance of such cancellation and so leads to results which can be generalized with more confidence. The use of more than five spins requires excessive computation and should not give qualitatively different results. A simulation of a one-pulse spectrum of this model spin system shows the natural linewidth to be 20 kHz.

The value of numerical simulations to multiple-pulse design was demonstrated by early simulations of SWW-16 on the three-spin system [15]. These showed that the gradient-dependent increase in linewidth noticed in the original work [5] was largely due to error terms introduced by simulating gradient pulses as missets in the homogeneous

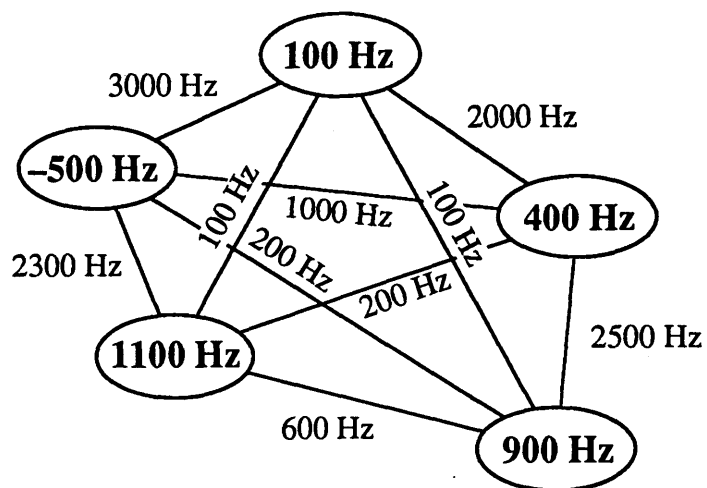


Figure 4.5: Chemical shift values (in the ovals) and dipolar couplings, D_{ij} , of the model five-spin system used in the simulations described below.

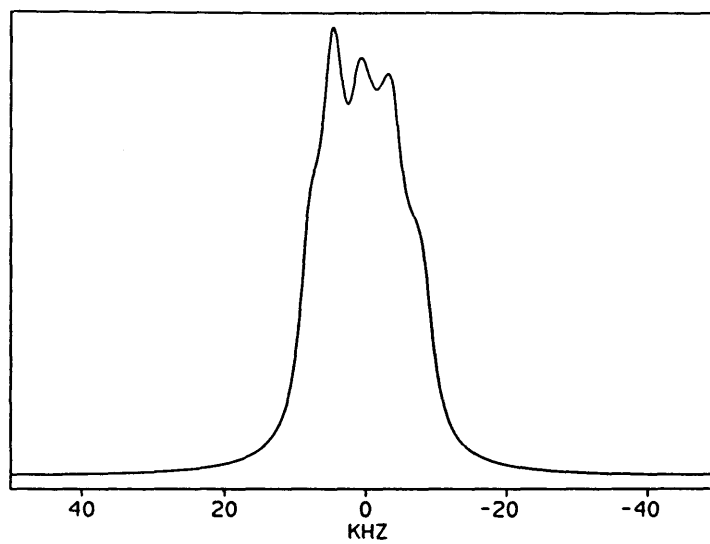


Figure 4.6: One-pulse simulation on the model five-spin system. The linewidth is 20 kHz.

pulse lengths. The gradient-dependent increase in linewidth is substantially less if the gradient pulses are simulated as extra homogeneous pulses in the windows of the line-narrowing sequence. The average Hamiltonian describing the sequence with pulse missets is identical to that describing the sequence with extra homogeneous pulses. The difference lies in the various correction terms to the average Hamiltonian, some of which are non-trivial to calculate. Simulations provided a convenient method for ascertaining the effects of these correction terms.

The simulations below are of nutation spectra, rather than of images; the rf gradient pulses are simulated as homogeneous pulses. This is accurate because spins close enough to interact experience the same applied field. The results of the simulations are displayed as stack plots with $\sum_n \theta_n(\mathbf{r})$, the cumulative gradient-induced nutation angle, increasing incrementally from $0^\circ/t_c$ in the first spectrum of each stack to $360^\circ/t_c$ in the last. In this way, each nutation spectrum represents a “point-image” at a different location along the gradient.

In the simulations presented, the gradient strength is increased to the point where the peak moves past the Nyquist frequency and is folded in. This is done to simulate the possibility of sampling twice per cycle. The resulting peak widths are a valid representation of this; however, in the case of sampling twice per cycle, the spectral width would be doubled and so these peaks would not be folded in. Also notice that only half the spectral width is used (i.e., $\sum_n \theta_n(\mathbf{r}) \leq 0$).

4.8.1 RF vs. DC Gradients

SWW-16 not only has twelve windows in which an rf gradient pulse can be applied to yield a net nutation about z , but also has five windows in which a DC gradient can be applied. Garroway and coworkers have used SWW-16 in combination with pulsed DC gradients to image the polyether imide [17]. In both cases the toggling frame gradient

Hamiltonian is symmetric, so the first order correction term to the average Hamiltonian vanishes. Simulations comparing the theoretical performance of pulsed DC gradients and rf gradients are shown in Figure 4.7. The rf gradient simulations assume the coil arrangement used for 1-D imaging. In these simulations the pulsed DC gradients were simulated as a time-dependent resonance offset. The simulations are quite similar. There is a small difference in lineshape and the peaks near the Nyquist frequency look a bit narrower for the DC gradient simulations. It is unclear, however, whether this slight difference would be experimentally observable. This indicates that ideal pulsed rf and DC gradients should perform comparably well. The rf gradients do have the advantage that there are more windows in which they can be applied and which allows one to use a much higher gradient duty factor. Assuming δ -function timing, the maximum duty factor for rf gradient pulses is $2/3$ while that for DC gradient pulses is $1/3$. To produce the same effective gradient, $\sum_n \theta_n(\mathbf{r})$, then, the DC gradient would have to be twice as large as the rf gradient.

4.8.2 Unwanted Gradient Terms

With the quadrupole coil arranged vertically for 2-D imaging there are two orthogonal components to the gradient. One produces the desired nutation. The second is effectively averaged to zero. At the level of the average Hamiltonian, then, it is possible to select one component of the gradient at a time. The presence of the second orthogonal component will, however, introduce contributions to the correction terms of the average Hamiltonian. Such correction terms are undesirable because they increase the linewidth.

Simulations comparing imaging with the coils in the 1-D arrangement and imaging with coils in the 2-D arrangement are shown in Figures 4.8, 4.9, and 4.10. The simulations in Figure 4.8 assume a $2.7 \mu\text{s} \pi/2$ time and a $304.8 \mu\text{s}$ cycle time, values similar to those used experimentally. The simulation in Figure 4.8(a) assumes the presence of gradient

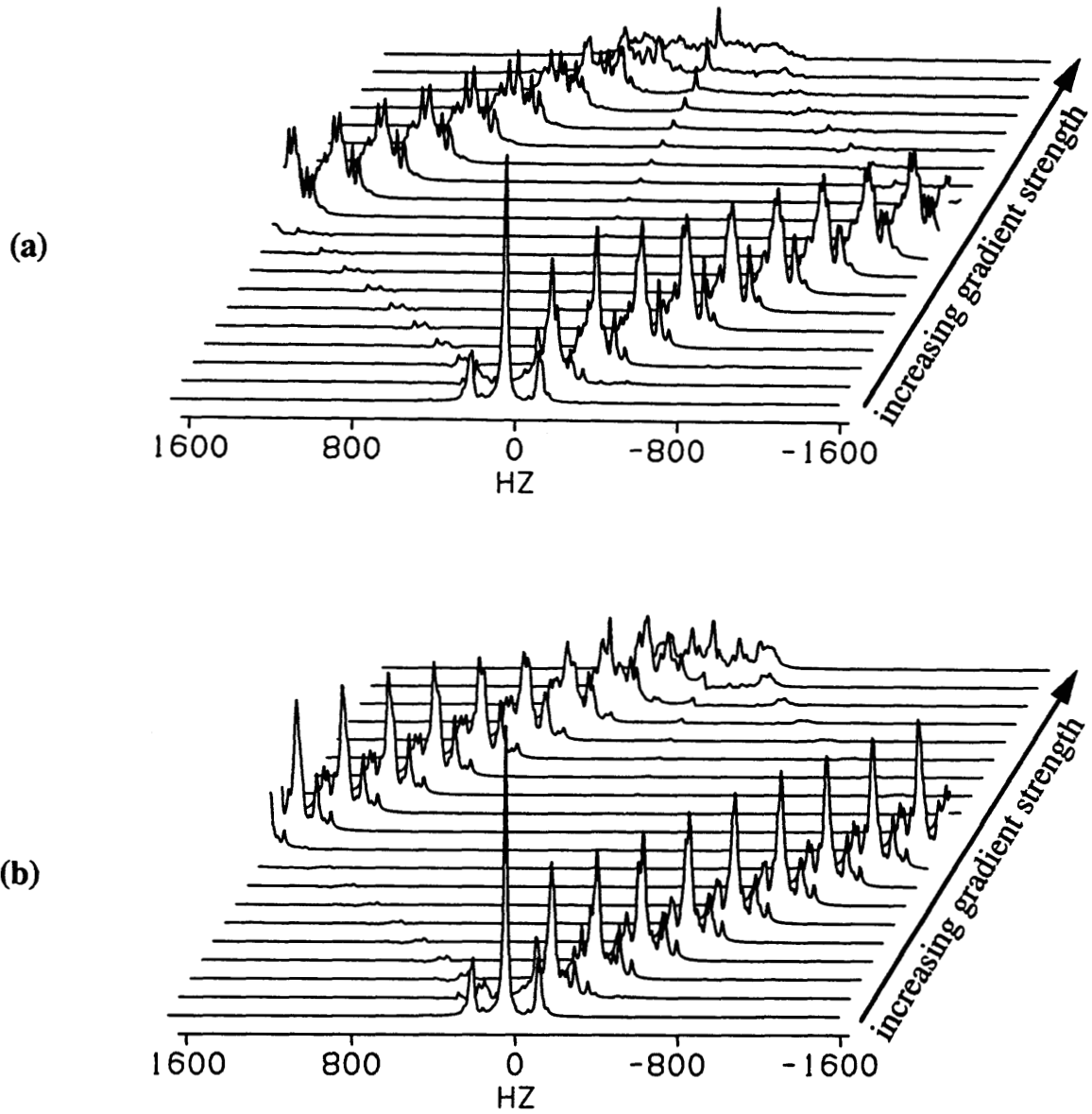


Figure 4.7: Comparison of DC and rf gradients. These simulations are of SWW-16 assuming a $2.7 \mu\text{s}$ $\pi/2$ time and a $304.8 \mu\text{s}$ cycle time. (a) SWW-16 with rf gradients. (b) SWW-16 with DC gradients.

component G_{xx} only, corresponding to the coil arrangement used for 1-D imaging. The simulation in Figures 4.8(b) assumes the presence of gradient components G_{xx} and G_{yy} , corresponding to the coil arrangement used for 2-D imaging. The 20 points in (b) are chosen along the line $B_{1x} = B_{1y}$. The simulations are nearly identical for the first few points in (a) and (b). Differences appear closer to the Nyquist frequency where peaks in (b) look slightly narrower than those in (a) and a small peak begins to appear in (b) at 0 Hz. Past the Nyquist frequency the peak at 0 Hz rapidly becomes dominant in (b) but not in (a). This peak represents spin-locked magnetization due to the error terms associated with the extra gradient component of the 2-D coil. It would appear as a bright spot in the center of an image.

For the simulations in Figures 4.9 and 4.10 the cycle time has been reduced to $152.4 \mu\text{s}$. The error terms are now much less of a problem for the 2-D coil arrangement. In Figure 4.9 the $\pi/2$ time has been reduced to $1.35 \mu\text{s}$, while in Figure 4.10 it remains at $2.7 \mu\text{s}$. The shorter $\pi/2$ time adds some additional improvement, although not as dramatic an improvement as does the shorter cycle time. Experimentally, the shortest cycle time used was $218 \mu\text{s}$ and the shortest $\pi/2$ time was $2.1 \mu\text{s}$ and sampling occurred once per cycle. The conclusion from the calculations is that for the cycle times and sampling rates used there is no significant loss of resolution in using a single vertical quadrupole coil rather than two orthogonal gradient coils (as described in Chapter 3). The experimental results presented in Chapter 5 suggest that resolution is degraded by a spatially varying rf phase of the solenoid coil. The spatially varying phase is expected to degrade resolution more so for images obtained with a single vertical gradient coil than for images obtained with two orthogonal gradient coils (see Chapter 5) [19]. For the actual experiments to date, it is most likely that by using a single vertical quadrupole coil the image resolution has been degraded.

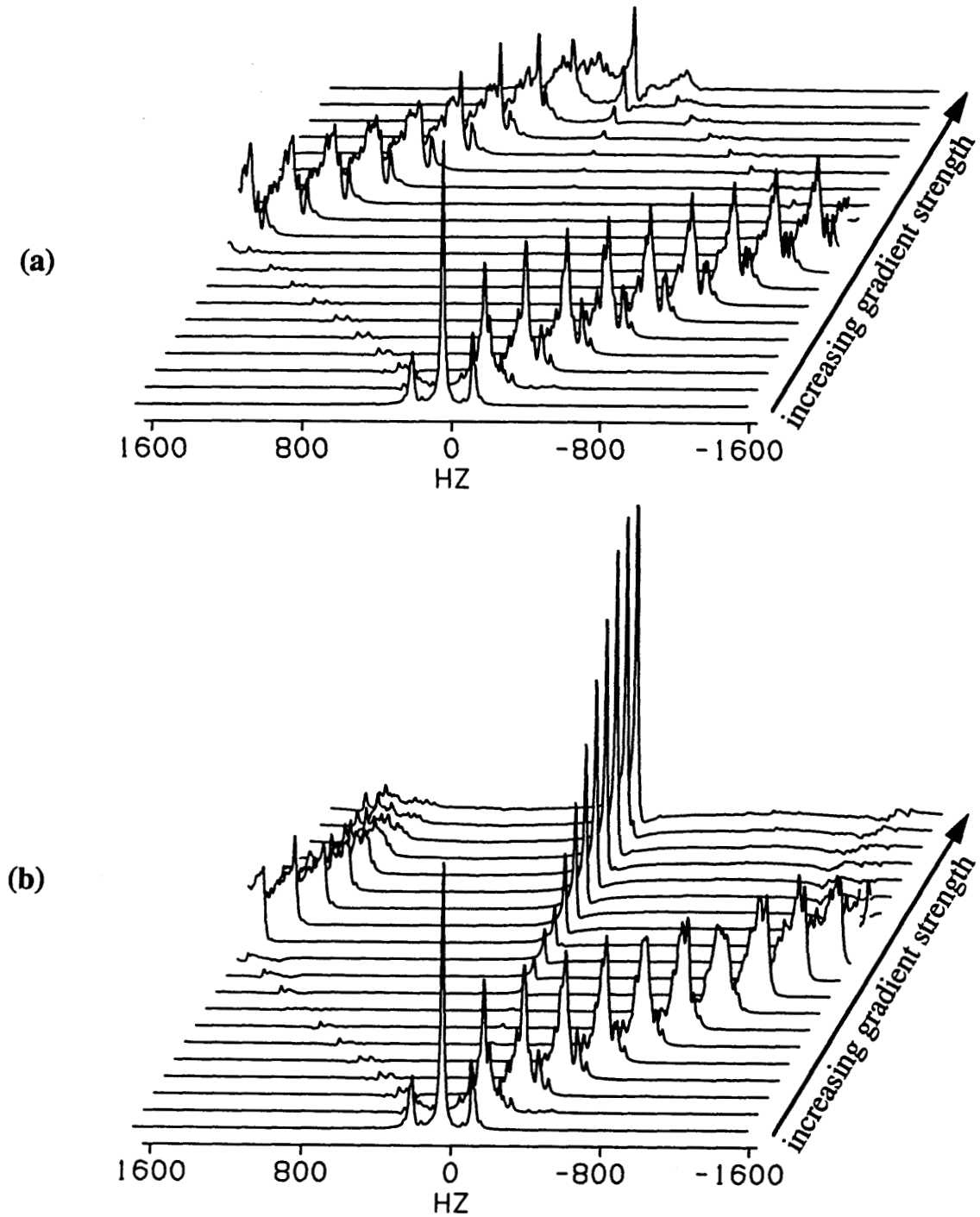


Figure 4.8: The effect of unwanted gradient terms. The $\pi/2$ assumed is $2.7 \mu\text{s}$ and the cycle time is $304.8 \mu\text{s}$. The simulations in (a) assume the presence of gradient G_{xx} only, as is the case for the coil arrangement used in 1-D imaging. The simulations in (b) assume the presence of gradients G_{xx} and G_{yy} , corresponding to the case for 2-D imaging. The 20 gradient points in (b) are selected along the line $B_{1x} = B_{1y}$.

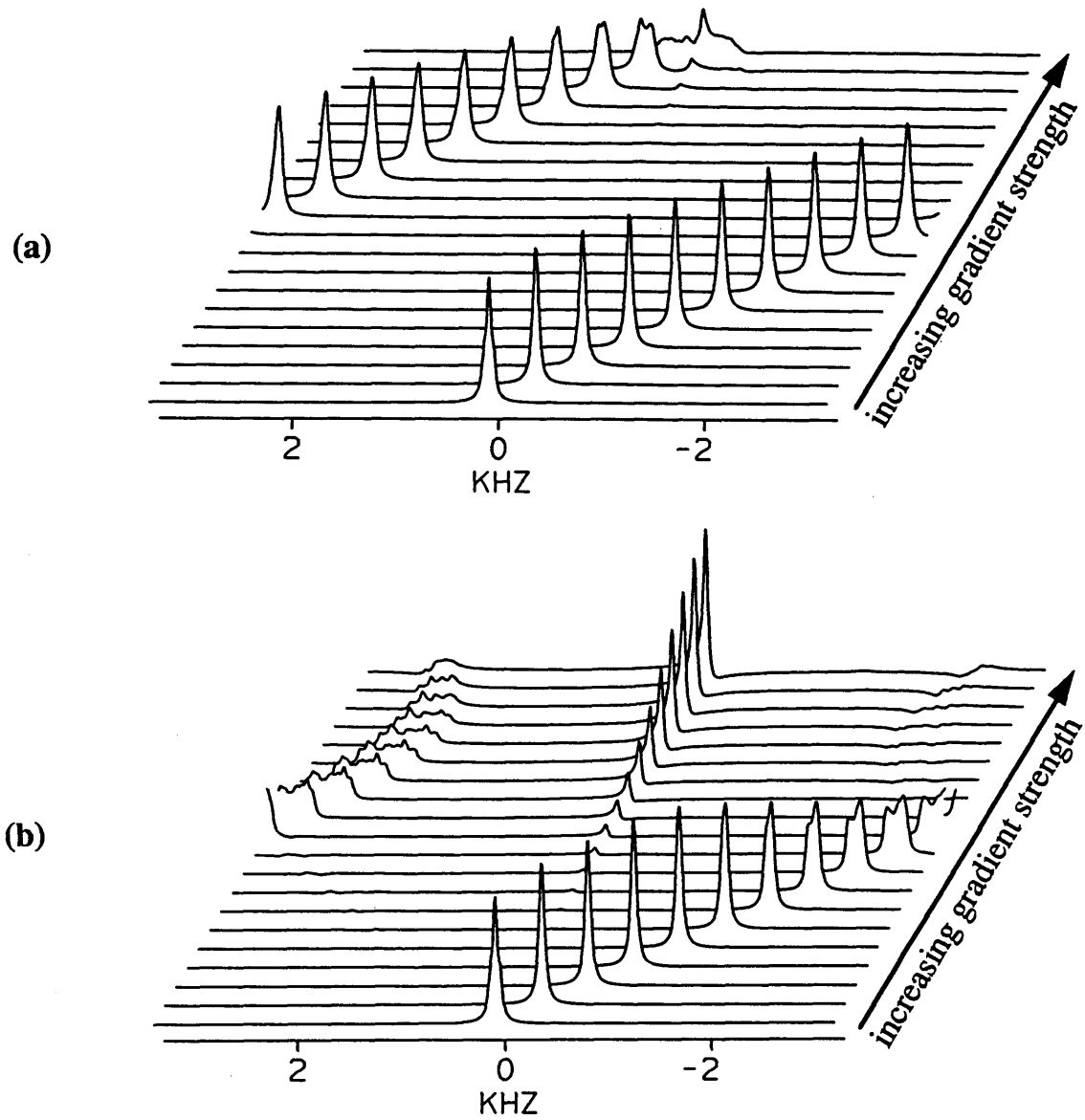


Figure 4.9: The effect of unwanted gradient terms. The $\pi/2$ assumed is $1.35 \mu s$ and the cycle time is $152.4 \mu s$. (a) G_{xx} only (1-D imaging coil). (b) G_{xx} and G_{yy} (2-D imaging coil). The 20 gradient points in (b) are selected along the line $B_{1x} = B_{1y}$.

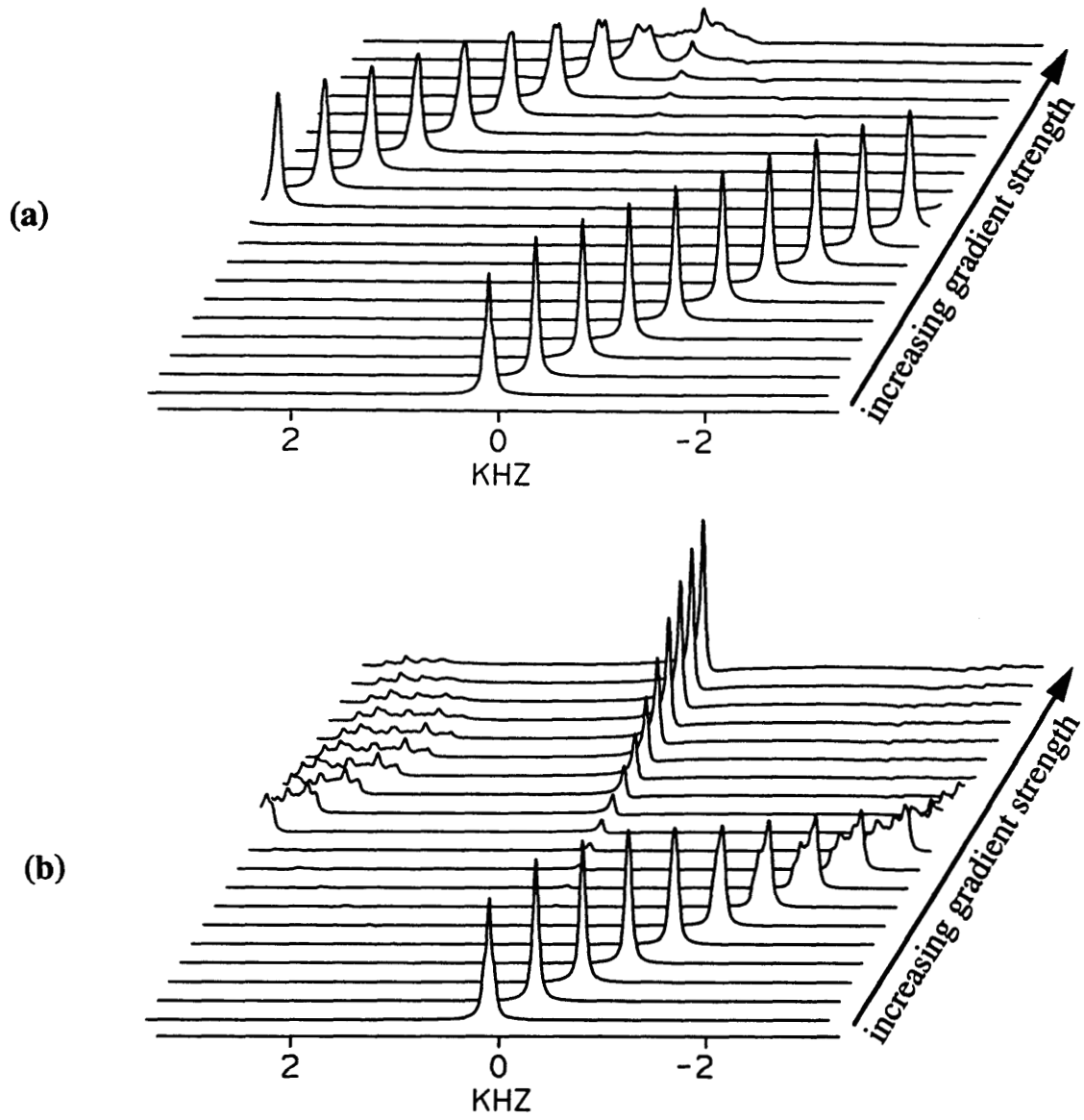


Figure 4.10: The effect of unwanted gradient terms. The $\pi/2$ assumed is $2.7 \mu\text{s}$ and the cycle time is $152.4 \mu\text{s}$. (a) G_{xx} only (1-D imaging coil). (b) G_{xx} and G_{yy} (2-D imaging coil). The 20 gradient points in (b) are selected along the line $B_{1x} = B_{1y}$.

4.8.3 Comparison of SWW-16 and LW-24

Since LW-24 eliminates $\overline{\mathcal{H}}_D^{(2)}$ while SWW-16 does not, LW-24 is expected to provide better line narrowing. The simulations shown in Figure 4.11 indicate that LW-24 has a substantially better line-narrowing ability than SWW-16. Since the dominant term in the average Hamiltonian of LW-24 is $\overline{\mathcal{H}}_G(t)$ which is proportional to I_z , second averaging effects [10] can be expected to average the Hamiltonian terms with a non-zero azimuthal quantum number n . An operator T is said to have an azimuthal quantum number n when $[I_z, T] = nT$ [14, 20]. This second averaging fails at pathological values of the gradient-induced nutation $\sum_n \theta_n(\mathbf{r})$. These points are given by $\sum_n \theta_n(\mathbf{r}) = 2\pi N/|n|$, for all integers N . For $|n| = 2$ terms, then, second averaging fails at $\sum_n \theta_n(\mathbf{r}) = 0$ and π . This is evident in Figure 4.11(b), where the line-narrowing efficiency is degraded for the peak at zero and for that at the Nyquist frequency. By phase stepping the pulse sequence, that is by incrementing the phase of the carrier rf of both the line-narrowing and the gradient pulses between each pulse cycle, it is possible to shift the values of gradient-induced evolution which fail to cause second averaging. By selecting the phase step, it is possible to obtain optimal second averaging at any value of $\sum_n \theta_n(\mathbf{r})$. For a full image with optimized second averaging, it is necessary to interleave data acquired with several different phase steps. This has been done in Figure 4.11(c).

There are terms in $\overline{\mathcal{H}}_{O,G}^{(2)}$, $\overline{\mathcal{H}}_{D,G}^{(2)}$, and $\overline{\mathcal{H}}_{D,O,G}^{(2)}$ which have zero azimuthal quantum numbers and so are not second averaged. These terms are particularly important because they lead to the gradient-dependent line broadening observed in the LW-24 simulations in Figure 4.11. These can be reduced by means of “gradient compensation” in which the amplitude of the gradient pulse during a given window is stepped from negative to positive values. Gradient compensation is also applied in the simulations shown in Figure 4.11(c). Applying a combination of phase stepping and gradient compensation

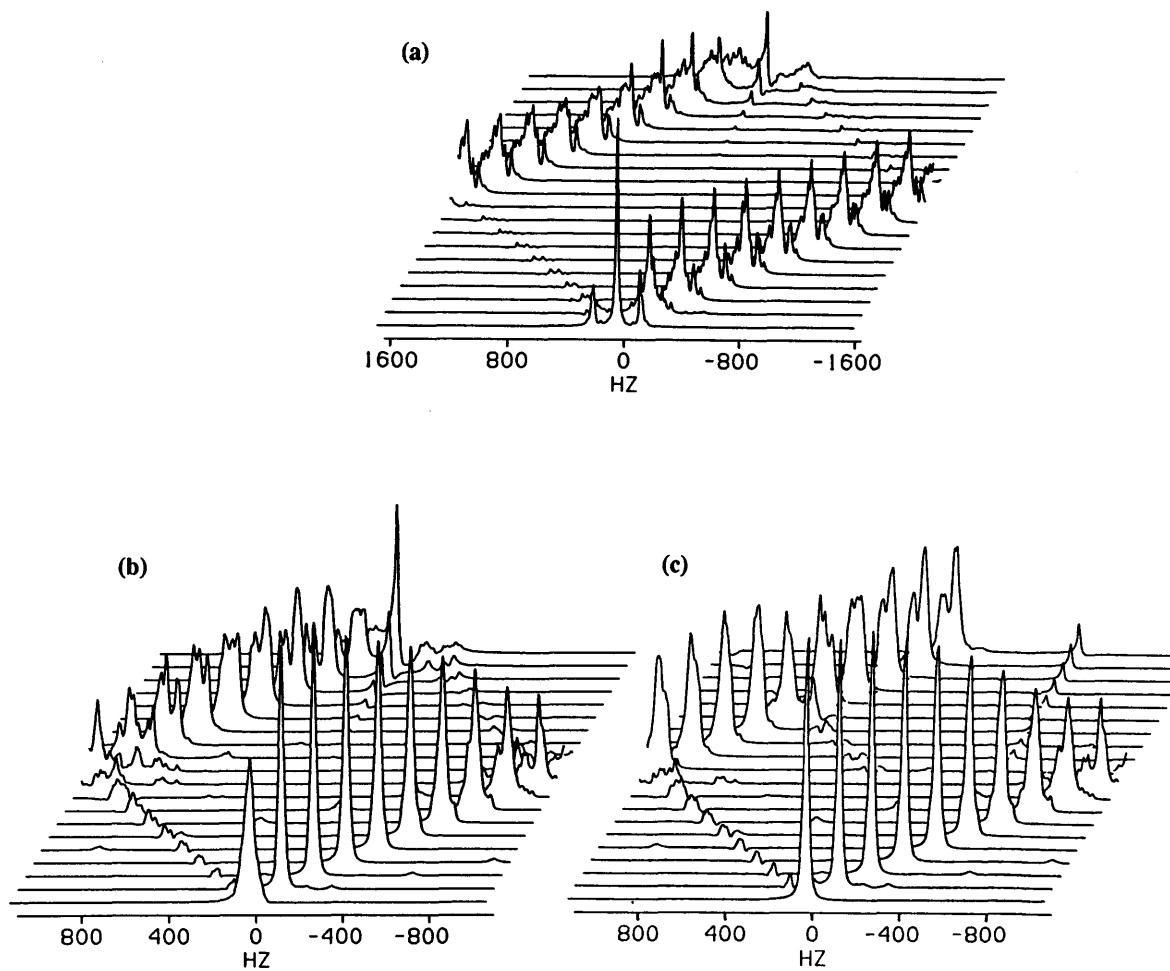


Figure 4.11: A comparison of SWW-16 and LW-24. These simulations assume the 1-D coil arrangement. (a) SWW-16 with a $2.7 \mu\text{s}$ $\pi/2$ time and a $304.8 \mu\text{s}$ cycle time. (b) LW-24 with a $2.7 \mu\text{s}$ $\pi/2$ time and a $457.2 \mu\text{s}$ cycle time. (c) As in (b) but now the gradient trick and phase stepping have been applied to obtain further line narrowing.

noticeably improves the performance of LW-24. Gradient compensation does have the drawback that the effective gradient is reduced. It is also experimentally demanding. No gradient compensation was attempted in any of the experiments associated with this body of research.

In general, these simulations indicate that the increased resolution available from LW-24, as compared with SWW-16, is more than sufficient to account for the decreased spectral width due to LW-24's longer cycle time. In practice, however, LW-24 was found to yield approximately the same resolution as SWW-16. This did vary some from day to day, however, possibly as a result in variations in the phase and amplitude adjustments of the rf pulses, or more probably due to changes in the probe tuning and matching. These observations suggest that experimental imperfections not modeled by these simulations hinder the line-narrowing capability of LW-24 more so than they hinder the line-narrowing capability of SWW-16.

4.9 Conclusions

Average Hamiltonian considerations show that SWW-16 is compensated for $\overline{\mathcal{H}}_D^{(0)}$, $\overline{\mathcal{H}}_O^{(0)}$, and $\overline{\mathcal{H}}^{(1)}$. It is also compensated for symmetric phase transients and rf inhomogeneity at the level of the average Hamiltonian. The largest correction term and a major source of the residual line-broadening is $\overline{\mathcal{H}}_D^{(2)}$. It is possible to design pulse sequences which eliminate this last term, and the sequence LW-24 is an example of this.

Simulations show that pulsed rf and DC gradients perform comparably when combined with SWW-16. Similar results, though not presented here, have been obtained for LW-24. DC gradients do have the disadvantage of having fewer windows in which they can be applied, thus reducing proportionally the gradient-induced nutation per cycle. Further simulations show that the error terms introduced by the vertical quadrupole coil arrange-

ment used in 2-D imaging should not be problematic if the sampling is restricted to once per multiple-pulse cycle. Other simulations show that LW-24 should enable imaging with higher resolution than SWW-16, although this has not been observed experimentally.

References

- [1] M. Mehring, "Principles of High Resolution NMR in Solids," 2nd edition, Springer-Verlag, Berlin, 1983.
- [2] W.-K. Rhim, D. D. Elleman, and R. W. Vaughan, *J. Chem. Phys.* **59**, 3740 (1973).
- [3] W.-K. Rhim, D. D. Elleman, L. B. Schreiber, and R. W. Vaughan, *J. Chem. Phys.* **60**, 4595 (1974).
- [4] D. P. Burum and W.-K. Rhim, *J. Chem. Phys.* **71**, 944 (1979).
- [5] H. M. Cho, C. J. Lee, D. N. Shykind, and D. P. Weitekamp, *Phys. Rev. Lett.* **55**, 1923 (1985).
- [6] W. A. B. Evans, *Ann. Phys. (Leipzig)* **48**, 72 (1968).
- [7] U. Haeberlen and J. S. Waugh, *Phys. Rev.* **175**, 453 (1968).
- [8] P. Mansfield, *J. Phys. C: Solid St. Phys.* **4**, 1444 (1971).
- [9] W.-K. Rhim, D. D. Elleman, and R. W. Vaughan, *J. Chem. Phys.* **58**, 1772 (1973).
- [10] U. Haeberlen, "High Resolution NMR in Solids: Selective Averaging," Academic Press, New York, 1976.
- [11] W. Magnus, *Commun. Pure Appl. Math.* **7**, 649 (1954).
- [12] C. H. Wang and J. D. Ramshaw, *Phys. Rev. B* **6**, 3253 (1972).

- [13] J. S. Waugh, L. Huber, and U. Haeberlen, *Phys. Rev. Lett.* **20**, 180 (1968).
- [14] T. J. Lenosky and D. P. Weitekamp, in preparation.
- [15] D. N. Shykind, Ph.D. Thesis, University of California, Berkeley (1989).
- [16] N. D. Kurur, Ph.D. Thesis, California Institute of Technology (1992).
- [17] J. B. Miller, D. G. Cory, and A. N. Garroway, *Phil. Trans. R. Soc. Lond. A* **333**, 413 (1990).
- [18] J. B. Miller, D. G. Cory, and A. N. Garroway, *Chem. Phys. Lett.* **164**, 1 (1989).
- [19] J. A. Marohn, personal communication.
- [20] D. G. Cory, J. B. Miller, R. Turner, and A. N. Garroway, *Mol. Phys.* **70**, 331 (1990).

Chapter 5

Two Dimensions of NMR Imaging from a Single Radiofrequency Gradient Coil

5.1 Introduction

We have previously demonstrated one-dimensional NMR images of solids obtained by delivering rf gradient pulses in the windows of multiple-pulse line-narrowing sequences which average away all of the static contributions to the linewidth, thereby increasing sensitivity and spatial resolution. We now demonstrate a two-dimensional Fourier transform technique by which solids are imaged using a single radiofrequency gradient coil. The multiple-pulse sequence used now serves to select orthogonal components of the gradient as well as to perform its customary line-narrowing function. The fact that the image is reconstructed via a two-dimensional Fourier transform obviates the need for sample rotation and projection-reconstruction, which are required with other imaging techniques utilizing a single gradient circuit.

Imaging with rf gradients requires bringing two or more resonant circuits, tuned to the same frequency, in close proximity within the NMR probe. It is important to take active measures to decouple these coils. The technique used here is a form of active Q-switching, which is described in Chapter 6.

5.2 The Quadrupole Coil

The rf gradient coil used in our imaging experiments is a quadrupole coil. Quadrupole coils have been used previously in NMR to produce gradients in the static magnetic field \mathbf{B}_0 in diffusion studies [1, 2], and have also been used as rf coils in molecular beam deflection [3].

An ideal linear gradient coil can be described as a quadrupolar distribution of axial current I on the surface of a cylinder so that the angular current density $dI/d\varphi$, as a function of the azimuthal angle φ , is described by

$$\frac{dI}{d\varphi} = I_0 \sin 2\varphi, \quad (5.1)$$

as shown in Figure 5.1. This distribution produces the largest volume of constant magnetic field gradient [4]. The field inside the coil is easily calculated from the vector potential produced by the current distribution described by Equation 5.1 [1]. The vector potential is parallel to the coil and so, assuming a coil oriented with its axis along y as in Figure 5.1(a), has the value inside the coil

$$A_y = \mu_0 \frac{I}{4} \left(\frac{r}{a} \right)^2 \sin 2\varphi, \quad (5.2)$$

where a is the coil radius, r is the distance from the y -axis to the field point, φ is the angle between r and the z -axis, and μ_0 is the permeability of free space. Since $\mathbf{B} = \nabla \times \mathbf{A}$, the components of the field strength are

$$B_{1z} = \mu_0 \frac{I}{2a^2} z \quad (5.3)$$

and

$$B_{1x} = -\mu_0 \frac{I}{2a^2} x. \quad (5.4)$$

In practice, quadrupole coils are wound with discrete wires. For 1-D imaging a four-wire approximation to the quadrupole coil was used. The direction of the instantaneous

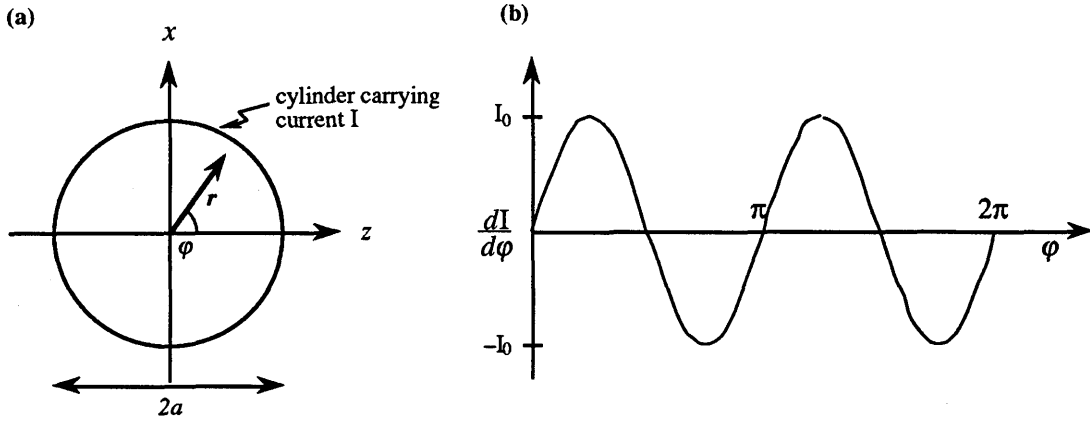


Figure 5.1: The ideal quadrupole coil is a distribution of current I on the surface of a cylinder as shown in (a). The angular current density $dI/d\varphi$ as a function of the azimuthal angle φ is shown in (b).

current in the wires, as well as the orientation of the coil with respect to the solenoid coil is shown in Figure 5.2(a). Near the center of the coil, the field produced by the four wires approximates the ideal case. Furthermore, for an rf quadrupole coil the constant current I in Equations 5.1 through 5.4 can be replaced with the time varying current $I(t)$ provided the size of the coil is much less than the wavelength of the rf used to drive the coil (which is about 1 m for 200 MHz). So, the components field strength of the four-wire quadrupole coil can be approximated as

$$B_{1z} = \mu_0 \frac{I(t)}{2a^2} z \quad (5.5)$$

and

$$B_{1x} = -\mu_0 \frac{I(t)}{2a^2} x. \quad (5.6)$$

Since $I(t)$ is oscillating at the carrier frequency (200 MHz in our case), when B_{1z} and B_{1x} are transformed into the rotating frame, only the component of B_1 along x is time-independent. B_{1z} retains its time dependence and so does not have a significant effect on the spin system. For this orientation, then, the only effective gradient is $G_{xx} = \partial B_{1x} / \partial x$. We refer to this as the “horizontal” quadrupole coil.

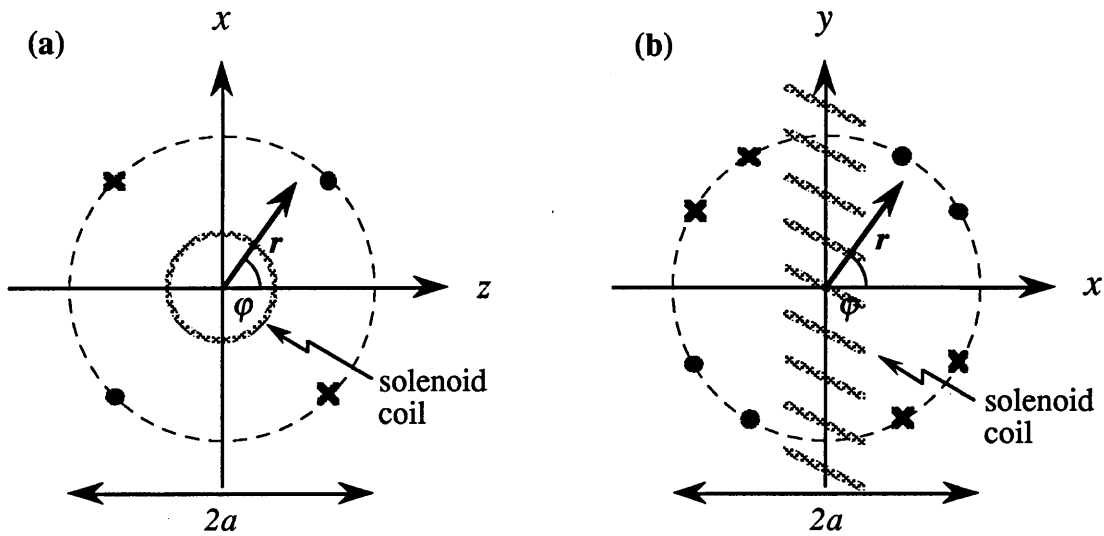


Figure 5.2: Four- and eight-wire quadrupole coils. (a) The four-wire coil in the horizontal arrangement used for 1-D imaging. (b) The eight wire coil in the vertical arrangement used for 2-D imaging. For both (a) and (b) the orientation of the quadrupole coil with respect to the solenoid coil is shown.

As an important aside, notice that if the coil is rotated 45° counterclockwise about the y -axis, the components of the field strength become

$$B_{1z} = \mu_0 \frac{I(t)}{2a^2} x \quad (5.7)$$

and

$$B_{1x} = \mu_0 \frac{I(t)}{2a^2} z. \quad (5.8)$$

In this case, $G_{zx} = \partial B_{1x} / \partial z$ is time dependent in the rotating frame and so has a negligible effect on the spin system. The effective gradient, then, is $G_{xz} = \partial B_{1z} / \partial x$. This means that two quadrupole coils, both colinear with the y -axis (which can also be the solenoid coil axis), but rotated 45° with respect to one another, can be combined to produce gradients for 2-D imaging in the xz plane. We did not choose this coil arrangement for our first 2-D imaging experiments because it would have been necessary to decouple three rf coils. The Q-switching scheme used here can be extended to decouple

three rf coils, but rather than build the additional apparatus required to accomplish this, we chose to use an alternate orientation of the quadrupole coil.

For 2-D imaging, two changes were made to the quadrupole coil. First, an eight-wire coil was used as shown in Figure 5.2(b). This provides a better approximation to the ideal quadrupole coil, and hence a more linear gradient, than does the four-wire coil [4]. Second, the coil was rotated 90° about the x -axis, with respect to the horizontal coil, to the orientation shown in Figure 5.2(b). The components of the field strength for this orientation are

$$B_{1x} = \mu_0 \frac{I(t)}{2a^2} x \quad (5.9)$$

and

$$B_{1y} = -\mu_0 \frac{I(t)}{2a^2} y. \quad (5.10)$$

In this case, both components are time-independent in the rotating frame and so both have a significant effect on the spin system. This coil arrangement is referred to as the “vertical” quadrupole coil. Obviously, it is not possible electrically to select one gradient component at a time. However, using the proper pulse sequence, for example SWW-16 as shown in Figure 5.3, it is possible to force the spins to experience one component on average. So, in combination with the proper pulse sequence, a single rf quadrupole coil in this orientation can provide the gradients necessary for 2-D imaging in the xy plane. How this works can be explained by means of average Hamiltonian theory.

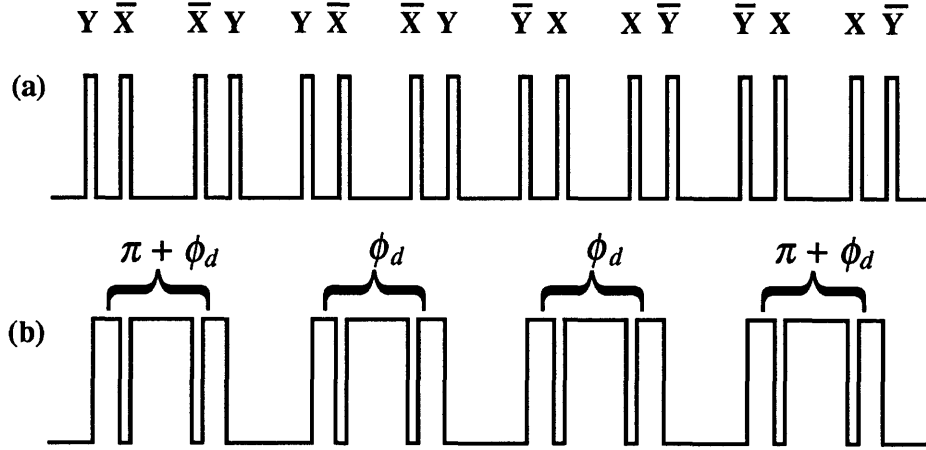


Figure 5.3: SWW-16. (a) Line-narrowing pulses delivered by a solenoid coil. (b) Gradient pulses delivered by a quadrupole coil. The rotating frame phases of the gradient pulses are expressed as $\phi(t) + \phi_d$, where $\phi(t) = \pi$ is equivalent to an \bar{X} pulse with respect to the solenoid rf carrier and ϕ_d is the phase difference between the quadrupole and solenoid rf carriers. We denote a cycle in which $\phi_d = 0$ by “SWW-16- G_x ” and one in which $\phi_d = \pi/2$ by “SWW-16- G_y .”

5.3 The Gradient Hamiltonian

A magnetic field gradient \mathcal{G} is a second-rank tensor and can be written in terms of a dyad in Cartesian coordinates,

$$\mathcal{G} = \nabla B^t = \begin{pmatrix} G_{xx} & G_{xy} & G_{xz} \\ G_{yx} & G_{yy} & G_{yz} \\ G_{zx} & G_{zy} & G_{zz} \end{pmatrix}, \quad (5.11)$$

where B^t is the transpose of B and the gradient components indicate the corresponding partial derivatives, for example, $G_{xy} = \partial B_y / \partial x$ [5, 6, 7]. Most often, in NMR imaging the gradients used are gradients in the main static magnetic field B_0 , i.e., nominally DC gradients. The spatial dependence of the magnetic field can be approximated to first order in $|\mathbf{r}|$ by

$$\mathbf{B} = B_0 + \mathcal{G}^t \cdot \mathbf{r}. \quad (5.12)$$

The component of a DC gradient parallel to \mathbf{B}_0 (traditionally taken to define the z axis in the laboratory frame) has the largest effect. In fact, the effects of gradient components perpendicular to this average away in the rotating frame of the NMR experiment. Therefore, for DC gradients only the z component of $\mathcal{G}^t \cdot \mathbf{r}$ is relevant and the \mathcal{G} tensor is usually treated as a vector \mathbf{G} , with components $G_x = \partial B_z / \partial x$, $G_y = \partial B_z / \partial y$, and $G_z = \partial B_z / \partial z$. The scalar needed is then

$$(\mathcal{G}^t \cdot \mathbf{r})_z = \left(\frac{\partial B_z}{\partial x} x + \frac{\partial B_z}{\partial y} y + \frac{\partial B_z}{\partial z} z \right) = \mathbf{G} \cdot \mathbf{r}. \quad (5.13)$$

We want to consider the case of rf gradients, that is, gradients in the transverse magnetic field \mathbf{B}_1 applied perpendicular to the static field to excite the nuclear spins. Depending on the type and configuration of rf coil used to produce a gradient in \mathbf{B}_1 , different components of the tensor will be important. For now we will consider all components of the tensor and we will use the notation

$$G_{xy} = \frac{\partial B_{1y}}{\partial x}, \quad (5.14)$$

and so forth.

The laboratory frame Hamiltonian for an isolated spin at position \mathbf{r} in a static magnetic field along z and in the presence of a field gradient may be written

$$\mathcal{H} = \omega_0 I_z + \gamma \mathbf{I} \cdot \mathcal{G}^t \cdot \mathbf{r}. \quad (5.15)$$

In the 2-D imaging experiments described below, the gradient is produced by a quadrupole coil with its axis oriented along z . There are only two non-vanishing components of the magnetic field intensity, given in Equations 5.9 and 5.10, and so \mathcal{G} reduces to

$$\mathcal{G} = \begin{pmatrix} \left(\frac{\mu_0}{2a^2} I(t) \right) & 0 & 0 \\ 0 & \left(-\frac{\mu_0}{2a^2} I(t) \right) & 0 \\ 0 & 0 & 0 \end{pmatrix} \quad (5.16)$$

and

$$\gamma \mathbf{I} \cdot \mathcal{G}^t \cdot \mathbf{r} = \gamma \left(\frac{\mu_0}{2a^2} I(t) I_x x - \frac{\mu_0}{2a^2} I(t) I_y y \right). \quad (5.17)$$

The goal here is to describe the effect of the gradient pulses. This will be done with average Hamiltonian theory, a form of time-dependent perturbation theory in which a propagator is expressed in terms of a time independent averaged Hamiltonian. To this end, \mathcal{H} must be transformed into the rotating frame and then into the toggling frame defined by the line-narrowing sequence.

The Hamiltonian \mathcal{H} is transformed into the frame rotating at the carrier frequency ω by

$$\mathcal{H}^{\text{RF}} = U^{-1} \mathcal{H} U - i U^{-1} \dot{U}, \quad (5.18)$$

where

$$U = \exp(+i\omega t I_z). \quad (5.19)$$

This yields

$$\mathcal{H}^{\text{RF}} = -\Delta\omega I_z + \exp(-i\omega t I_z) \gamma \mathbf{I} \cdot \mathcal{G} \cdot \mathbf{r} \exp(+i\omega t I_z). \quad (5.20)$$

Traditionally $I(t)$ is expressed as

$$I(t) = I_0 \cos(\omega t - \phi(t)), \quad (5.21)$$

where ω is the carrier frequency and $\phi(t)$ is the phase relative to the rf carrier. For multiple-pulse sequences, of course, $\phi(t)$ is highly time dependent. Although both the solenoid and the quadrupole coils operate at the same frequency, there is a phase difference, ϕ_d , between the rf carrier at the solenoid coil and the rf carrier at the quadrupole coil. This phase difference also needs to be included in $I(t)$:

$$I(t) = I_0 \cos[\omega t - (\phi(t) + \phi_d)], \quad (5.22)$$

(where ϕ_d is time-independent over the course of an experiment, but is under experimenter control). Therefore, transforming $\gamma \mathbf{I} \cdot \mathcal{G}^t \cdot \mathbf{r}$ into the rotating frame yields (as shown in

the appendix at the end of this chapter)

$$\begin{aligned} \mathcal{H}_G^{\text{RF}}(t) = & \gamma \frac{I_0 \mu_0}{4a^2} \{x [I_x \cos(\phi(t) + \phi_d) + I_y \sin(\phi(t) + \phi_d)] + \\ & y [I_x \sin(\phi(t) + \phi_d) - I_y \cos(\phi(t) + \phi_d)]\} . \end{aligned} \quad (5.23)$$

This gradient Hamiltonian is treated as a perturbation on the Hamiltonian describing the line-narrowing pulses, in analogy to the standard toggling frame treatment of uncontrolled pulse-angle errors [8]. The toggling frame is defined by the line-narrowing pulse Hamiltonian; it is the interaction representation in which the action of these $\pi/2$ pulses is transformed away. The gradient Hamiltonian in this toggling frame can be written down with the help of Table 5.1, which shows the toggling frame values of I_x and I_y as well as the rotating frame values for $(\phi(t) + \phi_d)$.

The gradient term of the average Hamiltonian of SWW-16 is (as shown in the appendix at the end of this chapter)

$$\overline{\mathcal{H}}_G^{(0)} = \frac{1}{t_c} \int_0^{t_c} \tilde{\mathcal{H}}_G(t_1) dt_1 \quad (5.24)$$

$$= \frac{2}{3} \cdot \gamma \frac{I_0 \mu_0}{4a^2} \{x \cos \phi_d + y \sin \phi_d\} I_z . \quad (5.25)$$

In Equation 5.25 the integral has been taken for the limit of vanishingly short $\pi/2$ pulses. This assumption is dropped below.

These results may be contrasted with those for the horizontal quadrupole coil:

$$\mathcal{H}_G^{\text{RF}} = -\gamma \frac{I_0 \mu_0}{4a^2} \{x [I_x \cos(\phi(t) + \phi_d) + I_y \sin(\phi(t) + \phi_d)]\} , \quad (5.26)$$

and

$$\overline{\mathcal{H}}_G^{(0)} = \frac{2}{3} \cdot \gamma \frac{I_0 \mu_0}{4a^2} \{-x \cos \phi_d\} I_z . \quad (5.27)$$

Thus the case of an isolated spin has been considered. In reality, there will be many spins present so Equations 5.25 and 5.27 need to be summed over all the spins in the sample. However, since SWW-16 is compensated for dipolar and offset contributions, the

homog. rf	Y	\bar{X}	\bar{X}	Y	Y	\bar{X}	\bar{X}	Y	
window #	0	1	2	3	4	5	6	7	8a
length	τ	τ	2τ	τ	2τ	τ	2τ	τ	τ
\tilde{I}_x	X	\bar{Z}	\bar{Z}	\bar{Z}	X	Z	Z	Z	X
\tilde{I}_y	Y	Y	\bar{X}	\bar{Y}	\bar{Y}	\bar{Y}	\bar{X}	Y	Y
gradient rf	—	$\pi + \phi_d$	$\pi + \phi_d$	$\pi + \phi_d$	—	ϕ	ϕ	ϕ	—

homog. rf	\bar{Y}	X	X	\bar{Y}	\bar{Y}	X	X	\bar{Y}	
window #	8b	9	10	11	12	13	14	15	16
length	τ	τ	2τ	τ	2τ	τ	2τ	τ	τ
\tilde{I}_x	X	Z	Z	Z	X	\bar{Z}	\bar{Z}	\bar{Z}	X
\tilde{I}_y	Y	Y	\bar{X}	\bar{Y}	\bar{Y}	\bar{Y}	\bar{X}	Y	Y
gradient rf	—	ϕ	ϕ	ϕ	—	$\pi + \phi_d$	$\pi + \phi_d$	$\pi + \phi_d$	—

Table 5.1: RF gradient phase and toggling frame values of I_x and I_y for SWW-16. The sixteen windows of SWW-16 are numbered and their lengths shown. \tilde{I}_x and \tilde{I}_y are the toggling frame values of I_x and I_y . The rotating frame phase of each rf gradient pulse is expressed as $(\phi(t) + \phi_d)$, where $\phi(t)$ is the phase with respect to the quadrupole rf carrier and ϕ_d the phase difference between the quadrupole and solenoid rf carriers.

average Hamiltonian for SWW-16 is just $\overline{\mathcal{H}}_C^{(0)}$ summed over all the spins in the sample.

This may be written

$$\overline{\mathcal{H}}^{(0)} = \frac{1}{t_c} \sum_n \theta_n(\mathbf{r}) I_z, \quad (5.28)$$

where t_c is the cycle time and $\theta_n(\mathbf{r})$ is the spatially dependent angle of the n^{th} gradient pulse of a cycle. Here I_z is implicitly the angular momentum operator for any spin in a volume centered at \mathbf{r} over which the rf field varies negligibly (\leq one part per thousand). This volume will always span distances long ($> 10^{-4}$ cm) compared with the range of spin-spin interactions ($< 10^{-6}$ cm). Thus all interacting spins have the same rf Hamiltonian. For a quadrupole coil with magnetic field strength components $B_x \propto x$ and $B_y \propto -y$, these angles can be written

$$\theta_n(\mathbf{r}) = G_n \{ x \cos \phi_d + y \sin \phi_d \} t_n, \quad (5.29)$$

where $G_n = \gamma I_0 \mu_0 / 4a^2$ (assuming it is constant over the entire sample) is dependent on the radius of the quadrupole coil and the amplitude of the current applied to the coil, x and y are the components of \mathbf{r} (\mathbf{r} giving the position of the spins in question), t_n is the length of gradient pulse n , and ϕ_d is the phase difference between the quadrupole rf carrier and the solenoid rf carrier. Note that at a given position \mathbf{r} , all the terms $\theta_n(\mathbf{r})$ in Equation 5.28 have the same sign when the phases are chosen as in Table 5.1. The phase difference ϕ_d may be varied by phase shifting the rf excitation of the quadrupole with respect to the solenoid coil. For example if ϕ_d is chosen to be zero, θ_n is selected to be proportional to r_x , that is,

$$\theta_n = G_n x t_n \quad (\phi_d = 0). \quad (5.30)$$

A cycle in which $\phi_d = 0$ is denoted by "SWW-16-G_x" (see Figure 5.3). On the other hand if ϕ_d is chosen to be $\pi/2$, θ_n is selected to be proportional to y , that is,

$$\theta_n = G_n y t_n \quad (\phi_d = \pi/2). \quad (5.31)$$

A cycle in which $\phi_d = \pi/2$ is denoted by “SWW-16-G_y.” By an overall 90° phase shift of the gradient pulses relative to the line-narrowing pulses, then, it is possible to select two orthogonal spin density projections (for example x and y in the laboratory frame, or any linear combination thereof). Thus a single vertical quadrupole coil, in conjunction with the SWW-16 pulse sequence, can be used to produce effectively a gradient along one direction in the xy plane during the evolution time t_1 of a two-dimensional experiment, and a gradient along the direction perpendicular to this during the acquisition time t_2 of the experiment.

5.4 Error Terms Introduced by the Gradient Pulses

At the level of the average Hamiltonian, then, it is possible to select one component of the gradient at a time. The presence of the second orthogonal component will, however, introduce contributions to the correction terms of the average Hamiltonian. Such correction terms are undesirable because they increase the linewidth and hence degrade the resolution obtainable. Exact numerical simulations of SWW-16 at 20 points along the gradient have been performed to determine to what extent these added error terms hinder the line-narrowing capability of the sequence. The simulations are discussed in Chapter 4. In general, the simulations indicate that the error terms introduced by the second component of the gradient are not a problem for the cycle times used here if SWW-16 is sampled once per cycle.

5.5 Two-Dimensional Images

The rf coils used for two-dimensional imaging are shown schematically in Figure 5.4. The solenoid coil has an inner diameter of 5 mm and a length of approximately 27 mm. The eight-wire quadrupole coil has a diameter of 20 mm and a length of 35 mm. With

the quadrupole coil in the vertical arrangement, the gradient produced has components along the solenoid axis and normal to the plane containing the solenoid axis and the static magnetic field.

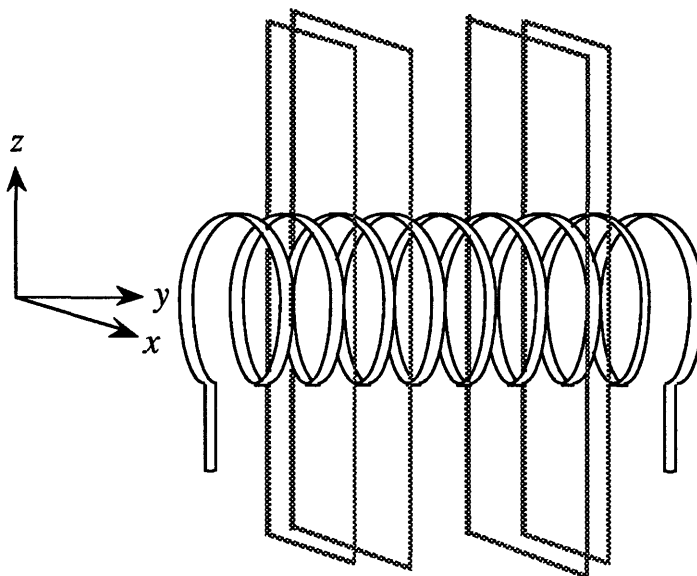


Figure 5.4: Radiofrequency coils for 2-D imaging. The solenoid coil has an inner diameter of 5 mm and a length of 27 mm. The eight-wire quadrupole coil has a diameter of 20 mm and a length of 35 mm. In this orientation, the quadrupole produces gradients $G_{xx} = \partial B_{1x}/\partial x$ and $G_{yy} = \partial B_{1y}/\partial y$.

For 2-D imaging SWW-16- G_x and SWW-16- G_y are combined to form a sequence analogous to that used in liquid-state 2-D Fourier imaging [12]. The sequence for acquiring an $M \times N$ image is shown in Figure 5.5. Here cycles of SWW-16- G_x occur during the evolution period t_1 . N Cycles of SWW-16- G_y , with data points acquired once per cycle, occur during the detection period t_2 . Spatial information is encoded in t_1 by incrementing the number of SWW-16- G_x cycles from $m = 0$ to M while holding the gradient strength constant. Note that for the 5-point adamantane image shown below, sampling occurred *after* every SWW-16- G_y cycle during t_2 ; thus the $t_2 = 0$ point was omitted. It is better to sample once at the beginning of t_2 and then following each SWW-16- G_y cycle.

This procedure was followed for all subsequent 2-D images.

A spin warp [13] analog for solids imaging is also possible. In this experiment the number of SWW-16- G_x cycles during t_1 is held constant while the gradient strength is incremented. This technique has the advantage (discussed in Chapter 2) that whatever non-gradient spin evolution occurs during t_1 (for example, $T_{1\rho}$ relaxation) is constant from acquisition to acquisition, and so is unobserved in the final image. This leads to increased resolution in the ω_1 dimension of the image. Unfortunately, this experiment also suffers the signal energy disadvantage of other constant time techniques. Since t_1 will be some fixed minimum time determined by the maximum gradient strength available, the attenuation of the signal intensity may be quite large, depending on the $T_{1\rho}$ of the sample and the gradient strength available. For example, with the cycle times used here, the signal had almost always decayed to the level of the noise by the $m = 32$ scan. Our experimental apparatus did not permit the gradient strengths to be changed in an automated fashion; hence, no spin warp experiments were performed.

5.5.1 Five-Point Adamantane Phantom

Spectra of adamantane, obtained using a simple one-pulse experiment and also a line-narrowing SWW-16 experiment, are shown in Figure 5.6. The one-pulse spectrum has a spectral width of 40 kHz, a linewidth of 14 kHz and a S/N of 8.5. The SWW-16 spectrum has a spectral width of 3.28 kHz, a linewidth of 85 Hz and a S/N of 109. This demonstrates that line narrowing improves both resolution and signal-to-noise ratio.

The five-point adamantane phantom imaged is shown in Figure 5.7. Adamantane is packed into five cylindrical holes in a boron nitride matrix. Each cylinder of adamantane has diameter 1 mm and depth 1 mm. The separation between cylinders is 2 mm. One-dimensional projections of the adamantane phantom obtained with SWW-16- G_x and SWW-16- G_y are shown in Figure 5.8(a) and (b), respectively. These images, as well as

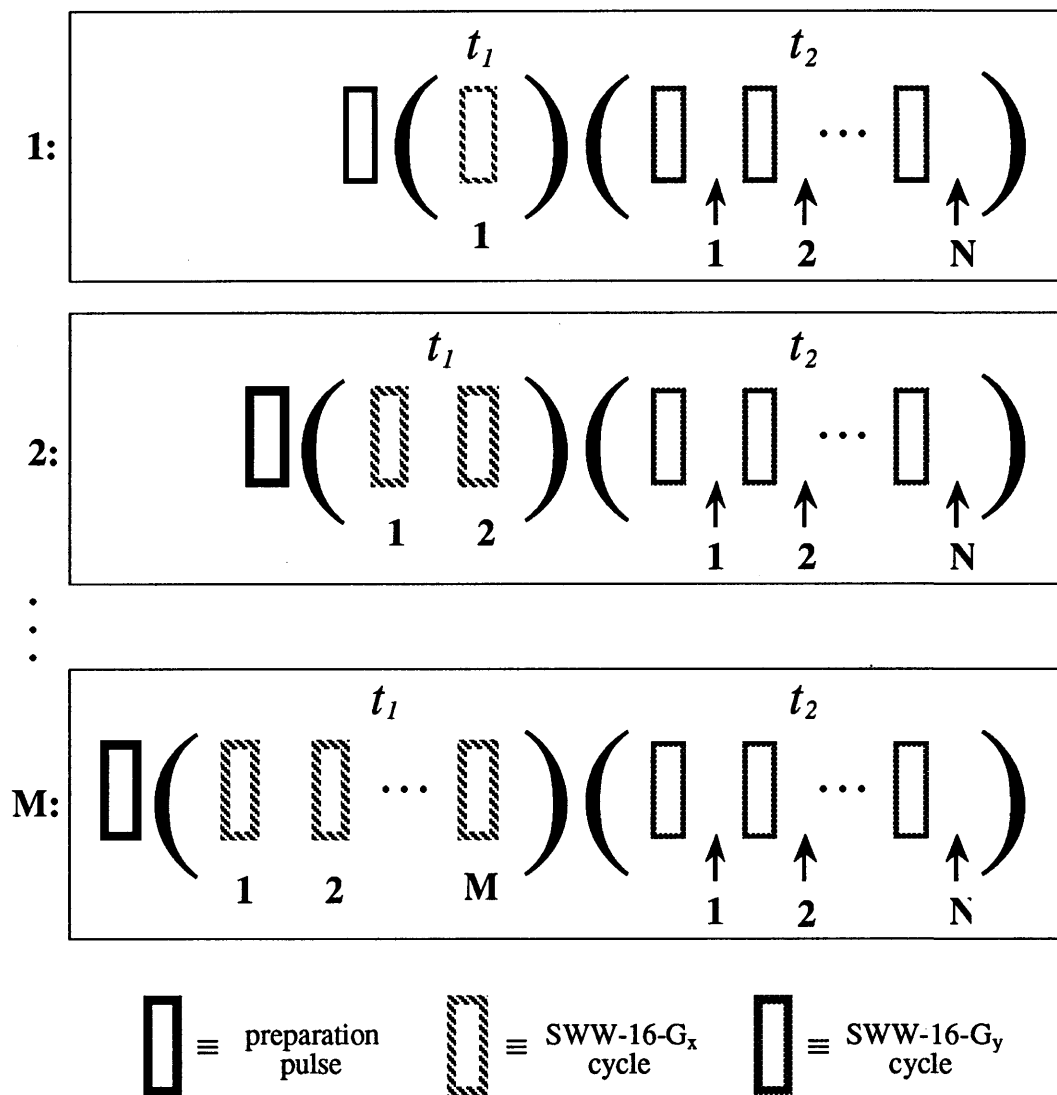


Figure 5.5: A 2D-FT solid imaging sequence for obtaining an $M \times N$ image. The evolution time t_1 is increased by increasing the number of SWW-16- G_x cycles. Data points are collected between SWW-16- G_y cycles during t_2 . The data thus collected is Fourier transformed along t_2 and t_1 to yield an image.

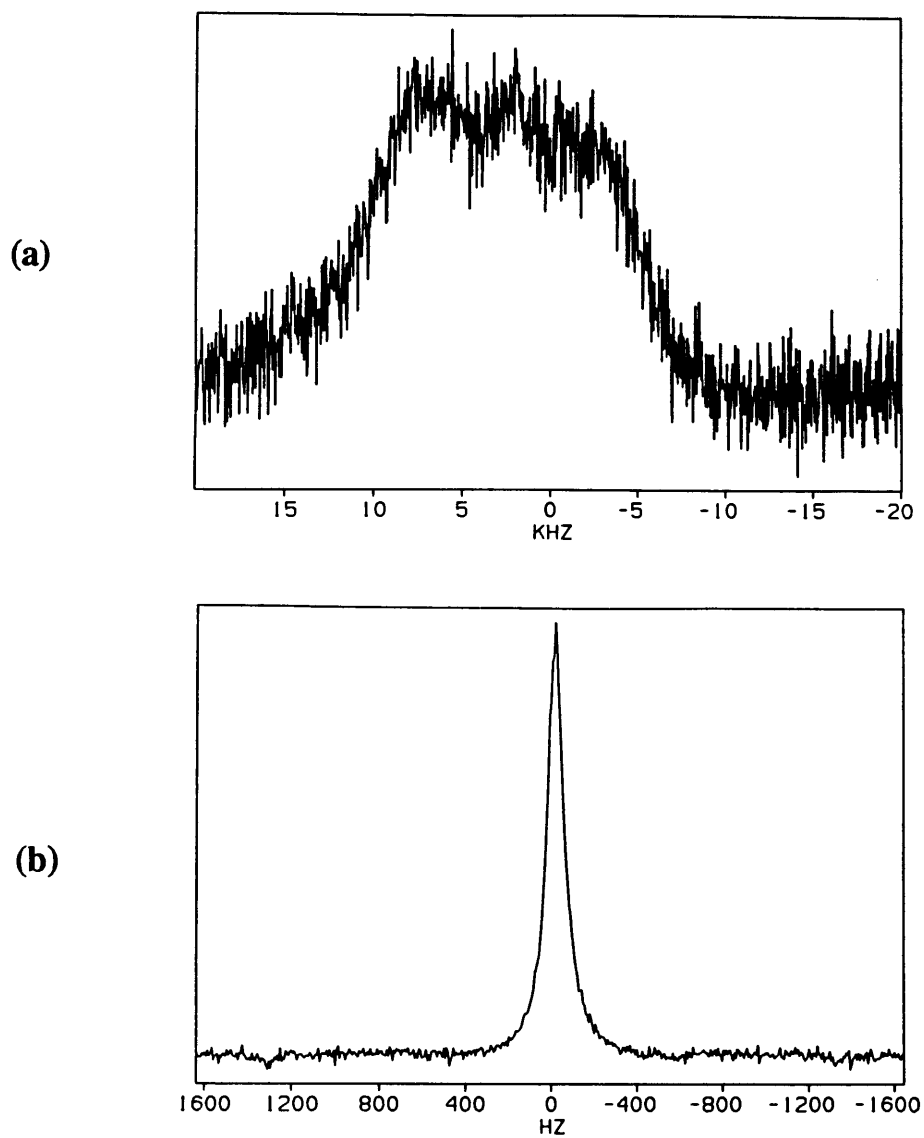


Figure 5.6: Adamantane spectra. (a) The unnarrows linewidth of adamantane is 14 kHz. (b) SWW-16 with a 304.8 μs cycle time and 2.7 μs $\pi/2$ time reduces the linewidth to 85 Hz.

the full two-dimensional image shown below, were obtained on a homebuilt spectrometer operating at 200 MHz. The rf pulse strengths used were 25 W for the gradient and 200 W for the line-narrowing pulses. The $\pi/2$ time used was $2.7 \mu\text{s}$, the cycle time $304.8 \mu\text{s}$, and the total gradient time $90 \mu\text{s}$. In addition, pulse-length missets [9] of $\pm 0.3 \mu\text{s}$ were added to eight of the line-narrowing pulses to center the image in ω_1 .

As can be seen in Figure 5.8, SWW-16- G_x and SWW-16- G_y successfully select orthogonal projections of the phantom. That peaks appear at frequencies above and below the carrier frequency in Figure 5.8(b) is an indication that SWW-16 is distinguishing between positive and negative nutation frequencies. This is also seen in Figure 5.8(a) by the absence of any residual signal at 600 Hz. Thus, the rf gradient pulses are effectively producing a nutation about the z axis.

In the 1-D projection shown in Figure 5.8(b), the five peaks are centered at about 980, 510, 110, -390 , and -880 Hz along ω_2 , all with an uncertainty of ± 30 Hz. Thus, the effective rf gradient strength is 0.37 ± 0.03 G/cm. The unscaled gradient strength is 1.2 ± 0.1 G/cm, where the scaling factor is just the gradient duty cycle. The observed linewidths of the five peaks are about 220, 200, 110, 160, and 180 Hz, also with an uncertainty of ± 30 Hz. Given the effective gradient of 0.37 ± 0.03 G/cm, a sample of 1 mm extent would be expected to yield a peak of 160 ± 10 Hz linewidth, provided that the narrowed linewidth is less than this. The linewidth variation and the spike at zero offset (the carrier frequency) are evidence of image distortion.

The 2-D image of five cylinders of adamantane is shown in Figure 5.9. The image size is 64×64 pixels. Twenty-five signal averages were acquired. The image took approximately 45 minutes to acquire, although most of this time was due to spectrometer "overhead." The 2-D image is presented as a magnitude image.

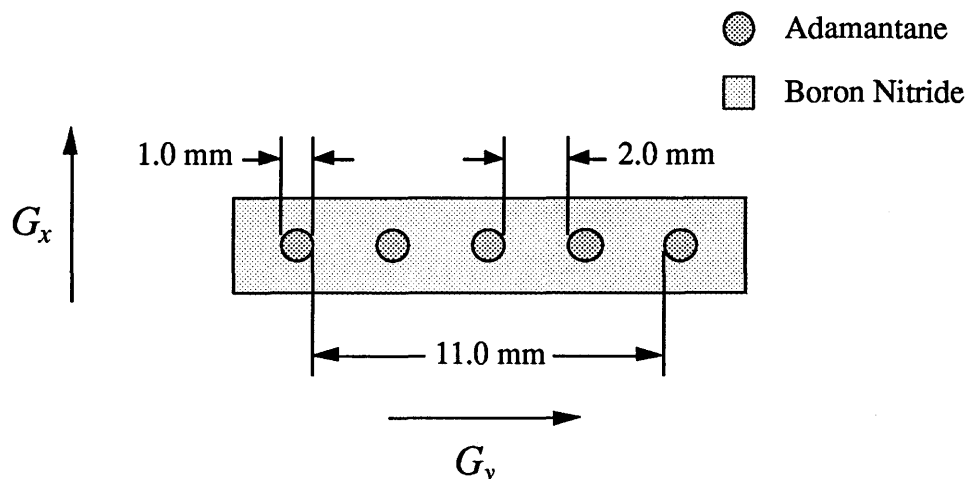


Figure 5.7: The five point adamantane phantom. Adamantane is packed into five cylindrical holes in a boron nitride matrix. Each cylinder of adamantane has diameter 1 mm and depth 1 mm. The separation between cylinders is 2 mm.

Phase Cycling

The spurious peak at the origin of the 1-D projections, and also evident in the 2-D image, can be largely eliminated by simple two-step phase cycling as shown in Figure 5.10. The importance of phase cycling in obtaining good quality solids images has been discussed previously [11]. Here, the phase of the preparation pulse is stepped by 180° and consecutive scans are subtracted. No magnetization is cancelled by this phase cycling scheme, so the fact that the spurious peak is largely eliminated indicates that it is due primarily to rf at the carrier frequency (e.g., receiver ringing). The rf is detected because data points are sampled only a few microseconds after an rf pulse. The significance of this result is that it indicates that there is almost no detectable spin-locked magnetization, i.e., magnetization which does not nutate during the course of the multiple-pulse train [10]. Spin-locked magnetization arises when the magnetization after the preparation pulse is not orthogonal to the effective field of the multiple pulse sequence. Since, ideally, the effective field of SWW-16 is along z , detectable spin-locked magnetization could result

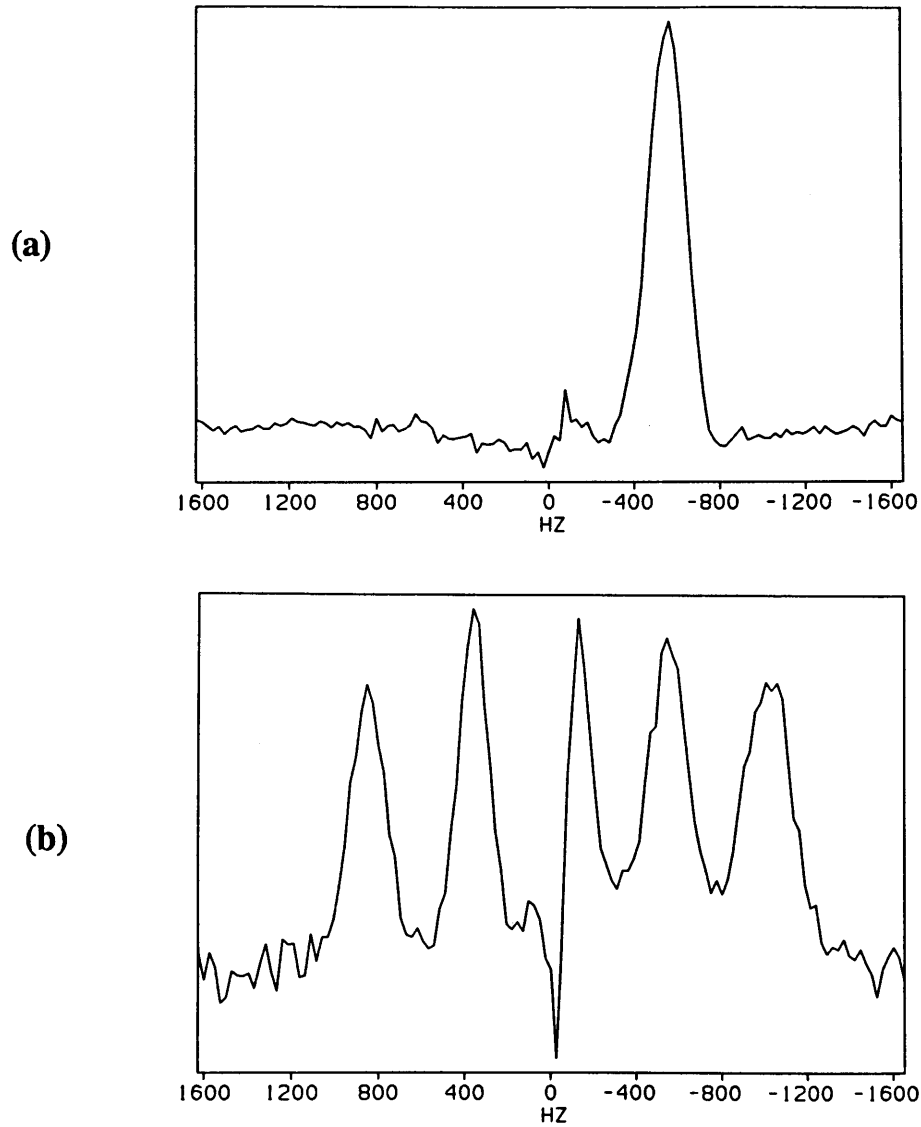


Figure 5.8: 1-D projections of the five-point adamantane phantom. (a) The projection along the axis perpendicular to the solenoid axis (obtained with SWW-16- G_x). (b) The projection along the solenoid axis (obtained with SWW-16- G_y).

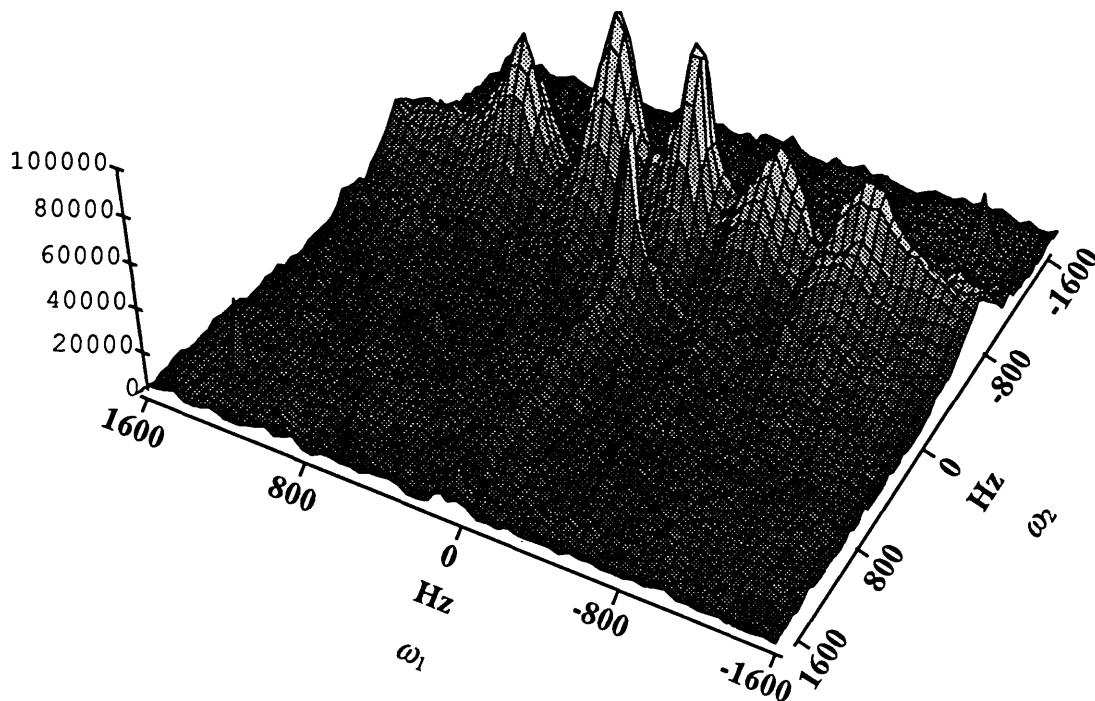


Figure 5.9: Two-dimensional image of the five-point adamantane phantom.

from a small transverse rf field in the toggling frame, which would arise during the rise and fall times of the rf pulses (i.e., the phase transients). The fact that essentially no spin-locked magnetization is observed indicates that the SWW-16 effective field is very nearly along z .

Recentering the Image Along x

In many of the images obtained, it was observed that the apparent gradient strength along the x direction in the laboratory frame, i.e., perpendicular to the solenoid axis, was less than that along the y direction. Furthermore, many images appeared off-center along

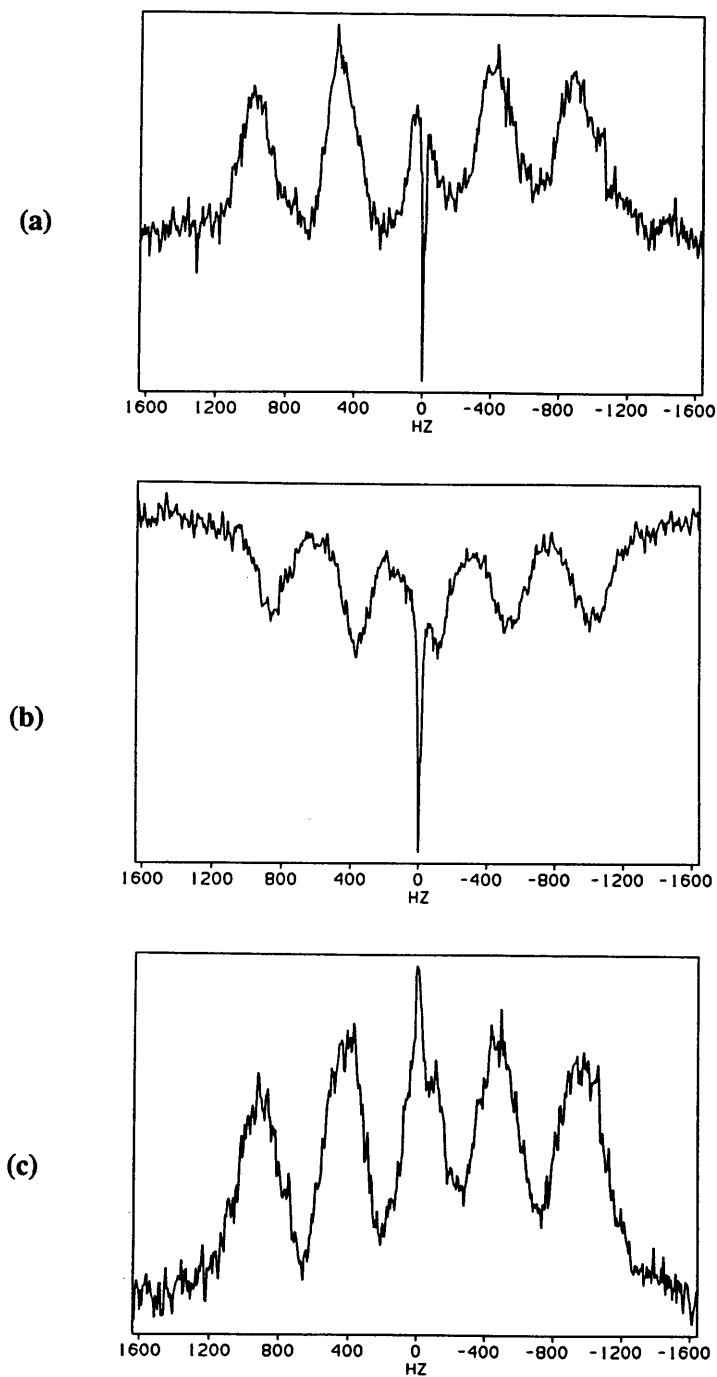


Figure 5.10: Phase cycling to cancel the signal from the spin-locked magnetization. (a) SWW-16-G_y applied with a y preparation pulse. (b) SWW-16-G_y applied with a \bar{y} preparation pulse. (c) Signal obtained by subtracting (b) from (a).

x , even when precautions were taken to center the phantom in the solenoid coil. One explanation for this is that there was still residual coupling between the coils; hence, the gradient pulses drove the solenoid coil to produce small homogeneous pulses, in addition to the gradient pulses, in the windows of the line-narrowing sequence.

For the adamantane image discussed above, when the strength of the gradient pulses was increased to the point where satisfactory resolution was obtained along y , the projection along x was found to be near the Nyquist frequency and so partially folded in. To address this problem, small pulse-length missets were added to the line-narrowing pulses during the SWW-16- G_x cycles, as were used in the original paper proposing combined multiple-pulse line narrowing and rf gradient imaging [9]. The effect of the pulse missets is equivalent, to first order, to that of extra homogeneous pulses in the gradient windows of SWW-16: the line position is shifted to a frequency proportional to the length of the missets in the former case, or to the strength of the extra homogeneous pulses in the latter. By selecting the missets properly, then, it was possible to recenter the image along x .

While the average Hamiltonian describing the line-narrowing sequence with homogeneous pulses in the windows is the same as that for the case of pulse-length missets, exact numerical simulations have shown that the higher order correction terms are not the same for both cases [14]. Pulse-length missets lead to increased linewidths at higher nutation rates, which leads to a decrease in resolution towards the edges of the image. This is much less of a problem with pulses in the windows. Since improved resolution at higher nutation rates is obtained with rf pulses in the windows compared to pulse missets, it might be desirable to use small homogeneous pulses to recenter the image along x .

5.5.2 Six-Point Hexamethylbenzene Phantom

The six-point hexamethylbenzene (HMB) phantom is shown in Figure 5.11. The six cylinders of adamantane were each approximately 0.9 mm in diameter and 1 mm in depth and were held in a Kel-F matrix. The cylinders were arranged slightly asymmetrically, as indicated in the figure.

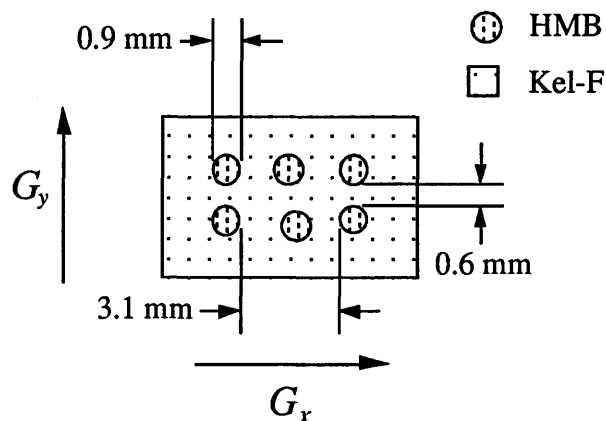


Figure 5.11: The six point hexamethylbenzene (HMB) phantom. The six HMB cylinders are each of about 0.9 mm diameter and 1 mm depth and are held in a Kel-F matrix. As shown, the array is slightly asymmetric.

Spectra of this phantom obtained using a simple one-pulse experiment and an SWW-16 line-narrowing experiment are shown in Figure 5.12. For both spectra, four signal averages were acquired. The one-pulse spectrum has a spectral width of 66.67 kHz, a linewidth of 14 kHz, and a S/N of 4.8. The SWW-16 spectrum has a spectral width of 3.44 kHz, a linewidth of 85 Hz, and a S/N of 28. The filters were left fully open (2 MHz) for both experiments.

The line-narrowed signals from this phantom using SWW-16 cycle times of 290.4 μs and 218.4 μs are shown in Figure 5.13. The shorter cycle time yields improved line-narrowing, as expected if higher order correction terms are contributing to the residual linewidth.

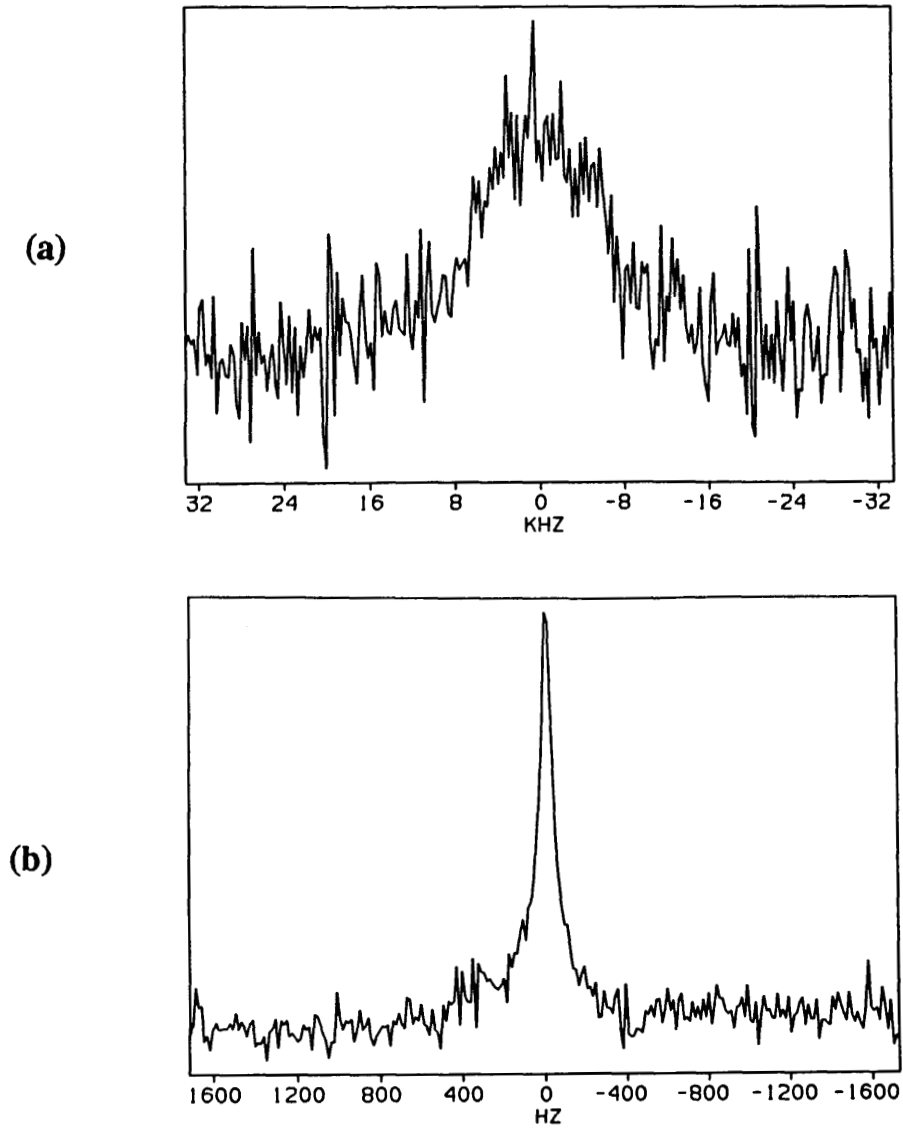


Figure 5.12: HMB spectra. (a) The unnarrows linewidth of the six-point HMB phantom is 14 kHz. (b) SWW-16 with a 290.4 μs cycle time and 2.1 μs $\pi/2$ time reduces the linewidth to 85 Hz.

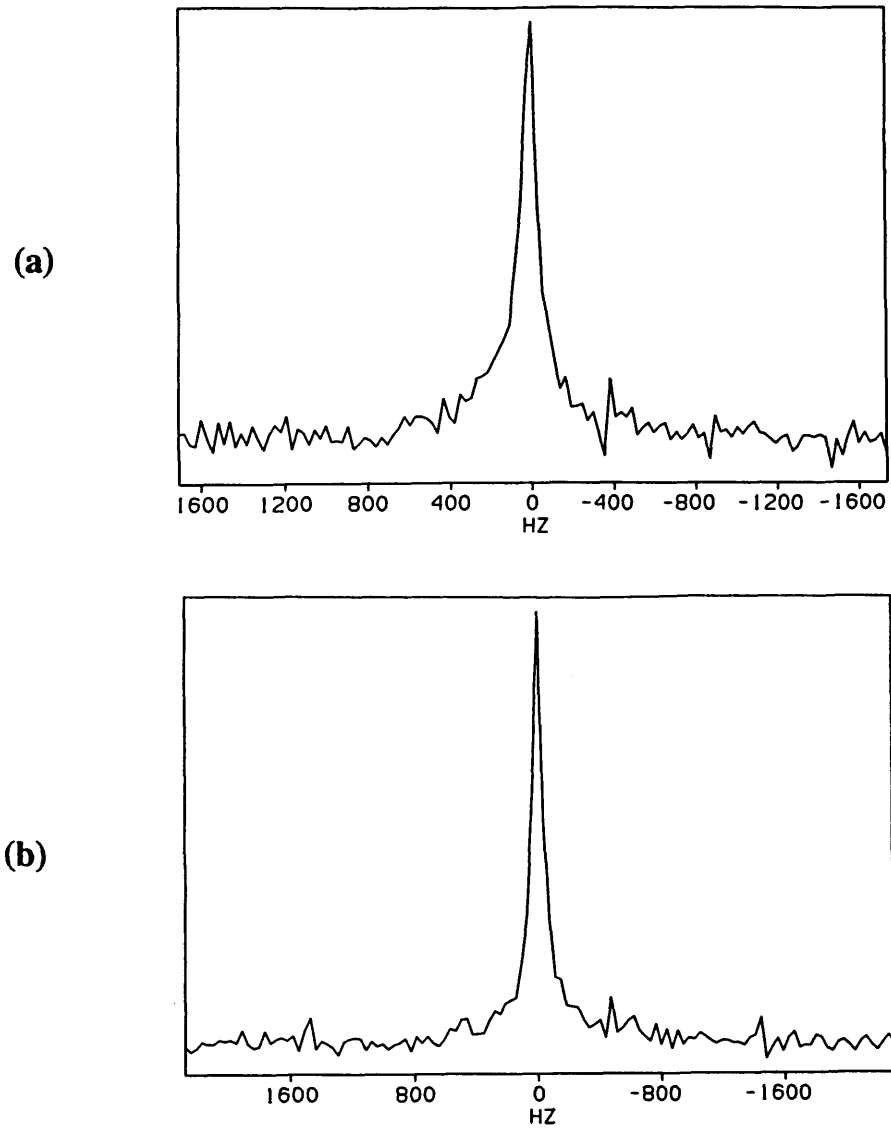


Figure 5.13: HMB line-narrowed spectra. (a) SWW-16 with a $290.4 \mu\text{s}$ cycle time yields a linewidth of 95 Hz. (b) SWW-16 with a $218.4 \mu\text{s}$ cycle time reduces the linewidth to 80 Hz.

A 2-D image of this phantom was obtained on a Bruker MSL200 solids NMR spectrometer. The gradient pulses were about 60 W and the solenoid pulses were about 300 W. The $\pi/2$ time was $2.1 \mu\text{s}$, the cycle time $218.4 \mu\text{s}$, and total gradient time $84.4 \mu\text{s}$. Twenty-four signal averages were acquired and a data set of 128×64 was collected, taking approximately one hour. No pulse missets were necessary.

The 2-D magnitude image is shown in Figure 5.14. The 1-D projections are shown in Figure 5.15. The effective gradient strength, as determined from the peak splittings, is $0.85 \pm 0.15 \text{ G/cm}$ corresponding to an unscaled gradient strength of $2.2 \pm 0.4 \text{ G/cm}$. The irregularities in peak height and shape are evidence of image distortion which is most likely due to the spatial variation of the phase of the solenoid rf field, discussed below.

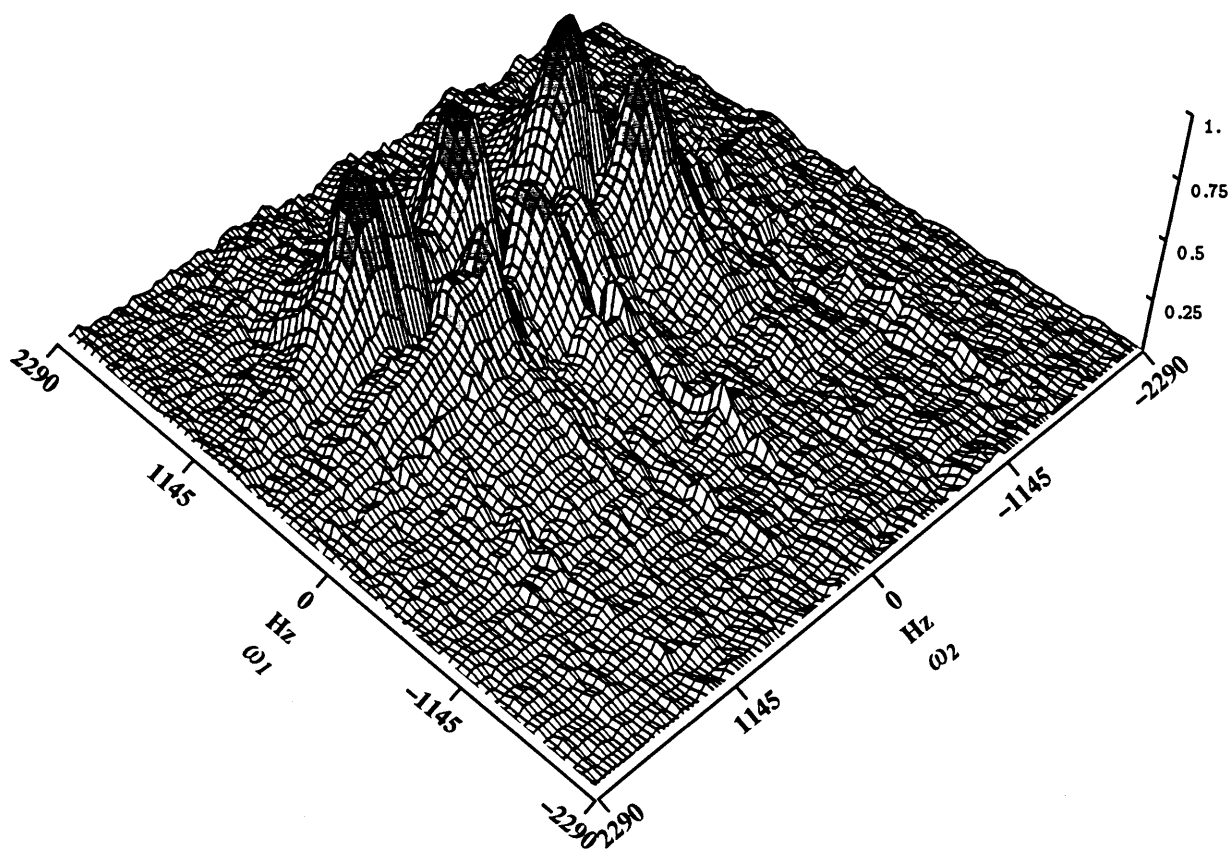


Figure 5.14: Two-dimensional image of HMB phantom.

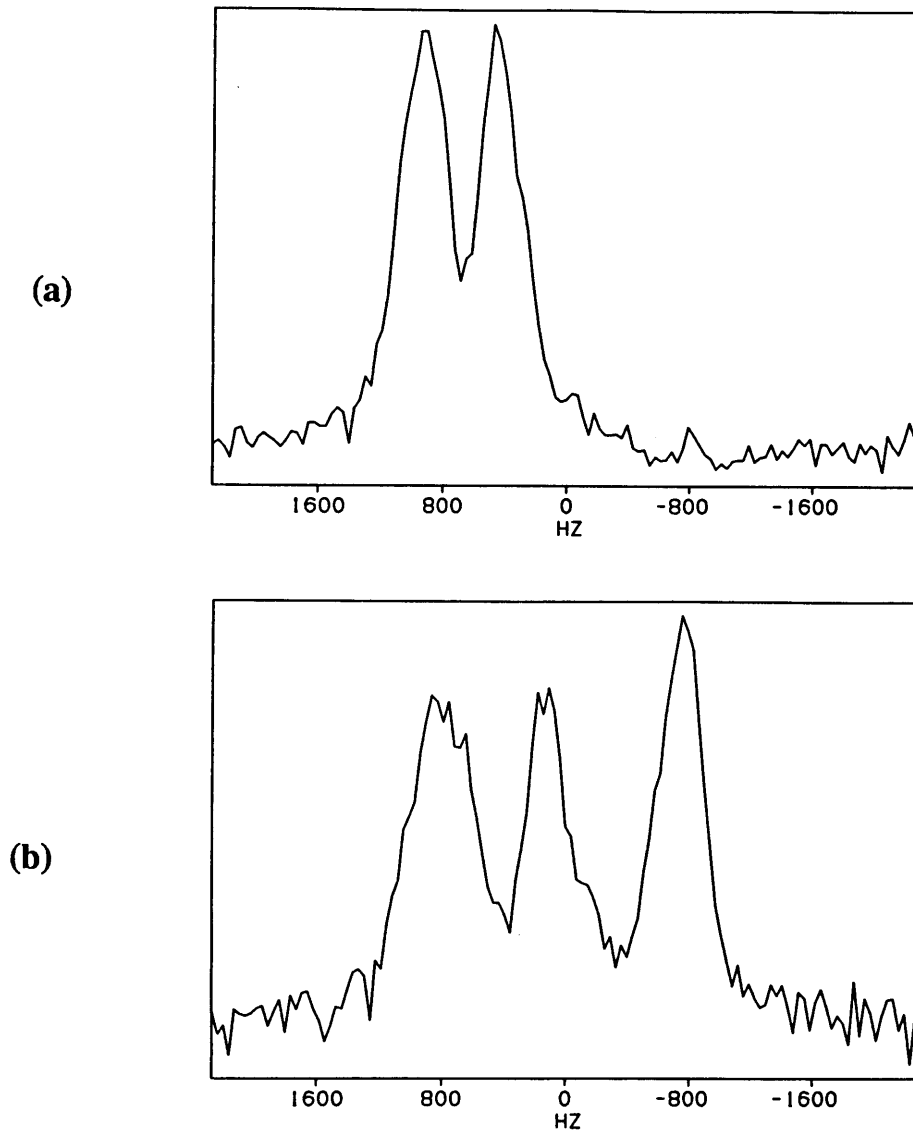


Figure 5.15: One-dimensional projections of HMB phantom. (a) Projection perpendicular to solenoid axis. (b) Projection along solenoid axis.

5.5.3 Obtaining a Phased Two-Dimensional Image

The images of both the adamantane and the HMB phantoms are presented as magnitude images, obtained as follows:

$$|S|(\omega_1, \omega_2) = \left\{ [\mathbf{Re}\{S(\omega_1, \omega_2)\}]^2 + [\mathbf{Im}\{S(\omega_1, \omega_2)\}]^2 \right\}^{1/2}. \quad (5.32)$$

While this circumvents the need for phase correcting the image, it is less than ideal because magnitude lineshapes have much lower resolution than pure 2-D absorption lineshapes. The width of the magnitude lineshape is increased relative to that of the absorption lineshape because of the influence of the greater frequency range about the line center of the dispersive component.

Here the magnitude display is necessary, however, because the signal is phase modulated along both t_1 and t_2 by gradient evolution. This yields a mixed phase, or “phase twisted,” 2-D lineshape, a superposition of pure 2-D absorption and dispersion peaks, and from this it is not possible to obtain the desired purely absorptive lineshape. This is a well-known problem in 2-D spectroscopy. In other words, the shortcoming of the 2D-FT sequence used here is that it allows only two independent components $S_r(\omega_1, \omega_2)$ and $S_i(\omega_1, \omega_2)$ to be distinguished, where the subscripts r and i refer to the real and imaginary (absorptive and dispersive) parts of the signal in the ω_2 dimension. In order to allow for an independent phase adjustment with respect to the two frequency variables ω_1 and ω_2 , it is necessary to distinguish four signal components in such a way that the real and imaginary parts can be combined independently in both dimensions. One technique that fulfills this requirement, and has been used in 2-D spectroscopy, is the hypercomplex 2-D Fourier transformation [15].

Briefly, the hypercomplex Fourier transformation converts a four-component time-domain signal ${}^4s(t_1, t_2)$ into a four-component frequency-domain spectrum ${}^4S(\omega_1, \omega_2)$. It is denoted “hypercomplex” because two independent imaginary units i and j are defined.

Here, i and j refer to the two orthogonal axes t_2 and t_1 , respectively, and of course, $i^2 = j^2 = -1$. The hypercomplex time-domain function is the sum of all the combinations of real and imaginary t_1 and t_2 components:

$${}^4s(t_1, t_2) = s_{rr}(t_1, t_2) + is_{ri}(t_1, t_2) + js_{jr}(t_1, t_2) + ijs_{ji}(t_1, t_2). \quad (5.33)$$

The real and imaginary parts in t_2 are measured by the quadrature detection in t_2 . The distinction of the real and imaginary parts in t_1 is accomplished in two independent experiments which differ in the rotating frame phase of one or more pulses. The hypercomplex Fourier transformation then yields the frequency domain signal ${}^4S(\omega_1, \omega_2)$ with the four components:

$${}^4S(\omega_1, \omega_2) = S_{rr}(\omega_1, \omega_2) + iS_{ri}(\omega_1, \omega_2) + jS_{jr}(\omega_1, \omega_2) + ijs_{ji}(\omega_1, \omega_2). \quad (5.34)$$

So now there are two independent phase variables associated with the imaginary units i and j and it is possible to adjust the phase independently along both frequency axes by linear combinations of the four components of ${}^4S(\omega_1, \omega_2)$.

In the 2D-FT imaging experiment one example of a pair of independent experiments that allows for the distinction of the real and imaginary parts in t_1 is shown in Figure 5.16. The $(\pi/2)_x$ pulse inserted between the t_1 and t_2 periods has the net effect of converting the y -component of the magnetization into longitudinal magnetization which is unobservable during t_2 . It follows then that if this imaging sequence is preceded by a $(\pi/2)_y$ preparation pulse, the signal is cosine modulated by the evolution due to G_x during t_1 , while if it is preceded by a $(\pi/2)_x$ preparation pulse, the signal is sine modulated during t_1 . Regardless of the phase of the preparation pulse, the signal is still phase modulated by evolution due to G_x during t_2 . These signals provide the real and imaginary parts of the hypercomplex signal, which can then be transformed and phased to yield a purely absorptive two-dimensional lineshape [16].

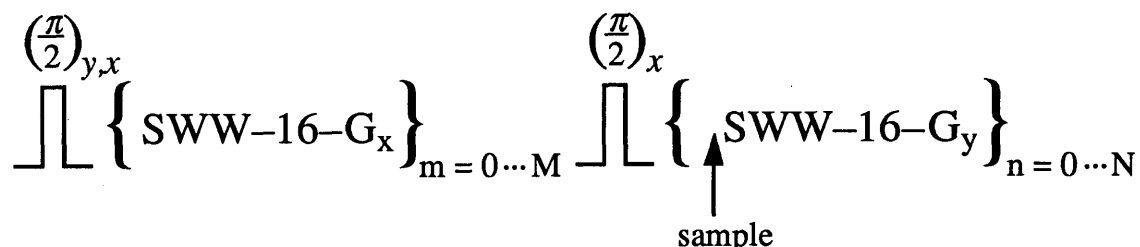


Figure 5.16: 2D-FT Pulse Sequence for a Phaseable Image. The $(\pi/2)_x$ pulse between the t_1 and t_2 periods converts the y -magnetization to longitudinal magnetization which is unobservable during t_2 . A $(\pi/2)_y$ preparation pulse then yields cosine modulation of the signal by the x -gradient evolution during t_1 , whereas a $(\pi/2)_x$ preparation pulse yields sine modulation. These signals provide the real and imaginary parts of a hypercomplex signal which can be Fourier transformed and phased to give a purely absorptive two-dimensional lineshape.

5.5.4 Polyphenylene Sulfide Phantom

The polyphenylene sulfide (PPS) phantom, shown in Figure 5.17, consisted of three groups of PPS pieces each extending 0.5 mm along the solenoid axis, separated by 2 mm spacers of Kel-F, a perfluorinated polymer. The PPS pieces extended approximately 3 mm along the direction perpendicular to the solenoid axis, and 3 mm in the non-imaging (z) direction. PPS, supplied by Lockheed, is a polymer used in composite materials with aerospace applications.

The PPS spectra of a simple one-pulse experiment and of a SWW-16 line-narrowing experiment are shown in Figure 5.18. For both spectra, 24 signal averages were acquired. The lineshape of the PPS phantom under a simple one-pulse experiment consisted of a broad (36 kHz) and a narrow (5 kHz) component. Applying SWW-16 with a cycle time of 249.6 μ s and a $\pi/2$ time of 2.1 μ s narrows the signal to less than 300 Hz. The S/N of the one-pulse spectrum including the narrow peak is 27; without the narrow peak it is 14. That for the SWW-16 spectrum is 68. Again, the filters were left fully (2 MHz) open for both spectra.

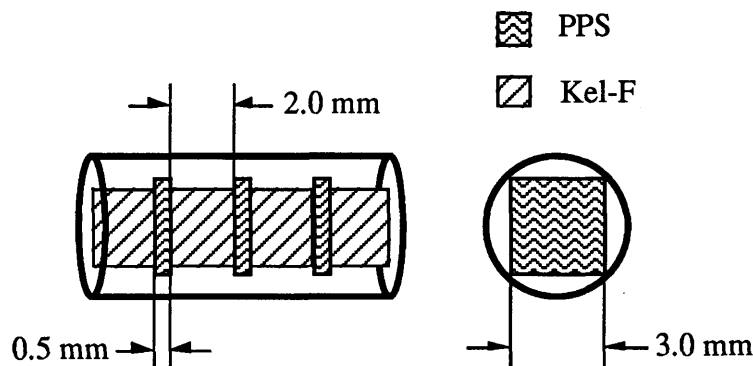


Figure 5.17: The polyphenylene sulfide (PPS) phantom. The three groups of PPS pieces each extend 0.5 mm along G_{yy} , 3 mm along G_{xx} , and 3 mm along the non-imaging direction. They are separated by 2 mm Kel-F spacers and the whole assembly is held together inside a glass tube.

The larger linewidth of PPS under SWW-16, as compared to the linewidths of adamantane, Delrin, and HMB, is most likely due to molecular motions which occur with periods comparable to the SWW-16 cycle time. These lead to a decreased $T_{1\rho}$ relaxation time.

A phased 2-D image of the PPS phantom is shown in Figure 5.19. This image was obtained on the MSL200. The $\pi/2$ time used was 2.1 μs , the cycle time 249.6 μs , and the total gradient time 105.2 μs . The effective gradient strength is 0.94 ± 0.06 G/cm, corresponding to an unscaled gradient strength of 2.2 ± 0.1 G/cm. The two data sets necessary to produce the purely absorptive 2-D image were obtained separately rather than in an interleaved manner. The latter would be favorable to minimize the effects of drift between corresponding points of the two data sets. For example, the line narrowing achieved before an hour-long imaging scan was frequently different than that observed afterwards. A likely explanation for this is that probe heating during the experiment caused drift in the phase transients present. For images acquired on the MSL200, phase drift between the solenoid and quadrupole rf carriers may also be a problem for longer scans. As discussed in Appendix B, it was not observed to be a problem over time periods

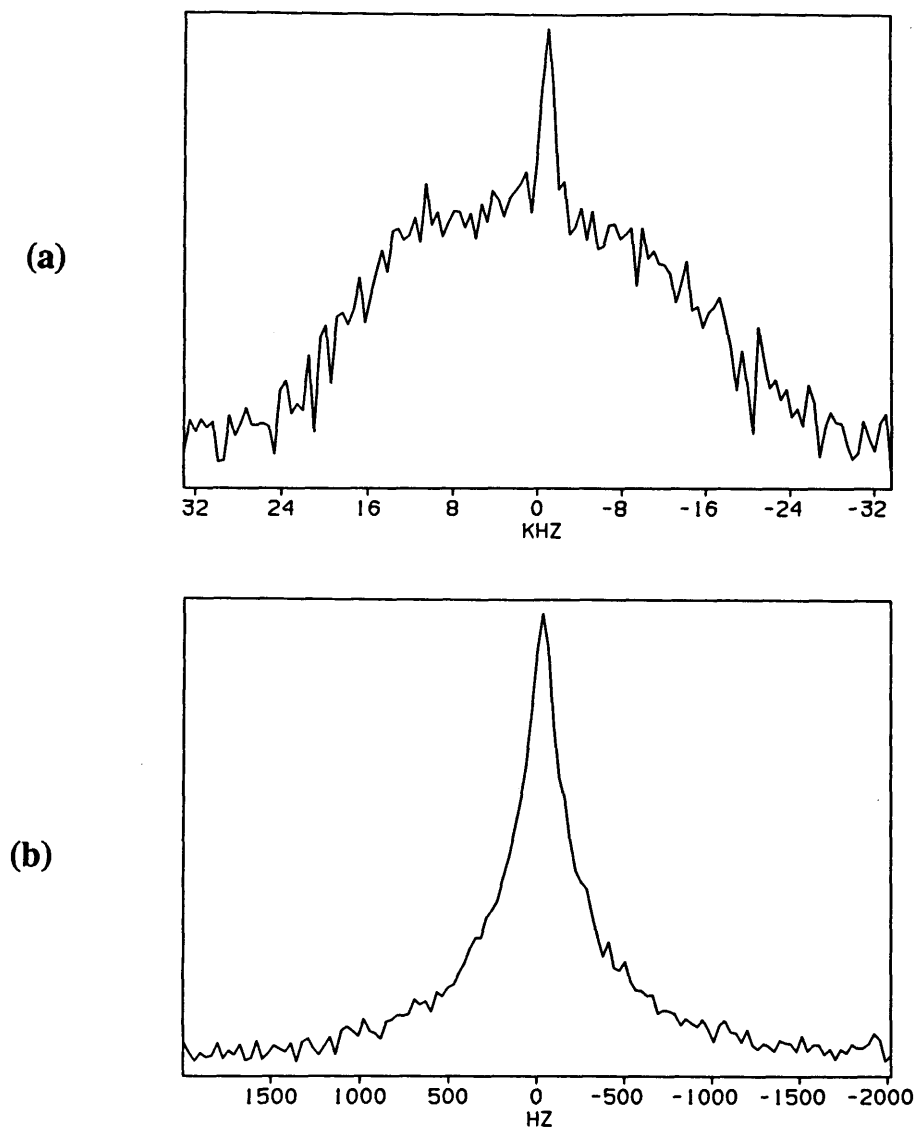


Figure 5.18: Polyphenylene sulfide spectra. (a) A simple one-pulse experiment reveals a broad (36 kHz) and a narrow (5 kHz) component to the PPS linewidth. (b) An SWW-16 line-narrowing experiment with a 249.6 μs cycle time and 2.1 μs $\pi/2$ time reduces the linewidth to less than 300 Hz.

of about an hour.

The magnitude image reconstructed from the same data sets as the phased image is shown in Figure 5.20. The resolution is clearly degraded relative to that of the phased image. Slices taken along ω_2 of both images are shown in Figure 5.21. From these it is possible to determine the improvement in resolution obtained in the phased image. Here the resolution is defined to be the width of a Lorentzian which when convolved with the expected linewidth (based on spatial extent and observed gradient strength) yields the observed linewidth. For the phased image the resolution is approximately $500 \mu\text{m}$ while for the magnitude image the resolution is about $1200 \mu\text{m}$. The improvement in resolution obtained is then about a factor of two.

One other noticeable feature of the phased image is that the peaks are not quite evenly spaced and seem slightly twisted with respect to one another. As seen from the simulations discussed in Chapter 4, the pulses delivered by an ideal solenoid do not narrow a broad solid lineshape equally well at all points along an rf gradient. Solenoid inhomogeneity adds a component to these spatially dependent linewidths. Furthermore, gradient nonlinearities cause spatially dependent line shifts in the image, resulting in points equally spaced in the sample being unequally spaced in the image. These effects can be modelled by an image-spread matrix. Ideally, it would be possible to determine this image-spread matrix by imaging a phantom composed of a regular array of small points, invert this matrix and use this to obtain corrected images of other samples imaged. In practice, noise in the image makes this simplistic approach impossible to apply. One solution is to use the pseudoinverse of the image-spread matrix, calculated from its singular value decomposition [16]. This is currently being investigated.

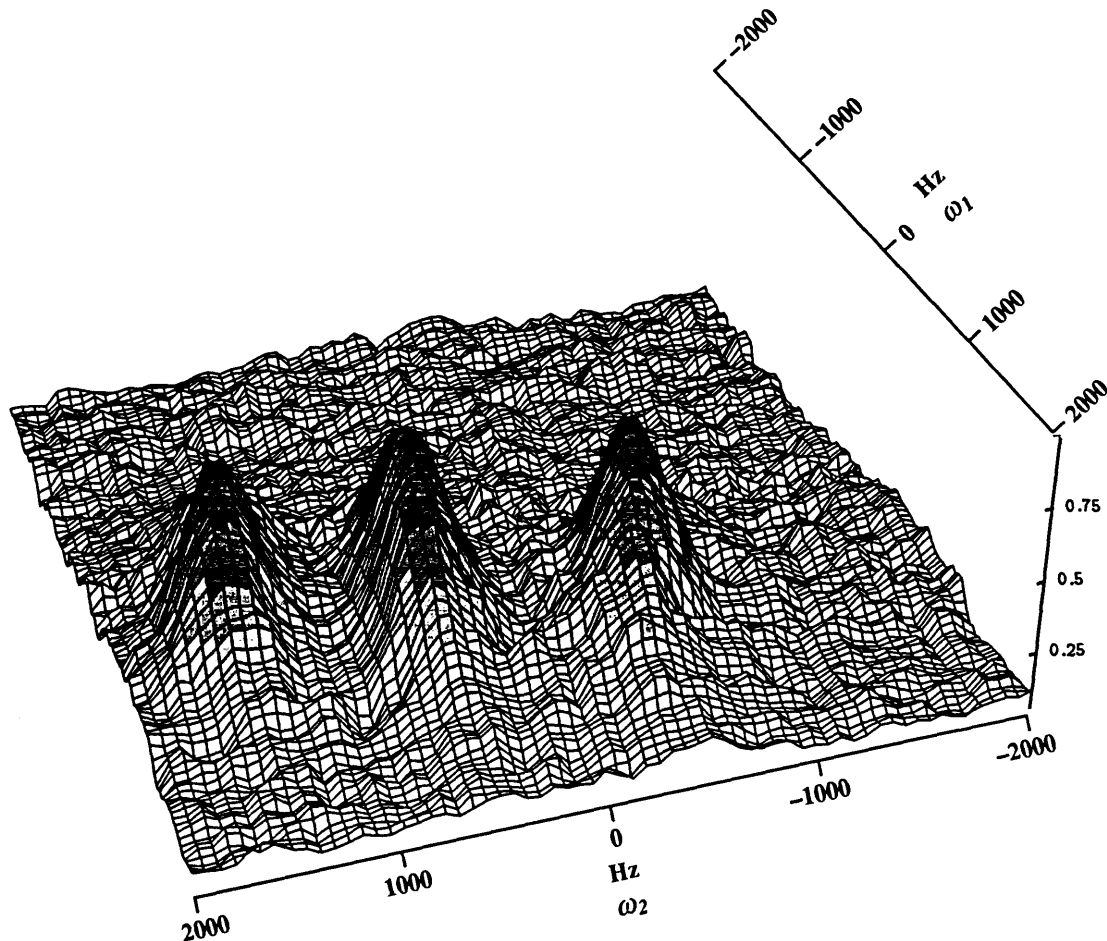


Figure 5.19: Phased image of polyphenylene sulfide.

5.6 Resolution and S/N

Three types of resolution for the adamantane, HMB, and PPS images are shown in Table 5.2. The digital resolution is determined from the effective gradient strength and the Hz per point. The expected resolution is determined, assuming Lorentzian lineshapes, from the effective gradient strength and the narrowed linewidth in the absence of gradient. The observed resolution is the width of a Lorentzian which when convolved with the expected linewidth (determined by the spatial extent and observed gradient strength) yields the observed linewidth. In all cases, the digital resolution is less than the expected resolution. For adamantane and HMB the expected resolution is also less than the ob-

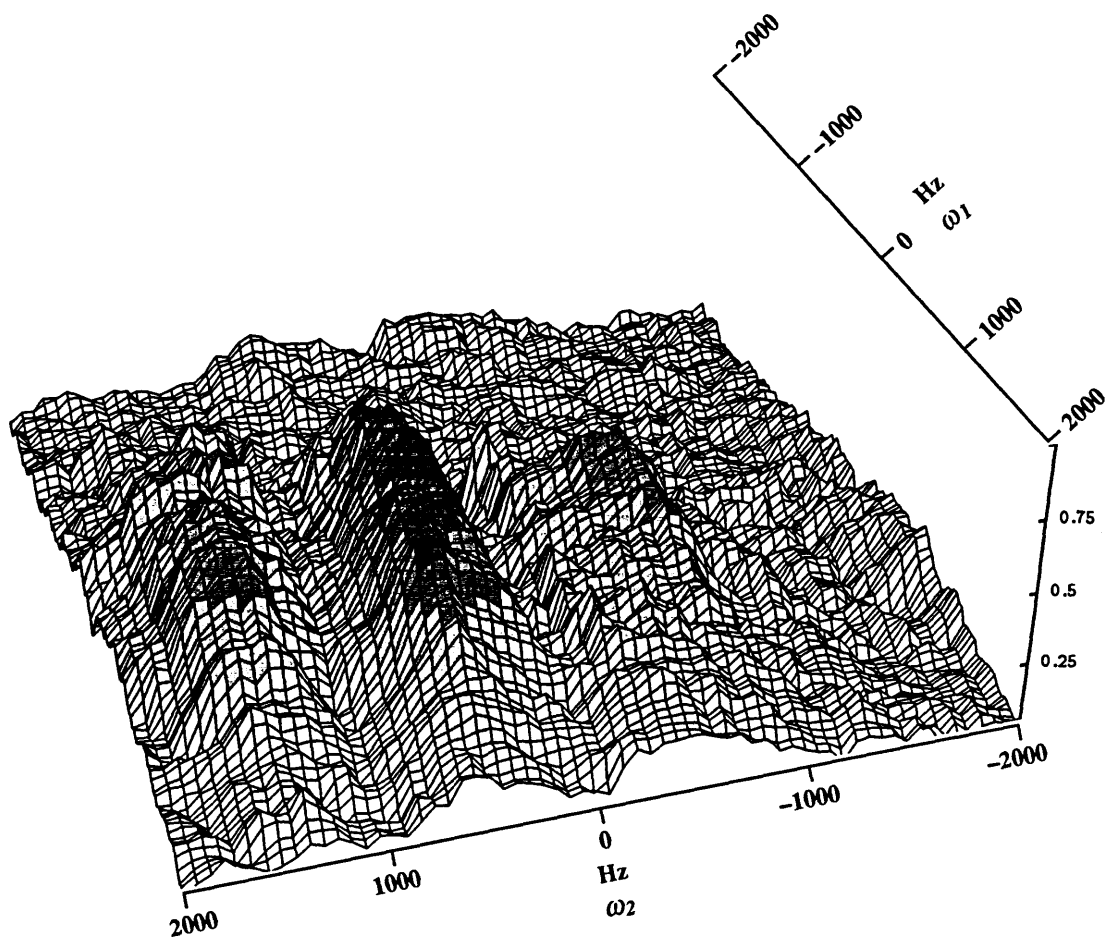


Figure 5.20: Magnitude image of polyphenylene sulfide.

served resolution. This is not the case for PPS. The most likely explanation for this is that part of the signal is obscured by the “striping” effect discussed below. It should also be noted, that, as discussed in Chapter 4, second averaging fails at zero offset. The presence of small gradient pulses actually improves line narrowing. Thus, the linewidth in the absence of gradient pulses does not necessarily set the lower limit on resolution.

In general, the resolution of an image under multiple-pulse line narrowing may be characterized by the parameter N_e , the number of data points after which the signal has dropped to $1/e$ of its original intensity in the absence of a gradient [18, 19]. For an optimal gradient (the largest possible that avoids aliasing) an effective transverse

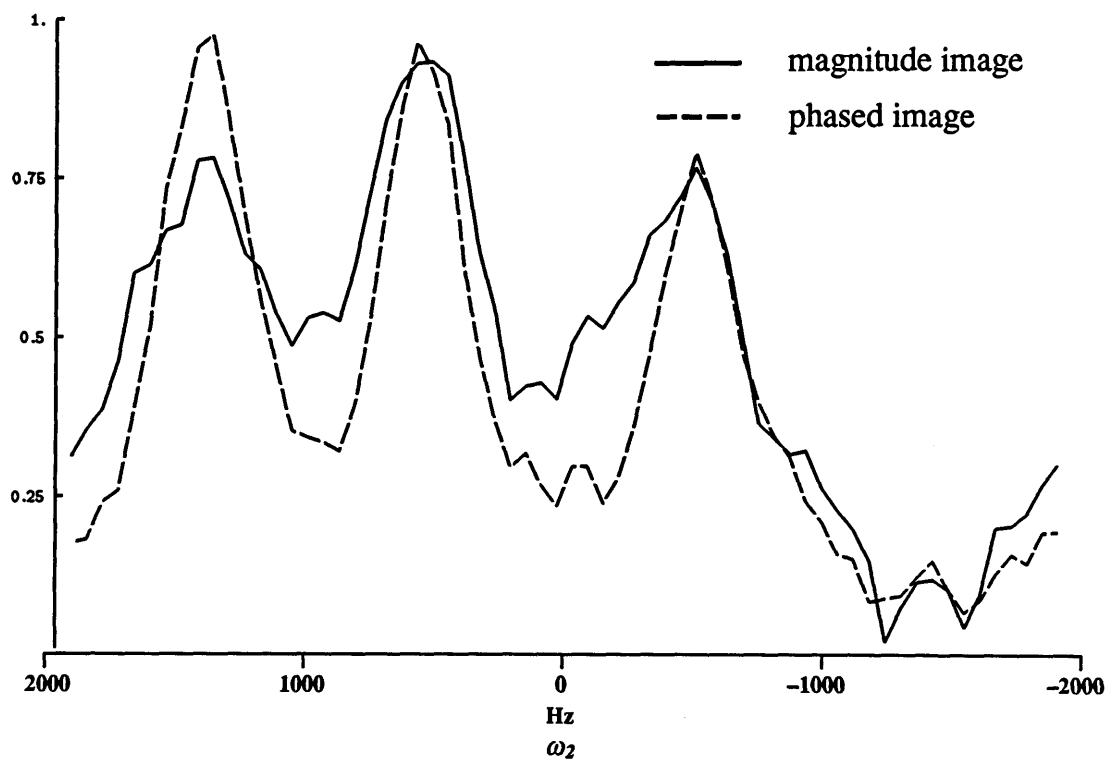


Figure 5.21: Comparison of the phased and magnitude polyphenylene sulfide images showing a cut taken along the ω_2 axis. The dashed line is taken from the phased image while the solid line is taken from the magnitude image.

phantom	digital resolution	expected resolution	observed resolution
adamantane	330 μm	540 μm	600 μm
HMB	70 μm	150 μm	300 μm
PPS	160 μm	700 μm	500 μm

Table 5.2: Image resolution for the adamantane, HMB, and PPS phantoms. The observed resolution quoted for PPS is for the phased image.

relaxation time T_{2e} may be defined as N_e/l_s , where l_s is the length of the sample along the gradient direction. The image resolution assuming a Lorentzian line is the full width at half-height $\Delta\nu_{1/2}$ which corresponds to T_{2e} . That is, the resolution is given by the following:

$$\Delta\nu_{1/2} = \frac{l_s}{\pi N_e}. \quad (5.35)$$

The first obvious conclusion to be drawn from this is that poorer resolution is obtainable for larger samples, unless of course one images only a portion of the sample. The second conclusion is that in order to obtain the optimal resolution, N_e should be maximized. Ignoring sensitivity arguments for the moment, the highest resolution is obtained by maximizing the ratio of the spectral width to the narrowed linewidth. This can be done using a longer, more highly compensated, pulse sequence provided that the increased line-narrowing more than compensates for the increased cycle time. Alternatively, oversampling can be used to increase the spectral width [20]. As mentioned previously, however, for imaging with the vertical quadrupole coil oversampling to increase the spectral width is expected not to improve the resolution due to the increased effect of error terms for gradient-induced nutation frequencies past the Nyquist frequency of the sequence sampled once per cycle. Using separate coils for the two (or three) gradient directions would remove this limitation.

During a multiple-pulse cycle, the magnetization is sampled stroboscopically during a window, and thus within microseconds of a strong rf pulse. This requires the receiver bandwidth to be open far wider than the actual spectral width. This introduces noise into the spectrum, which would otherwise be filtered out. Thus, although multiple-pulse sequences increase the intensity of a peak by concentrating all the signal energy into a narrower line, they also increase the noise present in the spectrum. The expected improvement in S/N of a multiple-pulse spectrum compared to a one-pulse spectrum

of the same sample may be calculated from the different receiver bandwidths, spectral widths, and linewidths. The S/N values quoted for the HMB and PPS phantoms imaged were obtained with the same large filter settings. The expected ratio of S/N for a fixed filter bandwidth is

$$\frac{(S/N)_1}{(S/N)_2} = \frac{\Delta\nu_2}{\Delta\nu_1} \left(\frac{(t_c)_2}{(t_c)_1} \right)^{1/2}, \quad (5.36)$$

where $\Delta\nu$ is the linewidth and t_c the cycle time. For the HMB phantom the ratio of SWW-16 S/N to one-pulse S/N is 5.9, while that expected for the sampling rates, linewidths, and receiver bandwidths used here is 37. For PPS, the improvement in S/N is a factor of 5.0 if the narrow component of the one-pulse spectrum is neglected and 2.5 if it is not. Since it is not known what fraction of the PPS spins contribute to the narrow component, an expected ratio of S/N values cannot be calculated. In any case, these results seem rather discouraging. A similar comparison can be made from the results of the S/N comparison of the 2-D imaging probe and standard probe discussed in Chapter 6. For the parameters used there the expected improvement in S/N by using SWW-16 is between 40- and 50-fold. The observed improvement, however, is between 7.5- and 9.5-fold. This is the case for both probes. Thus whatever is causing the extra noise is related to the multiple-pulse sampling, but not to the imaging probe.

The S/N of a multiple-pulse pulse sequence can be improved in several ways. First, the signal detected can be integrated over the sampling window length [21]. Integration was used for the adamantane images and spectra obtained on the homebuilt spectrometer. In this case, the expected ratio of S/N is

$$\frac{(S/N)_1}{(S/N)_2} = \frac{\Delta\nu_2}{\Delta\nu_1} \left(\frac{(t_{\text{int}})_1}{(t_{\text{int}})_2} \right)^{1/2}, \quad (5.37)$$

where t_{int} is the integration time of a sampling period. For the adamantane phantom, the ratio of the SWW-16 S/N to the one-pulse S/N is 12.8. The ratio expected for linewidths and integration times used is 116; however, it was never clearly demonstrated that the

integrator was functioning correctly.

A second means by which to improve the S/N of a multiple-pulse sequence is, again, by oversampling. This can be accomplished either by oversampling to increase the spectral width, or to increase effectively the number of acquisitions. For example, sampling twice during a pulse cycle doubles the possible signal bandwidth and spreads the noise over twice the bandwidth, increasing the S/N by $2^{1/2}$ [18]. Alternatively, a sequence can be sampled twice per cycle and the data added to increase S/N by $2^{1/2}$. The main difficulty with oversampling is that the data acquired in different windows need to be corrected individually before recombination.

Ultimately, S/N limits the resolution available in solid-state NMR imaging. A recent 3-D image of the solid polycarbonate had a resolution of $150\ \mu\text{m}$ in all three dimensions [22]. Lower-dimensional images can have even better resolution than this, since the voxel size can be effectively enlarged along the non-imaged dimensions. The resolution we have achieved to date is clearly not at the lower limit set by S/N . Equally clear is that the S/N obtained can be improved by an order of magnitude by an effective implementation of integration over each sampling window and extension of sampling to all the Z and \bar{Z} windows.

5.7 Spatial Variation of the Phase of the Solenoid RF Field

Images of phantoms having continuous distributions of spins extending along the solenoid coil showed striping with a periodicity of the solenoid coil turns. This striping may also explain some of the variations in lineshape and intensity observed in the images discussed above. To better understand the source of this striping, images of water phantoms were obtained. The water phantoms imaged are shown in Figure 5.22.

The image of the single capillary tube of water placed along the solenoid axis shows

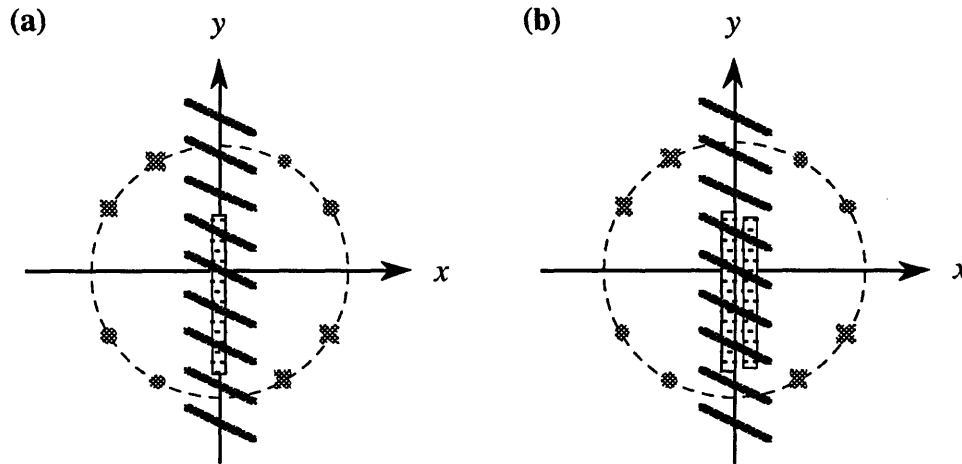


Figure 5.22: Two water phantoms. (a) The capillary tube of inner diameter 0.9 mm is filled with 14 mm of water and positioned along the axis of the solenoid coil. (b) Two capillary tubes of inner diameter 0.9 mm are filled with water and positioned as shown. The tube on the right has 13.5 mm of water and is 1 mm away from the edge of the solenoid coil. The tube on the left has 14 mm of water and is 2 mm away from the edge of the solenoid coil.

the excellent linearity of the gradient over this region. Some ripple is noticeable along the peak in the image, however, and the high intensity region at the end of the peak is troubling. The 1-D projections are shown in Figure 5.23 and the full 2-D image is shown in Figure 5.24.

The striping is particularly distinct in the image of two capillary tubes of water. The 1-D projections are shown in Figure 5.25 and the 2-D image in Figure 5.26. This striping has the periodicity of the turns of the solenoid coil and is obviously worse towards the edge of the coil.

Since the periodicity of the stripes is the same as that of the solenoid coil, one possible cause would be a spatial dependence of the solenoid field amplitude. Simulations have shown, however, that SWW-16 is well compensated for pulse angle errors. For example, excellent line narrowing is observed even for 75° pulses [17]. A more probable cause is a

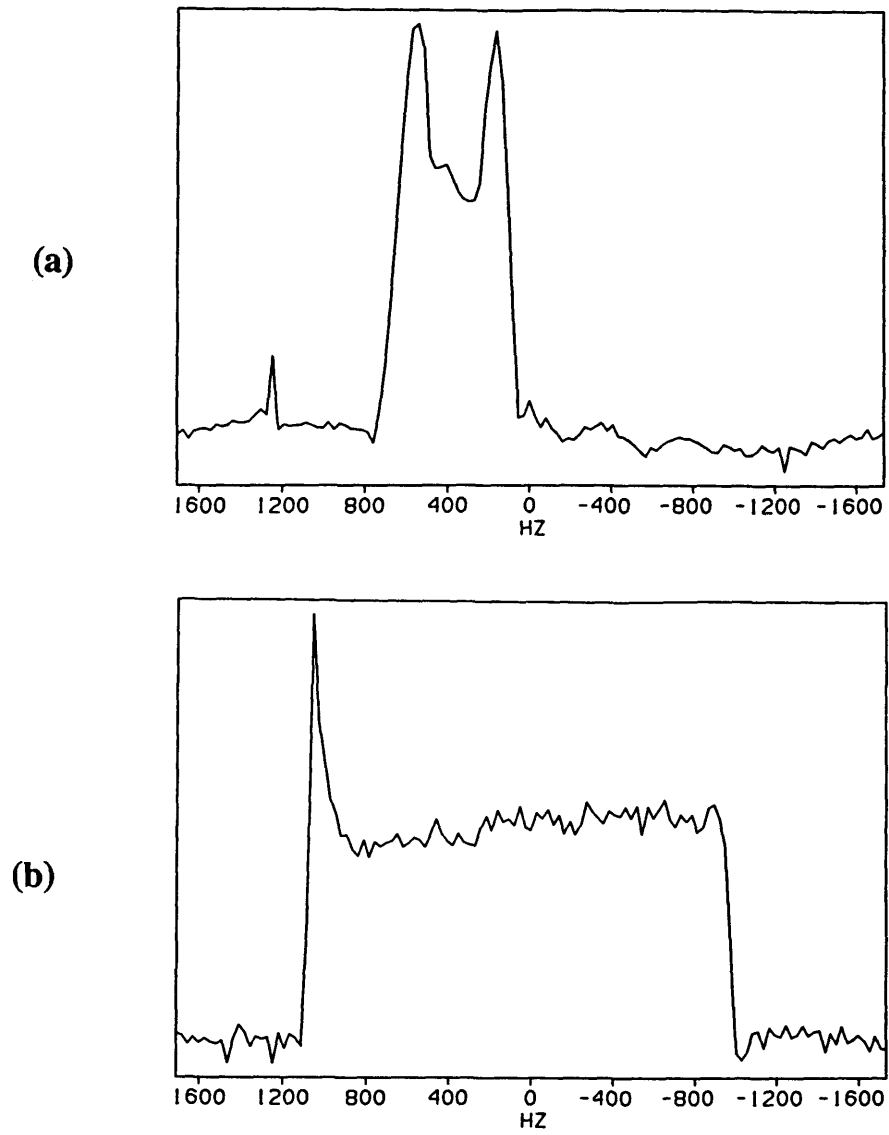


Figure 5.23: One-dimensional projections of a single capillary tube of water.

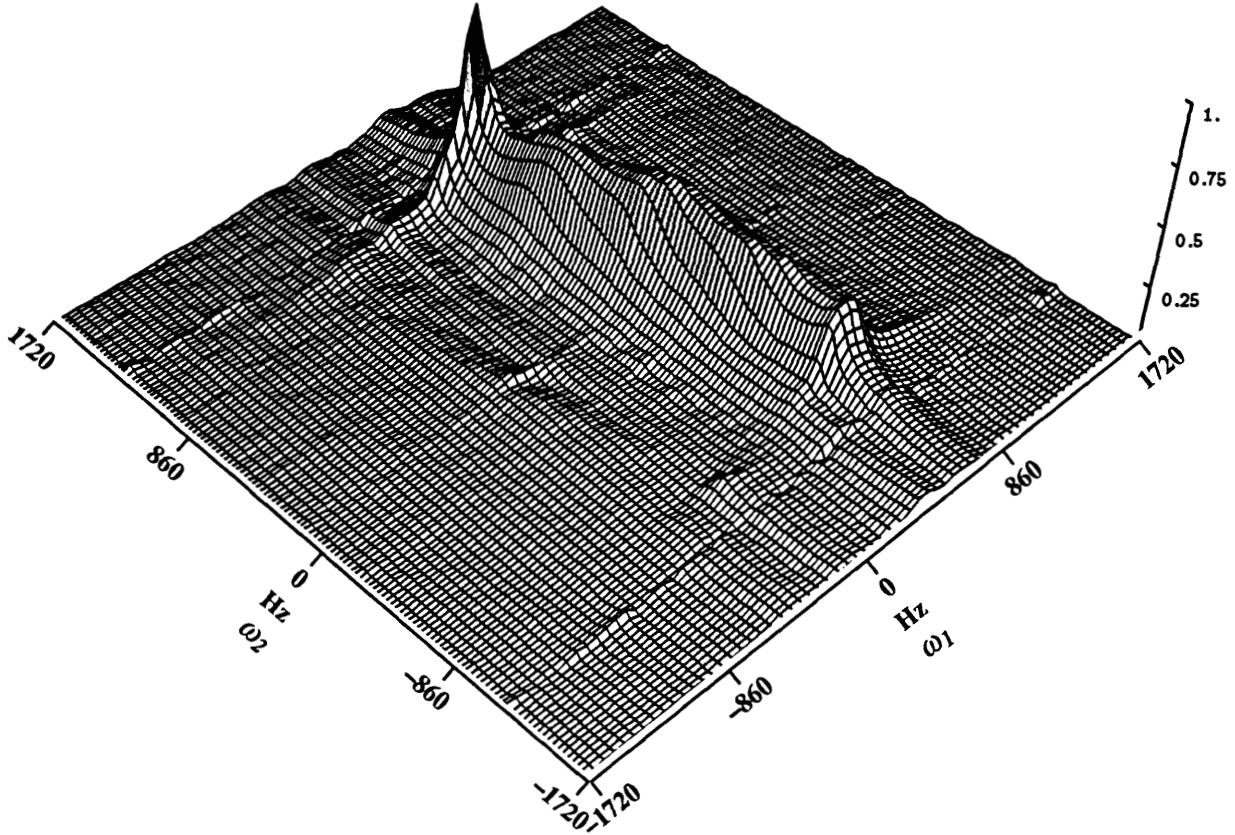


Figure 5.24: Two-dimensional image of a single capillary tube of water.

spatial dependence of the solenoid field phase. This is normally not a concern in NMR experiments employing only one rf coil. Hamiltonians truncated in the rotating frame are unaffected by the transition to the tilted frame which accounts for the spatial dependence of the rf phase. Thus, all internal Hamiltonians are unaffected. The Hamiltonian describing the gradient pulses is affected, however. The spatially dependent phase ϕ_r appears in the gradient term of the average Hamiltonian for SWW-16 so that

$$\overline{\mathcal{H}}_G^{(0)} = \frac{2}{3} \cdot \gamma \frac{I_0 \mu_0}{4a^2} \{x \cos(\phi_d + \phi_r) + y \sin(\phi_d + \phi_r)\} I_z, \quad (5.38)$$

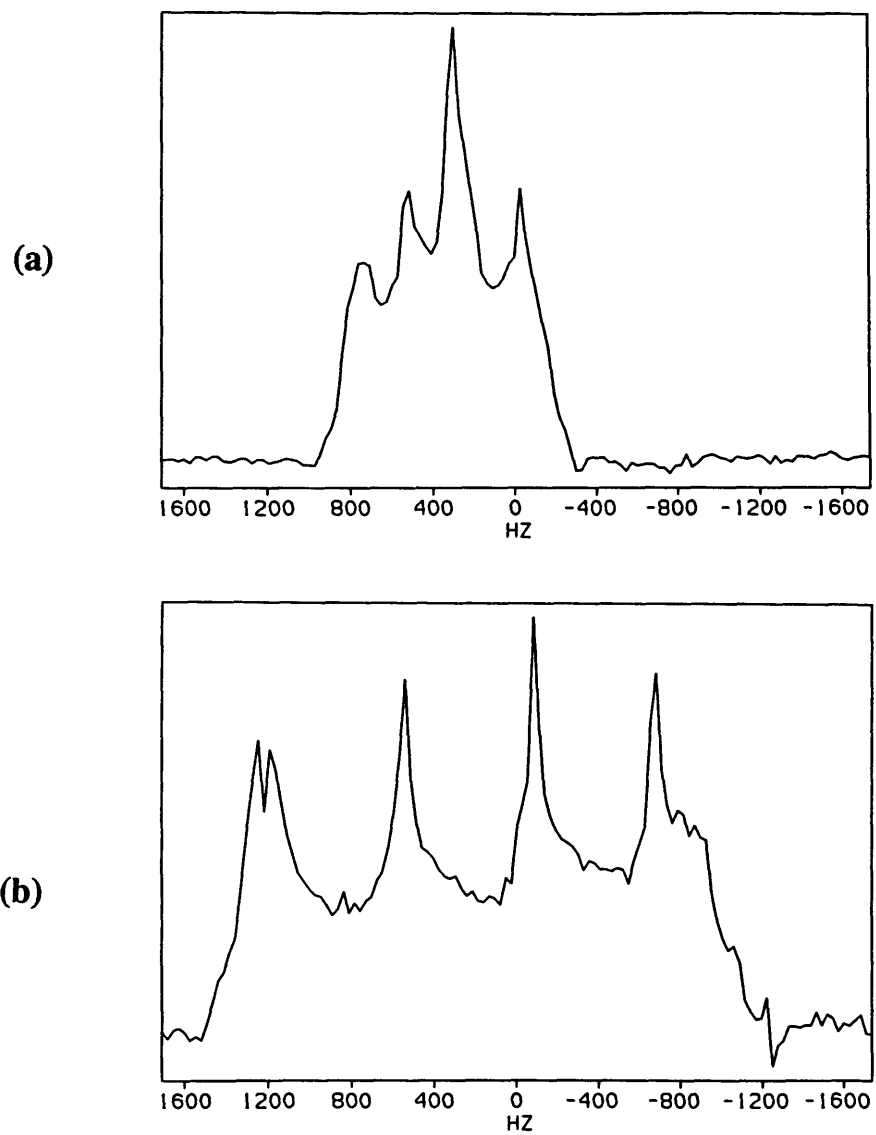


Figure 5.25: One-Dimensional projections of two capillary tubes of water.

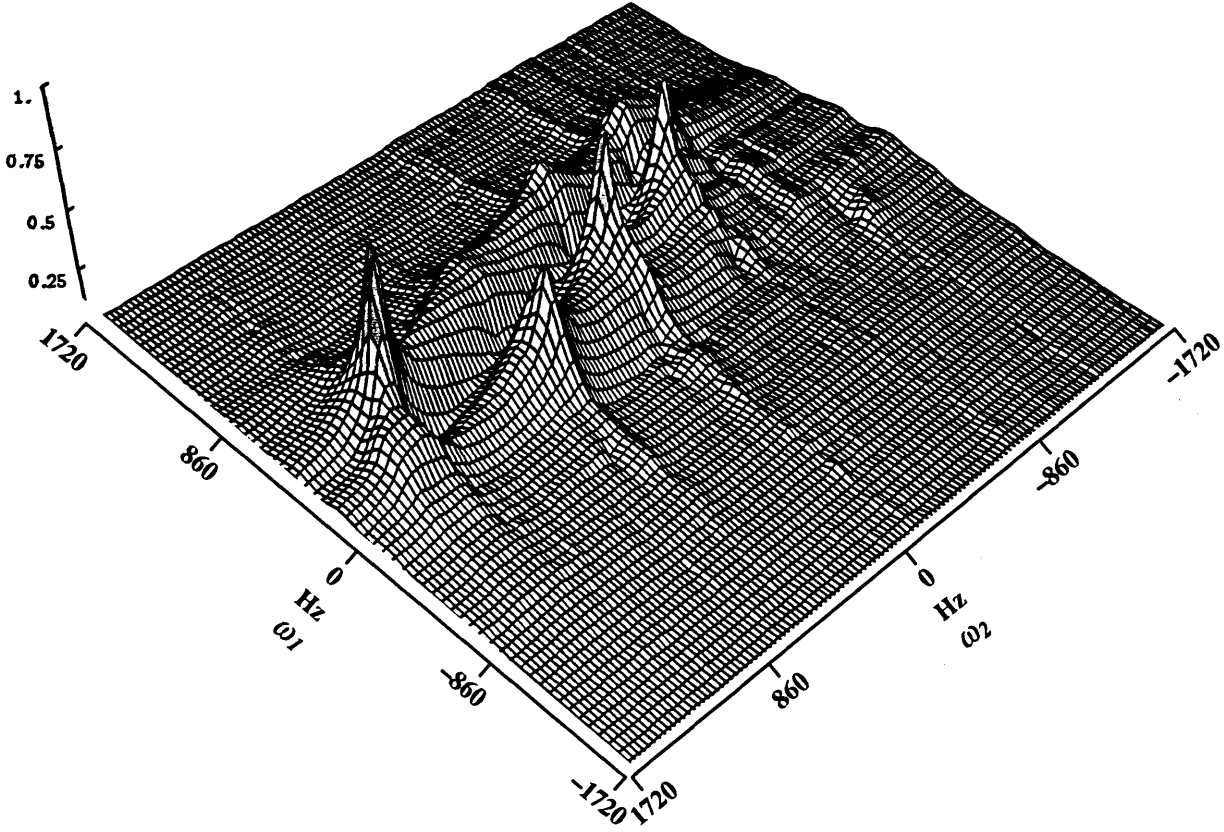


Figure 5.26: Two-dimensional image of two capillary tubes of water.

for the quadrupole coil arranged vertically, and

$$\overline{\mathcal{H}}_G^{(0)} = \frac{2}{3} \cdot \gamma \frac{I_0 \mu_0}{4a^2} \{-x \cos(\phi_d + \phi_r)\} I_z, \quad (5.39)$$

for the case of the quadrupole coil arranged horizontally. This is particularly problematic for the case of the vertical quadrupole coil, because it leads to an effective spatial mixing of the x and y gradients. Simulations [17] have shown that a 1° phase error in the line-narrowing pulses would be detectable as striping of the image near the edges of the solenoid coil for images obtained with a vertical quadrupole coil. A similar phase error would not be detectable in images obtained with a horizontal quadrupole coil. Similarly, 5° phase error would be disastrous for vertical quadrupole coil images, whereas the stripes

produced would be much less pronounced for horizontal quadrupole coil images.

These simulations suggest that two-dimensional images of superior resolution can be obtained by using two orthogonal horizontal coils. This would allow imaging in the xz plane. An alternative to this solution would be to construct a solenoid coil with exceptionally high phase homogeneity. Also, a solenoid coil of larger diameter would enable samples of the size imaged here to be kept farther from the regions of higher phase inhomogeneity near the turns of the solenoid.

5.8 Conclusions

Multiple-pulse line narrowing and rf gradients have been successfully combined in a two-dimensional imaging experiment. With this, images of adamantane, hexamethylbenzene, and polyphenylene sulfide phantoms have been obtained. These are the first two-dimensional NMR images produced with a single gradient circuit without sample rotation and back-projection. The gradient coil used here, an eight-wire approximation to a quadrupole coil, produced gradients of 1.2 to 2.2 G/cm when driven with rf pulses of 25 to 60 W. Coherent averaging theory calculations show how SWW-16 selectively averages the effects of one of the two orthogonal gradient components of this coil. The images are clear demonstration that SWW-16 is performing as expected. In particular, the absence of quadrature ghosts and spin-locked magnetization are evidence that SWW-16 continues to perform well even in the presence of the second gradient component.

The first two-dimensional phased image has also been presented. For this, two data sets are necessary, from which it is possible to obtain purely absorptive 2-D lineshapes. The improvement in resolution observed is a factor of two.

The resolution observed, on the order of 500 μm , was partially limited by the gradient strength available. A more significant limiting factor, though, was the spatial variation

of the solenoid rf phase. This can be remedied by using two orthogonal quadrupole coils, or by using a solenoid with a diameter twice that of the sample.

5.9 Appendix: Calculating the Quadrupole Coil Gradient Term of the Average Hamiltonian

5.9.1 Vertical Quadrupole Coil

Recall that the gradient Hamiltonian, \mathcal{H}_G , for the vertical quadrupole coil can be written

$$\mathcal{H}_G = \gamma \mathbf{I} \cdot \mathcal{G}^t \cdot \mathbf{r} \quad (5.40)$$

$$= \gamma \left(\frac{\mu_0}{2a^2} I(t) I_x x - \frac{\mu_0}{2a^2} I(t) I_y y \right). \quad (5.41)$$

\mathcal{H}_G is transformed into the rotating frame defined by the solenoid carrier frequency as follows:

$$\begin{aligned} \mathcal{H}_G^{\text{RF}} &= \gamma U^{-1} \mathbf{I} \cdot \mathcal{G}^t \cdot \mathbf{r} U \\ &= \exp(-i\omega t I_z) \gamma \mathbf{I} \cdot \mathcal{G}^t \cdot \mathbf{r} \exp(+i\omega t I_z) \\ &= \gamma \frac{I_0 \mu_0}{2a^2} \left\{ \exp(-i\omega t I_z) [x I_x \cos(\omega t - (\phi(t) + \phi_d)) - \right. \\ &\quad \left. y I_y \sin(\omega t - (\phi(t) + \phi_d))] \exp(+i\omega t I_z) \right\} \\ &= \gamma \frac{I_0 \mu_0}{2a^2} \left\{ \exp(-i\omega t I_z) \left[\frac{x}{2} [I_x \cos(\omega t - (\phi(t) + \phi_d)) - \right. \right. \\ &\quad \left. \left. I_y \sin(\omega t - (\phi(t) + \phi_d))] + \right. \right. \\ &\quad \left. \frac{x}{2} [I_x \cos(\omega t - (\phi(t) + \phi_d)) + I_y \sin(\omega t - (\phi(t) + \phi_d))] + \right. \\ &\quad \left. \frac{y}{2} [I_x \sin(\omega t - (\phi(t) + \phi_d)) - I_y \cos(\omega t - (\phi(t) + \phi_d))] - \right. \\ &\quad \left. \frac{y}{2} [I_x \sin(\omega t - (\phi(t) + \phi_d)) + \right. \\ &\quad \left. I_y \cos(\omega t - (\phi(t) + \phi_d))] \right] \exp(+i\omega t I_z) \right\} \quad (5.42) \end{aligned}$$

$$\begin{aligned}
&= \gamma \frac{I_0 \mu_0}{4a^2} \{ x [\cos(\omega t - (\phi(t) + \phi_d)) (I_x \cos \omega t + I_y \sin \omega t) - \\
&\quad \sin(\omega t - (\phi(t) + \phi_d)) (I_y \cos \omega t - I_x \sin \omega t) + \\
&\quad \cos(\omega t - (\phi(t) + \phi_d)) (I_x \cos \omega t + I_y \sin \omega t) + \\
&\quad \sin(\omega t - (\phi(t) + \phi_d)) (I_y \cos \omega t - I_x \sin \omega t)] + \\
&\quad y [\sin(\omega t - (\phi(t) + \phi_d)) (I_x \cos \omega t + I_y \sin \omega t) - \\
&\quad \cos(\omega t - (\phi(t) + \phi_d)) (I_y \cos \omega t - I_x \sin \omega t) - \\
&\quad \sin(\omega t - (\phi(t) + \phi_d)) (I_x \cos \omega t + I_y \sin \omega t) - \\
&\quad \cos(\omega t - (\phi(t) + \phi_d)) (I_y \cos \omega t - I_x \sin \omega t)] \} \tag{5.43}
\end{aligned}$$

$$\begin{aligned}
&= \gamma \frac{I_0 \mu_0}{4a^2} \{ x [I_x (\cos(\omega t - (\phi(t) + \phi_d)) \cos \omega t + \\
&\quad \sin(\omega t - (\phi(t) + \phi_d)) \sin \omega t + \\
&\quad \cos(\omega t - (\phi(t) + \phi_d)) \cos \omega t - \sin(\omega t - (\phi(t) + \phi_d)) \sin \omega t) + \\
&\quad I_y (\sin \omega t \cos(\omega t - (\phi(t) + \phi_d)) - \sin(\omega t - (\phi(t) + \phi_d)) \cos \omega t + \\
&\quad \sin \omega t \cos(\omega t - (\phi(t) + \phi_d)) + \sin(\omega t - (\phi(t) + \phi_d)) \cos \omega t)] + \\
&\quad y [I_x (\sin(\omega t - (\phi(t) + \phi_d)) \cos \omega t + \sin \omega t \cos(\omega t - (\phi(t) + \phi_d)) - \\
&\quad \sin(\omega t - (\phi(t) + \phi_d)) \cos \omega t + \sin \omega t \cos(\omega t - (\phi(t) + \phi_d))) + \\
&\quad I_y (\sin(\omega t - (\phi(t) + \phi_d)) \sin \omega t - \cos(\omega t - (\phi(t) + \phi_d)) \cos \omega t - \\
&\quad \sin(\omega t - (\phi(t) + \phi_d)) \sin \omega t - \cos(\omega t - (\phi(t) + \phi_d)) \cos \omega t)] \} \tag{5.44}
\end{aligned}$$

$$\begin{aligned}
\mathcal{H}_G^{\text{RF}} &= \gamma \frac{I_0 \mu_0}{4a^2} \{ x [I_x (\cos(\phi(t) + \phi_d) + \cos(2\omega t - (\phi(t) + \phi_d))) + \\
&\quad I_y (\sin(\phi(t) + \phi_d) + \sin(2\omega t - (\phi(t) + \phi_d)))] + \\
&\quad y [I_x (\sin(2\omega t - (\phi(t) + \phi_d)) + \sin(\phi(t) + \phi_d)) + \\
&\quad I_y (-\cos(2\omega t - (\phi(t) + \phi_d)) - \cos(\phi(t) + \phi_d))] \} . \tag{5.45}
\end{aligned}$$

So, dropping the ineffective high frequency terms, the gradient term of the rotating frame Hamiltonian can be written

$$\begin{aligned} \mathcal{H}_G^{\text{RF}} = & \gamma \frac{I_0 \mu_0}{4a^2} \{ x [I_x \cos(\phi(t) + \phi_d) + I_y \sin(\phi(t) + \phi_d)] + \\ & y [I_x \sin(\phi(t) + \phi_d) - I_y \cos(\phi(t) + \phi_d)] \} . \end{aligned} \quad (5.46)$$

The SWW-16 toggling frame values of I_x and I_y , as well as the rotating frame phase of each gradient pulse, are shown in Table 5.1. With this information, it is straightforward to write down the toggling frame gradient Hamiltonian, $\tilde{\mathcal{H}}_G(t)$. To calculate the gradient term of the average Hamiltonian, $\bar{\mathcal{H}}_G(t)$ is integrated over one SWW-16 cycle:

$$\bar{\mathcal{H}}_G^{(0)} = \frac{1}{t_c} \int_0^{t_c} \tilde{\mathcal{H}}_G(t_1) dt_1 . \quad (5.47)$$

Of course, $\tilde{\mathcal{H}}_G(t)$ is piecewise constant, so the integral in Equation 5.47 can be replaced by the sum over all the windows and $\bar{\mathcal{H}}_G^{(0)}$ calculated as follows:

$$\begin{aligned} \mathcal{H}_G^{(0)} = & \frac{1}{24\tau} \cdot \gamma \frac{I_0 \mu_0}{4a^2} \{ x [-I_z \cos(\pi + \phi_d) \tau + I_y \sin(\pi + \phi_d) \tau - \\ & I_z \cos(\pi + \phi_d) 2\tau - I_x \sin(\pi + \phi_d) 2\tau - \\ & I_z \cos(\pi + \phi_d) \tau - I_y \sin(\pi + \phi_d) \tau + \\ & I_z \cos \phi_d \tau - I_y \sin \phi_d \tau + \\ & I_z \cos \phi_d 2\tau - I_x \sin \phi_d 2\tau + \\ & I_z \cos \phi_d \tau + I_y \sin \phi_d \tau + \\ & I_z \cos \phi_d \tau + I_y \sin \phi_d \tau + \\ & I_z \cos \phi_d 2\tau - I_x \sin \phi_d 2\tau + \\ & I_z \cos \phi_d \tau - I_y \sin \phi_d \tau - \\ & I_z \cos(\pi + \phi_d) \tau - I_y \sin(\pi + \phi_d) \tau - \\ & I_z \cos(\pi + \phi_d) 2\tau - I_x \sin(\pi + \phi_d) 2\tau - \end{aligned}$$

$$\begin{aligned}
& I_z \cos(\pi + \phi_d) \tau + I_y \sin(\pi + \phi_d) \tau] + \\
& y [-I_z \sin(\pi + \phi_d) \tau - I_y \cos(\pi + \phi_d) \tau - \\
& I_z \sin(\pi + \phi_d) 2\tau + I_x \cos(\pi + \phi_d) 2\tau - \\
& I_z \sin(\pi + \phi_d) \tau + I_y \cos(\pi + \phi_d) \tau + \\
& I_z \sin \phi_d \tau + I_y \cos \phi_d \tau + \\
& I_z \sin \phi_d 2\tau + I_x \cos \phi_d 2\tau + \\
& I_z \sin \phi_d \tau - I_y \cos \phi_d \tau + \\
& I_z \sin \phi_d \tau - I_y \cos \phi_d \tau + \\
& I_z \sin \phi_d 2\tau + I_x \cos \phi_d 2\tau + \\
& I_z \sin \phi_d \tau + I_y \cos \phi_d \tau - \\
& I_z \sin(\pi + \phi_d) \tau + I_y \cos(\pi + \phi_d) \tau - \\
& I_z \sin(\pi + \phi_d) 2\tau + I_x \cos(\pi + \phi_d) 2\tau - \\
& I_z \sin(\pi + \phi_d) \tau - I_y \cos(\pi + \phi_d) \tau] \} , \tag{5.48}
\end{aligned}$$

which reduces to

$$\overline{\mathcal{H}}_G^{(0)} = \frac{2}{3} \cdot \gamma \frac{I_0 \mu_0}{4a^2} \{x \cos \phi_d + y \sin \phi_d\} I_z . \tag{5.49}$$

5.9.2 Horizontal Quadrupole Coil

The gradient Hamiltonian, \mathcal{H}_G , for the horizontal quadrupole coil can be written

$$\mathcal{H}_G = \gamma \mathbf{I} \cdot \mathcal{G}^t \cdot \mathbf{r} \tag{5.50}$$

$$= \gamma \left(-\frac{\mu_0}{2a^2} I(t) I_x x + \frac{\mu_0}{2a^2} I(t) I_z r_z \right) . \tag{5.51}$$

In this case, \mathcal{H}_G is transformed in to the rotating frame defined by the solenoid carrier frequency to yield:

$$\mathcal{H}_G^{\text{RF}} = -\gamma \frac{I_0 \mu_0}{4a^2} \{x [I_x \cos(\phi(t) + \phi_d) + I_y \sin(\phi(t) + \phi_d)]\} . \quad (5.52)$$

And, in a manner analogous to that of the previous section, $\mathcal{H}_G^{\text{RF}}$ is transformed into the toggling frame to yield $\tilde{\mathcal{H}}_G(t)$, which is then integrated over an SWW-16 cycle to yield the gradient term of the average Hamiltonian. For this arrangement of the quadrupole coil, $\overline{\mathcal{H}}_G^{(0)}$ is given by

$$\overline{\mathcal{H}}_G^{(0)} = \frac{2}{3} \cdot \gamma \frac{I_0 \mu_0}{4a^2} \{-x \cos \phi_d\} I_z . \quad (5.53)$$

References

- [1] G. Ödberg and L. Ödberg, *J. Magn. Reson.* **16**, 342 (1974).
- [2] P. Stilbs, *Progr. NMR Spectr.* **19**, 1 (1987).
- [3] M. Bloom, E. Enga, and H. Lew, *Can. J. Phys.* **45**, 148 (1967).
- [4] D. S. Webster and K. H. Marsden, *Rev. Sci. Instrum.* **45**, 1232 (1974).
- [5] P. Mansfield and P. G. Morris, in "Advances in Magnetic Resonance," Supplement 2 (J. S. Waugh, Ed.), Academic Press, New York, 1982.
- [6] P. Mansfield, in "Physics of NMR Spectroscopy in Biology and Medicine," Proceedings, International School of "Enrico Fermi," Course C (B. Maraviglia, Ed.), pp. 345-369, North-Holland, Amsterdam, 1988.
- [7] G. Schauss, B. Blümich, and H. W. Speiss, *J. Magn. Reson.* **95**, 437 (1991).
- [8] W.-K. Rhim, D. D. Elleman, L. B. Schreiber, and R. W. Vaughan, *J. Chem. Phys.* **60**, 4595 (1974).
- [9] H. M. Cho, C. J. Lee, D. N. Shykind, and D. P. Weitekamp, *Phys. Rev. Lett.* **55**, 1923 (1985).
- [10] (a) L. Quiroga and J. Virlet, *J. Chem. Phys.* **81**, 4774 (1984); (b) M. E. Stoll, W.-K. Rhim, and R. W. Vaughan, *J. Chem. Phys.* **64**, 4808 (1976); (c) E. D. Ostroff and J. S. Waugh, *Phys. Rev. Lett.* **16**, 1097 (1966).

- [11] G. C. Chingas, J. B. Miller, and A. N. Garroway, *J. Magn. Reson.* **66**, 530 (1986).
- [12] A. Kumar, D. Welti, and R. Ernst, *J. Magn. Reson.* **18**, 69 (1975).
- [13] W. A. Edelstein, J. M. S. Hutchison, G. Johnson, and T. Redpath, *Phys. Med. Biol.* **25**, 751 (1980).
- [14] D. N. Shykind, Ph. D. Thesis, University of California, Berkeley (1989).
- [15] R. R. Ernst, G. Bodenhausen, and A. Wokaun, "Principles of Nuclear Magnetic Resonance in One and Two Dimensions," Clarendon Press, Oxford, 1987.
- [16] M. H. Werner, J. A. Marohn, D. N. Shykind, and D. P. Weitekamp, "33rd Experimental NMR Spectroscopy Conf. Abstracts," p. 258 (1992).
- [17] J. A. Marohn, personal communication.
- [18] J. B. Miller and A. N. Garroway, *J. Magn. Reson.* **82**, 529 (1989).
- [19] D. G. Cory, J. B. Miller, R. Turner, and A. N. Garroway, *Mol. Phys.* **70**, 331 (1990).
- [20] D. G. Cory, A. N. Garroway, and J. B. Miller, *J. Magn. Reson.* **87**, 202 (1990).
- [21] R. W. Vaughan, D. D. Elleman, L. M. Stacy, W.-K. Rhim, and J. W. Lee, *Rev. Sci. Instrum.* **43**, 1356 (1972).
- [22] S. L. Dieckman, P. Rizo, N. Gopalsami, J. P. Heeschen, and R. E. Botto, *J. Am. Chem. Soc.* **114**, 2717 (1992).

Chapter 6

Experimental Apparatus

6.1 Introduction

This chapter describes the novel imaging probes constructed for multiple-pulse rf gradient imaging. These probes required a somewhat different procedure for tuning and matching than that used to tune and match conventional probes. A signal-to-noise ratio comparison of the 2-D imaging probe and a conventional solid-state spectroscopy probe is discussed, as is an NMR experiment to measure the strength of the gradient coil. The procedure used to adjust the phases and amplitudes of the rf pulses is outlined. This procedure was used at the start of every imaging session. Finally Q-switching, the method used to actively decouple the solenoid and quadrupole circuits, is discussed. This is contrasted with previous decoupling techniques. The PIN diodes utilized are described, as is the diode driver circuitry, and Q-switching times under various conditions are presented.

6.2 Solids Imaging Probes

6.2.1 General Description

Two probes were constructed for the experiments described in this dissertation. The first is capable of only 1-D imaging, while the second is capable of 1- and 2-D imaging. Both finished probes have an outer diameter of 100 mm and are able to fit in the 200 MHz

Nalorac magnet associated with the homebuilt spectrometer in the Weitekamp laboratory. The probes also fit in the magnet of a Bruker MSL200 spectrometer, provided that the room temperature shims are removed. The probe base and shield are aluminum, with 3.2 mm wall tubing used for the shield.

A photograph of the 2-D imaging probe, with its outer aluminum shield removed, is shown in Figure 6.1. Copper clad circuit board was used as shielding between the quadrupole coil resonant circuit (visible in the photograph) and the solenoid coil resonant circuit (not visible in the photograph). Copper clad circuit board (for the 1-D imaging probe) or 3.2 mm brass plate (for the 2-D imaging probe) was also used as shielding between the coils and the rest of the probe circuitry. This shield was supported by means of three brass threaded rods. The shield between the two resonant circuits was also attached to the threaded rods. For the stability of the probe tuning, it was necessary that this shield be rigid.

A photograph of the coils of the 2-D imaging probe is shown in Figure 6.2. The solenoid coils of both probes were free standing. The solenoid coil used in the 1-D probe was eight turns of 2 mm wide flat copper wire wound to have an inner diameter of 8 mm and a length of 25 mm. This solenoid coil had a Q of 100. Several solenoid coils were used in the 2-D probe, almost all of which were 7 to 9 turns of flat copper wire and approximately 25 mm in length. The inner diameter of these coils varied from about 4 mm to 7 mm. The Q of these coils was typically 75.

The quadrupole coil of the 1-D probe was also free standing. This four-wire approximation to an ideal quadrupole coil consisted of two rectangular loops of 16 gauge copper magnet wire, connected in parallel, and had a diameter of 28 mm and a length of 45 mm.

An eight-wire approximation to the quadrupole coil was chosen for the 2-D probe to improve the linearity of the field gradient [1]. This coil was partially supported by

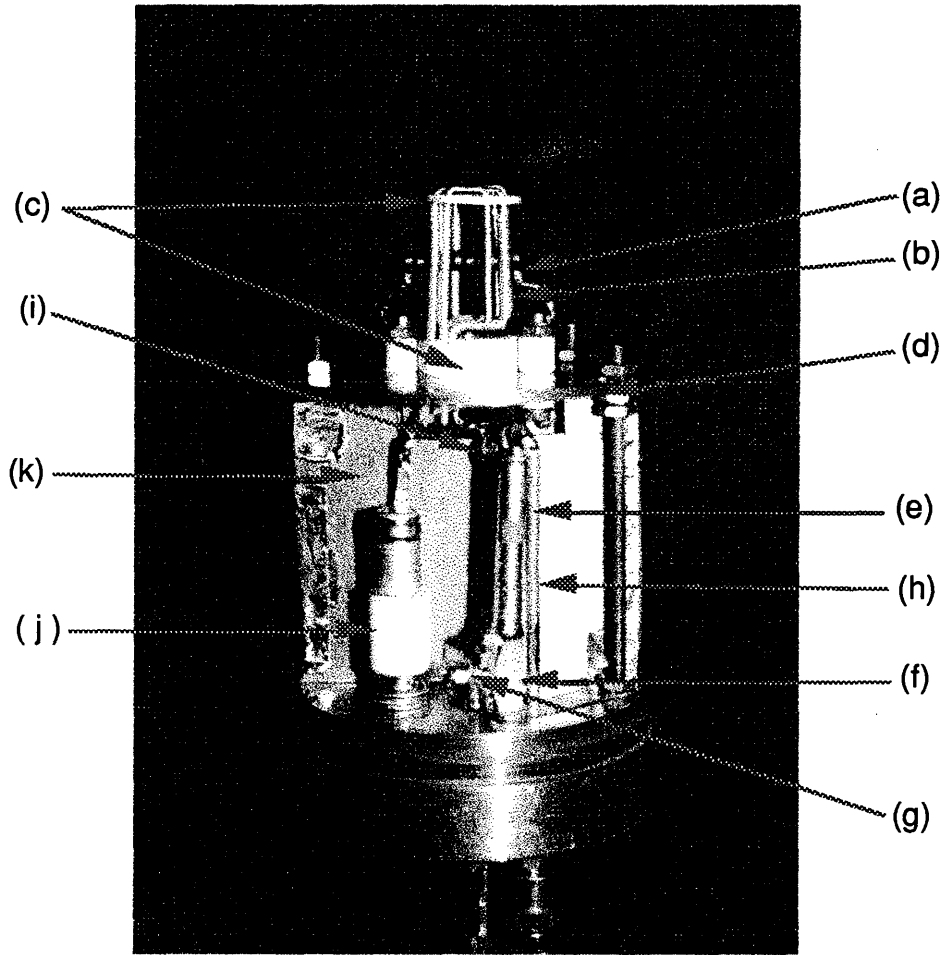


Figure 6.1: Probe for 2-D imaging, shown with its outer aluminum shield removed. In this photograph the probe is oriented with the quadrupole circuit facing forward. The free-standing solenoid coil (a) wound of 2 mm wide copper strip and the quadrupole coil (b) with its Macor spacers (c) are visible on top. A brass plate (d) shields the coils from the rest of the tuning and matching circuitry. Below the brass plate, the Voltronics matching capacitor C_M (e) on its Nylon standoff (f) can be seen on the right-hand side. Two M/A-COM PIN diodes (g) are inserted between this capacitor and ground. A small copper plate is used as a heat sink for the diodes. The rf choke is partially hidden behind the diodes and the Nylon standoff. RF enters the probe body through the semirigid coaxial cable (h) adjacent to C_M . The fixed Centralab ceramic capacitor (i) inserted between C_M and the quadrupole coil is visible just above and behind the top of this coaxial cable and the top of C_M . The Polyflon tuning capacitor C_T (j) can be seen on the left-hand side. C_T is connected directly to the coil. Copper clad circuit board (k) provides shielding between the quadrupole and the solenoid resonant circuits and, in this photograph, obscures the solenoid resonant circuit from view.

means of two Macor spacers, as shown in Figure 6.2. The bottom Macor spacer was approximately 9.5 mm thick and held the leads securely in place. The top Macor spacer was approximately 1.6 mm thick and held the eight wires at 30° , 60° , 120° , 150° , 210° , 240° , 300° , and 330° around a cylinder of diameter 20 mm. The eight wires were four rectangular loops, two smaller loops and two larger loops. Each small loop was connected in series with its neighboring larger loop and the two pairs of loops were then connected in parallel. The coil was wound of 16 gauge tinned copper wire fitted with Teflon sleeving at the portions where the leads were in close proximity with one another or other surrounding metal. The length of this quadrupole coil was approximately 35 mm.

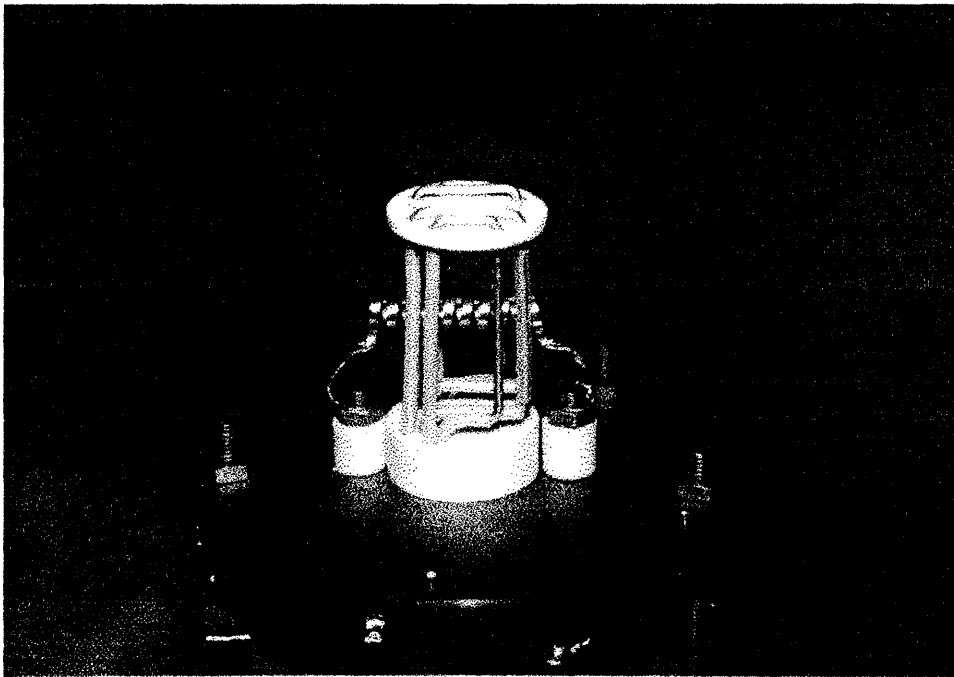


Figure 6.2: Detail of the rf coils. This shows the quadrupole coil and one of the solenoid coils used for 2-D imaging. The quadrupole coil consists of four rectangular loops of wire. The two loops appearing in front of the solenoid coil in the photograph are connected in series, as are the two loops behind the solenoid coil. The two pairs of loops are then connected in parallel.

6.2.2 Resonant Circuits

The rf coils were tuned and matched by means of a series-tuned, parallel-matched resonant circuit. For each resonant circuit, the tuning capacitor was a Polyflon NRP-VC-10-12-36 series VC/RF high voltage non-magnetic trimmer capacitor. These have a capacitance range of 0.8 to 10 pF, a peak working voltage of 6 kV, and Teflon dielectric. The matching capacitor was a Voltronics NMTM120CE non-magnetic precision trimmer capacitor. These have a capacitance range of 2.0 to 120 pF, a peak working voltage of 1 kV, and glass dielectric.

Several solenoid coils were used; all were 7 to 9 turns, approximately 25 mm in length, and varied in inner diameter between 4 mm and 8 mm. In order to tune these to 200 MHz it was necessary to reduce the tuning capacitance. This was accomplished by placing three to four Centralab series 850 ceramic capacitors in series with C_T . The Centralab capacitors used have a fixed capacitance of 3, 5, or 10 pF and a working voltage of 5 kV. Because of their lower inductance, the quadrupole coils used could easily be tuned to 200 MHz without recourse to a similar stack of capacitors. However, it was usually necessary to add a fixed capacitor between C_M and the coil. This was a Centralab series 850 capacitor with fixed capacitance of between 5 and 40 pF, depending on the coil. To properly tune and match the solenoid coils used in the 2-D imaging probe, it was necessary to add a similar fixed capacitor between C_M and the coil. In general, the capacitance needed to tune and match a new coil was determined by trial and error, although some helpful guidelines are given in Appendix C. Lumped element analysis of tuned circuits at 200 MHz is inadequate for calculating required component values due to the fact that electronic components and interconnections are difficult to model accurately at VHF.

A photograph of the M/A-COM diodes in the solenoid resonant circuit of the 2-D

imaging probe is shown in Figure 6.3. To accommodate the PIN diodes necessary for Q-switching, a hollow Nylon standoff was machined to raise the matching capacitor of both the solenoid and the quadrupole circuits off the ground plane. This standoff also enabled access to the screw-driver adjust beneath the capacitor. For the 1-D probe, the DC bias pulses to the diodes entered the probe body through thin coaxial line fed through the support tube of the probe. These coaxial lines were secured to the semirigid coaxial cable used to carry the rf into the probe body. For the 2-D imaging probe, the bias pulses entered the probe body through semirigid coaxial cable mounted directly to the probe base. This arrangement was favorable as it led to increased stability of the probe matching. A 1 or 2.2 μH inductor was used as an rf choke to block rf from the DC bias lines and the diode driver circuitry. Some of these chokes were hand wound according to the specifications in the ARRL handbook for well-designed rf chokes with low parasitic capacitance [2].

6.2.3 Low Power Tuning and Matching

Once Q-switching was implemented, it was necessary to tune and match the imaging probes using a somewhat different procedure than that used to tune and match standard probes. In particular, it was necessary to forward bias the diodes of a given resonant circuit during tuning and matching. The configuration used for low-power tuning and matching is shown in Figure 6.4. Following probe alterations, such as replacement of the solenoid coil or the diodes, the probe was roughly tuned and matched at low power and final adjustments were then made at high power.

During low power tuning and matching the diodes of the circuit being tuned were forward biased continuously, so it was necessary to tune the solenoid and quadrupole circuits separately. Usually, there was some interaction between the coils so that, initially, changing the tuning and matching of one circuit slightly changed the tuning and

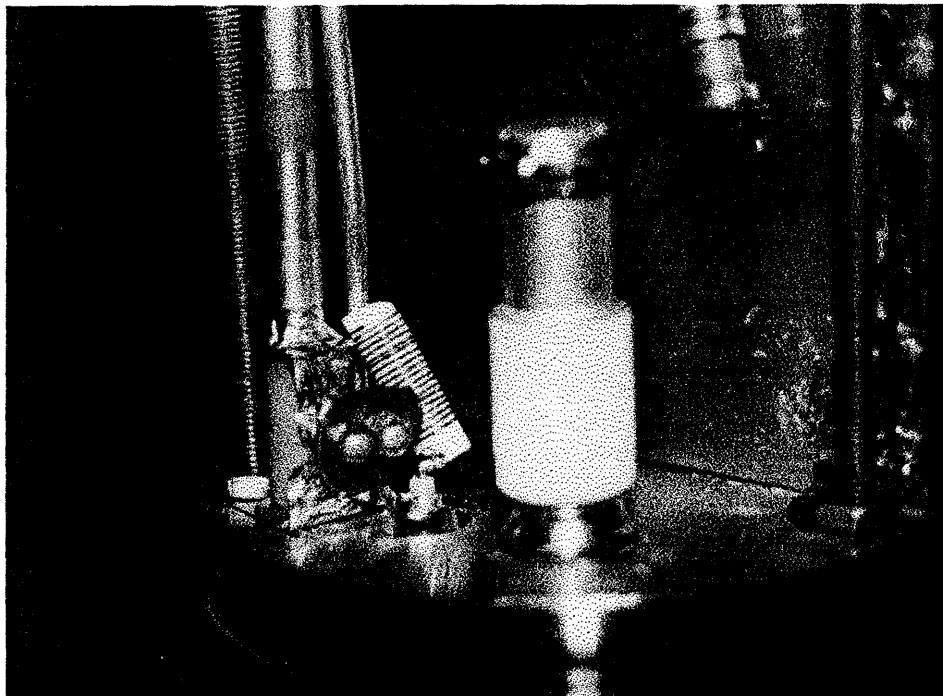


Figure 6.3: Two M/A-COM diodes, in parallel, are shown in the matching network of the solenoid resonant circuit. Brass nuts attach a small copper plate to the threaded heat sink of the diodes (which, for these diodes, is isolated from both the anode and cathode). The hand-wound rf choke can be seen connecting the DC bias input to the top of the diodes.

matching of the other. However, it was almost always sufficient to tune and match the solenoid circuit first, then tune and match the quadrupole circuit, and finally readjust the solenoid circuit. These final readjustments to the solenoid circuit did not generally cause a noticeable change to the tuning and matching of the quadrupole circuit.

6.2.4 High Power Tuning and Matching

For high power tuning and matching, the probe and spectrometer were set up as for an imaging experiment. A pulse sequence was used consisting of a continuous train of $3 \mu\text{s}$ rf pulses and $4 \mu\text{s}$ DC bias pulses interspersed with delays of a few hundred μs .

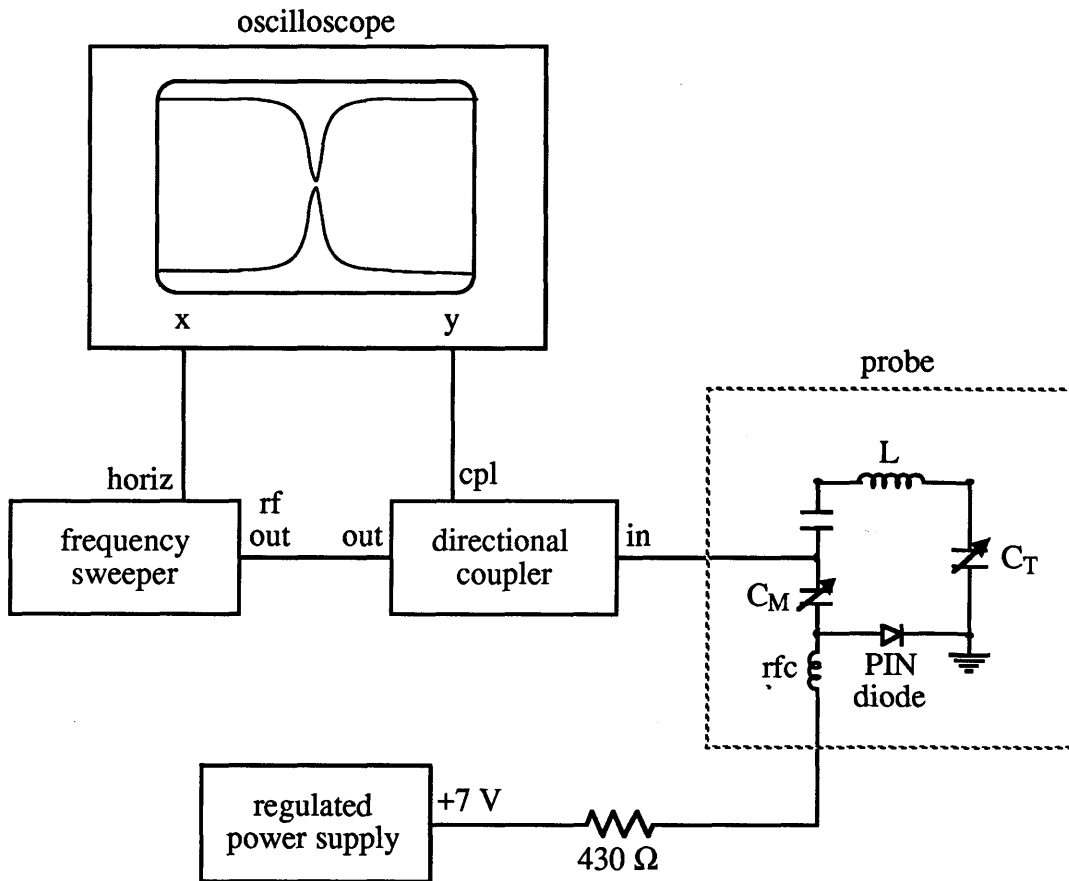


Figure 6.4: Configuration used for low power tuning and matching of the imaging probes. The frequency synthesizer is a PTS 500 set to 198.34 MHz (for imaging on the homebuilt spectrometer) or 200.13 MHz (for imaging on the MSL200). The frequency sweeper is a Wavetek 1062, the power supply a Lambda LM-F5M, and the directional coupler a MiniCircuits ZDC-20-3, with 20 dB attenuation between the couple port and the in and out ports.

The DC bias pulse began 1 μs before each rf pulse and continued for the duration of the rf pulse. The tuning and matching capacitors of a resonant circuit were adjusted while observing the reflected voltage of that circuit using a directional coupler. In general, it was possible to obtain a forward to reflected voltage ratio of at least 10:1, and often 20:1 was obtained. Again, the solenoid circuit was adjusted first, followed by the quadrupole circuit, and finally the solenoid circuit was readjusted. The matching was somewhat dependent on sample and pulse sequence duty cycle.

6.3 S/N Comparison of the Q-Switched Imaging Probe and a Standard Solids Probe

To determine whether Q-switching was adversely affecting the signal-to-noise ratio (S/N) of the imaging probe, a comparison was made of the performance of the 2-D imaging probe and a standard (homebuilt) ^1H solids probe. Spectra of 2 and 16 signal averages were obtained using both a one-pulse sequence and the line-narrowing pulses of SWW-16. Adamantane packed into a cylinder of 2.3 mm diameter and 6.5 mm length was the test sample. The spectra were obtained on the Bruker MSL200 and are shown in Figures 6.5 to 6.8.

The $\pi/2$ time used in all experiments was 3.1 μs . The spectral width for the one-pulse experiments was 50 kHz, and the cycle time used for the SWW-16 experiments was 304.8 μs , corresponding to a spectral width of 3280.8 Hz. The S/N values are shown in Table 6.1.

In these experiments, the receiving coil geometry was the same for both probes (i.e., both had solenoid coils). In addition, the same sample, magnet, preamplifier, probe temperature, and receiver bandwidth were used and the same nucleus observed. Therefore, the ratio of the expected imaging probe S/N to the expected standard probe S/N

probe	onepulse S/N		SWW-16 S/N	
	NS = 2	NS = 16	NS = 2	NS = 16
standard	11	22	80	204
imaging	9.5	31	87	247

Table 6.1: Comparison of signal-to-noise ratios for a standard solids probe and a Q-switched imaging probe. The results from a simple one-pulse experiment and an SWW-16 experiment with 2 and 16 signal averages (NS) are shown.

following a 90° pulse is given by

$$\frac{(S/N)_{\text{img}}}{(S/N)_{\text{std}}} = \frac{\eta_{\text{img}} (Q_{\text{img}} V_{C\text{img}})^{1/2}}{\eta_{\text{std}} (Q_{\text{std}} V_{C\text{std}})^{1/2}}, \quad (6.1)$$

where η_n , Q_n , and V_{Cn} are the filling factor (sample volume divided by coil volume), quality factor, and volume, respectively, of coil n [3, 4, 5]. In this case, then, the signal-to-noise ratio of the imaging probe to the standard probe is expected to be

$$\frac{(S/N)_{\text{img}}}{(S/N)_{\text{std}}} = \frac{0.88 \text{ cm}^3 (75 \cdot 0.53 \text{ cm}^3)^{1/2}}{0.53 \text{ cm}^3 (200 \cdot 0.88 \text{ cm}^3)^{1/2}}, \quad (6.2)$$

which is about 80%. Equation 6.1 was also assumed to be valid for comparing the SWW-16 results, given that the same pulse sequence timing was used for both probes. In fact, for all experiments conducted, the S/N obtained with the imaging probe was at least 80% of that obtained with the standard probe, and for three of the four experiments it was greater than 100%. This is an indication that Q-switching is not adversely affecting the signal-to-noise ratio.

6.4 Gradient Strength of the Vertical Quadrupole Coil

The inhomogeneity of the transverse magnetic field B_1 within the sample can be measured by means of a 1-D nutation sequence, i.e., a train of pulses of identical phase

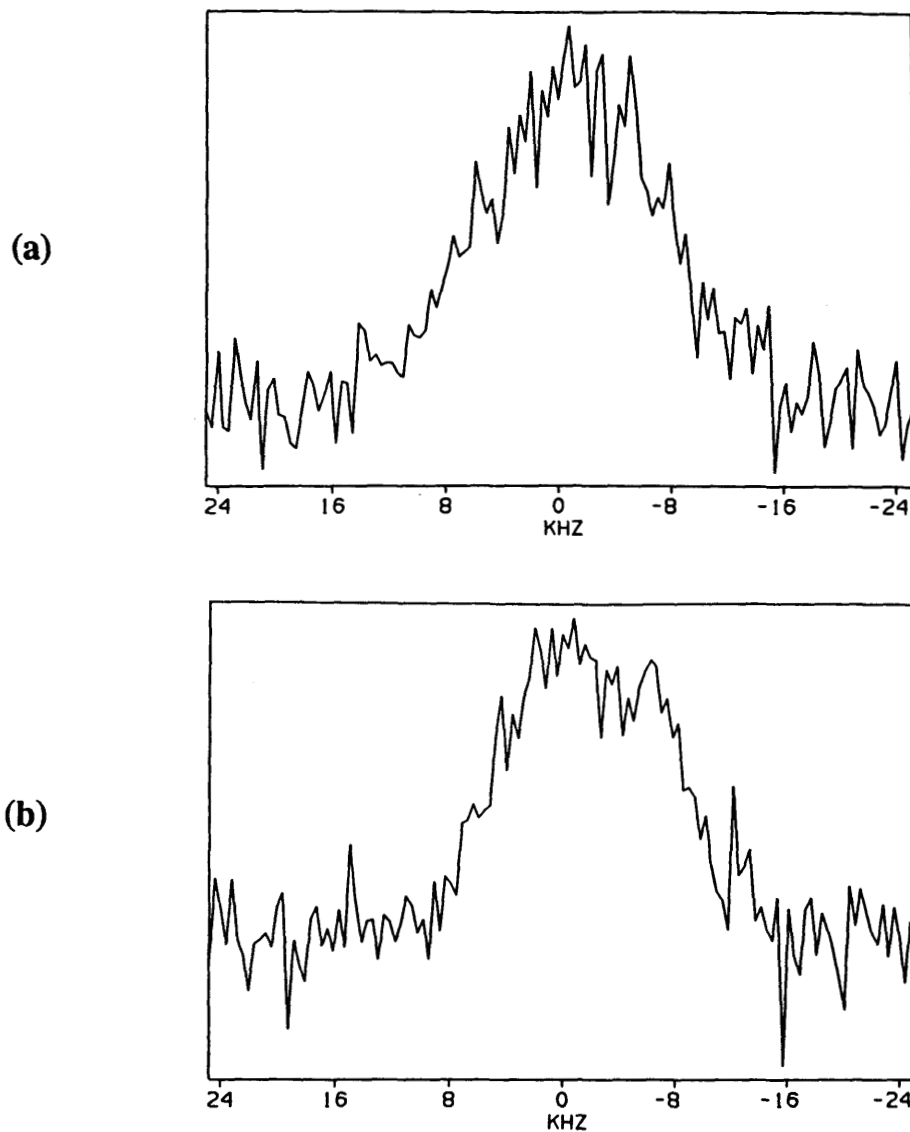


Figure 6.5: A signal-to-noise comparison of two signal averages of a one-pulse experiment. (a) The results obtained with a standard ^1H solids probe. (b) The results obtained with the Q-switched 2-D imaging probe. The sample used in this and the following figures was adamantane packed into a cylinder of 2.3 mm diameter and 6.5 mm length.

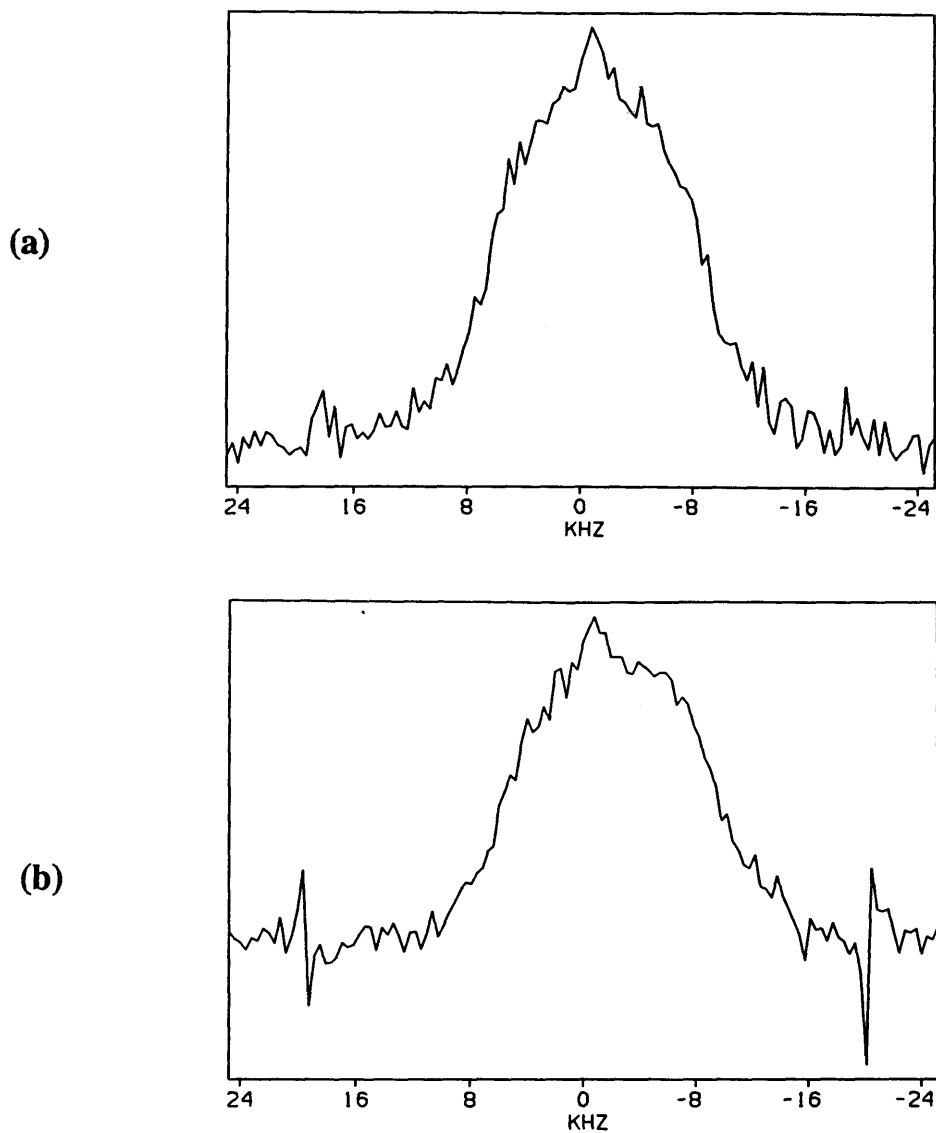


Figure 6.6: A signal-to-noise comparison of 16 signal averages of a one-pulse experiment. (a) The results obtained with a standard ^1H solids probe. (b) The results obtained with the Q-switched 2-D imaging probe. The glitches noticeable in the spectra obtained with the imaging probe (appearing at ± 20 kHz for the one-pulse spectra and ± 400 Hz for the SWW-16 spectra) were noticed intermittently in the imaging experiments described in this dissertation. Other MSL200 users have noticed similar glitches in their data, so they are most likely due to the spectrometer and not the imaging probe.

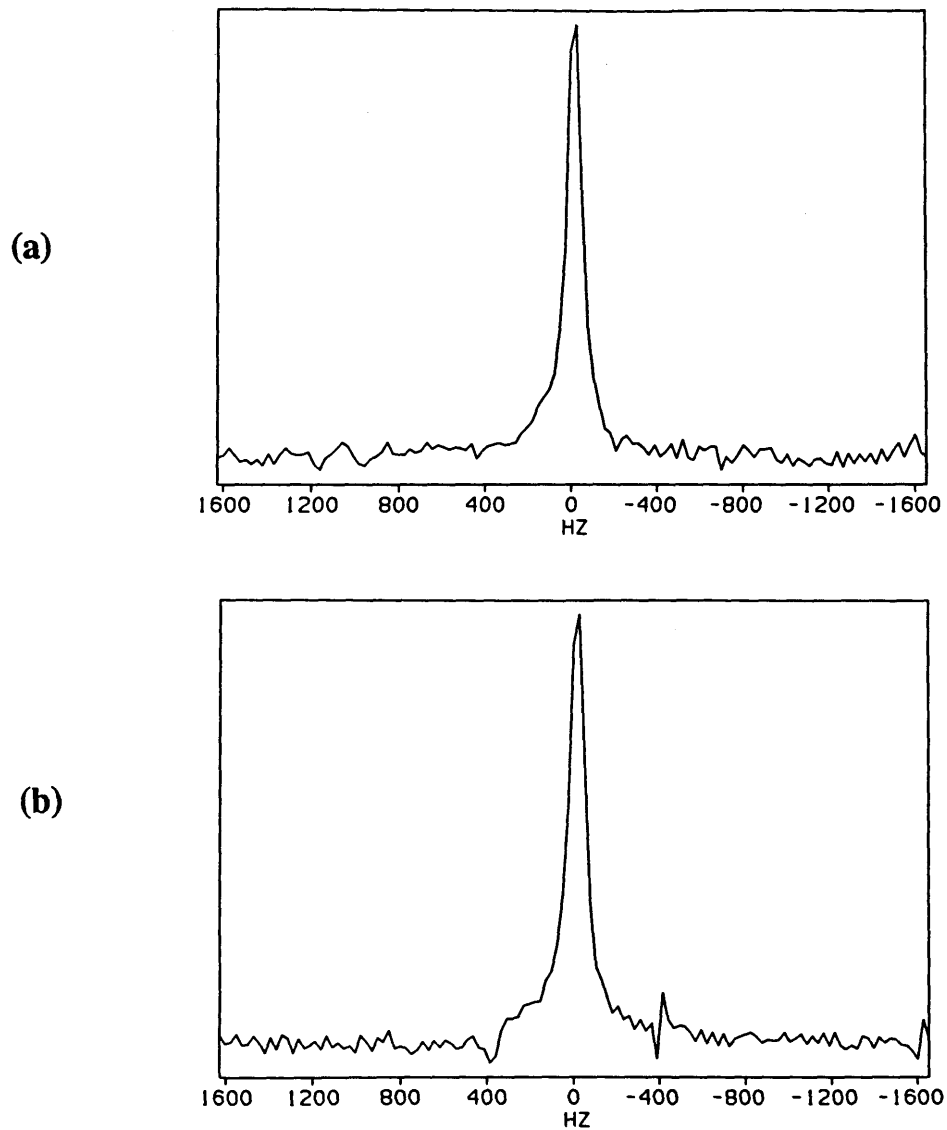


Figure 6.7: A signal-to-noise comparison of two signal averages of SWW-16. (a) The results obtained with a standard ^1H solids probe. (b) The results obtained with the Q-switched 2-D imaging probe.

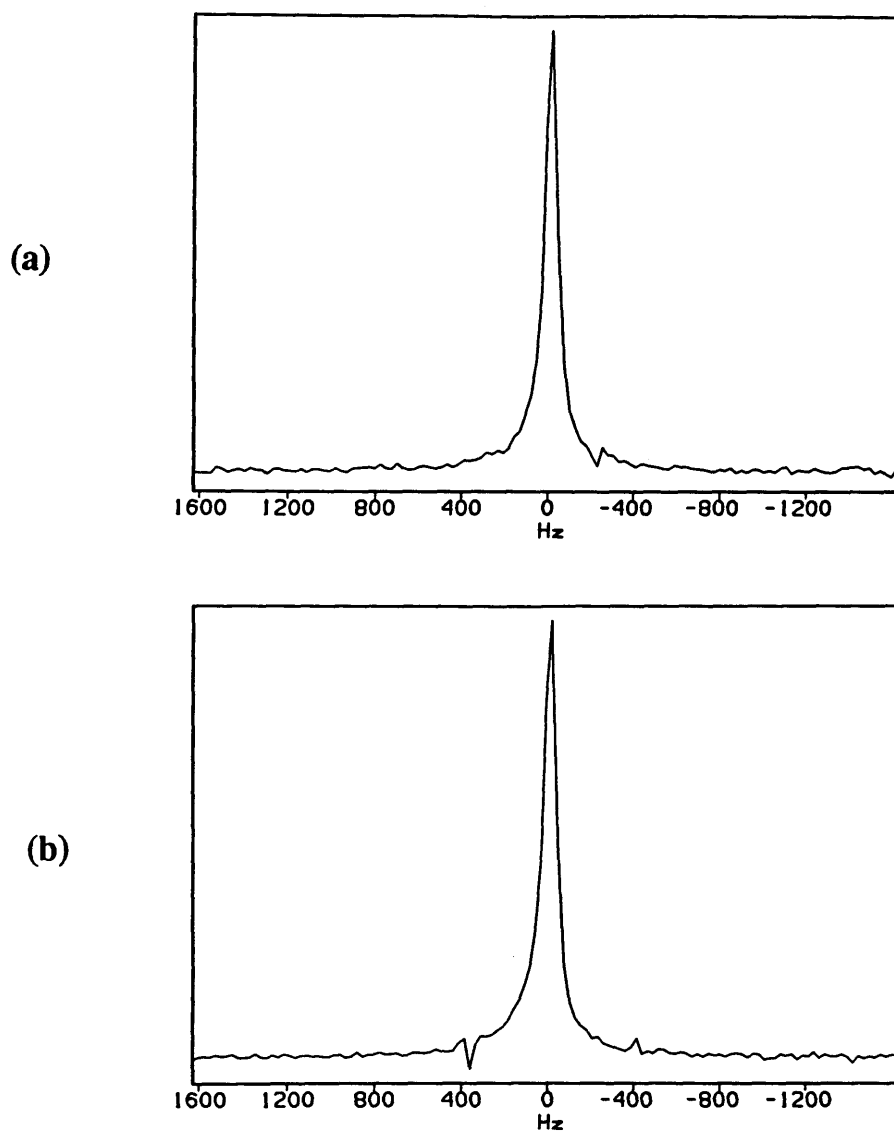


Figure 6.8: A signal-to-noise comparison of 16 signal averages of SWW-16. (a) The results obtained with a standard ^1H solids probe. (b) The results obtained with the Q-switched 2-D imaging probe.

and amplitude [6, 7]. When the pulses are delivered on, or very near, resonance and the magnetization is sampled after every pulse, the nuclei appear to precess about the rotating frame axis defined by the rf phase of the pulses with a nutation frequency proportional to the B_1 field strength. Inhomogeneity in B_1 appears as a spread in the observed nutation frequency. Therefore, applied to a liquid sample so that internal interactions do not dominate the effects of rf inhomogeneity, this nutation sequence can be used to measure the strength of the rf gradient.

As discussed in Chapter 5, the components of the field strength inside the vertical quadrupole coil are

$$B_{1x} = \mu_0 \frac{I(t)}{2a^2} x \quad (6.3)$$

and

$$B_{1y} = -\mu_0 \frac{I(t)}{2a^2} y. \quad (6.4)$$

Thus, the magnitude of the field strength B_1 is

$$B_1 = \mu_0 \frac{I(t)}{2a^2} [x^2 + y^2]^{1/2}. \quad (6.5)$$

The nutation experiments described below determine only the magnitude of B_1 , since nutation occurs about an axis in the transverse (xy) plane so that positive and negative nutation frequencies are indistinguishable. Thus, the rf field strength at a given point is proportional to r , where $r = (x^2 + y^2)^{1/2}$ is the distance in the xy plane from the center of the gradient coil to that point.

A series of nutation experiments was performed on a phantom of four capillary tubes filled with 10 mm of water and arranged as shown in Figure 6.9. These experiments were performed before the solenoid coil was added to the probe.

As expected, the nutation spectra showed an anti-phase doublet of quartets with peaks placed symmetrically about the carrier frequency. In each spectra, four nutation frequencies, corresponding to the four samples of water, were observed. Several gradient

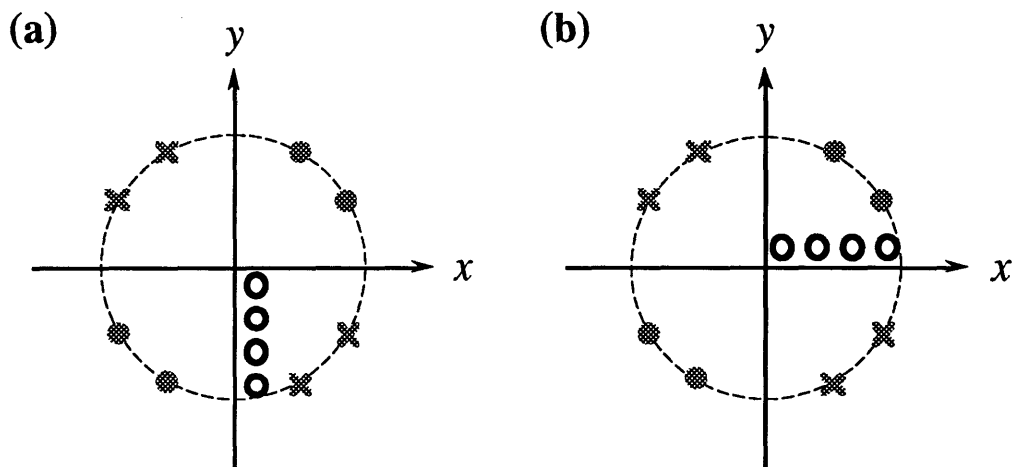


Figure 6.9: Four-Point phantom for measuring gradient strength. The four samples of water extended 10 mm in the z direction. Two arrangements, (a) and (b) were used in the nutation experiments.

duty cycles were used for each set of experiments, where the duty cycle was altered by changing both pulse and delay lengths. The observed nutation frequencies, ν_{obs} , were corrected for the gradient duty cycle. The corrected nutation frequencies, ν_1 , plotted as a function of the radial distance, r , of the water samples from the center of the gradient coil are shown in Figure 6.10. The gradient strength is determined from the slope divided by $\gamma/2\pi$, which for ^1H 's is 4.258 kHz/G. The observed gradient strength for this coil, driven with 290 W rf pulses, is 3.8 ± 0.3 G/cm. A gradient of this size used in SWW-16, assuming a typical gradient duty factor of 40% and spectral width of 4 kHz, would spread a 0.6 cm long sample across the full spectral width.

6.5 Tuning the Spectrometer

For a multiple-pulse line-narrowing sequence to work properly, it is necessary that the phases and amplitudes of the rf pulses be accurately adjusted. The standard procedure for adjusting the rf phases and amplitudes [6, 8, 9] was used on the rf channel providing the pulses to the solenoid coil and is summarized below.

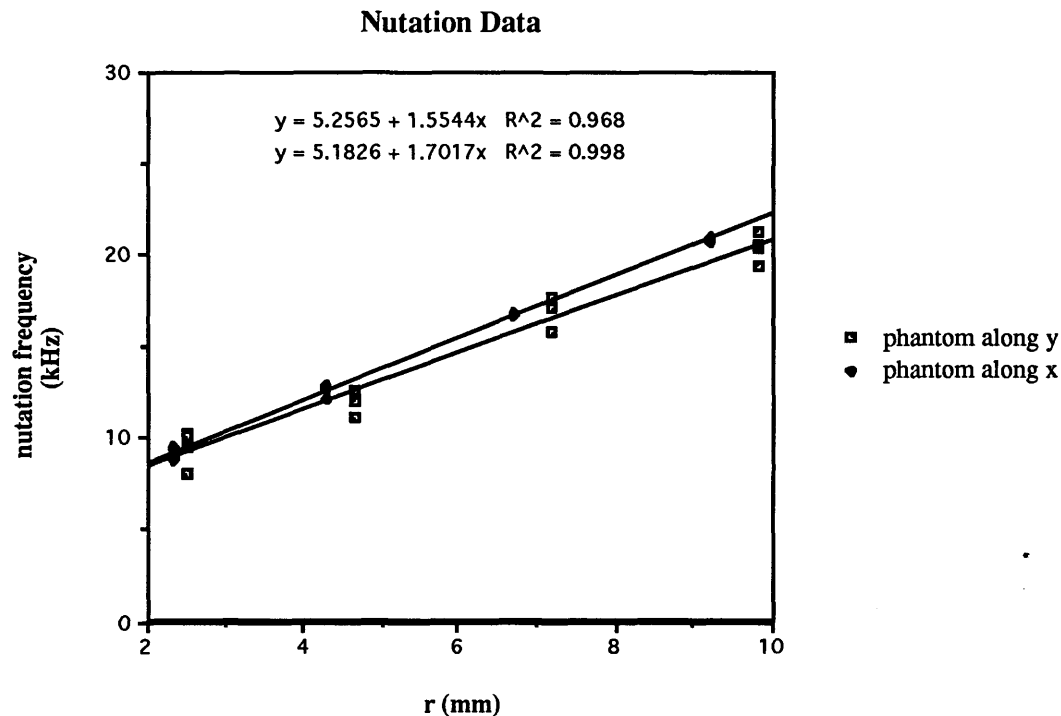


Figure 6.10: Four-point phantom nutation data.

A one-pulse experiment on water was used to shim the magnet, as was occasionally necessary, and to determine the exact resonance frequency. The spectrometer was set to the resonance frequency, and the receiver phase was adjusted so that all of the signal was in either the real or the imaginary channel. Next, four separate nutation (flip-flip) experiments were performed to adjust independently the amplitudes of the x , \bar{x} , y , and \bar{y} pulses. The proper amplitude to give a 90° pulse of a given length was identified by the time domain signal of the nutation experiment. The rf inhomogeneity of the solenoid coil was also determined using a nutation sequence. The observed inhomogeneity was typically 2 to 3 per cent over a cylindrical sample volume 5 mm in diameter and length.

Four versions of the pulse sequence described by Haubenreisser and Schnabel [9] were used to adjust the phase of y relative to that of x , \bar{x} relative to that of y , \bar{y} relative to that of \bar{x} , and as a check \bar{y} relative to that of x . Several iterations of this cycle were

sometimes necessary in order to obtain the proper quadrature phases.

A flip-flop (MW-2) sequence on water was used to determine the effects of phase transients (the asymmetric variety are not averaged out by the pulse sequences used for imaging, and are a function of probe tuning) [6, 8]. By performing MW-2 at various resonance-offset frequencies and plotting the observed resonance offset as a function of the actual resonance offset, a straight line is obtained whose y -intercept is a measure of the phase transient effects. Ideally, the y -intercept is zero. As long as its magnitude is less than the narrowed linewidths of the solids to be studied, phase transient effects should not interfere with the multiple-pulse line narrowing. Phase transient effects measured in this way varied from 100 Hz on a bad day to 0.3 Hz on a very good day, and were typically in the range of 20–50 Hz.

The phases and amplitudes of the rf pulses used to drive the gradient coil were much less critical. These were usually adjusted while monitoring the 30 MHz output of the quadrature generator with a vector voltmeter.

6.6 Decoupling the Solenoid and Quadrupole Circuits

Multiple-pulse rf gradient imaging requires operating several tuned rf circuits tuned to identical frequencies in close proximity to each other. Capacitive and inductive coupling between the circuits cause their resonance frequencies to “split” so that it is generally not possible to tune all the circuits to the same frequency. Another aspect of coupling is that the rf field in one coil induces an alternating current in the second coil by induction. Thus, the sample in effect sees a weak pulse from the unintended coil and a diminished pulse from the intended coil.

With hopes that the nominal orthogonality of the solenoid and quadrupole coils would provide sufficient decoupling between their resonant circuits, the 1-D imaging probe was

originally constructed with no means of active decoupling. The manifestation of coil coupling most detrimental to the multiple pulse imaging techniques used here is the disturbance of the rf field homogeneity of the solenoid coil by the presence of the rf gradient coil. Nutation experiments, like those used to determine the gradient strength of the vertical quadrupole coil, were used to determine whether the quadrupole coil was spoiling the solenoid rf homogeneity. The phantom used was a pair of capillary tubes filled to a few millimeters with water and placed side-by-side in the solenoid coil. The solenoid coil was used to deliver the rf pulse train and to detect the NMR signal. The nutation spectra obtained did indeed show peak splitting, indicating that the quadrupole coil was spoiling the homogeneity of the solenoid field.

Results from a series of 1-D images taken with increasing gradient strengths also indicated that the quadrupole coil was driving the solenoid coil. As the gradient strength was increased, the dominant effect was to move the center of the image out towards the Nyquist frequency rather than to spread the image out across the spectral width. This can be explained by the gradient pulses driving the solenoid to produce homogeneous pulses in the windows.

These results indicated that further measures needed to be taken to decouple the solenoid and quadrupole circuits. The problem of coupled rf coils has arisen previously in NMR probes using separate transmit and receive coils. This is frequently the case in *in vivo* applications in which a surface coil is used as the receive coil. In such probes problems associated with coil coupling plague both the transmit and receive portions of the NMR experiment. Problems that interfere with reception include the following:

1. The presence of a resonant transmit coil detunes the receive coil.
2. If both the receive and transmit coils are tuned and matched, noise currents flowing in the transmit coil induce noise currents in the receive coil by way of the mutual

inductance between the coils, causing extra noise in the signal [14].

3. The tuning of the receive coil is very dependent on the relative orientation and coupling of the two coils.

The primary difficulty associated with transmission is that the current induced in the receive coil produces a field which opposes and distorts the rf B_1 field applied by the transmit coil. This means that the desired spatial distribution of pulse angles will not be produced.

6.7 Previous Decoupling Schemes

Several schemes have been proposed to cope with the problems of inductive coupling between coils in a multi-coil probe. Quite a few of these are discussed by Bendall *et al.* [18]. Of these, all the “successful” methods have essentially relied on the principle that a large impedance in series with a coil prevents induced current from flowing in the coil [13]. This largely eliminates the inductive coupling, but has practical limitations which are described below.

6.7.1 “Orthogonal” Coils

One solution to the decoupling problem has been to place the rf coils so that their rf magnetic fields are orthogonal and to make the transmit coil much larger than the receive coil. However, in order to use this method to reduce interactions to a tolerable level, a high degree of accuracy is required. This is especially tricky when one coil has an inhomogeneous rf distribution. Furthermore, while an orthogonal orientation may minimize interactions, it does not eliminate them.

6.7.2 Crossed Diodes

Another solution, originally used by Bendall [21], was to put crossed diodes in the probe circuit in the same way that they are used in the passive transmit-receive switch of the spectrometer itself. The basic idea is that in the presence of some minimum rf voltage the diodes have a low impedance (but also a low Q) and conduct freely. Below this minimum voltage the diodes have a high impedance and so do not conduct. Thus, series crossed diodes are used in the transmit coil circuit. In the presence of an rf pulse the diodes conduct. In the absence of an rf pulse the diodes do not conduct and part of the circuit is removed, detuning the circuit. On the other hand, parallel (shunt) crossed diodes are used in the receive coil circuit. Here, in the presence of an rf pulse the diodes conduct, removing part of the circuit and detuning the coil. In the absence of an rf pulse, the diodes do not conduct and the coil can be properly tuned and matched. Crossed diodes have been used by Styles *et al.* to decouple concentric surface coils [15].

One problem with passive detuning of the transmit circuit by series crossed diodes is that the diodes have a low Q when conducting. This reduces the Q of the resonant circuit and effectively “broadbands” the coil, enabling it to interact with a wide range of frequencies. Finally, crossed diodes do not provide a fast enough “switch” for use in multiple-pulse applications.

6.7.3 $\lambda/4$ lines

A $\lambda/4$ coaxial cable inserted in the appropriate location in the probe circuit can also be used for coil decoupling [19]. A $\lambda/4$ cable acts as an impedance transformer, described by

$$|Z|^2 = Z_i Z_o, \quad (6.6)$$

where Z is the characteristic impedance of the cable (generally 50Ω), Z_i is the input impedance, and Z_o is the output impedance. So, for example, if the output end is a short circuit, $Z_o = 0$ is transformed into $Z_i = \infty$ and there is an open circuit at the input. A standing wave pattern develops in the cable such that V_{\max} and I_{\min} are found at the input, and V_{\min} and I_{\max} at the output. Thus, no current can flow at the input (the probe end of the cable). Conversely, if there is an open circuit at the output there is a short circuit at the input and current can flow.

Generally, $\lambda/4$ lines are used in conjunction with crossed diodes. A $\lambda/4$ line in series with the coil (as suggested by Haase [19]) effectively blocks currents in the coil during transmission. However, the $\lambda/4$ line becomes part of the coil during reception and may adversely affect the Q and hence the S/N .

6.7.4 Previous Active Means

There have been a few previous schemes for active decoupling. Bendall *et al.* designed an active detune switch for use in volume-localized *in vivo* spectroscopy [16]. However, this switch made use of magnetic reed relays. The relays were placed at the end of $\lambda/4$ cables so that they could be kept outside the main magnetic field, a necessity so that they could switch properly. Later, Bendall *et al.* replaced the magnetic reed relays with PIN diodes. With the design used, however, $30 \mu\text{s}$ were required for rf pulses to be switched from one coil to the other [20]. This is not sufficiently rapid for multiple-pulse sequences.

Edelstein *et al.* used PIN diodes to decouple a surface-coil receiver [14]. These were used in a crossed arrangement as part of a resonant blocking circuit. In order for the blocking circuit to work properly, it required a high Q ; thus the use of PIN diodes rather than conventional crossed diodes. (PIN diodes have a very low impedance when forward biased and so do not degrade the circuit Q). Series crossed diodes were used in the transmit coil.

More recently, Li and Sotak have used PIN diodes to actively decouple a transmit coil from a surface-coil receiver [17]. Their design uses the PIN diodes in the tuning arm of the probe, which is not so problematic for the lower rf powers used in *in vivo* experiments, but is problematic for the high rf powers used in solids experiments.

6.8 Q-Switching

The method chosen to decouple the solenoid and gradient coils is a novel type of active Q-switching in which circuits are switched from resonant to non-resonant, Q-spoiled states. Other forms of Q-spoiling have been used previously to reduce coil ringdown time [10, 11, 12].

Active decoupling schemes to date have placed the switching components in the tuning arm of the resonant circuit. This has the disadvantage that the rf voltage present in the tuning arm is roughly a factor of Q larger than that applied to the probe. In solid-state experiments the high rf power (200 W to 1 kW) delivered to the probe is enough to destroy the switching component in the tuning arm. On the other hand, the voltage in the matching network is just the applied voltage from the transmitter (which is typically $\approx 280 V_{pp}$ for 200 W input). Several commercially available PIN diodes can withstand these voltages and also switch rapidly.

Chingas has shown that overcoupling a series-tuned parallel-matched circuit effectively lowers the Q [22]. Our Q-switching scheme is a means to switch a resonant circuit from its normal critically coupled state to an extremely overcoupled state. That is, it may be considered a means of pulsed overcoupling.

6.8.1 Pulsed Overcoupling

Simple series-tuned, parallel-matched (or parallel-tuned, series-matched) NMR probe circuits may be viewed as the equivalent circuits for the resonant modes of a cavity res-

onator coupled to a transmission line or waveguide [23]. This means that the impedance functions or s-parameters of a tuned and matched probe circuit are indistinguishable from a single cavity mode at the end of a length of transmission line. The cavity model provides both a quantitative description of a probe circuit as a function of frequency, and an intuitive qualitative model for understanding the effects of coupling (matching) on the resonant circuit.

A simple example of a cavity resonator is a length of waveguide which is closed at one end and connected to a transmission line or waveguide at the opposite end. Radiofrequency energy is admitted into the cavity through a coupling structure, which is usually a distributed circuit element such as an iris for microwave cavities, and a lumped element such as a simple capacitor for NMR probe circuits in the HF through UHF frequency ranges. The coupling structure determines how much rf energy enters the cavity and also what fraction escapes from the cavity back into the line. The ratio of stored to dissipated energy inside the cavity is given by the quality factor Q for a given resonant frequency. This is often referred to as the internal or unloaded Q for the cavity (Q_{internal}). The actual energy storage is also influenced by the amount of rf which escapes back into the transmission line and dissipates due to line losses or other terminations. This leakage is another dissipative load for the cavity, and is described by the external or radiation Q (Q_{external}) for the cavity mode. The actual Q for a cavity or probe resonance is described by the parallel combination of Q_{internal} and Q_{external} , given by Q_{total} :

$$\frac{1}{Q_{\text{total}}} = \frac{1}{Q_{\text{internal}}} + \frac{1}{Q_{\text{external}}} . \quad (6.7)$$

The line-induced loading can therefore exert a profound influence on the energy stored in a cavity or probe resonance. The degree of coupling is expressed by a dimensionless coupling coefficient (m). The coupling coefficient has three significant values: $m = 0$ or complete undercoupling, $m = m_c$ or critical coupling, and $m = 1$ or complete over-

coupling. Complete undercoupling implies that the resonator is completely disconnected from the line and no energy can enter or leave. In this case, Q_{total} is equivalent to Q_{internal} . Critical coupling corresponds to the case where the amount of rf energy leaking out of the coupling structure is equal to the amount dissipated per cycle inside the cavity. This represents the case of a perfectly matched probe. Any further coupling allows sufficient rf to leak back out of the cavity with each rf cycle, which loads the cavity and decreases Q_{total} . When the cavity is completely overcoupled, $Q_{\text{total}} < 1$, which means that the cavity is no longer resonant; as much energy escapes as is inserted each cycle.

The tuning and matching network of a coil with inductance L is used to select the resonance frequency of the circuit and also to transform the circuit impedance to the desired 50Ω . The transformer ratio N for the series-tuned parallel-matched resonant circuit can be expressed

$$N^2 = \left(1 + \frac{C_M}{C_T}\right)^2. \quad (6.8)$$

The coupling coefficient m is related to this transformer ratio by the following [23]:

$$m = \left[1 - \left(\frac{N^2 - 1}{N^2 + 1}\right)^2\right]^{1/2}. \quad (6.9)$$

The NMR probe circuit is overcoupled ($m = 1$) when $N = 1$, or $C_M \ll C_T$. Thus, by reducing C_M it is possible to overcouple the circuit. As mentioned above, the Q_{total} of the circuit is also related to the coupling coefficient. This relationship is

$$Q_{\text{total}} = Q_{\text{internal}} \frac{(1 - e^{-\alpha})(1 + \sqrt{1 - m^2})}{2(1 - e^{-\alpha}\sqrt{1 - m^2})}, \quad (6.10)$$

where $\alpha = 1/2Q_{\text{internal}}$. The Q which is actually observed is Q_{total} . Q_{internal} can be estimated from this, however, since at critical coupling Q_{total} is roughly half of Q_{internal} . For example, the solenoid Q measured for the 1-D probe when properly matched was 100, so Q_{internal} was approximately 200. Therefore, in the case of complete overcoupling

$$Q_{\text{total}} = 200 \frac{(1 - e^{-0.003})}{2}, \quad (6.11)$$

and Q_{total} is 0.25, which is small enough that any energy that leaks over to this circuit from another nearby circuit does not build up in the coil to produce an rf field which significantly influences the spins. So by switching C_M from its normal value to a much smaller value, it is possible to switch a circuit from a resonant state to a non-resonant, Q-spoiled state. In practice, by reducing C_M , over 99% overcoupling was achieved, so the Q_{total} was reduced to very nearly 0.25 [23].

One important observation made was that this scheme of decoupling worked best when the coils were oriented with their rf fields orthogonal. For example, at one point a larger quadrupole coil was tried (4 cm diameter). This coil was large enough that, unlike the case for previous quadrupole coils used, the ends of the solenoid were contained within the quadrupole coil volume. With these coils it was observed that the residual coupling between the coils was far worse than that observed for previous coils. In particular, increasing the gradient strength led primarily to a shift in the center frequency of the image, and not to the desired spread in frequencies. Presumably this was because of the end effects of the solenoid, where the solenoid and quadrupole magnetic fields were no longer orthogonal.

Critical to the implementation of Q-spoiling by pulsed overcoupling is a means to rapidly switch the value of C_M . This was achieved by placing diodes in series with the matching capacitor. The first diodes tried were 1N914B diodes, which are commonly used as the crossed diodes in the passive transmit-receive switch of an NMR spectrometer. Two diodes were placed in parallel between C_M and ground. With these diodes in place both the solenoid and quadrupole coils could easily be tuned and matched under low power. However, under high power the negative swing of the rf voltage effectively “unbiased” the diodes, thus degrading the circuit matching. Increased rf power could be applied to the probe without degrading the matching if the bias current was increased. This

was an unacceptable solution, however, because the diodes were not able to handle the higher power. Schottky rectifier diodes were then tried because of their increased power handling capability. These also proved unacceptable. Because of the fast response time of the Schottky diodes, an unreasonably large DC bias current was necessary to control the rf voltages used.

The correct diodes to use for this application are those which can control several hundred watts of rf power and also switch rapidly (within a few hundred nanoseconds). PIN diodes fill both these criteria.

6.8.2 PIN Diodes

A PIN diode is silicon semiconductor device composed of a highly resistive region of pure silicon, which has a long carrier lifetime and is known as the intrinsic region or I-region, sandwiched between highly doped P-type and N-type regions. PIN diodes operate as variable resistors at rf and microwave frequencies. The resistance value is determined only by the DC excitation, or bias. An important feature of the PIN diode is its ability to control large rf signals via smaller levels of DC bias.

Two types of PIN diodes were used successfully in Q-switching the resonant circuits of the imaging probes. The first were HP 5082-3203 diodes, whose specifications are shown in Table 6.2. These were later replaced by M/A-COM MA4P504 diodes, whose specifications are shown in Table 6.3.

Forward Bias

When a PIN diode is forward biased, charge, consisting of holes and electrons, is injected into the intrinsic region. The holes and electrons have a finite lifetime, the carrier lifetime τ , before recombination. This causes an average stored charge, Q , which lowers the effective resistance of the I-region to a value R_S . The quantity of stored charge,

V_{BR}	300 V
Maximum R_S at 100 mA ^a	1.2 Ω
Maximum C_j at 50 V ^b	0.32 pF
Carrier Lifetime ^c	100 ns

^aMaximum series resistance is specified at 100 MHz at the indicated current.

^bMaximum capacitance is specified at 1 MHz at the indicated voltage.

^cMinimum carrier lifetime is specified at $I_F = 50$ mA.

Table 6.2: Specifications for HP 5082-3203 PIN diodes (at 25°C).

Voltage Rating ^a	500 V
Maximum R_S at 100 mA ^b	0.60 Ω
Maximum C_j at 100 V ^c	0.20 pF
Carrier Lifetime ^d	1 μ s
I-Region Width	2 mils
Chip Size	20 mils \times 20 mils
Contact Diameter	5 mils
Thermal Resistance	20 °C/W

^aMaximum reverse current is 10 μ A at specified voltage rating.

^bMaximum series resistance is specified at 100 MHz at the indicated current.

^cMaximum capacitance is specified at 1 MHz at the indicated voltage.

^dNominal carrier lifetime is specified at $I_F = 10$ mA.

Table 6.3: Specifications for M/A-COM MA4P504 PIN diodes (at 25°C).

Q , depends on τ and the level of forward bias current, I_F , as follows:

$$Q = I_F \tau \quad [\text{coulombs}] . \quad (6.12)$$

The forward bias current used for the HP diodes was 80 mA, while that for the M/A-COM diodes was 125 mA. The resistance, R_S , of the I-region under forward bias is inversely proportional to Q and may be written

$$R_S = \frac{W^2}{(\mu_n + \mu_p)Q} \quad [\text{ohms}] , \quad (6.13)$$

where W is the I-region width, μ_n the electron mobility, and μ_p the hole mobility.

Resistances typically range from 0.1Ω at 1 A forward bias to about $10,000 \Omega$ at $1 \mu\text{A}$ forward bias [26]. The lowest frequency for which Equation 6.13 applies is the transit time frequency, $f_T = 1/2\pi\tau$, above which the period is shorter than the transit time of the I-region. This is primarily a function of W and can be written

$$f_T > \frac{1300}{W^2} \quad [\text{MHz}] , \quad (6.14)$$

where W is the I-region thickness in μm . The lifetime τ of PIN diodes is designed to be typically in the range of $0.0005 \mu\text{s}$ to over $3 \mu\text{s}$, depending on the switching speed desired [25]. For the HP diodes, $\tau = 100 \text{ ns}$ and so f_T is about 1.6 MHz, while for the M/A-COM diodes, $\tau = 1 \mu\text{s}$ and so f_T is about 160 kHz. At frequencies well above f_T , the diode appears essentially as a pure linear resistance whose value can be controlled by the DC bias level.

Reverse Bias

When a PIN diode is at zero or reverse bias there is no stored charge in the I-region and the diode appears to high rf frequencies as a capacitor C_T shunted by a parallel resistance R_P . The capacitor C_T represents the I-layer capacitance which may be written

$$C_T = \frac{\epsilon A}{W} \quad [\text{farads}] , \quad (6.15)$$

where ϵ is the dielectric constant of silicon and A is the area of diode junction.

The parallel resistance, R_P , represents the net dissipative resistance in the reverse biased diode [26]. At low reverse voltages the finite resistivity of the I-region results in a lossy I-region capacitance. As the reverse voltage is increased carriers are depleted from the I-region resulting in an essentially lossless silicon capacitor. R_P is proportional to reverse voltage and inversely proportional to frequency. In most rf applications its value is higher than the reactance of the capacitance C_T and so is less significant.

Under reverse bias the diode should not be biased beyond its DC voltage rating V_R . In a typical application, in order for the intrinsic region to remain in a low loss state, the maximum instantaneous reverse or negative voltage swing should never exceed V_{BR} , the avalanche or bulk breakdown voltage which is proportional to the I-region width W . An instantaneous excursion of the rf signal into the positive bias direction generally does not cause the diode to go into conduction because of the slow reverse to forward switching speed T_{RF} (discussed below); however, the positive voltage excursion must not cause thermal losses to exceed the diode's dissipation rating [26].

The large number of interacting parameters in high-power applications (e.g., breakdown voltage, bias voltage, peak rf voltage, circuit losses, carrier lifetime, frequency, rf pulse length, duty cycle, and ambient temperature) frequently makes actual test and experimentation the only practical way to determine a proper bias voltage. In general the voltage rating V_R (the voltage below which it is guaranteed that no more than $10 \mu\text{A}$ reverse current will flow) must always exceed the applied DC reverse voltage but it need not be as high as the maximum rf voltage swing [26]. No reverse bias voltage was necessary for the HP diodes, but a reverse bias voltage of 25 V was used for the M/A-COM diodes.

Switching Time

In rf switching applications, the switching speed may be loosely defined as the time required either to fill up or remove the charge from the I-region. The switching speed depends on the driver circuit as well as the PIN diode [24]. When the diode forward bias is suddenly removed, the negative and positive charges in the diode eventually recombine. The time required for this is the carrier lifetime, τ . If, however, a sufficiently large reverse voltage is applied to the forward conducting diode, producing an initial reverse current I_R , the “forward to reverse” switching time T_{FR} (turn-off time) may be expressed as follows [26]:

$$T_{FR} = \ln \left(1 + \frac{I_F}{I_R} \right) . \quad (6.16)$$

This is almost always shorter than the “reverse to forward” switching time T_{RF} (turn-on time). T_{RF} is the time necessary to fill the I-region with stored charge. It depends primarily on the thickness of the diode and the levels of reverse voltage and forward current which the driver circuit can supply [26]. For the M/A-COM diodes, which have an I-width of 50 μm , T_{RF} is 200 ns, assuming a reverse voltage of 10 V and a forward current of 100 mA. The typical reverse recovery time quoted for the HP diodes is 100 ns for a forward bias current of 20 mA and a reverse bias voltage of 10 V.

Maximum Controlable RF

When a PIN diode is forward biased, the maximum rf current the diode can control depends on the amount of stored charge Q supplied by the DC forward bias relative to the charge variations q produced by the rf current I_{RF} . Q must be much greater than q in order to prevent the rf current from drawing out the entire stored charge [24]. In other words,

$$I_{DC} \tau \gg \frac{I_{RF}}{2\pi f} \quad [\text{coulombs}] , \quad (6.17)$$

where I_{RF} is the rf peak current, I_{DC} the diode forward bias current, f the operating frequency, and τ the diode carrier lifetime.

This means that the DC stored charge in the PIN diode will be able to withstand larger rf currents as the frequency of the rf signal increases. It also means that an instantaneous diode current excursion may occur in the negative (reverse bias) direction without adversely affecting the diode low resistance state. Assuming a peak rf current and a DC current of equal magnitude, for frequencies below the transit time frequency f_T , q is roughly equivalent to Q . Above f_T , however, the ratio of q to Q decreases by about 6 dB per octave [25]. Recall that for the HP diodes $f_T = 1.6 \text{ MHz}$, while for the M/A-COM diodes $f_T = 160 \text{ kHz}$. At an operating frequency of 200 MHz, then, q/Q is down by 42 dB for the HP diodes and by 60 dB for the M/A-COM diodes. This means for the HP diodes that the DC current produces a charge 100 times as large as does the rf current, and for the M/A-COM diodes, a charge 1000 times as large. Generally, it is recommended that the value of DC stored charge be designed to be at least 10 times the rf stored charge [26], so for the HP diodes a DC bias current will control a peak rf current 10 times as large as itself, while for the M/A-COM diodes a DC bias current will control a peak rf current 100 times as large.

Maximum Signal Power

The maximum rf signal power that a PIN diode can handle is limited either by the breakdown voltage or the power dissipation capability of the device. Power dissipation usually sets the lower upper bound for continuous wave power, while the power limit determined from the breakdown voltage parameters is relevant at low duty cycle and is more straightforward to calculate. The maximum power, into 50Ω , determined by the

voltage breakdown limit for diodes in a series circuit is

$$P_{\max} = \frac{(V_{BR} - V_{BIAS})^2}{400}, \quad (6.18)$$

where V_{BIAS} is the reverse bias. Here V_{BR} and V_{BIAS} are in volts and P_{\max} is in watts. This limit is optimized by using zero reverse bias. However, a reverse bias voltage may be necessary in high power applications, where forward current may otherwise flow during the positive swing of the rf voltage (thus reducing the diode impedance), or in order to reduce switching time. No reverse bias was used for the HP diodes. However, V_{BR} for these diodes is 300 V, leading to a maximum rf power of 225 W. The rf applied to the solenoid coil was only slightly less than this (200 W). The rf applied to the quadrupole coil was significantly more than this (300 W), and so led to the demise of quite a few diodes.

The M/A-COM diodes have a voltage rating of 500 V, and hence a breakdown voltage at least that large, leading to a maximum power rating of 625 W, if no reverse bias voltage is used. In fact, because of the increased carrier lifetime compared to that of the HP diodes, the turn off time was unacceptably long and reverse biasing was found to be necessary. In general a 25 V reverse bias voltage was used, which lowered the maximum power to 560 W.

6.8.3 Implementation of Q-switching

The success of coil decoupling by active Q-switching is demonstrated in Figure 6.11. Shown in the figure are oscilloscope traces of the reflected voltage of the 1-D probe solenoid circuit. The bottom trace shows the coupling between the solenoid and quadrupole coils observed before the diodes were added to the circuits. The separation between the peaks is 5 MHz. The top trace was taken after diodes were added. Here the solenoid diodes are forward biased and the quadrupole diodes are at zero bias. The splitting has

been eliminated, and both circuits can now be tuned to 200 MHz.

The diode driver used was homebuilt. The optoisolator circuit for the bipolar PIN diode driver is shown in Figure 6.12 and the bipolar PIN diode driver circuit is shown in Figure 6.13.

Low Power Diode Switching Time with Forward Bias Only

The low power switching time of the HP and M/A-COM diodes incorporated into the probe was determined using the apparatus shown schematically in Figure 6.14. The reflected voltage of the probe was observed as a train of DC forward bias pulses was applied to the diodes. The Wavetek function generator provided 4 V, 5 μ s pulses with 35 μ s delays both to channel 1 of the oscilloscope and to the trigger input of the homebuilt diode driver (this input required 50 Ω driving capability). The Wavetek 1062 frequency sweeper, set to CW mode, provided 200 MHz CW rf to the probe. The diode driver provided 40 V pulses through a 250 Ω current limiting resistor, or 80 mA forward bias pulses to each PIN diode. With this configuration the time from the beginning of a bias pulse to the minimum observed reflected voltage (the effective turn on time) was 270 ns for the HP diodes. The time from the end of a bias pulse until the reflected voltage had reached 95% of its final amplitude (the effective turn off time) was approximately 2 μ s.

The M/A-COM diodes had an effective turn on time of 460 ns and an effective turn off time of 11 μ s. This is an unacceptably long time, and was clear indication that reverse biasing would be necessary for these diodes.

Diode Switching Time with Forward and Reverse Bias

With M/A-COM diodes in the matching networks of both the solenoid and quadrupole coils, it was necessary to implement reverse bias pulses to ensure that the diodes of a given network were held "off" at any time they were not forward biased. At this point

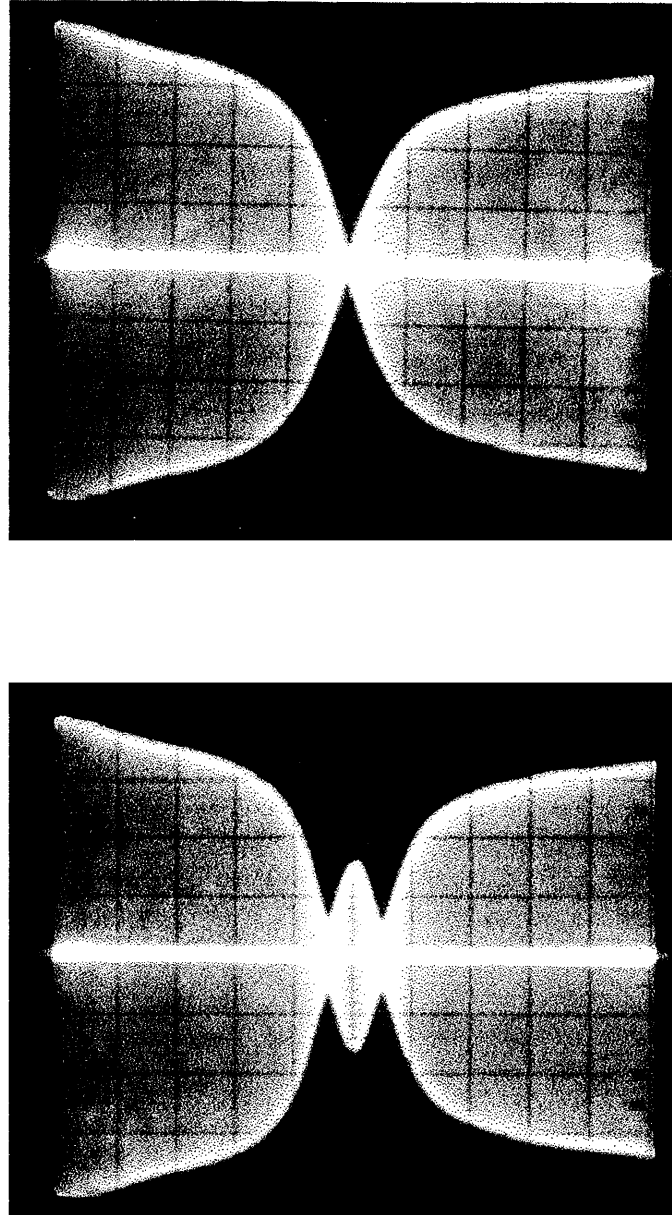


Figure 6.11: Oscilloscope traces of the reflected voltage of the 1-D imaging probe solenoid coil taken before (bottom) and after (top) Q-switching was implemented. The splitting in the peaks observed in the bottom trace, caused by coupling with the quadrupole coil, is 5 MHz. In the top trace this splitting has been removed by Q-spoiling the quadrupole resonant circuit with the scheme discussed in the text.

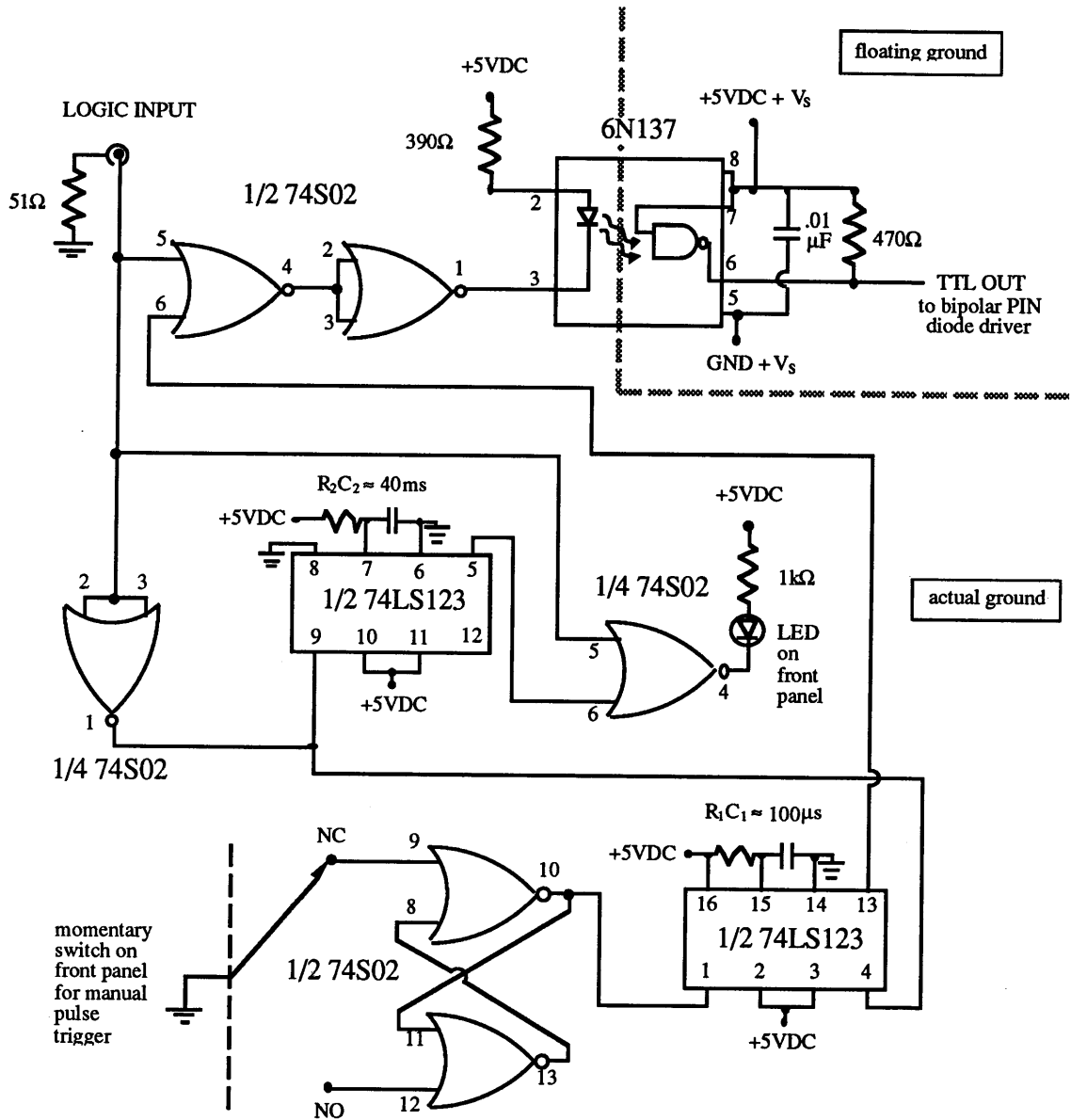


Figure 6.12: Optoisolator circuit for bipolar PIN diode driver. Each TTL chip is bypassed with a 0.47 μF and a 0.01 μF ceramic capacitor at the chip.

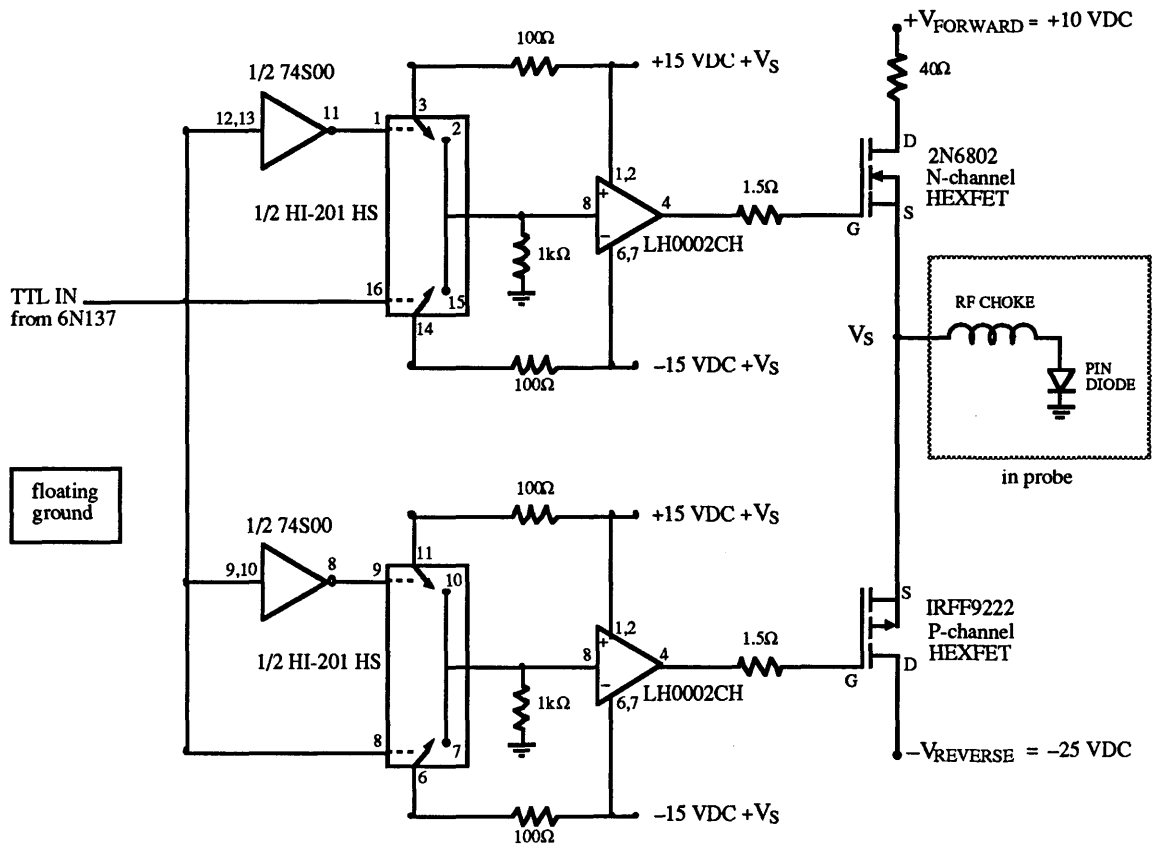


Figure 6.13: Bipolar PIN diode driver. Each TTL chip is bypassed with a $0.47 \mu\text{F}$ and a $0.01 \mu\text{F}$ ceramic capacitor at the chip.

the current limiting resistor for the forward bias pulses was also changed from 250Ω to 40Ω and the forward bias voltage was changed from $+40 \text{ V}$ to $+10 \text{ V}$ for a forward bias current of 125 mA in each diode. The reverse bias voltage was -25 V . Since the diodes had a high resistance under reverse bias, there was no perceived requirement for a current limiting resistor in the negative bias portion of the diode driver circuit. This proved problematic since several diodes failed as short circuits.

Under these conditions, and using the apparatus and procedure described above, the effective turn on time was approximately 600 ns and the effective turn off time was 700 ns .

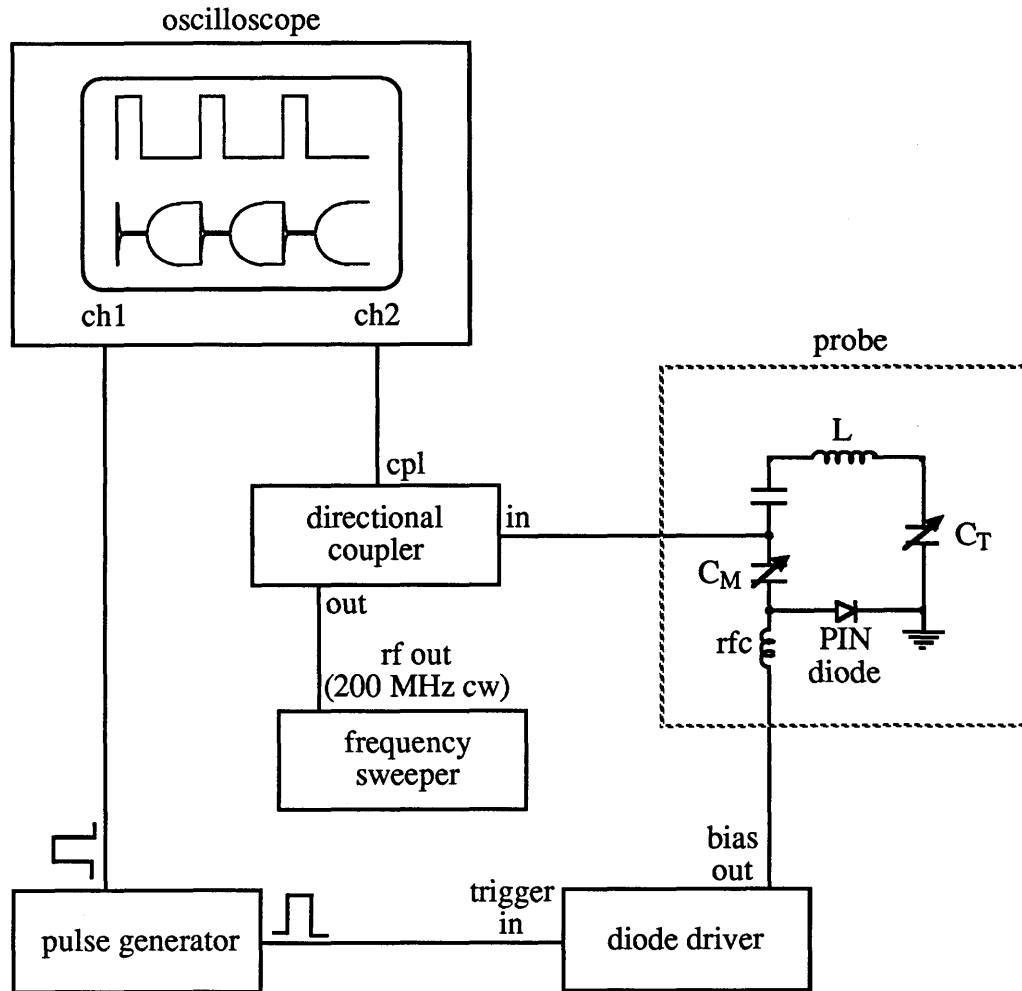


Figure 6.14: Configuration used for determining the low power switching time of the PIN diodes.

6.9 Conclusions

The novel imaging probes described in this chapter enabled the successful implementation of multiple-pulse rf gradient imaging. Both the solenoid coil used to deliver the line-narrowing pulses and the quadrupole coil used to deliver the rf gradient pulses are part of series-tuned parallel-matched resonant circuits, much like those typically used in solid-state NMR probes constructed to operate at 200 MHz. The fundamental difference, however, is the need to decouple the two circuits. This was achieved by “pulsed overcoupling,” a means of actively switching a circuit from a resonant to a non-resonant,

Q-spoiled state. The advantage of this technique over previous techniques is that the switching components are placed in the matching network of the resonant circuit. This protects them from the high voltages present in the tuning arm of the circuit. Q-switching requires the use of high power PIN diodes which are also able to switch rapidly. The diodes used here enabled Q-switching to occur in a few hundred nanoseconds. It should be pointed out that the diodes were the “Achilles heel” of the imaging probes. Often, device failure was the result of neglecting to arm the diode driver, failure to maintain the proper forward bias current, or other experimental error. However, this was not always the case. It was generally observed that the diodes had a lifetime of a few months when used in this application.

That Q-switching does not adversely affect the obtainable signal-to-noise ratio of a probe has been demonstrated by a performance comparison of the 2-D imaging probe and a conventional solid-state spectroscopy probe. Q-switching may also be useful in applications where it is necessary to reduce probe ringdown time. The success of Q-switching in decoupling two resonant circuits has been demonstrated by the solid-state images obtained, which were discussed in Chapters 3 and 5.

An important aspect of the Q-switching scheme is that it can be generalized to any number of circuits as long as one circuit at a time is “on.” This will allow combinations of the rf gradient coils discussed to be implemented for 3-D imaging without sample rotation or back-projections data analysis.

References

- [1] D. S. Webster and K. H. Marsden, *Rev. Sci. Instrum.* **45**, 1232 (1974).
- [2] "The ARRL Handbook for the Radio Amateur," Ed., K. A. Kleinschmidt, 67th edition, p. 31-30, American Radio Relay League, Newington, CT, 1990.
- [3] A. Abragam, "The Principles of Nuclear Magnetism," pp. 82-83, Clarendon Press, Oxford, 1961.
- [4] H. D. W. Hill and R. E. Richards, *J. Phys. E, Ser. 2* **1**, 977 (1968).
- [5] D. I. Hoult and R. E. Richards, *J. Magn. Reson.* **24**, 71 (1976).
- [6] R. W. Vaughan, D. D. Elleman, L. M. Stacey, W.-K. Rhim, and J. W. Lee, *Rev. Sci. Instrum.* **43**, 1356 (1972).
- [7] W.-K. Rhim, D. D. Elleman, and R. W. Vaughan, *J. Chem. Phys.* **59**, 3740 (1973).
- [8] W.-K. Rhim, D. D. Elleman, L. B. Schreiber, and R. W. Vaughan, *J. Chem. Phys.* **60**, 4595 (1974).
- [9] U. Haubenreisser and B. Schnabel, *J. Magn. Reson.* **35**, 175 (1979).
- [10] G. L. Samuelson and D. C. Ailion, *Rev. Sci. Instrum.* **41**, 1606 (1970).
- [11] K. E. Kisman and R. L. Armstrong, *Rev. Sci. Instrum.* **45**, 1159 (1974).
- [12] E. R. Andrew and K. Jurga, *J. Magn. Reson.* **73**, 268 (1987).

- [13] D. I. Hoult, C.-N. Chen, and L. K. Hedges, *Annals NY Acad. Sci.* **508**, 366 (1987).
- [14] W. A. Edelstein, C. J. Hardy, and O. M. Mueller, *J. Magn. Reson.* **67**, 156 (1986).
- [15] P. Styles, M. B. Smith, R. W. Briggs, and G. K. Radda, *J. Magn. Reson.* **62**, 397 (1985).
- [16] M. R. Bendall, J. M. McKendry, I. D. Cresshull, and R. J. Ordidge, *J. Magn. Reson.* **60**, 473 (1984).
- [17] L. Li and C. H. Sotak, *J. Magn. Reson.* **93**, 207 (1991).
- [18] M. R. Bendall, A. Connelly, and J. M. McKendry, *Magn. Reson. Med.* **3**, 157 (1986).
- [19] A. Haase, *J. Magn. Reson.* **61**, 130 (1985).
- [20] M. R. Bendall, D. Foxall, B. G. Nichols, and J. R. Schmidt, *J. Magn. Reson.* **70**, 181 (1986).
- [21] M. R. Bendall, *Chem. Phys. Lett.* **99**, 310 (1983).
- [22] G. C. Chingas, *J. Magn. Reson.* **54**, 153 (1983).
- [23] D. N. Shykind, personal communication. A helpful discussion can also be found in "Principles of Microwave Circuits," Ed., G. C. Montgomery, R. H. Dickey, and E. M. Purcell, pp. 207-239, Dover Publications, New York, 1965.
- [24] G. Hiller, "Design with PIN Diodes," M/A-COM Semiconductor Products Division publication AG312.
- [25] "Applications of PIN Diodes," Hewlett Packard publication AN922.
- [26] Unitrode Corporation PIN diode data book.

Appendix A

Modifications to the Homebuilt NMR Spectrometer

In the course of the research described in this dissertation, several modifications were made to the homebuilt NMR spectrometer in the Weitekamp lab. The first series of modifications, necessary before any of the rf gradient imaging experiments could be performed, was to add a second rf channel to the spectrometer. The second series of modifications had as its aim the improvement of the spectrometer receiver noise figure.

A.1 Second RF Channel

The components required for a second rf channel included a second quadrature generator, transmit control, and rf amplifier. The original rf amplifier, an ENI 5100L-NMR, was used for the line-narrowing pulses. One of two rf amplifiers was used for the gradient pulses: for early experiments an AR 500LM8, and for later experiments an AR 200L. The new quadrature generator and transmit control were constructed in house and are described below.

A.1.1 Quadrature Generator

The new quadrature phase generator was built according to the design of the adjustable quadriphase modulator (QPM) of Shykind *et al.* [1, 2]. The QPM minimizes problems of thermal drift, interchannel crosstalk, and coarse settability common to other

quadrature generators. The QPM maintains quadrature phase balance to 0.005° , and exhibits less than 0.03 dB of amplitude drift over a 24 hour period. It also enables fine phase and amplitude adjustment and has a switching speed of 30 ns. Since the performance of the QPM is superior to that of the original quadrature generator, the QPM was used to produce the quadrature phases for the line-narrowing pulses. The phases of the gradient pulses were not nearly as critical, so these were produced by the original quadrature generator. In addition, a Merrimac PSM-2A-30 phase shifter was added at the 30 MHz input of the original quadrature generator to allow the overall phase of the gradient pulses (ϕ_d) to be adjusted with respect to that of the line-narrowing pulses.

A.1.2 Transmit Control

The new transmit control was built essentially identical to the original transmit control. Shown in Figure A.1, the transmit control mixes the 30 MHz output of the quadrature generator to 200 MHz. The output is then fed through a 200 MHz band-pass filter and into the rf amplifier.

A.2 Improvements to the Receiver

The original receiver of the homebuilt spectrometer was found to have both poor noise figure and poor stability. The noise figure, measured by the “hot/cold resistor” test [3], was found at the time of measurement to be 20 dB. The minimum detectable signal (MDS) of the receiver may be determined as follows:

$$\text{MDS} = 10 \log \left(\frac{p}{10^{-3}} \right) + \text{NF}, \quad (\text{A.1})$$

where MDS is in dBm and NF is the noise figure in dB. The thermal noise power p is given by

$$p = k_B T B, \quad (\text{A.2})$$

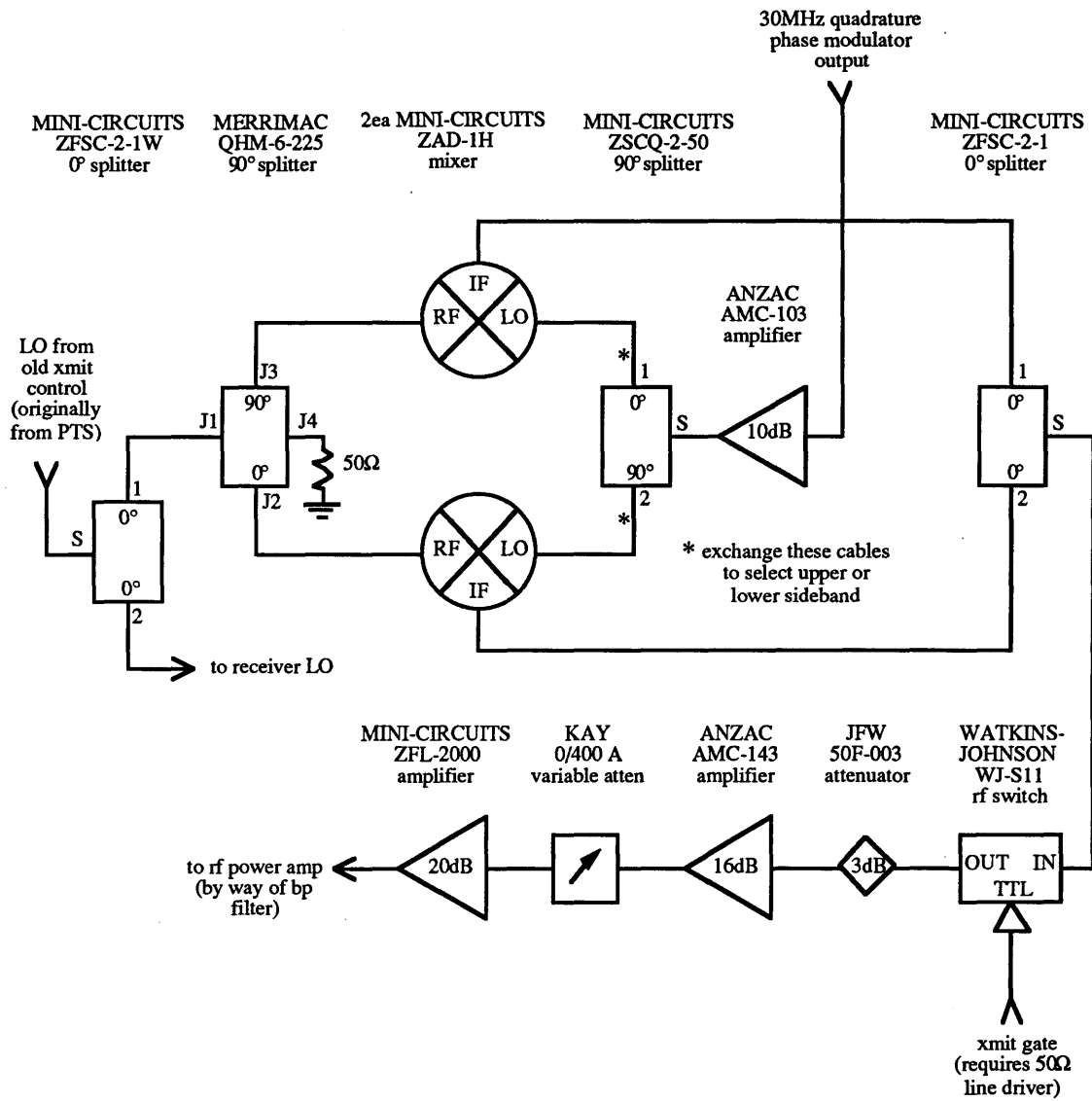


Figure A.1: New transmit control (ESG10870 with minor modifications).

where k_B is Boltzmann's constant, T the temperature in Kelvins, and B the bandwidth in Hz. Assuming a temperature of 300 K and a bandwidth of 1 MHz, then, a noise figure of 20 dB corresponds to a minimum detectable signal of approximately -94 dBm. This is unacceptable since a functioning spectrometer should not have difficulty detecting an NMR signal that produces $1 \mu\text{V}_{\text{pp}}$ in the coil. This corresponds to 2.5×10^{-15} W, assuming the probe is matched to 50Ω , or about -116 dBm. With hopes of improving the spectrometer noise figure, and hence the minimum detectable signal, a new receiver front end and a new audio stage were built.

A.2.1 Receiver Front End

The new receiver front end, including the preamp and first stage, is shown in Figure A.2. The Avantek amplifiers in the system were selected for their low noise figure and high gain: the UTC-210-1 is specified to have a gain of 8 dB and a maximum noise figure of 1.5 dB and the UTC-221-1 a gain of 28.5 dB and a maximum noise figure of 2.0 dB. The final Avantek amplifier in the first stage may be bypassed by means of a switch on the front panel if only low gain is required. This allows for variable gain with a high gain of about 54 dB and a low gain of about 27 dB. Both the preamp and the receiver first stage require deblanking signals to control the Anzac SW-239 rf switches. This protects the receiver from pulse breakthrough and allows for fast recovery of the preamp. The system recovery time is approximately 200 ns, so it is suggested that 500 ns to $1 \mu\text{s}$ be allowed for deblanking. The output of the receiver front end is fed into the IF amplifier and from there, the signal proceeds to the phase sensitive detector and audio stage.

With the new receiver front end in place, the noise figure of the spectrometer was measured again and found to be about 9.0 ± 0.3 dB. Actually, this was somewhat dependent on the IF amplifier gain setting, ranging from 8.9 ± 0.2 dB for low IF gain and 9.1 ± 0.4 dB for high IF gain. The noise figure did not appear to be dependent on the

gain setting of the receiver first stage [4].

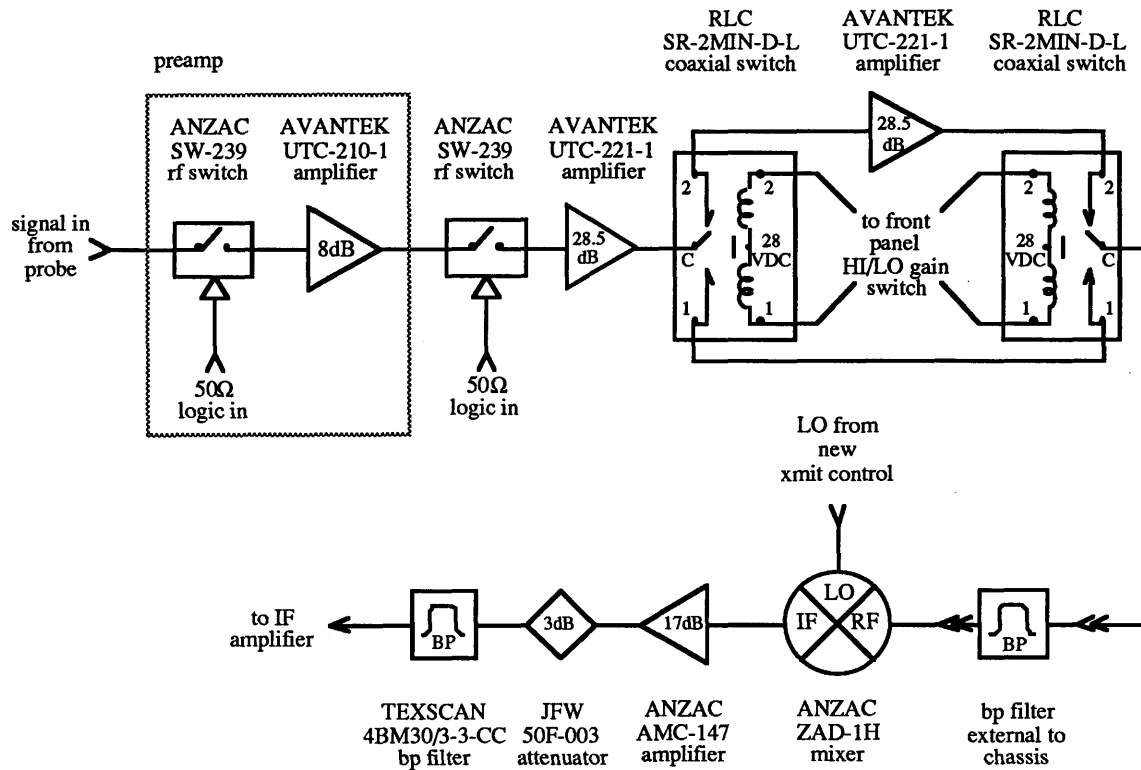


Figure A.2: New receiver front end including preamp and first stage. The preamp is housed in a separate stand-alone box. The first stage is housed in a rack-mounted box. A HI/LO gain switch on the front panel of the first stage switches the second Avantek UTC-221-1 amp in and out of the circuit.

A.2.2 Audio Stage

The new audio stage consists of two portions: the DC voltage reference board, shown in Figure A.3, and the audio stage itself, shown in Figure A.4. Both of these were incorporated into the original phase sensitive detector, which provides the audio stage with its 0° and 90° audio inputs. The DC voltage reference board provides the regulated ± 7 VDC and the DC offset adjusts required by the audio stage. The advantage of this design is that the DC offset control comes from a stable voltage reference, whereas previously it

had come directly from the power supply. Similarly, the 10-turn potentiometers on the front panel turn this into a precision voltage divider which enables precise control of the DC offset. Finally, the use of the fast recovering ComLinear CLC401 op amps in the audio stage also helped improve the receiver recovery time.

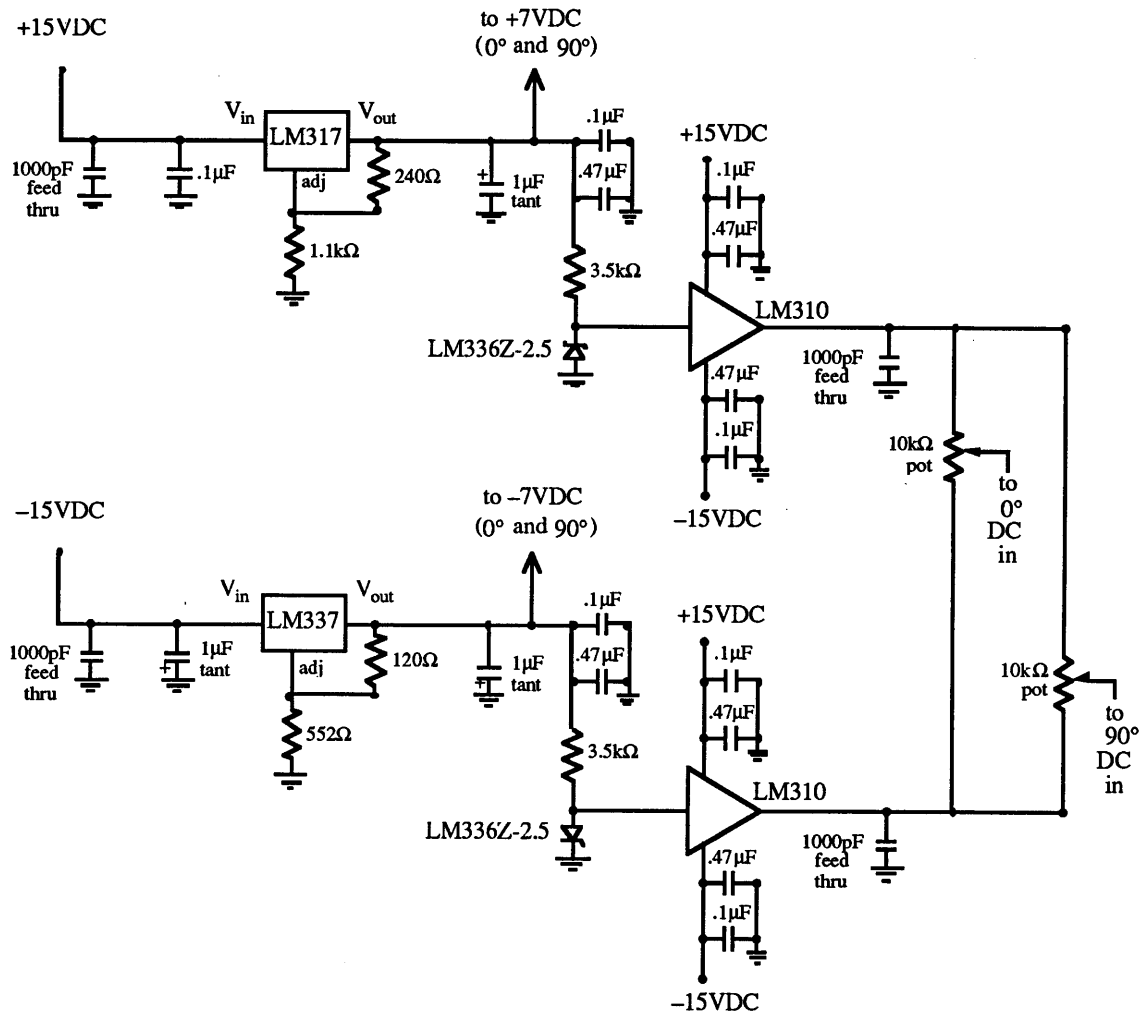


Figure A.3: Audio stage DC voltage reference. This circuit provides the regulated ± 7 VDC, as well as the DC offset adjust, required by the audio stage circuit shown in Figure C.4.

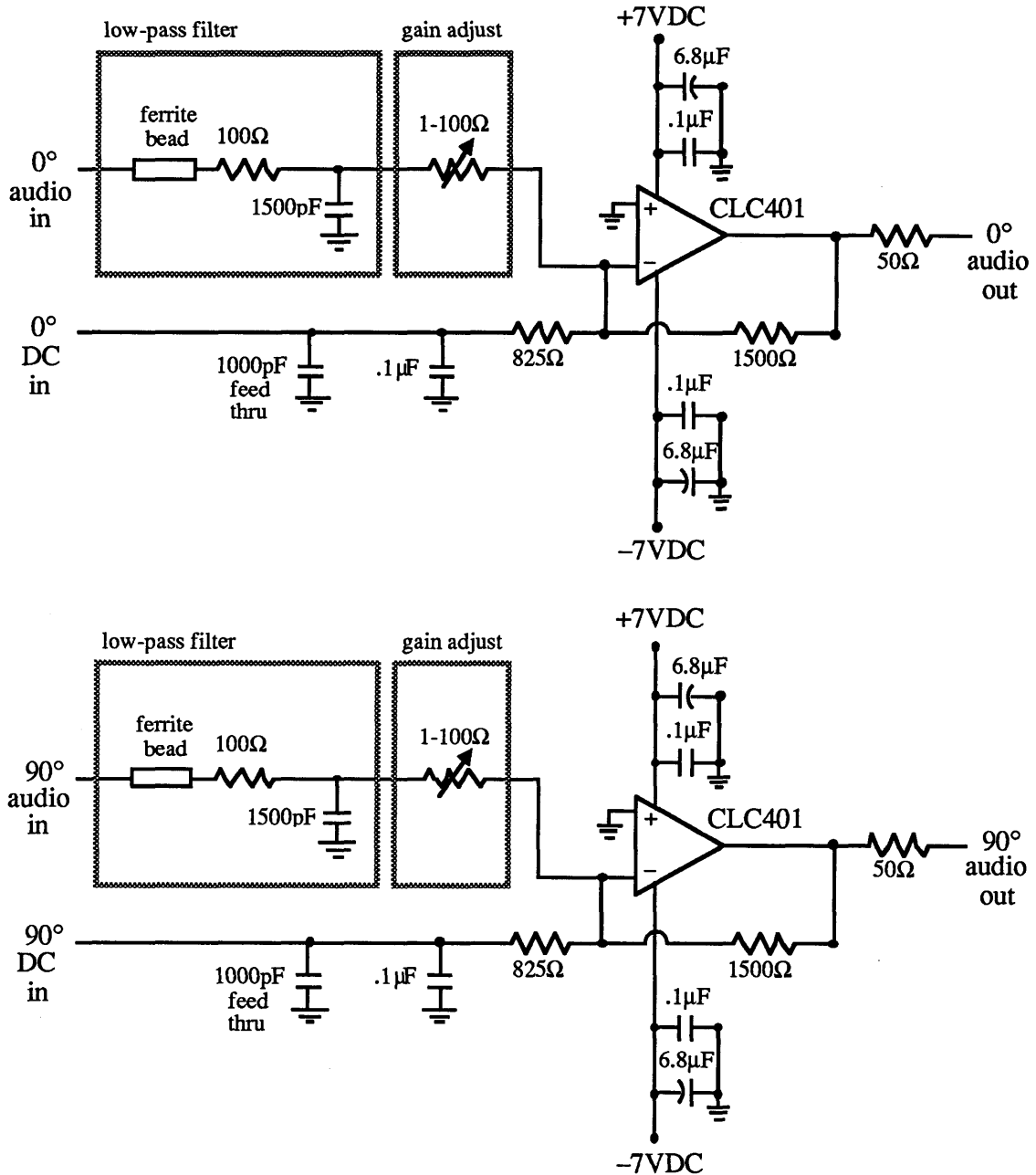


Figure A.4: Audio stage. Included in this diagram are the low-pass audio filter and summing-inverting-amplifier circuits. The 1-100 Ω trimpots enable independent adjustment of 0° and 90° audio gain. The 6.8 μF capacitors are tantalum, whereas the 0.1 μF capacitors are ceramic.

References

- [1] D. N. Shykind, Ph.D. Thesis, University of California, Berkeley (1989).
- [2] D. N. Shykind, G. C. Chingas, A. Pines and A. J. Shaka, *Rev. Sci. Instrum.* **61**, 1474 (1990).
- [3] (a) "System Noise Figure," Instrumentation Note 1, Fremont Magnetic Resonance, 1989; (b) "Noise Figure Determination of an NMR Spectrometer," Bruker Report 1/1979, p. 16.
- [4] J. A. Marohn, personal communication.

Appendix B

Multiple-Pulse NMR Imaging of Solids with Radiofrequency Gradients on a Commercial Spectrometer

B.1 Imaging on the MSL200

The Bruker MSL200 is equipped with two radiofrequency channels, F1, which operates over a wide frequency range, and F2, which is commonly used for decoupling and is fixed at 200 MHz. Each channel allows for independent phase and amplitude adjustment of its four quadrature phases (X, Y, $-X$, $-Y$). The high power pulse cabinet (HPPC) provided also houses two amplifiers capable of producing rf pulses of several hundred watts to one kilowatt, one which can be tuned over a wide frequency range and the other which is used for ^1H and ^{19}F (and ^3H) frequencies only. In this sense, then, the MSL200 is equipped to handle multiple-pulse NMR imaging with radiofrequency gradients. The MSL200 also has four external logic channels which can be used to provide the logic pulses necessary for the DC bias pulses necessary for active Q-switching. The only equipment necessary for multiple-pulse imaging with rf gradients which is not already provided with the spectrometer, then, is the probe and the diode driver circuitry. For the imaging experiments performed on the MSL200, we used the same probes and diode driver circuitry used for the experiments on the homebuilt spectrometer.

In practice, however, in order to implement successfully our imaging experiments on the MSL200, it was necessary to make two modifications. First, the “logic converter” box by which the four external logic channels are accessed was rebuilt. Second, it was also necessary, in order to obtain gradient pulses of stable amplitude and sufficiently fast turn-on time, to bypass the F2 transmitter and replace it with a separate amplifier. The MSL200 configuration used for multiple-pulse solids imaging experiments with rf gradients is shown in Figure B.1.

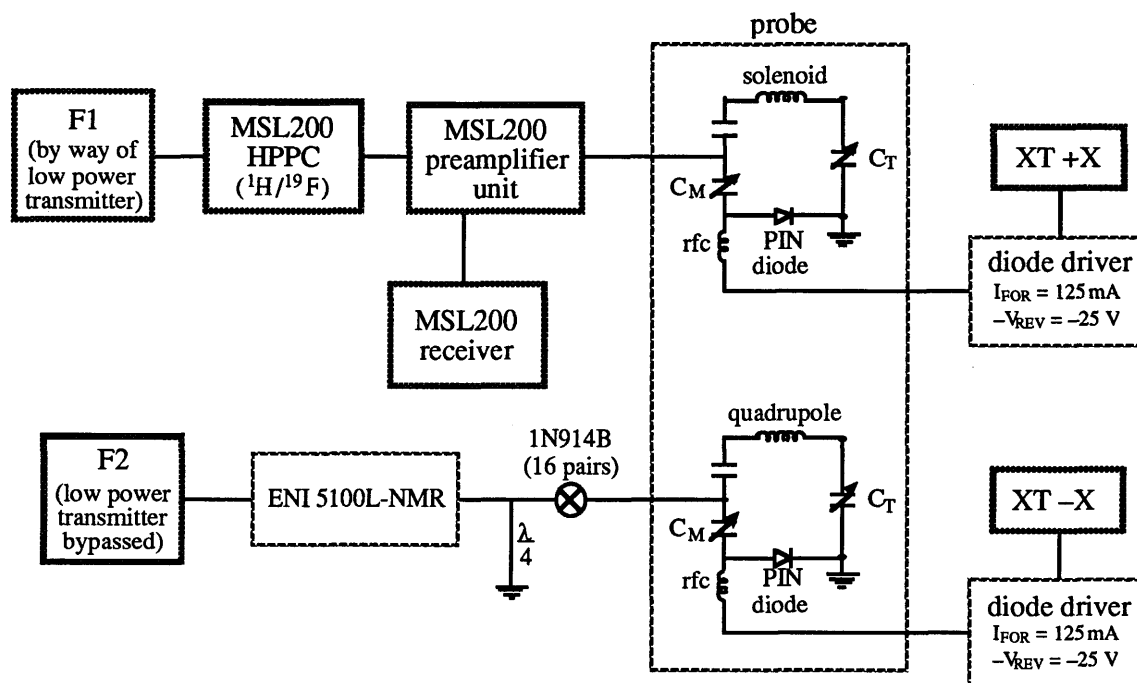


Figure B.1: MSL200 configuration for solids imaging. The F1 channel is configured for standard ^1H solids spectroscopy and delivers the line-narrowing pulses to the solenoid resonant circuit of the probe. Note that the preamplifier unit also houses the transmit/receive switching circuitry. The F2 amplifier is bypassed and the F2 pulses fed through a Kay variable attenuator to an ENI 5100L-NMR amplifier. The output from this amplifier is fed through a $\lambda/4$ DC filter and series crossed 1N914B diodes and then into the quadrupole resonant circuit.

B.2 External Logic Pulses

In order to decouple two rf resonant circuits by means of the active Q-switching described in Chapter 6, a spectrometer must be able to provide logic pulses to the diode driver of each resonant circuit. The MSL200 has four external (XT) logic channels which can be used for this purpose. However, in MSL200 units equipped to handle liquids imaging these external channels are normally routed through a “logic converter” box to the selective excitation unit (SEU) used to provide the shaped rf pulses required for slice selection. To access the XT channels for diode bias pulses, the logic converter box supplied with the MSL200 was rebuilt. Like the original, the new logic converter box consists of an inverting $50\ \Omega$ line driver (74LS28) and a +5 V regulator chip (LM340T-5.0). In addition, however, the new box has a four-pole double-throw switch so that the XT pulses can be routed either to the selective excitation unit (SEU), as they had been previously, or to four BNC panel mounts on the side of the box.

In the pulse programs written to perform the imaging experiments, the XT +X and XT -X channels were used to provide the logic inputs to the diode drivers for the solenoid and quadrupole circuits, respectively. For example an XT +X pulse forward biases the diodes in the solenoid resonant circuit. The diodes are forward biased for the duration of the XT +X pulse, and reverse biased in the absence of the XT +X pulse. In general the diodes of a given circuit were “pre-biased” for a short time before the application of an rf pulse. On the homebuilt spectrometer, $1\ \mu\text{s}$ was sufficient for this pre-biasing time period. On the MSL200, however, it was found that the minimum reliable time increment from the pulse programmer was $1.5\ \mu\text{s}$, so the diodes were pre-biased for $1.5\ \mu\text{s}$ prior to an rf pulse.

B.3 RF Amplifiers

The F1 channel routed through the high power pulse cabinet (HPPC) was used for the line-narrowing pulses. This is the standard high power ^1H configuration for the MSL200. With this arrangement 400 W pulses were routinely used to achieve a $2.1 \mu\text{s}$ 90° pulse time.

The F2 channel was used for the gradient pulses; however, the F2 transmitter (the low power amplifier as well as the HPPC) was bypassed. This was necessary for two reasons. First, the automatic gain circuitry (AGC) of the MSL200 F2 transmitter, which puts the F2 pulse amplitude under computer control, causes a minimum of $0.5 \mu\text{s}$ run-up delay before the transmitter begins to turn on, and an additional, unacceptably long rise-time of $1 \mu\text{s}$. In contrast, the fall time is much faster, about 60 ns. The second, and more important, reason was that the F2 transmitter was not able to output pulses of consistent amplitude if the duty cycle was increased to above approximately 0.07. This was unacceptable since the gradient duty cycle used was a minimum of 0.14, and often was up to 0.40.

The F2 pulses were, instead, routed through a Kay variable attenuator to an ENI 5100L-NMR broadband amplifier. The variable attenuator allowed coarse (1 dB) manual adjustment of the gradient pulse strength. The output of the ENI was routed through a $\lambda/4$ filter and 16 pairs of series crossed 1N914B diodes to the quadrupole side of the probe. The diodes were necessary to prevent 200MHz from leaking through to the solenoid side and causing a troublesome DC offset in the spectra and images. With this arrangement we are able to pulse a maximum of approximately 60 W rf into the quadrupole coil.

Again, since it was determined that the minimum reliable time increment was $1.5 \mu\text{s}$, all steps in the pulse programs used on the MSL200 (including rf pulses, logic pulses, and delays) were at least that long.

Finally, a comment about the stability of the phase difference ϕ_d between F1 and F2 is in order. Since the MSL200 used here was not equipped with a digital phase shifter, the separate frequency synthesizers used for F1 and F2 are locked together only in that the same 10 MHz reference is used for both. No phase locking occurs at higher frequencies. In practice, phase drift between F1 and F2 was not found to be a problem for the experiment times used here (typically 1–2 hours for a 2-D image). In fact, images obtained using the F2 carrier frequency to demodulate the rf signal from the sample down to the audiofrequency signal displayed as the time domain data, were identical to those obtained using the F1 carrier frequency for the same purpose. It is entirely possible, however, that phase drift between F1 and F2 may be a problem for images requiring many hours of signal averaging. In this case, it would be advisable to provide a more rigorous phase locking scheme, for example by dividing the output of a single Larmor frequency synthesizer for use in both channels.

Appendix C

Tuning and Matching Lumped Elements

This appendix is meant to be a guide to tuning and matching the resonant circuits used in NMR probes. Since NMR probes are resonant in the radiofrequency range, an important technique in tuning and matching a probe is the standard “cut and try” method. It is helpful, however, to know where to begin. Some of what is discussed below is adapted from References [1] and [2] and the rest is adapted from some notes that were passed down from the Pines group to the Weitekamp group. References [3] and [4] also have many useful discussions on this subject.

The basic equation relevant to resonant or tank circuits is the generalized version of Ohm’s law:

$$V = I \cdot Z , \quad (\text{C.1})$$

where the complex impedance, Z , is composed of a resistive and a reactive part, R and X , respectively:

$$Z = R + iX . \quad (\text{C.2})$$

The lumped circuit elements used in NMR probes are resistors, capacitors, and inductors. These have the following complex impedances as a function of angular frequency ω :

$$Z_R = R \quad (\text{C.3})$$

$$Z_C = -\frac{i}{\omega C} \quad (\text{C.4})$$

$$Z_L = i\omega L. \quad (\text{C.5})$$

Notice, that because $V = IZ$ and $Z_C = -i/\omega C$ and $Z_L = i\omega L$, the phase of the applied voltage lags behind the current by 90° in a capacitor whereas the phase of the applied voltage leads the current by 90° in an inductor. Therefore, the reactance of a capacitor and an inductor in series tend to cancel one another. This is shown in Figure C.1.

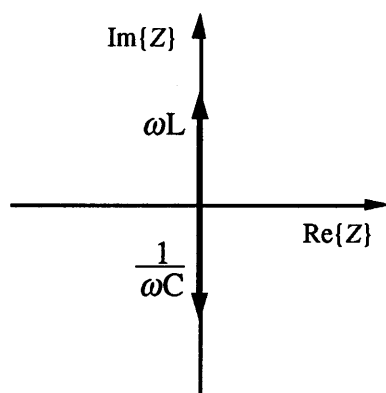


Figure C.1: Impedances of a capacitor and an inductor.

C.1 Tuned Resonant Circuits

Resonant circuits are used in NMR probes to tune the probes to the desired frequency, in our case 200 MHz. Two types of resonant circuits are used in NMR probes: parallel resonant and series resonant.

C.1.1 Parallel Resonant Circuits

A parallel resonant circuit is shown in Figure C.2. The impedance of this circuit, assuming an ideal inductor and capacitor, may be written:

$$\frac{1}{Z} = \frac{1}{Z_L} + \frac{1}{Z_C}, \quad (\text{C.6})$$

thus

$$Z = \frac{i}{\frac{1}{\omega L} - \omega C}. \quad (\text{C.7})$$

As ω nears $1/\sqrt{LC}$, the resonance condition, Z approaches infinity. This ideal circuit is very sharply resonant. In reality, the components are not ideal due to losses in the conductor and dielectric. These can be modeled as a small resistance R in series with the inductor, as shown in Figure C.3.

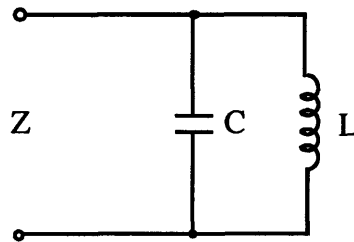


Figure C.2: Parallel resonant circuit.

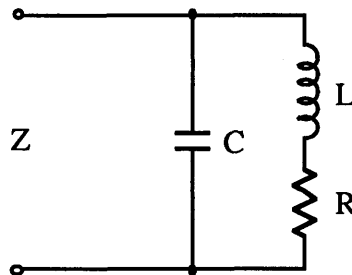


Figure C.3: Parallel resonant circuit with coil resistance.

Including the resistance R , the impedance of a parallel resonant circuit may be written:

$$\frac{1}{Z} = \left[\frac{1}{i\omega L + R} + i\omega C \right]^{-1} \quad (\text{C.8})$$

$$= \frac{R - i\omega L (1 - \omega^2 CL - R^2 C/L)^{-1}}{R^2 + \omega^2 L^2}. \quad (\text{C.9})$$

Here the resonance condition, i.e., when the impedance is real, corresponds to

$$1 - \omega^2 CL - \frac{R^2 C}{L} = 0, \quad (\text{C.10})$$

and so the impedance at resonance is

$$Z_0 = \frac{R^2 + \omega^2 L^2}{R}. \quad (\text{C.11})$$

However, assuming $\omega L \gg R$, which is typically the case for coils of NMR probes,

$$Z_0 \approx \frac{(\omega L)^2}{R}, \quad (\text{C.12})$$

which is very large, but not infinite.

The frequency response of a parallel tuned circuit, shown in Figure C.4, peaks at $\omega_0 = 1/\sqrt{LC}$. The sharpness of the peak, or in other words the efficiency of the tank circuit, is limited by the losses in the inductor and capacitor and is characterized by the Q of the circuit, where Q may be measured from the frequency response:

$$Q \approx \frac{\text{resonance frequency}}{\text{width at } -3\text{dB point}} \quad (\text{C.13})$$

$$= \frac{\omega_0}{\Delta\omega_{3dB}}, \quad (\text{C.14})$$

and may generally be defined as follows:

$$Q = \frac{\omega L}{R}. \quad (\text{C.15})$$

The Q of NMR probes is typically 100.

C.1.2 Series Resonant Circuit

The second type of resonant circuit used in NMR probes is a series resonant circuit, as shown in Figure C.5. For a series resonant circuit

$$Z = Z_L + Z_C = i \left(\omega L - \frac{1}{\omega C} \right). \quad (\text{C.16})$$

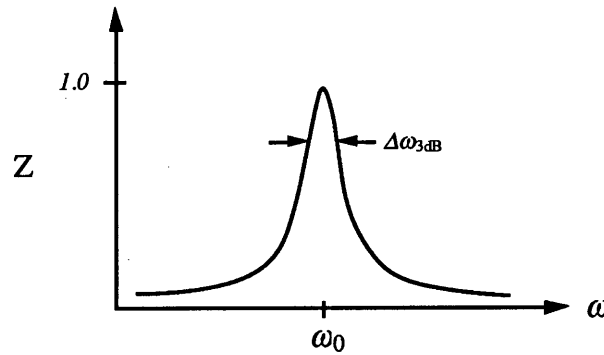


Figure C.4: Frequency response of a parallel tuned resonant circuit.

The resonance condition, the point where the impedance goes to zero, is $\omega_0 = 1/\sqrt{LC}$. At resonance, this is a low impedance circuit. The inductive and capacitive reactances have opposite signs ($i\omega L, -i/\omega C$) and the current through L and C gives rise to opposite voltage drops. Ideally, at resonance the voltages are equal and opposite and so $Z_0 = 0$. In reality, however, it is necessary to consider the losses of the components, as shown in Figure C.6.

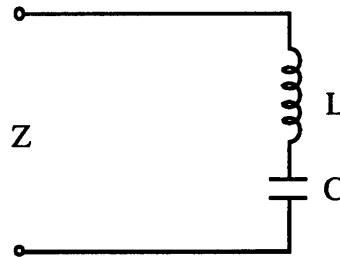


Figure C.5: Series resonant circuit.

Including the small resistance R , then, the complex impedance of a series tuned resonant circuit may be written

$$Z = i\omega L - \frac{i}{\omega C} + R, \quad (\text{C.17})$$

which is small and real-valued at resonance, as shown by the frequency response of the

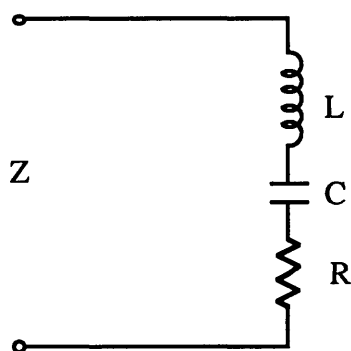


Figure C.6: Series resonant circuit with small resistance.

circuit in Figure C.7. A series tank circuit, then, behaves as a trap for signals at or near the resonance frequency, shorting them to ground.

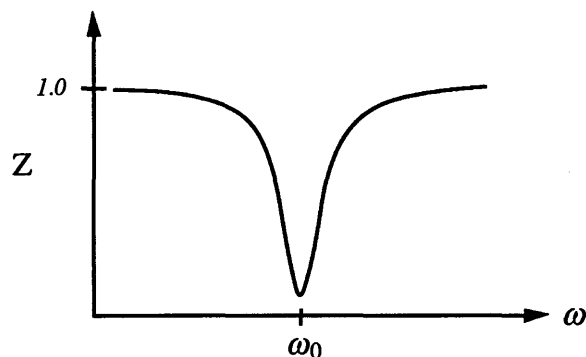


Figure C.7: Frequency response of a series tuned resonant circuit.

C.2 Tuned and Matched Resonant Circuits

For maximum transfer of power into the NMR probe, the impedance of the probe must equal the complex conjugate of the impedance of the source, which is $50\ \Omega$ for most NMR applications. Since a parallel tuned resonant circuit has a very high impedance at resonance, and a series tuned resonant circuit a very low impedance, a matching network is required in both cases to transform the probe to an impedance of $50\ \Omega$. Generally,

matching is achieved by means of a second capacitor. What follows below is a guide to selecting the appropriate capacitance to match a tuned circuit.

C.2.1 Series Tuned Parallel Matched

For the case of a series tuned resonant circuit, a parallel matching capacitor is required. A series tuned parallel matched resonant circuit is shown in Figure C.8.

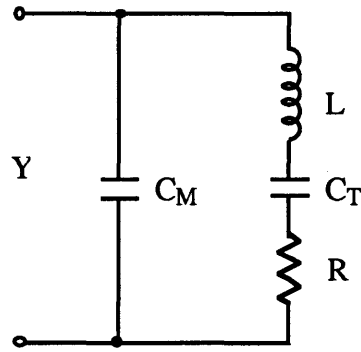


Figure C.8: Series tuned parallel matched resonant circuit.

Because of the parallel circuit, it is convenient to examine the admittance, rather than the impedance. The admittance of this circuit is

$$Y = \frac{1}{Z} = \frac{1}{Z_{C_M}} + \frac{1}{Z_L + Z_{C_T} + Z_R} \quad (\text{C.18})$$

$$= i\omega C_M + \left[i \left(\omega L - \frac{1}{\omega C_T} \right) + R \right]^{-1}. \quad (\text{C.19})$$

Now let

$$X = \omega L - \frac{1}{\omega C_T}, \quad (\text{C.20})$$

then

$$Y = i\omega C_M + (R + iX)^{-1} \quad (\text{C.21})$$

$$= i\omega C_M + \frac{R - iX}{R^2 + X^2} \quad (\text{C.22})$$

$$= \frac{R}{R^2 + X^2} + i \left(\omega C_M - \frac{X}{R^2 + X^2} \right). \quad (\text{C.23})$$

For resonance, the impedance, and thus the admittance, is real, so

$$Y_0 = \frac{1}{Z_0} = \frac{R}{R^2 + X^2}, \quad (\text{C.24})$$

and

$$X = + (RZ_0 - R^2)^{1/2}, \quad (\text{C.25})$$

where, since $Z_0 > R$, the positive square root is taken so that $C_M > 0$. This means that

$$\omega C_M - \frac{X}{R^2 + X^2} = 0 \quad (\text{C.26})$$

$$\omega C_M = \frac{X}{R^2 + X^2}, \quad (\text{C.27})$$

and

$$C_M = \frac{X}{\omega(R^2 + X^2)}. \quad (\text{C.28})$$

Finally, for $Z_0 \gg R$,

$$X \approx (RZ_0)^{1/2}, \quad (\text{C.29})$$

and

$$C_M \approx \frac{X}{\omega R(R + Z_0)} \approx \frac{X}{\omega RZ_0}. \quad (\text{C.30})$$

The suggested tuning procedure is as follows:

1. Determine the R of the series LC_T circuit near resonance without C_M .
2. Calculate X and C_M using Equations C.25 and C.30.
3. Detune the series LC_T circuit, again without C_M , so that it is inductively off resonance and $\text{Im}\{Z\} = X$. Since ϕ , the phase of Z is approximately $\pi/2$, $|Z| \approx X$.
4. Add C_M to the circuit.
5. If everything has worked correctly, $Z = Z_0$.

6. If $Z \neq Z_0$ use the observed Z to calculate a new value of R and repeat steps 2–5. This takes care of the possible error in measuring a small R with uncalibrated equipment.

C.2.2 Parallel Tuned Series Matched

Conversely, a parallel tuned resonant circuit requires series matching. Such a circuit is shown in Figure C.9. A parallel tuned, series matched resonant circuit works for frequencies up to approximately 50 MHz.

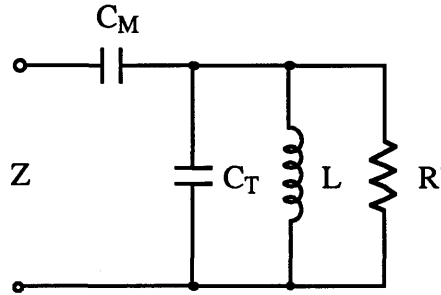


Figure C.9: Parallel tuned series matched resonant circuit.

In this case it is useful to examine the impedance of the circuit. The impedance is

$$Z = Z_{C_2} + \left[\frac{1}{Z_{C_1}} + \frac{1}{Z_L} + \frac{1}{Z_{R'}} \right]^{-1} \quad (\text{C.31})$$

$$= -\frac{i}{\omega C_M} + \left[i\omega C_T + \frac{1}{i\omega L} + \frac{1}{R'} \right]^{-1}. \quad (\text{C.32})$$

Now let

$$\frac{1}{X} = \omega C_T - \frac{1}{\omega L}, \quad (\text{C.33})$$

then

$$Z = -\frac{i}{\omega C_M} + \left[\frac{i}{X} + \frac{1}{R'} \right]^{-1} \quad (\text{C.34})$$

$$= -\frac{i}{\omega C_M} + \left[\frac{X + iR'}{XR'} \right]^{-1} \quad (\text{C.35})$$

$$= -\frac{i}{\omega C_M} + \frac{XR'(X - iR')}{X^2 + R'^2}, \quad (\text{C.36})$$

and so

$$Z = \frac{X^2 R'}{X^2 + R'^2} + i \left[-\frac{1}{\omega C_M} - \frac{X R'^2}{X^2 + R'^2} \right]. \quad (\text{C.37})$$

Again, for resonance, the impedance is real, so

$$Z_0 = \frac{X^2 R'}{X^2 + R'^2}, \quad (\text{C.38})$$

and

$$X = - \left(\frac{R'^2 Z_0}{R' - Z_0} \right)^{1/2}, \quad (\text{C.39})$$

where, since $R' > Z_0$, the negative square root is taken so that $C_M > 0$. Thus,

$$-\frac{1}{\omega C} - \frac{X R'^2}{X^2 + R'^2} = 0, \quad (\text{C.40})$$

$$\omega C_M = -\frac{X^2 + R'^2}{X R'^2}, \quad (\text{C.41})$$

and

$$C_M = -\frac{X^2 + R'^2}{\omega X R'^2}. \quad (\text{C.42})$$

Finally, for $R' \gg Z_0$, $X \approx -(R' Z_0)^{1/2}$, and

$$C_M \approx -\frac{R'(Z_0 + R')}{\omega X R'^2} \approx -\frac{R'^2}{\omega X R'^2} = -\frac{1}{\omega X}. \quad (\text{C.43})$$

In this case the suggested tuning procedure is as follows:

1. Determine the R' of the parallel LC_T circuit near resonance and without C_M .
2. Calculate X and C_M using Equations C.39 and C.42.
3. Detune the parallel LC_T circuit, again without C_M , so that it is inductively off resonance and $\text{Im}\{Y\} = -1/X$. Since $\phi \approx \pi/2$, $|Z| \approx X$.
4. Add C_M to the circuit.
5. If everything has worked correctly, $Z = Z_0$.
6. If $Z \neq Z_0$ use the observed Z to calculate a new value of R' and repeat steps 2–5.

References

- [1] P. Horowitz and W. Hill, "The Art of Electronics," Cambridge University Press, Cambridge, 1980.
- [2] E. Fukushima and S. B. W. Roeder, "Experimental Pulse NMR," Addison-Wesley, Reading, MA, 1981.
- [3] F. E. Terman, "The Radio Engineer's Handbook," McGraw-Hill, New York, 1943.
- [4] F. E. Terman, "Measurement in Radio Engineering," McGraw-Hill, New York, 1935.